Synthesis of New Metal Complexes as Chromophores for Dye-Sensitised Solar Cells.

By Alessandro Sinopoli

University of Huddersfield

A Thesis Submitted in Partial Fulfilment of the Requirements for the

Degree of Doctor of Philosophy

Department of Chemistry

The University of Huddersfield

November 2015

Copyright statement

Acknowledgements

First and foremost, I would like to thank Dr. Paul Elliott for giving me the opportunity to carry out this work, and his support and guidance throughout this project. Thanks a lot to Dr Paul Scattergood, Dr Bal Uppal and Dr Christine Welby for their help inside and outside the laboratory. I would also like to thank the Leverhulme Trust and the University of Huddersfield for the funding of this doctorate. I have fond memories that I shall take with me wherever I go and whatever I do in the future.

I would also like to thank the following people within the Department of Chemistry for their support and help with understanding specific aspects of my research; Dr. Neil McLay for NMR and mass spectrometry, Dr Jack Blackburn and IPOS for mass spectrometry, Professor Craig Rice for X-ray crystallography, I would also like to thank Dr Elizabeth Gibson at the Newcastle University for allowing us use her instrumentation and Dr Chris Wood for his help. A big hug goes to all the past and present researchers and students working in X1/07 lab, especially Rob, Chris, Becca, Aaron, Jason, Daniel and Kieran. Thanks Janet for your patience and kindness in handing my last minute requests.

I also thank the entire XG/11 office crew who made my time in Huddersfield so enjoyable, especially the Kadi Shack and Laura. I will miss the fun we have had mostly at each other's expense!

The biggest *grazie di tutto* goes to the Italian Society fellas, for all their support they have provided, for all the good times together and for making me feel like home. Thanks to Alan Tobi for his impressive job with the international students.

Last but not least, I would like to thank my parents, my family and my friends for their support over recent years.

Abstract

Nowadays the production of energy originating from renewable sources is a burning issue, in particular a lot of efforts are made for a reduction of worldwide energy consumption for a sustainable world. The efficient and low-cost direct conversion of solar photons into electricity is one of the most important scientific and technological challenges of this century. Up to now, commercially available photovoltaic technologies are based on inorganic materials, which require high costs and highly energy consuming preparation methods. Organic photovoltaic can avoid those problems, but the best efficiencies of organic-based photovoltaic cells are at the moment around 7%. Dye-sensitised solar cells (DSSCs) represent a concrete solution for harnessing solar energy and converting it into electrical energy and 11% efficiencies have been reached with the most performing Ru(II) sensitizers, such as N3 (cis-di(thiocyanato)bis(2,2-bipyridyl-4,4′-dicarboxylate) ruthenium(II)) and N719 (bis(tetrabutylammonium)-cis-di(thiocyanato)-N,N′-bis(4-carboxylato-4′-carboxylic acid-2,2′-bipyridine) ruthenium(II)). The photosensitiser dye plays a strategic role in DSSCs, absorbing the solar light and promoting the formation of an electron-hole pair which is separated, transported, and then collected at the electrodes. Other organometallic complexes have also been used as dyes in DSSCs, for examples complexes of Pt(II), Fe(II), Os(I), Cu(I), Re(I) and Ir(III). Iridium complexes are potentially good candidates for application in DSSCs. The absorbed photon to current yield in iridium based DSSC devices is comparable to the ruthenium dyes. Moreover, the ruthenium dyes produce current only by injection from metal to-ligand charge transfer (MLCT) states whereas, for iridium dyes, it would be possible to combine injection from both MLCT and ligand-to-ligand charge transfer (LLCT). However, up to now, low molar extinction coefficient and a narrow absorption spectrum at relatively high energy (380 nm) are critical factors that limit the efficiency of Ir(III) dyes. For this reason, the reported DSSCs solar cells based on Ir(III) complexes are characterized by low efficiencies.

In this thesis, I present my results on the design and synthesis of new dyes for DSSC application.

Described in Chapter 2 is the synthesis of iridium (III) complexes where aryl-1,2,3-triazole ligands act as cyclometalating ligand and 4,4’-dicarboxy-bipyridine as N^N ancillary/anchoring ligand. The photophysical effects of these complexes were investigated. It was found that by using different substituents on the phenyl ring, or a different aryl system, it is possible to tune the absorption and the emission of these complexes. Computational studies showed HOMO-LUMO directionality of these

complexes is ideal for the electron injection once they are applied on DSSC devices. Preliminary efficiency test have been carried out with promising results.

Described in Chapter 3 is the synthesis of iridium (III) complexes designed as dyes for p-type DSSC. For these complexes a phenylpyridine containing a carboxylic group has been used as cyclometalating/anchoring ligand whereas different diimine ligands act as ancillary ligands. The photophysical effects of these complexes were investigated. It was found that using different π-systems on the ancillary ligand is possible to tune the absorption of these complexes and to enhance the spatial separation between HOMO and LUMO. Computational studies confirm the potential use of these complexes on DSSC devices. Preliminary tests on NiO devices have been carried out.

Described in Chapter 4 is the synthesis of a novel bipyridine-1,2,3-triazole based anchoring group. The novel triazole ligand might act as spacer between the metal oxide and the metal center insulating the electronic coupling and avoid the recombination. This N^N ligand, obtained through click of azido-bpy and acetylenedicarboxylate, was used as an anchoring ligand in ruthenium, iridium and rhenium complexes. The set of three metal complexes was compared with their dicarboxybipyridine analogues. Looking at the photophysical and electronic properties of these new complexes they seem comparable with their dicarboxybipyridine analogues. Preliminary anchoring tests on TiO_2 have been carried out.

Described in Chapter 5 is the design and synthesis of two cyclometalated Ir(III)–coumarin molecular arrays, which show intense absorption of visible light, one belonging to p-type dyes family and another belonging to n-type one. The two complexes have been characterised and tested on both TiO_2 and NiO cells.

Table of Contents

List of figures

List of schemes

List of tables

List of abbreviations

°	Degrees
°C	Degrees Celcius
^{13}C NMR	Carbon-13 nuclear magnetic resonance
^{1}H NMR	Proton nuclear magnetic resonance
^{1}MLCT	Singlet metal-to-ligand charge transfer
^{3}MLCT	Triplet metal-to-ligand charge transfer
Å	Angstrom
AM	air mass
aq	Aqueous
bpy	2,2'-bipyridyl
bpypz	bipyridine-pyrazole
bt	2-phenylbenzothiazole
btz	4,4-bi-1,2,3-triazol-4-yl
$CDCl_3$	Deuterated chloroform
CE	counter electrode
CH_3CN	Acetonitrile
cm^{-1}	Wavenumbers
COD	cyclooctadiene
COSY	Correlation Spectroscopy
CuAAC	Copper catalysed azide alkyne cycloaddition
dcb	dicarboxybipyridine
DCM	Dichloromethane
DFT	Density functional theory
DMF	Dimethyl formamide
DMSO	Dimethyl sulfoxide
DSSC	Dye sensitized solar cell
Ea	activaction energy
ESI-MS	Electrospray ionization mass spectrometry
eV	Electronvolt
Ff	fill factor
FT-IR	Fourier transform infra-red
FTO	Fluorine-Tin-Oxide
g	Grams
HOMO	Highest occupied molecular orbital
HPLC	High performance liquid chromatography

HRMS	High resolution mass spectrometry
Hz	Hertz
ILET	interligand electron transfer
IPCE	Incident photo-to-current efficiency
Isc	inter system crossing
ITO	Indium-Tin-Oxide
IV	current voltage
J	Coupling Constant Hz
K	Kelvin
K_B	Boltzmann costant
Kcal mol^{-1}	Kilocalories per molecule
K_{nr}	non radiative costant
K_r	radiative costant
LC	Ligand centred
LEEC	Light emitting electrochemical cell
LUMO	Lowest unoccupied molecular orbital
M	Molarity/Molar
m/z	mass/charge
MC	Metal centred
mCPBA	*meta*-chloroperbenzoic acid
mg	Milligram
mins	Minutes
mL	Millilitre
MLCT	Metal-to-ligand charge transfer
MLLCT	Metal-to-ligand-to-ligand charge transfer
mmol	Millimole
MO	molecular orbital
MOx	Metal Oxide
mV	milliVolt
mW	milliWatt
nm	Nanometer
ns	Nanosecond
n-type	negative charge type
OLED	Organic light emitting diode
PCE	Power conversion efficiency
PE	Petroleum ether
PL	photoluminescence

PLED	Polymer light emitting diode
ppm	Parts per million
ppy	2-phenylpyridine
ps	picosecond
p-type	positive charge type
PV	photovoltaic
py	Pyridine
q	magnitude of the electrical charge on the electron
S_0	Singlet ground state
T_1	Lowest triplet excited state
THF	Tetrahydrofuran
TMS	Trimethylsilyl
UV-vis	Ultraviolet-visible
Voc	Open circuit Voltage
WE	working electrode
δ	Delta (chemical shift)
Ω/sq	Ohm/square

1 Introduction

1.1 Global energetic demand

Energy is the pulsing heart of civilization. Since the discovery of fire and the advent of agriculture, the human technological progress has always been matched with the capacity of converting constantly bigger amount of energy in new forms. During the last 160 years, the use of fossil fuels led to impressive innovations in fields such as agriculture, medicine, transport and communications, definitely raising the standards of living for a conspicuous part of the planet's population. Unfortunately the global sources of fossil fuels are not limitless, not renewable and their use is becoming a big environmental issue because it is responsible for high emission of CO_2 in the atmosphere, hence global climatic changes. [1, 2]

Boosted by the population growth, the world energy demand is destined to increase by up to 25% during the next 25 years. [3] In order to satisfy this imminent energy need, massive investments will be necessary. The environmental issues will require a quick transition from the traditional to new, "green" and renewable energy sources. The key to this transition will be the development of new technologies to apply on both small and local scales. On a global scale, from a wide range of alternative sources as solar, wind and biomass, solar energy seems to be the one that better combines availability, direct conversion into electrical power and environmental impact requirements. Every hour our planet receives from sunlight an amount of energy equal to 4.3×10^{20} J; the use of this massive quantity of energy needs the development of systems able to catch the light and convert it in a "storable" form. Eons before the birth of human kind, nature started using photosynthesis as a sunlight conversion mechanism for many life forms. [4] Photosynthesis together with cellular respiration, represent a model to imitate in the design of devices able to convert solar energy into chemical energy and store it. In this perspective, satisfying the energy demand will mean the realisation of diffuse systems able to directly convert light in solar fuels, using abundant and low cost materials. [5]

Since the 1940, a growing interest to photo devices led to the birth of a class of silicon solar cell, based on a p-n junction of doped silicon, able to separate a hole and an electron under irradiation and to convert it in an electrical current. From there, solar cells have been integrated into satellites, calculators, watches, street lights, reaching conversion efficiencies of approximately 25%. [6, 7] Consequentially, industry for solar cells is growing quickly and photovoltaic (PV) energy production passed the value of 80.8 TWh in 2013 in Europe. [8] Silicon photovoltaic cells represent, nowadays, 80% of the photovoltaic market, however increasing device efficiencies and keeping production costs low is doubtless a key point for a fast PV energy development. Cost-effective PV devices are therefore extremely attractive. Different inorganic materials, such as

amorphous silicon, copper indium gallium diselenide (CIGS), gallium arsenide (GaAs) and cadmium telluride (CdTe) have been developed giving efficiencies of 10-32%. [7] However the use of these materials/technologies on a large scale might clash against their difficulties in large scale manufacture, their cost, the toxicity of some used materials and hence their environmental impact.

Dye-sensitised solar cells (DSSC) represent a considerable alternative to the aforementioned devices. In 1991, O'Regan and Grätzel gave a fundamental contribution to the evolution of DSSC, reporting devices with efficiencies of 7-8% (Figure 1.1), based on a trimeric ruthenium (II) complex ($Ru(dcb)_2[(\mu\text{-}(CN)Ru(CN)(bpy)_2]_2$) adsorbed onto nanoporous TiO_2 film. [9] The synergy between the high active surface area of titanium oxide and the adsorbed ruthenium complex, led to a tangible incident photon conversion. The understanding of the electronic mechanisms and working principles of the device [9] generated a substantial interest and attention from many research groups, hence innumerable papers have been published in this field during last two decades.

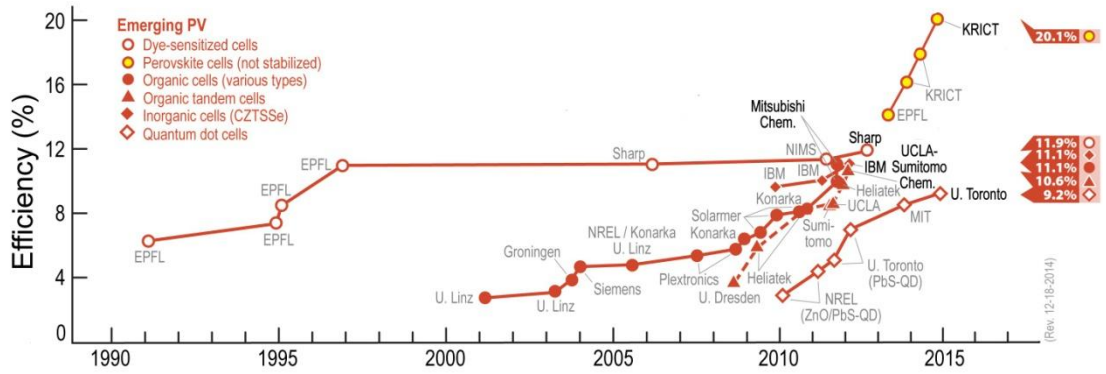

Figure 1.1. Photovoltaic cell efficiencies chart.[10]

1.2 Operating Principles of Dye-Sensitised Solar Cells

The dye sensitised solar cells, or Grätzel cells, are devices inspired by the principles of photosynthesis, able to convert light in electrical current; they are multi component devices made using a dye, able to absorb a wide range of the solar spectrum, [11] a nanocrystalline semiconductor, generally titanium oxide (anatase) and a redox mediator, to assist the redox processes inside the cell. The use of a nanoporous semiconductor oxide and the size of the nanoparticles are the keys to maximise the surface area and consequentially the dye adsorption. All the cell components are assembled together in a sandwich structure (Figure 1.2) between a working electrode, e.g. TiO_2 deposited on a transparent fluorine-doped tin oxide (FTO) conducting glass,

and a counter electrode consisting of typically a layer of platinum coated on FTO conducting glass. The two electrodes are sealed with a thermoplastic, and the cell is filled with the electrolyte.

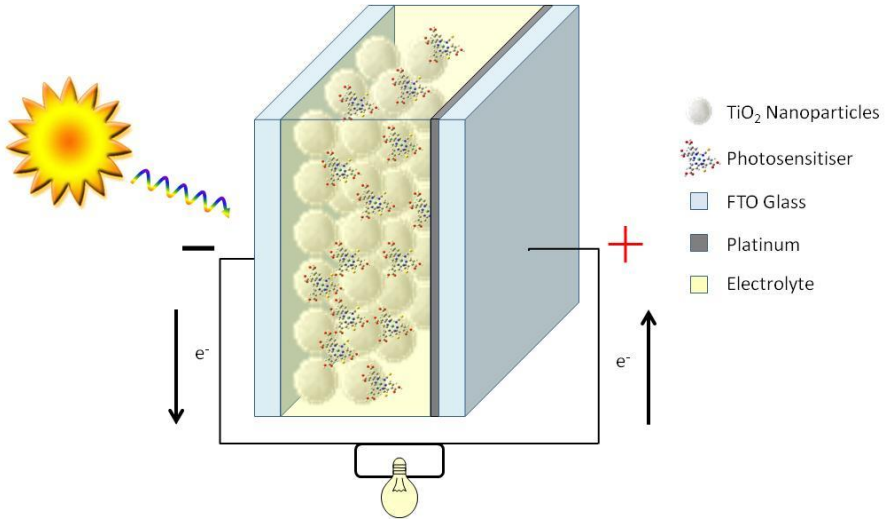

Figure 1.2 Schematic representation of the cross-section of a DSSC.

In Figure 1.3 are shown the main photoinduced and redox processes taking place inside the cell are shown.

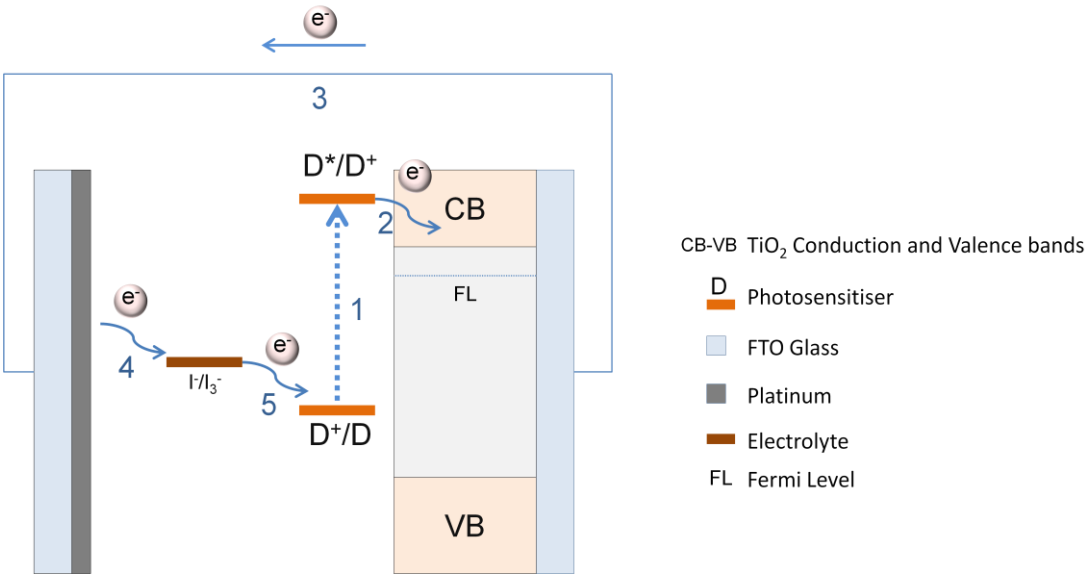

Figure 1.3 Main operating principles of a n-type dye-sensitised solar cell. D, D^+, D represent the photosensitiser in the ground, and the oxidised and excited states, respectively.(1) photon absorption, (2) electron injection to the TiO_2 conduction band, (3) external load, (4) regeneration of the electrolyte and (5) regeneration of the oxidised dye.*

All the charge transfer reaction reported in Figure 1.3 can be summed up by four main equations:

- (Equation 1) Photoexcitation: $D + hv \rightarrow D^*$
- (Equation 2) Electron injection: $D^* + TiO_2 \rightarrow D^+ + e^-\text{-}TiO_2$
- (Equation 3) Electrolyte regeneration: $I_3^- + 2e^- \rightarrow 3I^-$
- (Equation 4) Oxidised dye regeneration: $2D^+ + 3I^- \rightarrow 2D + I_3^-$

When an incident photon is absorbed by the dye, it causes the promotion from the ground state D to the excited state D* (Equation 1). Subsequently, the excited electron is injected into the semiconductor conduction band leaving the dye in an oxidised state D^+ (Equation 2). The injection reaction can be prevented by some loss reactions. One of these processes is represented by the deactivation of the dye excited state that, due to radiative or no-radiative reactions, can deactivate to its ground state without injecting the electron (Equation 5). The injected electron can recombine with the oxidised dye (Equation 6) or most probably, moving through the titanium network, arrives at the back contact and reaches the counter electrode (cathode) thanks to an external load. The cathode, with its layer of catalyst, reduces the triiodide to iodide present in the electrolyte (Equation 3). The iodine closes the circuit regenerating the oxidised dye (Equation 4). However the triiodine can be reduced by recombination with an electron injected in TiO_2 CB (Equation 7). In order to promote the direct reactions and avoid the loss reactions, it is necessary to use dyes with a LUMO higher in energy than the TiO_2 CB (for a more efficient injection), and a HOMO energy lower than the redox potential of the electrolyte (for a more efficient dye regeneration). To understand which the most favourable processes are between direct and loss ones, it's crucial to know the kinetic rates of these reactions. In fact, the reasonable efficiencies of DSSC devices are attributed to the timescale of the loss processes, which are generally orders of magnitude slower than the direct processes. [12] For example, the electron transfer (injection) from ruthenium **N3** (cis-Bis(isothiocyanato)-bis(2,2'-bipyridyl-4,4'-dicarboxylato) ruthenium(II)) and TiO_2, is one of the fastest known chemical processes. [13]

- (Equation 5) Dye excited state deactivation: $D^* \rightarrow D$
- (Equation 6) Back electron transfer: $e^-\text{-}TiO_2 + D^+ \rightarrow TiO_2 + D$

- (Equation 7) $I_3^- + 2e^-\text{-}TiO_2 \rightarrow 3I^- + 2TiO_2$

1.3 Solar cell parameters

Grätzel cells, under light irradiation, behave as current generators. In order to describe their mechanism and to characterise their performances, current-voltage (JV) and Incident photon-to-current efficiency (IPCE) measurements are applied.

Under irradiation, the total current generated by the device I_{tot} is described as:

$$I_{tot} = I_{sc} - I_0\left(e^{\frac{qV}{k_BT}} - 1\right)$$

Where I_{sc} (short circuit current) represents the photo-current, due to the photo-induced charge separation and so is directly proportional to the irradiation intensity. I_o defined as reverse saturation current is that part of the reverse current in a semiconductor diode caused by drift of minority carriers from the neutral regions to the depletion region. IPCE and current-voltage measurements represent the main characterization methods for DSSCs. In short circuit conditions, the current generated by the device I_{sc} has its maximum value, on the other side the voltage is zero, presenting no load resistance so no current is lost. Vice versa, in open circuit conditions, current is zero, so the ideal resistance is infinite, and the voltage reaches its maximum value V_{oc}, which is defined as:

$$V_{oc} = \frac{k_BT}{q}\ln\left(\frac{I_{sc}}{I_0} + 1\right)$$

Where k_B is the Boltzmann constant and q is the electrical charge on the electron. The maximum value that this parameter can assume is equal to the difference between the Fermi level on the semiconductor and the redox potential of I^-/I_3^- couple.

In a photovoltaic cell, the power generated grows together with the voltage up to a maximum value W_{max}. Beyond this value the voltage reaches the V_{oc} value but the power goes to zero. W_{max} is defined as the product of V_{max} (lower than V_{oc}) and I_{max} (lower than I_{sc}). The ratio between the power generated with a load and without is defined as the Fill Factor (FF):

$$FF = \frac{V_{max}I_{max}}{V_{oc}I_{max}}$$

Intuitively, the fill factor is an essential parameter to evaluate the losses inside the cell.

The efficiency η is calculated using the equation:

$$\eta = \frac{J_{max}V_{max}}{W_{in}} = \frac{FF(J_{sc}V_{oc})}{W_{in}}$$

Where J indicates the current density ($A \cdot cm^{-2}$) and W_{in} is the incident irradiation power.

The IPCE represents the ratio between the number of electrons generated by the photovoltaic effect and the number of incident photons on the device and is expressed as:

$$IPCE = 1240 J_{sc}/W_{in}\lambda$$

The value 1240 comes from the values of the constants *h*, *c* and *e* whilst *λ* is the wavelength of light in nm.

1.4 Main components of Dye-Sensitised Solar Cells

As previously mentioned, a DSSC is a multi component sandwich device where the synergy and cooperation between photosensitiser, metal oxide, electrolyte and counter electrode, are fundamental for achieving high efficiencies and optimising each individual component is the only rational way to improve the device performances.

The working electrode is doubtless the "engine" of the cell, here in fact the process of light harvesting, the charge injection and the electron transport take place. The electrode is made by a transparent glass contact, covered by a layer of conductive metal oxide, generally fluorine-doped tin oxide (FTO) or more rarely indium tin oxide (ITO). The latter is thermal unstable and its resistance increases after the TiO_2 sintering process; on the top of the glass conducting face, a layer of TiO_2 nanoparticle paste or gel is deposited and thermally sintered in order to create a solid metal oxide network with a high porosity. The titanium oxide with its wide band gap (about 3.2 eV), its crystal packing and the low cost, resulted to be the ideal candidate as semiconductor in DSSC in terms of porosity, surface area and electron diffusion. [14] However its absorption across the violet and the ultraviolet is the reason for the need for sensitisation with dyes able to absorb in the visible range of light. [11] The dye must also be able to chemically bind to the titanium oxide and inject an electron into its conduction band.

Compared to a silicon single crystal device, the use of a nanocrystalline metal oxide sounds disadvantageous because the mesoporous structure allows the permeation of the electrolyte, increasing the electron-hole recombination, also the conductivity of the metal oxide is low and its structural inhomogeneity decreases the electron diffusion rate. [15] However, the balance between direct and inverse reactions, the optical transparency of the nanocrystalline network, together with its massive surface area,

permit the adsorption of a large number of dye molecules on the semiconductor surface.

Another main "character" of a DSSC mechanism is the electrolyte within the redox couple. Generally the electrolytes used in DSSCs are divided in liquid, quasi-solid-state and solid electrolytes.[16] The principal characteristics of the electrolyte are high conductivity, high thermal, electrochemical and optical stability; furthermore, the redox couple should posses: a redox potential adequately positioned relative to oxidation potential of the dye to promote the regeneration; high solubility in the electrolytic media to increase the number of charge carrier; high diffusion rate for an efficient charge transport; high number of reduction/oxidation turnover; a negligible absorption in the visible range of the spectrum. Up to now, most of DSSC studies have been based on the used of the iodide/triiodide couple, dissolved in an organic solvent. The chemistry and electrochemistry of the I_3^-/I^- couple is extremely complicated, related to its two-electron radical processes. Its use also causes corrosion issues undermining the device sealing and stability. The pursuit of a new efficient redox mediator led to the used and study of many other pairs such as Br^-/Br_3^-, [17] $SCN^-/(SCN)_2$, [18] ferrocene/ferrocenium, [19] Co(II)/Co(III) complexes,[20] Ni(III)/Ni(IV) complexes, [21] thiolate/disulphide dimer [22] and Cu(I)/Cu(II) complexes. [23]

Cobalt polypyridine complexes seem to be good candidate to replace the I^-/I_3^- couple, in terms of low optical absorption, tunable redox potential and low corrosiveness.[20] However, for many DSSC systems the efficiencies obtained with cobalt electrolytes are still low compared to I^-/I_3^- couple, the reasons are attributable to the slow mass transport[24] and slow electrolyte regeneration [25] of these cobalt mediators. However, it is important to highlight how impressive performances have been recently [26] [27, 28] achieved with the use of cobalt electrolyte, specifically Feldt *et al.* achieved a V_{oc} of 1000 mV using cobalt phenanthroline redox shuttles, [29] and Yum *et al.* in 2012 reported a cell efficiency over 10% using $[Co(bpypz)_2]^{2+/3+}(PF_6)_{3/2}$ complex (bpypz = 6-(1H-pyrazol-1-yl)-2,2′-bipyridine)) as a redox mediator. [30]

The redox couple is not the only component of the electrolyte mixture; the counter ions of the anionic half play a fundamental role in tuning the conductivity and the overall voltage. In fact, small cations as Li^+, Na^+, K^+, Cs^+ can easily penetrate in the nanoporous semiconductor and, attracted by the excess of negative charges, adsorb on it shifting the Fermi Level, hence affecting the V_{oc}. [31] Whereas, the small cations are part of the redox salt, other molecules can be added on purpose to the electrolyte, in particular heterocyclic azo compounds. These additives, such as 4-tert-butylpyridine

(TBP) can be adsorbed on TiO_2 surface altering the FL,[32] [33] forming a Helmholtz layer able to reduce recombination at the I^-/I_3^- - TiO_2 interface. [34]

In order to efficiently regenerate the redox mediator, a counter electrode with low resistance and high reduction/oxidation rate is needed. As for the working electrode, the counter electrode is made by a transparent FTO glass coated with a conductive catalyst thin layer; platinum is widely used for this intent. [35] To avoid the use of this precious metal, other low-cost materials, such as steel, Ni, carbon material have been used [36] [37] achieving efficiencies still far from analogous devices using Pt coated electrodes. [37]

Between all the components of a solar cell, the sensitiser deserves a particular attention and for this reason it will be described in a specific section (Session 1.6).

1.5 P-type dye-sensitised solar cells (p-type DSSCs)

In the conventional photoanodic DSSCs (n-type), photocurrent generation results from dye-sensitised electron injection into conduction band semiconductors, such as TiO_2. In contrast, for photocathodic DSSCs (p-type), electron transfer takes place from the valence band of the p-type semiconductor (NiO being the most commonly used to date) to the photoexcited dye. The prospect of using p-type cathodes and combining them together with n-type anodes to realize dye-sensitised tandem devices has recently generated renewed interest in p-DSSCs.[38, 39]

Structurally wise a p-type DSSC is similar to a n-type cell, in other words a sandwich device made by a cathodic working electrode, based on sensitised NiO, an anodic Pt coated counter electrode and a redox mediator, mainly I^-/I_3^- or Co^{2+}/Co^{3+} based redox mediator [40, 41] (Figure 1.4). Additives are generally not used in electrolytes for p-type solar cells because the Fermi Level is very close to the valence band of NiO. A higher V_{oc} can be achieved doping the nickel with other metals (e.g. cobalt) shifting the Fermi Level to lower energies. [42]

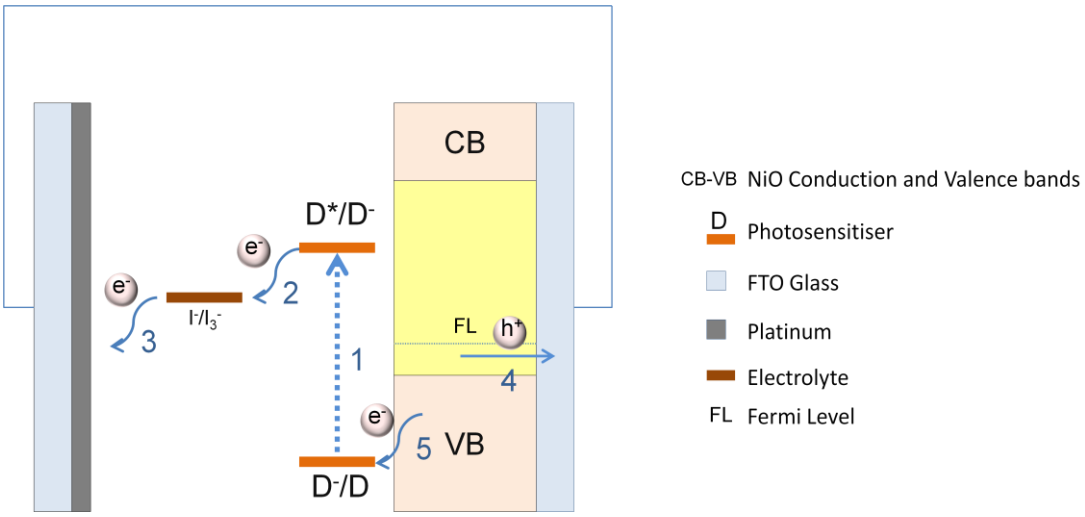

Figure 1.4 Main operating principles of a p-type dye-sensitised solar cell. D, D^-, D represent the photosensitiser in the ground, and the reduced and excited states, respectively.(1) photon absorption, (2) reduced dye regeneration, (3) regeneration of the electrolyte, (4) hole injection into NiO valence band, (5) electron transfer to the dye.*

All the charge transfer reaction reported in Figure 1.4 can be summed up in four main equations:

- (Equation 8) Photoexcitation: $D + hv \rightarrow D^*$
- (Equation 9) Hole injection: $D^* \rightarrow D^- + h^+(NiO)$
- (Equation 10) Reduced dye regeneration: $D^- + 1/2\ I_3^- \rightarrow D + 3/2\ I^-$
- (Equation 11) Electrolyte regeneration at the counter electrode: $3/2\ I^- \rightarrow 1/2\ I_3^- + e^-$ (Pt)

When an incident photon is absorbed by the dye, it causes the promotion from the ground state D to the excited state D* (Equation 8). Subsequently, an electron is injected form the semiconductor valence band to the excited dye leading in a reduced state D^- (Equation 9). The reduced dye is now regenerated by reducing the electrolyte (Equation 10). The anode, thanks to its Pt layer, regenerates the redox shuttle (Equation 11) and the collected electrons arrive at the back contact and reach the anode through to an external circuit. The main current loss affecting p-type cell is attributed to the recombination of the reduced dye with the holes injected into the NiO (Equation 12). Unfortunately most of the reported dyes exhibit geminate recombination rates mainly between 10-100 ps leading to inferior efficiencies relative to champion n-type cells. [43, 44]

- (Equation 12) Geminate recombination: $D^- + h^+(NiO) \rightarrow D$

1.6 The Molecular Sensitiser

1.6.1 Characteristics of Molecular Sensitisers

The incident photon to current conversion and the overall efficiency are the main parameters used to describe a solar cell in working conditions under irradiation. The cell performances are closely related to the amount of light harvested by the dye especially in the visible or near-IR range of the spectrum where the solar radiation intensity is stronger (Figure 1.5). In order to standardize the solar cell measurements, modern solar simulators reproduce the solar spectrum according with precise value of air mass (AM). The amount of air, in the atmosphere, crossed by a photon can vary in relationship to the inclination of sun rays. For this reason the air mass is defined by the ratio between the thickness of optical path crossed by a photon in the atmosphere and the same thickness considering the solar zenith. The AM value used by commercial solar simulator is AM 1.5, which corresponds to the air mass crossed by the sun light considering a solar zenith angle of 48.2°. The corresponding solar power is 982 Wm^{-2} (rounded to 1000 Wm^{-2}).

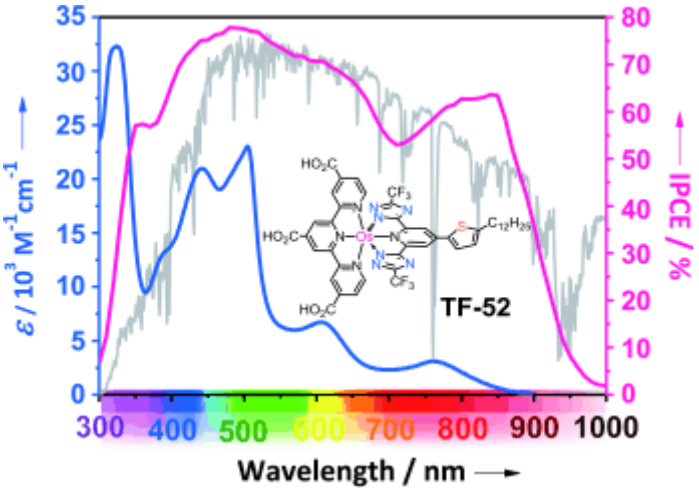

*Figure 1.5 AM 1.5 solar spectrum (grey line); absorption and IPCE spectrum of **TF-52** osmium (II) based dye (blue and magenta line respectively). Reproduced from ref [45] with permission of John Wiley & Sons.*

Because the role of the photosensitiser is crucial for the cell working, including key functions as absorbing light, injecting electrons into the metal oxide and being easily regenerated by the redox shuttle, it is essential to design the photosensitiser according to well studied photophysical and structural characteristics. [46]

Figure 1.6 General block design of an organic DSSC chromophore: an antenna (blue), a spacer (red), an anchoring group (yellow)

A general, but at the same time very pondered design is shown in Figure 1.6. The antenna fragment is the main responsible for the light harvest of the dye, it is usually made up of aromatic conjugated π systems and it can act as electron donor (in a n-type design) or electron acceptor (in a p-type design). The antenna is also responsible for the charge separation lifetime and it might act as reaction site between the electrolyte and the dye.

The introduction of π-conjugated systems, such as thiophenes or styrenes, between the antenna and the anchoring group represents a good strategy for extending and red shifting the absorption spectrum of the sensitiser, as result of the energy levels tuning. Also the addition of spacers that result in an increase of the spatial separation between the separated charges can lead to a lower recombination rate.

The anchoring group, not only determinates a strong binding to the metal oxide, but also the efficiency of the electron injection. Although a sensitiser can bind the semiconductor surface through hydrogen bonds, electrostatic or van der Waals forces, [47] the binding between the OH groups on the semiconductor surface and the sensitiser anchoring groups, ensure a strong and stable dye adsorption together with a solid orbital overlap.

Nowadays, the carboxylic acid represents the most commonly used anchoring group. Other moieties such as boronic acid, [48] cathecol, [49] phosphonic acid[50] and silanes have also been used. Despite the strong binding through the carboxylic acid, the process is reversible and a basic environment can lead to dye desorption. Depending on the semiconductor surface and the dye self, the carboxylic acid can attach using different motifs (Figure 1.7). [51, 52]

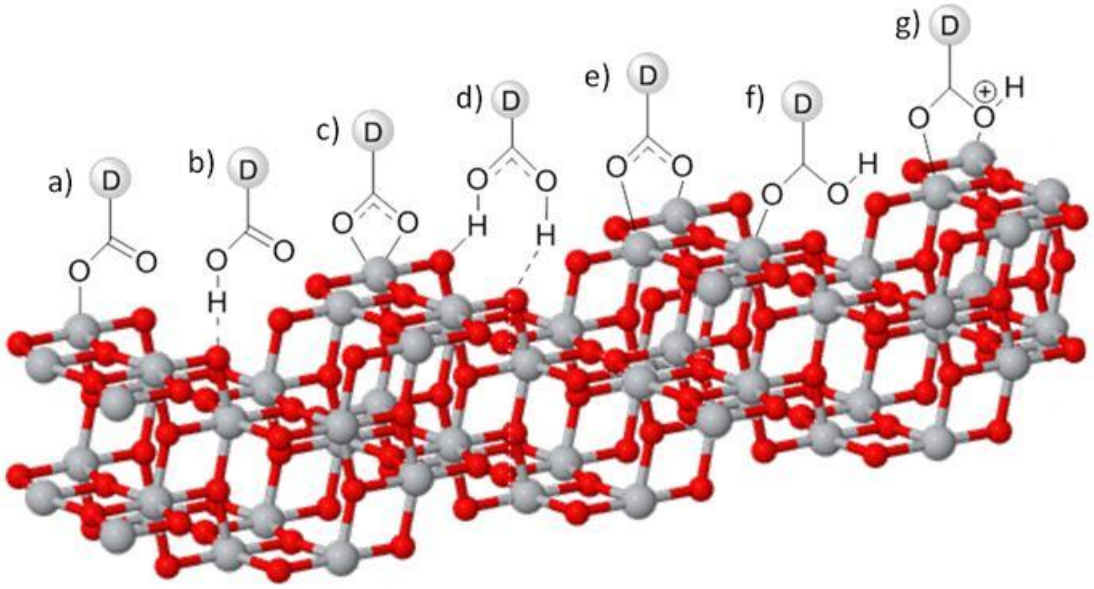

Figure 1.7 Possible binding modes of a carboxylic acid group to TiO_2-anatase. (a) Ester linkage, (b, d) hydrogen-bonding interactions, (c) chelate binding, (e, g) bidentate bridges and (f) monodentate binding through CO.

The structural design of a sensitiser is not the only need to ensure a good efficiency, even the energy levels need to be "designed". The HOMO-LUMO gap should be narrow enough to shift the absorption in the visible and a well distinct orbital localization should ensure an ideal charge separation or directionality. Specifically, for a n-type cell, the HOMO potential of the dye should be sufficiently positive compared to the electrolyte redox potential for efficient dye regeneration, whereas the LUMO potential should be sufficiently negative to be above the potential of the conduction band edge of the TiO_2 with electron density possibly delocalised across the anchoring ligand to promote the charge injection. Conversely, for a p-type cell, the LUMO potential of the dye should be sufficiently negative compared to the electrolyte redox potential for efficient dye regeneration, whereas the HOMO potential should be sufficiently positive to match the potential of the valence band edge of the NiO with electron density ideally located across the anchoring ligand to avoid the charge recombination.

Modifying the different blocks independently offers a systematic way to record the contributions of different groups and fine tune the HOMO and LUMO energies. In addition, the compatibility of novel dyes and future semiconductor-redox systems could more easily be investigated by using an already existing HOMO and LUMO energy library.

1.6.2 Classification of Molecular Sensitisers

During last three decades, a wide range of sensitiser have been studied, applied and developed in the solar cell field. Sensitisers can be divided in three main categories: organic, [53-55] natural [56] and metal-containing complexes. [57]

The use of organic dyes is undergoing intense investigations because they are characterised by high molar extinction coefficients and they allow a wide selection of structural designs and they do not include precious metals. The main organic dyes include structures as phthalocyanines, perylenes, squaraines, porphyrins, achieving medium to high efficiencies (Figure 1.9). [53, 54, 58]

A groundbreaking result was achieved by Koumura *et al.* in 2006 with the dye **MK-2**, characterised by alkyl oligothiophene linkers, reporting efficiency of 7.7%. [59] In 2011 Yella *et al.* combining the sensitisation of a electron-donor zinc porphyrinporphirin dye with a cobalt redox mediator obtained a conversion efficiency of 12% with a voltage of nearly 1V, [27] since then **YD-o-C8** has become a benchmark in the use of n-type dyes. In 2014 Luo *et al.* [60] modified **YD-o-C8** using a phenyl-functionalized N-perylene realising **WW-6** and achieving the same efficiency as the benchmark. In 2015 the N-perylene fragment was modified conjugating it with an ethynylbenzothiadiazolylbenzoic acid resulting in a 12.5% efficiency (Figure 1.8).[55]

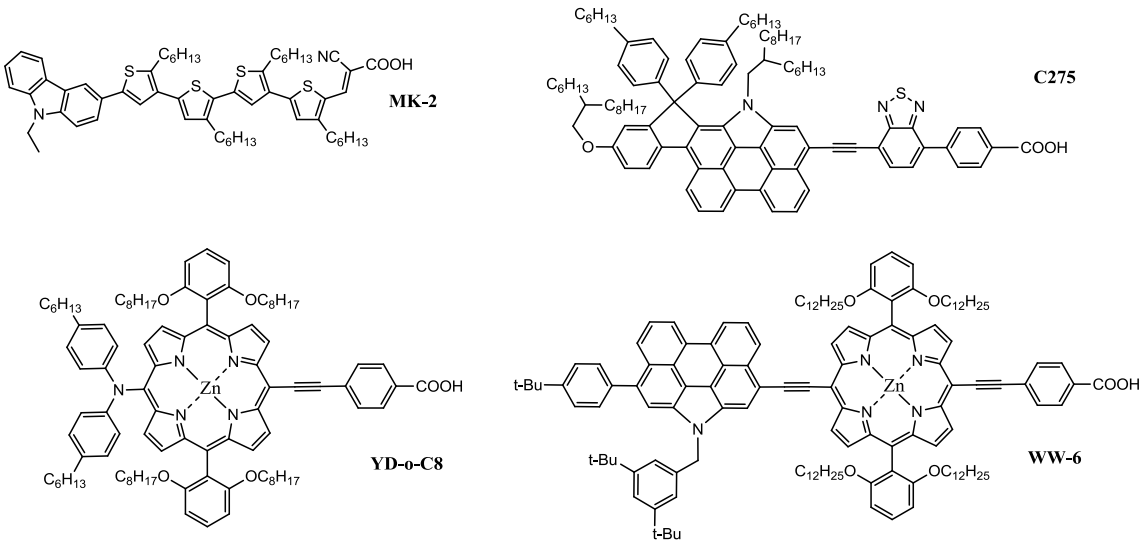

Figure 1.8 Molecular structures of a series of high efficiency organic dyes. ***MK-2*** *(top left);* [59] ***C275*** *(top right);* [55] ***YD-o-C8*** *(bottom left);* [27] ***WW-6*** *(bottom right).* [60]

However the use of organic dye is still limited due to some advantages compared to inorganic metal complexes dye. In particular their absorption profile can be narrow, e.g.

with phthalocyanines. Flat aromatic organic system, as perylenes, can also show aggregation phenomena reducing the electron inject rate. Chemical stability can also be poor as for squaraines.

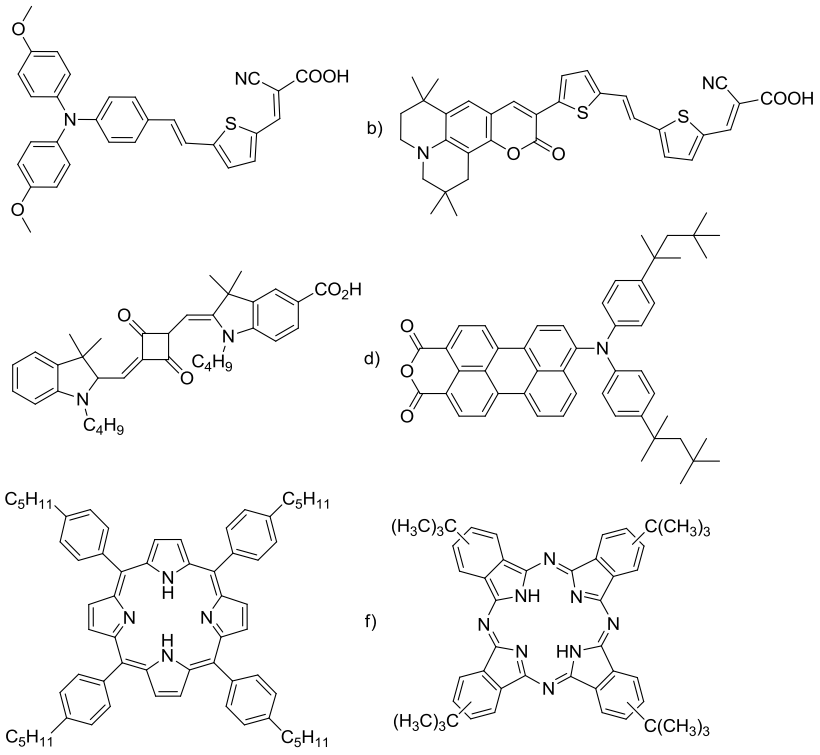

Figure 1.9 Molecular structures of a series of example organic dyes. (a) Donor–π-acceptor dye with a triphenylamine donor moiety, [61] (b) donor–π-acceptor dye with a coumarin donor moiety, [62] (c) squaraine dye, [63] (d) perylene dye,[64] (e) porphyrin dye [65] and (f) phthalocyanine dye.[66]

Natural dyes (Figure 1.10) extracted from plants, flowers and fruits can be used successfully as environmentally friendly, safe and easily available sensitisers for metal oxides in DSSCs. The most studied are anthocyanins, the characteristic of coloration for red fruits, aubergines and oranges, and chlorophylls, largely present in leaves and algae. However because their efficiencies are low, their use is limited mainly to educational purposes.

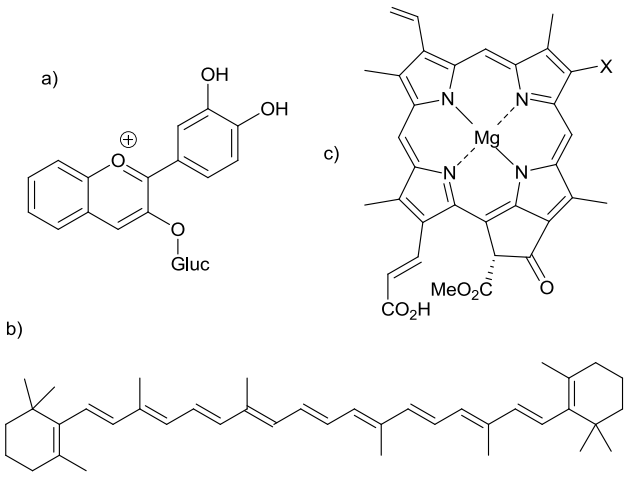

Figure 1.10 Molecular structures of example natural dyes used in DSSCs. (a) Cyanin dye,[56] (b) β-carotene dye [67] and (c) chlorophyll dye.[68]

Transition metal complexes have been widely investigated as dye for solar cells, [69]thanks to the possibility of designing and integrating a big library of chromophors and anchoring groups. The most studied metals include Ru(II), [70, 71], Os(II), [72, 73] Pt(II), [71, 74] Re(I), [75] Cu(I) [76], Ir(III) [77] or Fe(II) (Figure 1.11). [78]

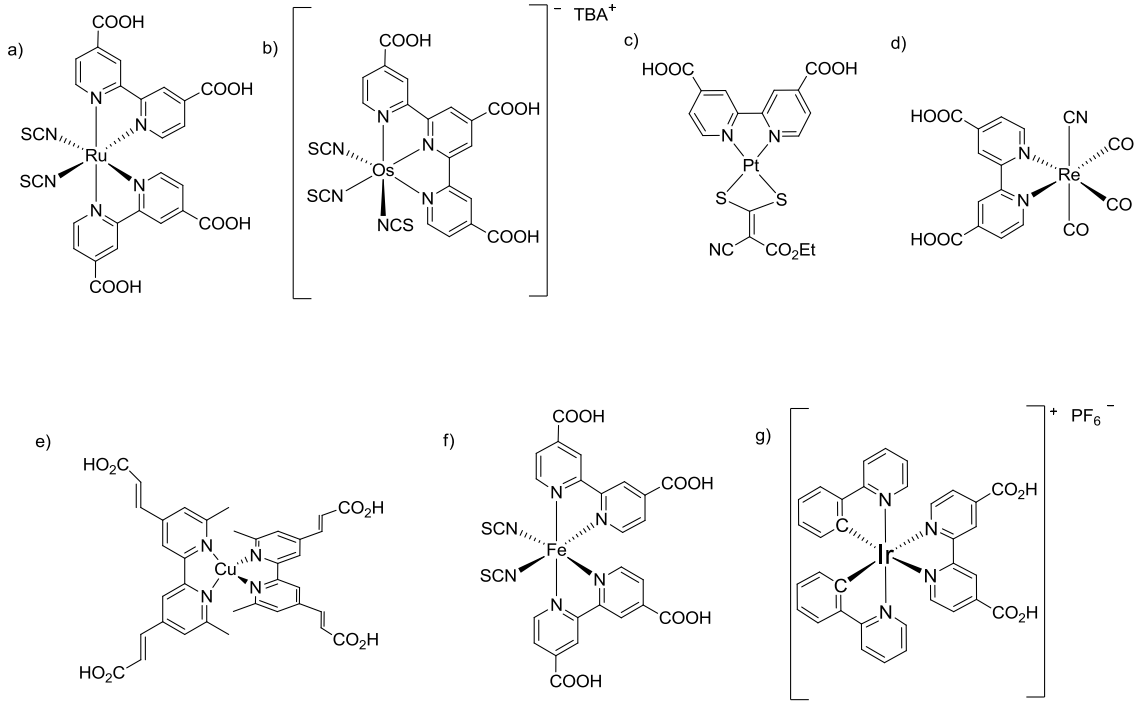

Figure 1.11 Molecular structures of transition metal-based dyes. (a) Octahedral Ru(II) complex,[70] (b) octahedral Os(II) complex,[79] (c) square planar Pt(I) complex,[71] (d) octahedral Re(I) complex[75] (e) tetrahedral Cu(II) complex [76],(f) octahedral Fe(II) complex. [78],(g) octahedral Ir(III) complex.[77]

1.7 Photophysical and Photochemical Properties of d^6 complexes

The synthesis and investigation of transition metal complexes has attracted during last twp decades an enormous interest from the scientific community, not only related to the fields of catalysis but also including all those scientific areas of interest in which the electronic, photophysical and redox properties of these complexes are involved. Inside the transition metals, those with a d^6 configuration, especially for the polypyridyl complexes, result in very attractive properties which include: accessible and tunable redox potentials and relative stability; absorption and emission of visible light; structural rigidity or flexibility in relationship with the applied ligands; long lived excited states; chemical stability in both excited or ground state.

Kinetically inert d^6 transition metal complexes are typically characterised by an octahedral geometry. Belonging to this class of metal ion we find Os(II), Rh(III), Ir(III), Re(I), Ru(II), and they all present some of the aforementioned properties. To better understand the photophysic of the d^6 octahedral metal complexes it is fundamental to describe the energy levels involved in the transition related to the absorption, or emission. As result of octahedral coordination, five *d* degenerate metal orbitals get split, so lose their degeneracy, in relation with their orientation toward the ligands. As consequence, two degenerate orbitals with e_g symmetry get destabilised, with respect to the energy barycentre, and three degenerate orbitals with t_{2g} symmetry get stabilised. The entity of the orbital splitting is indicated with Δ_o. To realistically describe the octahedral complexes we are going to use a molecular orbital theory approach, where the molecular orbitals are represented as linear combination of metal and ligand orbitals. In Figure 1.12 antibonding orbitals are indicated with "*".

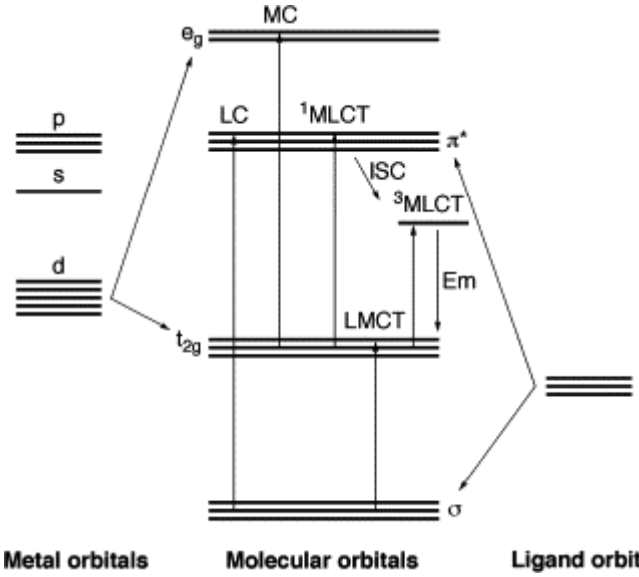

Figure 1.12 Molecular orbital diagram showing different electronic transitions for a transition-metal complex in an octahedral geometry, taking place upon irradiation. Reprinted from Ref [80], with permission from Elsevier.

In polypyridyl complexes the ligand π* are lower in energy than the Mσ* metal orbitals, hence the LUMO that results is ligand centred. In Figure 1.12 are represented all the different transition that can take place in a generic complex upon light absorption. The transition can be classified in relationship with the states involved in. Such transitions are indicated as:

- Metal Centred (MC), occurring from the non bonding, metal t_{2g} orbital π to the antibonding σ* e_g, known as d-d transitions.

- Metal-to-Ligand charge Transfer (MLCT), a charge transfer occurring from non bonding, metal t_{2g} orbital π to the ligand centred π* orbital, known as d-π* transitions.

- Ligand-to-Metal charge Transfer (LMCT), a charge transfer occurring from bonding, ligand π orbital to the metal centred either π t_{2g} or σ* e_g orbitals.

- Ligand Centred (LC), occurring from bonding, ligand π orbital to the antibonding ligand π* orbital, known as π-π* transitions.

The accessibility of an excited state has to keep in consideration also the spin multiplicity of the ground and excited states, allowing transition in accordance with specific selection rules. In metal ion complexes with d^6 configuration the ground state is

generally a singlet state (S_0) t_{2g}^6. According to spin selection rule, this multiplicity should not change when an electron is promoted to the lowest excited state. Upon promotion to a singlet excited state, the molecule can decay radiatively to the ground state (fluorescence) with a typical short life time (10^{-8}-10^{-5} s). Nevertheless, heavy metals are characterised by strong spin-orbit coupling which make the selection rules for metal complexes more "flexible". The spin-orbit coupling allows an efficient inter-system crossing (ISC) from the excited state S_n to an excited state T_n. [81] A triplet excited state T can decay both radiatively (phosphorescence, 10^{-5}-10^{0} s) and non-radiatively (decaying through ISC to a singlet state).

The behaviour of excited states is usually represented in a Jablonski diagram (Figure 1.13).

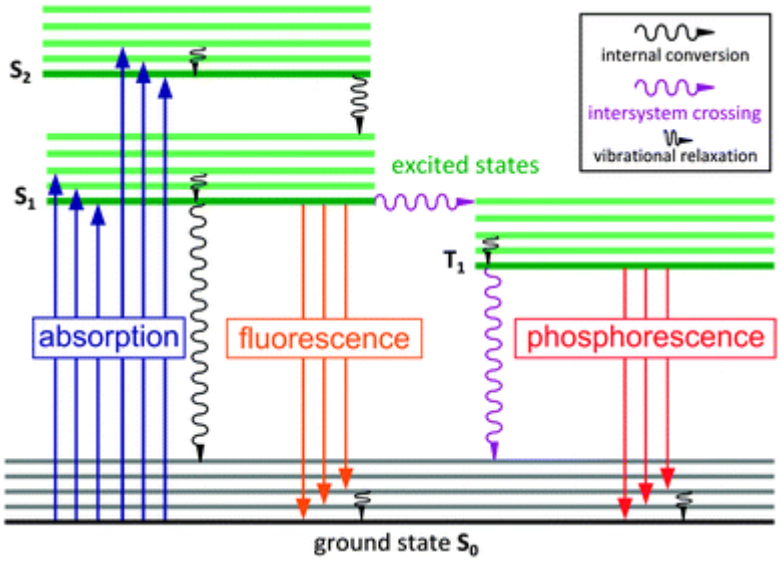

Figure 1.13 Jablonski diagram. Reproduced from Ref [82] with permission of The Royal Society of Chemistry.

To conclude, in an octahedral transition metal complex, MC, MLCT and LC transitions are strongly related to the ligand field strength, the metal ion redox potential and the intrinsic properties of the ligands. [83] Changes in the molecular design of the ligands would definitely alter the relative energy positions of the excited states, consequentially their photophysical properties would change too. [84]

1.7.1 Properties of Ruthenium Complexes with Polypyridyl Ligands

Inside the transition metal complexes, polypyridinic ruthenium(II) complexes are doubtless a paradigmatic class of molecules and $[Ru(bpy)_3]^{2+}$ (Figure 1.14) represents

the forefather of this class. This complex is a red solid which exhibit all the general properties described at the beginning of previous paragraph, making it probably the most studied complex since the 70s.[81, 85-88] In particular, the starting intention of using $[Ru(bpy)_3]^{2+}$-architectures for photoinducted water splitting has put the bases for the development of polypyridyl ruthenium complexes.

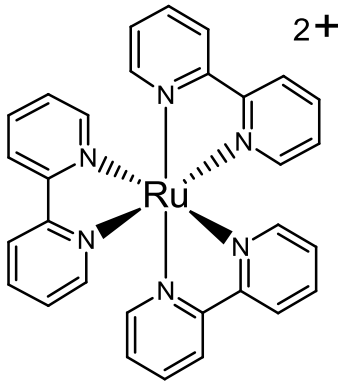

Figure 1.14 Structure of $[Ru(bpy)_3]^{2+}$.

The absorption, emission and intermolecular electron transfer properties make polypyridyl ruthenium complexes protagonist of thousands scientific studies and papers, focus on the optimization of the polypydyl ligands thus the tuning of electrochemical and photophysical properties of final complexes. Ru(II) complexes can be used in a big variety of research fields such as bio-targeting (because of their interaction with proteins and nucleotides), supramolecular photophysics, photocatalysis and solar energy conversion (as sensitisers in DSSCs).

As shown in Figure 1.15 the HOMO is centred on the metal orbitals whereas the LUMO is localised on the ligand π* orbitals.

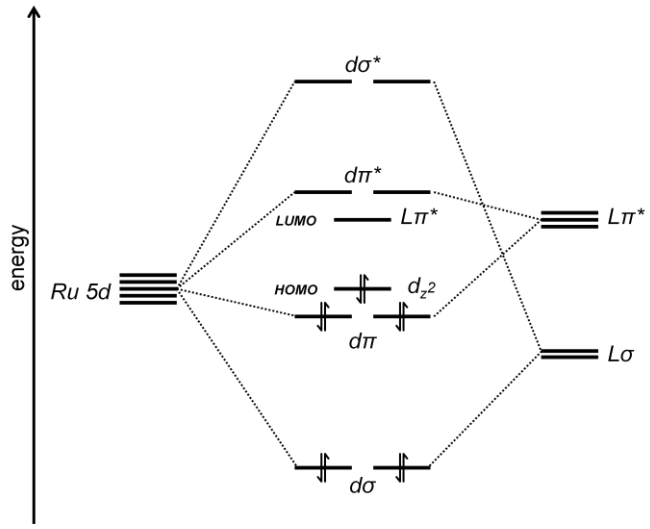

Figure 1.15 Simplified Molecular Orbital diagram for $[Ru(bpy)_3]^{2+}$

From the photophysical point of view, $[Ru(bpy)_3]^{2+}$ is characterised by an absorption band at 453 nm ($\varepsilon \approx 14000\ M^{-1}cm^{-1}$), assigned to ^{1}MLCT transition, and a peak at 290 nm, assigned as ^{1}LC state.[89] The emission, at 610 nm in acetonitrile, arises from a ^{3}MLCT with microsecond lifetimes at room temperature.[81] However, $[Ru(bpy)_3]^{2+}$ posses low lying triplet metal centred (^{3}MC) state, [90] very close in energy to ^{3}MLCT, this means that ^{3}MC can be easily thermally populated, sensibly reducing the excited state lifetime. Also, populating ^{3}MC states, anti-bonding e_g* molecular orbitals get populated, weakening the metal-ligand bonds and promoting the degradation through ligand loss of the complex.

It's easy to understand how the photophysical properties of a class of molecules comes from a fine balance between ligands and metal characteristics. In a deeper looking to this interaction, polypyridyne ligands interact with ruthenium ion through σ-donor orbitals located on the nitrogen atoms and π-donor and π*-acceptor molecular orbitals delocalised on the aromatic rings. [85]

The introduction of appropriate ligands tunes the properties of the final complex mainly in two ways: stabilising the LUMO, introducing ligands with low-lying π* molecular orbital involved in the MLCT and/or destabilising the HOMO, using π-donor or π-acceptor ligands (Figure 1.16). [91]

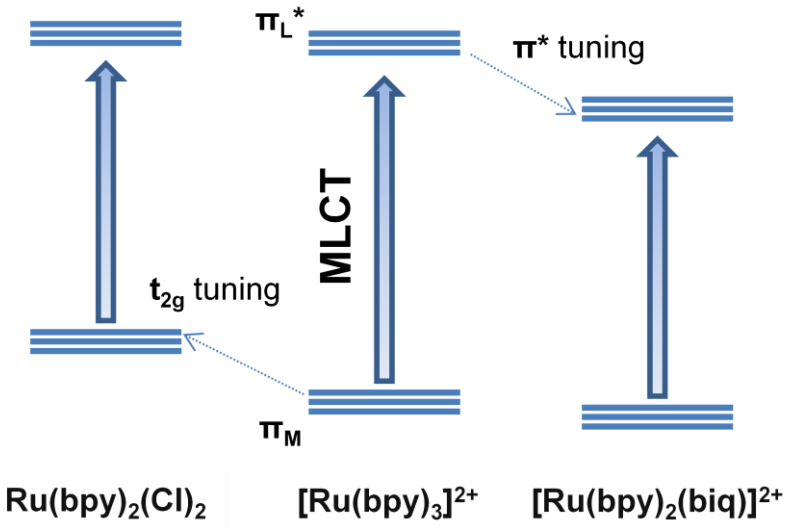

Figure 1.16 Tuning of HOMO (t_2g) and LUMO (π) orbital energy in various ruthenium polypyridyl complexes.*

MLCT transition of ruthenium complexes are then closely related to HOMO and LUMO modifications. The use of different polypyridyl ligands has a direct influence on the

excited state energy levels (e.g. $[Ru(bpy)_3]^{2+}$ *vs* $[Ru(bpy)_2(biq)]^{2+}$, biq = 2,2'-biquinoline), moreover, small changes in the LUMO energy levels can be induced introducing substituents on the bpy ligand fragment (e.g. $[Ru(bpy)_3]^{2+}$ *vs* [Ru(4,4'-dimethyl-2,2'-bipyridine)$_3$]$^{2+}$). With a different approach, the use of nonchromophoric donor ligand (e.g. $[Ru(bpy)_2(Cl)_2]$ and $[Ru(bpy)_2(acac)]^{+}$) destabilises the metal t_{2g} orbitals altering the spectral properties.

A clear example of HOMO-LUMO tunability for ruthenium polypyridyl complex has been reported by Welby *et al.* with an experimental and theoretical study on the systematic replacement of a bpy ligand with a btz. Figure 1.17 shows how the substitution of a bpy ligand has a strong effect on LUMO energy, leading to a higher band gap and so a blue-shifted absorption of the corresponding complexes. The destabilization of the LUMO energy has an effect also on the emission properties of the $[Ru(btz)_3]^{2+}$ complex because the ^{3}MLCT state is also destabilized thereby making thermal population of the ^{3}MC state easier, quenching emission and promoting photochemical ligand ejection.

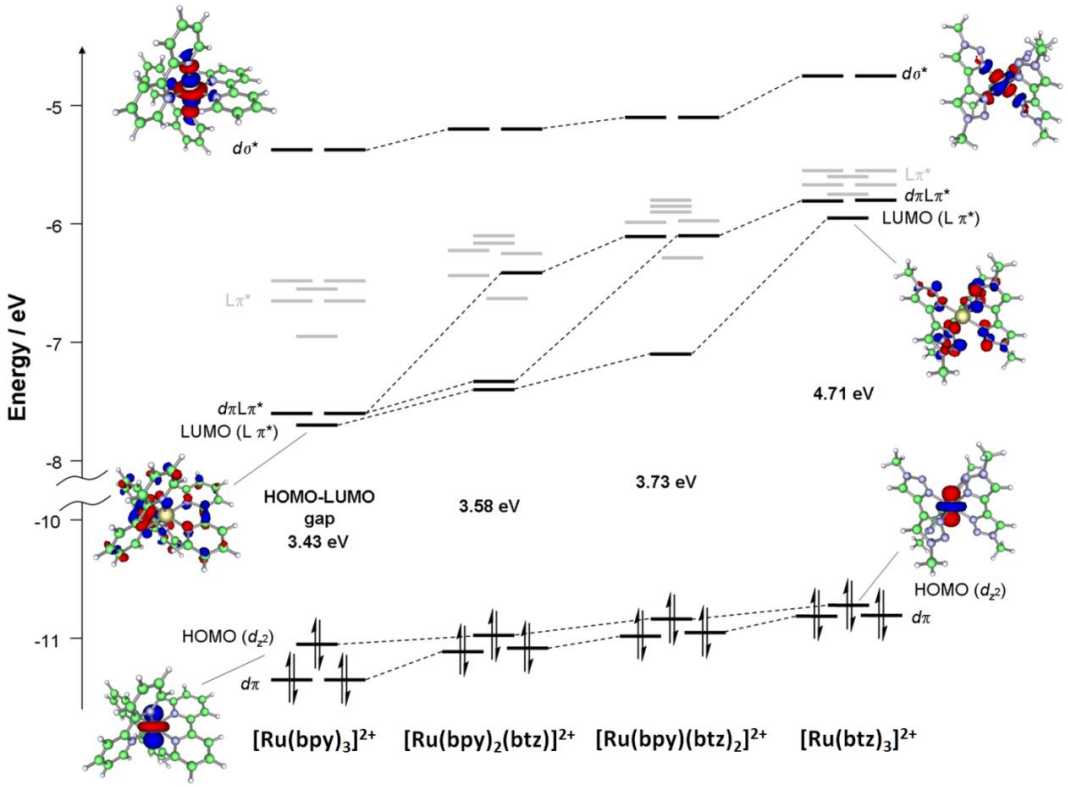

Figure 1.17 A comparison of the MO's reveals that there is an increase in the HOMO-LUMO gap with increasing btz content consistent with the shift in the UV-vis spectra. Reproduced from Ref [92] with permission of The Royal Society of Chemistry.

1.7.2 Cyclometalated iridium and rhenium tricarbonyl diimine complexes

The numerous studies on ruthenium (II) complexes opened the way to design luminescent complexes based on other d^6 transition metals. A very representative example comes from cyclometalated Ir(III) complexes. These species are very similar from the structural point of view to the discussed Ru(II) complexes, but photophysically more emissive and tunable. The iridium wide colour tunability and high phosphorescence quantum yield, [93, 94] make it very attractive for luminescent application as organic light-emitting diodes (OLEDs), [95-97] generating an explosion of new cyclometalated iridium(III) complexes reported in the last decade. [98]

Iridium complexes photophysical properties are reflection of the intrinsic characteristics. In fact iridium possess strong spin-orbit coupling then excited S_n states can be easily subjected to ISC to a T_n state resulting in high phosphorescence quantum yields.

If $[Ru(bpy)_3]^{2+}$ (Figure 1.14) represents the forefather of ruthenium polypyridine complexes, then $[Ir(ppy)_3]$ (ppy = 2-phenylpyridine) represents the one for iridium cyclometalated complexes. The cyclometalating ppy ligand (C^N) has a formal negative charge on the C atom. The stereochemistry of $[Ir(ppy)_3]$ is characterised by two different isomers, *fac* and *mer* respectively, as shown in Figure 1.18. Tamayo *et al.* showed new synthetic ways to isolate either *fac* or *mer* isomer, demonstrating that the facial isomer is thermodynamic product and the meridional isomer is the kinetic product. [99]

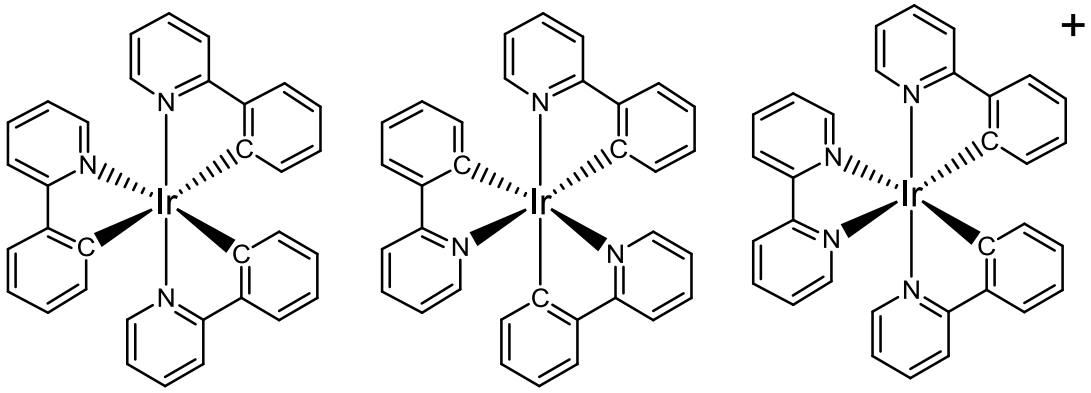

Figure 1.18 Structure of mer-$Ir(ppy)_3$ (left), fac-$Ir(ppy)_3$ (middle) and trans-$[Ir(ppy)_2(bpy)]^+$ (right)

The absorption spectrum for $[Ir(ppy)_3]$ display a strong LC transition together with two MLCT transitions in the UV and the visible region, ^{1}MLCT and ^{3}MLCT respectively (Figure 1.19). The emission spectrum consists of a broad and asymmetric band at 515 nm, commonly attributed to phosphorescence from ^{3}MLCT state. [100]

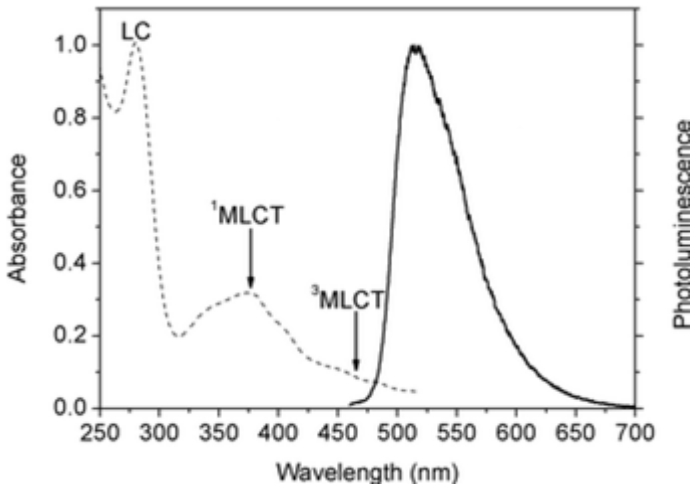

Figure 1.19 Normalized absorption (dashed line) and emission (solid line) spectra of $Ir(ppy)_3$ in dichloromethane. Reproduced from Ref [100] with permission of The Royal Society of Chemistry.

Spectral properties of $Ir(ppy)_3$ have been investigated by Hay[101] using DFT computational methods, finding out that the HOMO is principally composed of *p* orbitals of the phenyl ring and metal *d* orbitals, whereas the LUMO is centred on the neutral pyridyl fragment. [101] The HOMO/LUMO distribution indicates how an effective strategy to tune the photophysical properties in Ir(III) complexes depends on the selective stabilization or destabilization of the frontier orbitals. Moving from neutral $Ir(ppy)_3$ to cationic $[Ir(ppy)_2(bpy)]^+$ it's possible to get an architecture which allow a defined localization of frontier orbitals, with the HOMO localised between the C^N ligands and the metal and the LUMO on the N^N ligand, thus a lower quantum yield. [102, 103] From the stereochemical point of view, $[Ir(C^N)_2(N^N)]^+$ complexes, thanks to the *trans* effect determined by the cyclometalating carbons, are characterised by *trans* position of the nitrogen atoms of the C^N ligands. [104]

This clear orbital distribution is the key for a predictable and accessible tuning of $[Ir(ppy)_2(bpy)]^+$ based heteroleptic complexes, making it possible to functionalise independently the two types of ligand.[105]

Acting on the C^N ligand only, it's possible to insert electron withdrawing and electron donating substituents on the phenyl ring and varying their position (e.g. *para* substituents have a stronger influence). Electron withdrawing substituent have the effect of decreasing Ir donation to the metal and therefore stabilizing the HOMO with the opposite effect when using electron donating substituents. A different strategy would be to replace the pyridine ring with other groups as benzothienyl, isoquinoline, fluorene, triarylamine or carbazole [106, 107] or triazole as presented in this thesis.

When substituents are on the pyridine rings or on the N^N ligand, the effect will mostly be a stabilization of the LUMO for electron withdrawing substituents and destabilization for the electron donating ones. [102, 108 109]

Despite the same tuning strategies between tris-cyclometalated homoleptic complexes and bis-cyclometalated heteroleptic complexes, the latter can be synthesised under milder conditions, consequentially higher yields are obtained with fewer issues with isomers.

In summary, cyclometalated Ir complexes together with excellent tuning possibilities for luminescent applications, they may also land themselves to greater extent of spectroscopic properties compared to Ru complexes, hence comparable photovoltaic performances once applied as sensitisers in DSSCs.

Together with Ru(II) and Ir(III), Re(I) complexes deserve particular attention. Since the first studies during the 70s they have attracted much attention in particular for their application in luminescent bio-labelling, DNA probes and luminescent materials. [110-113] The most common architecture, characterising rhenium complexes is *fac*-$[Re(CO)_3(N^N)X]$ (where N^N is a polypyridyl ligand and X is a chloride or a N-donor ligand, Figure 1.20).

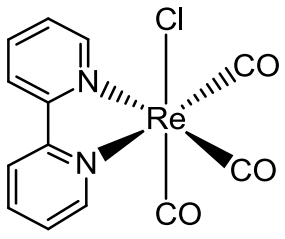

Figure 1.20 Structure of $[Re(CO)_3(bpy)Cl]$

The absorption spectra for rhenium N^N tricarbonyl complexes are characterised by a strong ^{1}LC transition in the UV and MLCT transitions among 390-450 nm (Figure 1.21). The blue shifted absorption profile of these complexes makes rhenium complexes not very attractive as sensitisers. Despite that, these rhenium complexes are typically characterised by a ^{3}MLCT phosphorescent emission in the visible with lifetimes up to a few microseconds. [114]

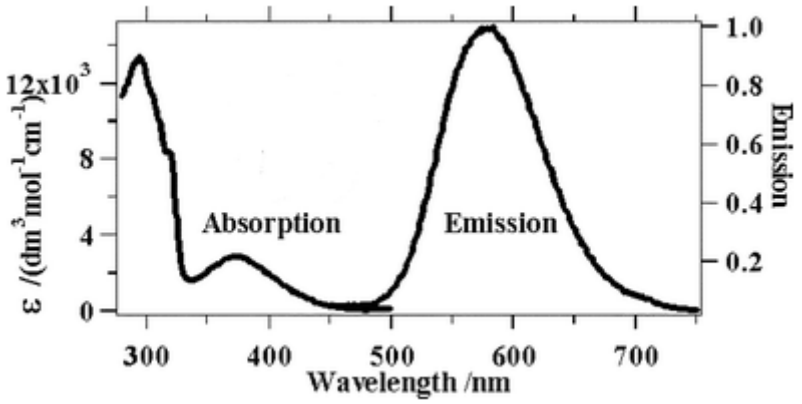

Figure 1.21 Absorption and emission spectra for [Re(CO)$_3$(bpy)Cl] in DMF. Adapted from Ref [114] with permission of The Royal Society of Chemistry.

From theoretical calculation emerged that for [Re(CO)$_3$(N^N)Cl] complexes the HOMO is composed of chloride p_z orbital interacting with metal d_{xz}, whilst the LUMO is bpy π* centred. [115]

The tuning strategies for rhenium complexes are mainly two: the first approach is to use different N^N ligands or to add substituents on the bpy fragment, in which electrondwithdrawing groups stabilise the π* level causing a red shift of the absorption and electron donating groups destabilise the π* level. The second approach includes the replacement of the chloride with other donor units. The replacement of weak field chloride with stronger field azo ring donor stabilises the HOMO, blueshifting the absorption and emission profiles of the final complex. [116]

1.8 The use of d^6 transition metal complexes as dyes for DSSCs

The characteristics discussed before for d^6 polypyridyl complexes of Ir(III),[98] Re(I) [111, 112, 117] and Ru(II)[118] make them attractive candidates as chromophores in DSSCs. These complexes are characterised by intense absorption bands in the visible region (generally attributed to MLCT transitions), chemical stability, electrochemical and photophysical tunability. The most widely used metal complexes by far in DSSC dyes

are based on ruthenium, especially because they are able to exhibit high extinction coefficients at wavelengths that are photovoltaically useful. The easily tunable redox and photophysical properties, the well known and studied synthetic strategies and the possibility to sequentially introduce different ligands, make these complexes ideal candidates as sensitiser for DSSCs.

1.8.1 The use of Ru(II) polypyridyl complexes as dyes for DSSCs

The pioneering work reported by O'Regan and Gratzel in 1991 [9] gave birth to a new class of ruthenium based sensitiser characterised by dicarboxybipyridyne as N^N anchoring ligands and σ donor thiocyanato ligands, to destabilise the HOMO and extend the spectral response of the dye. This first example of a ruthenium dye was *cis*-$[Ru(dcb)_2(NCS)_2]$ also known as **N3** (Figure 1.22). Also, this design guarantees the desired "directionality" of the excited state localising the LUMO on the anchoring ligand and the HOMO between the monodentate ligand and the Ru centre. Thus, excitation of the electron results in spatial movement towards the complex showing efficient charge injection.

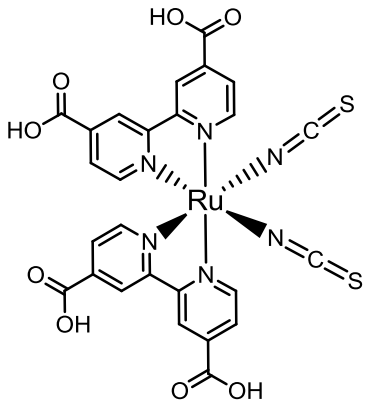

*Figure 1.22 Structure of Ruthenium **N3**.*[9]

As discussed in Section 1.4, negatively charge species adsorption on the TiO_2 surface have a direct influence on the FL hence on the V_{oc} of the device. For this reason ruthenium dyes with different degrees of protonation or different counterions have been tested. In particular, the substitution of protons by tetrabutylammonium cations (TBA), sodium cations or other counterions (Figure 1.23) [119] has the effect of enhancing the V_{oc} (compared to the protonated dyes) due the negative shift of the TiO_2 CB induced by the adsorption of the anionic complexes. For example, moving from **N3** (4 protons) to **N719** (2 protons) to the totally deprotonated complex the voltage increased from 600 to 730 to 900 mV respectively.[120, 121]

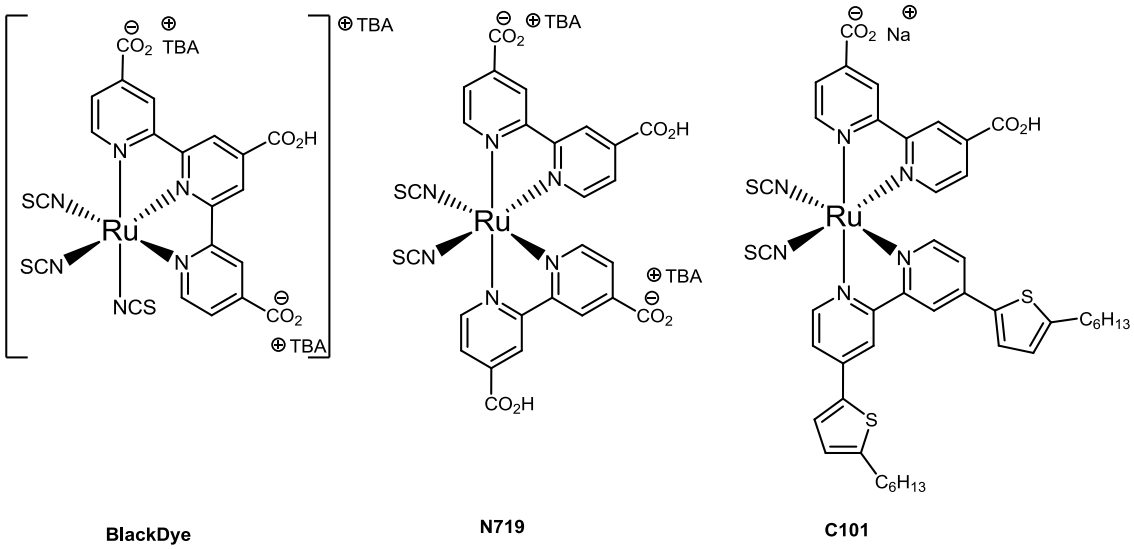

Figure 1.23 Ruthenium polypyridyl complexes with different protonation degrees.

The enhancement of their optical absorption properties is another crucial point in the development of the ruthenium dyes. Ideally, the absorption profile of the sensitiser should be centred in the visible spectrum and/or extend into the near IR region. [84] A red shifted absorption correspond to a narrower HOMO-LUMO gap, achievable with the incorporation of strong σ electron donor or low-lying π* groups. A successful strategy to improve the light-harvesting properties of ruthenium complexes relies on the introduction of π conjugated moieties extending the pyridyl ligands. [122] [123-125] These moieties include styrenyl or thiophene spacers. In Figure 1.24 four of these panchromatic and highly absorbing sensitisers are reported (*e.g.* $\varepsilon_{543\ nm} \approx 16.850\ M^{-1}\ cm^{-1}$ for **Z910** *vs* $\varepsilon_{538\ nm} \approx 14200\ M^{-1}\ cm^{-1}$ for **N3** [126]).

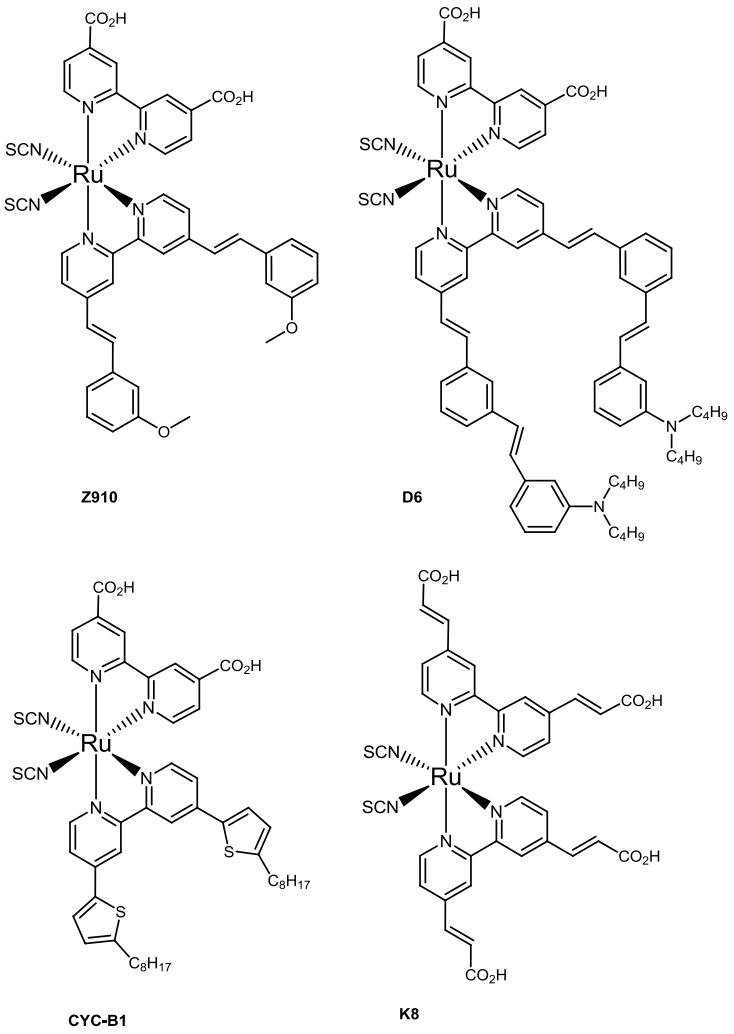

Figure 1.24 Examples of highly π-conjugated ruthenium sensitisers.

Achieving a fast and efficient electron injection is one of the main issues in designing a sensitiser. In this perspective, strong binding groups and a LUMO localised on the ligand to which they are attached, are needed. [127] As reported in Section 1.4, carboxylic acids are by far the most used anchoring groups in literature, however they might result in the desorption of the dye through hydrolysis in the presence of water or basic media. Several attempts have been made in order to find alternatives anchoring groups, such as phosphonic acid (e.g. **Z955** complex),[50, 128] or boronic acids [129], or to design amphiphilic dyes (e.g. **Z907**) (Figure 1.25). [130] Alternative binding groups have resulted in decent IPCE and efficiency values, but lower than their carboxylic analogues.

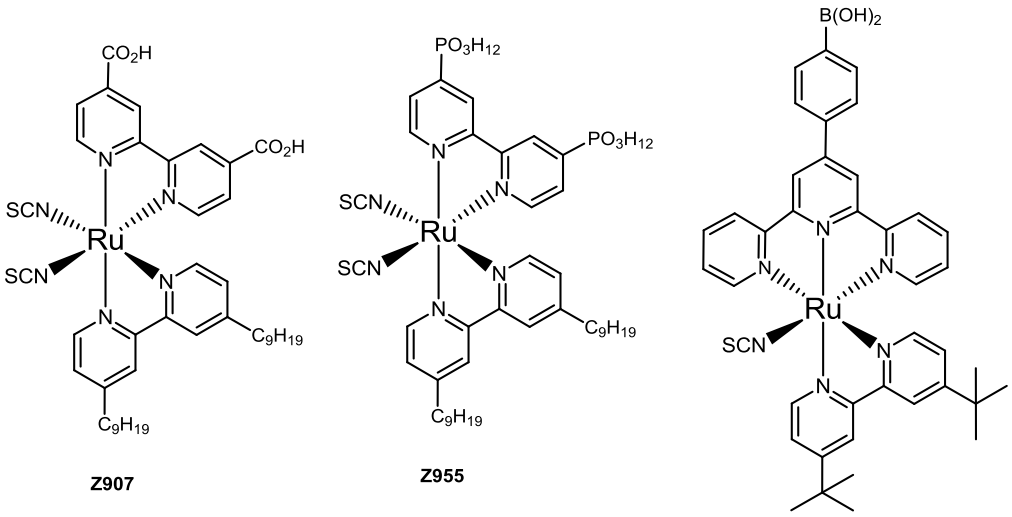

Figure 1.25 Examples of ruthenium polypyridyl complexes containing different anchoring groups or amphiphilic ligands.

Together with a specific delocalisation, the HOMO and LUMO must be well separated inside the complex structure in order to minimise recombination.[131] The introduction of flexible antennas (e.g. **N845** [132] or phenothiazine unit linked [133]) or rigid spacers [134] (Figure 1.26) had the consequence to significantly decrease the charge recombination rate constant compared to **N3** and is 3 orders of magnitude slower in the case of **N845**.

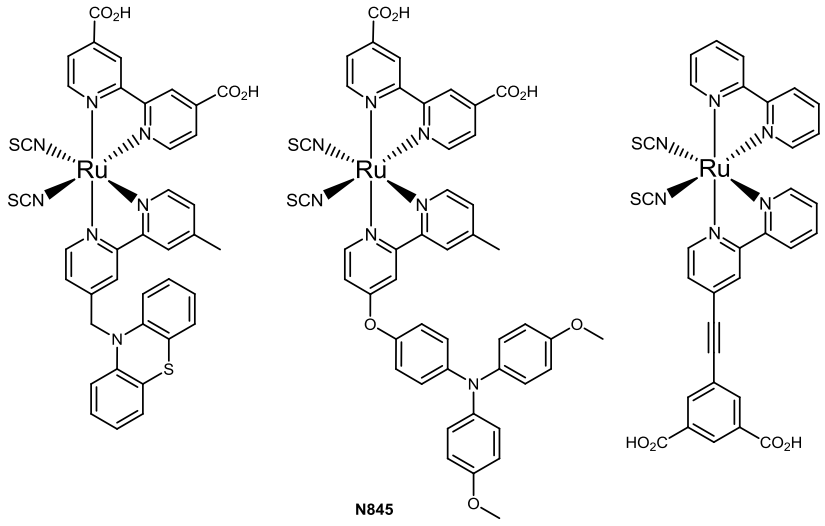

Figure 1.26 Examples of ruthenium complexes with pendant electron-donor groups or rigid spacers.

During the last two decades many efforts have been made to design efficient ruthenium sensitisers using many approaches or synthetic strategies. However despite more than

20 years from the 10% of efficiency reached by Nazeruddin *et al*. [119] nowadays the highest efficiencies are still inside that range.[124, 135-137]

In opposition to the broad literature about ruthenium dyes for n-type DSSCs, only few examples have been reported for NiO p-type cells. In 2011 Pellegrin *et al.* reported the synthesis of four polypyridyl ruthenium complexes with different anchoring ligands (Figure 1.27) as sensitisers for p-type DSSCs.[138]

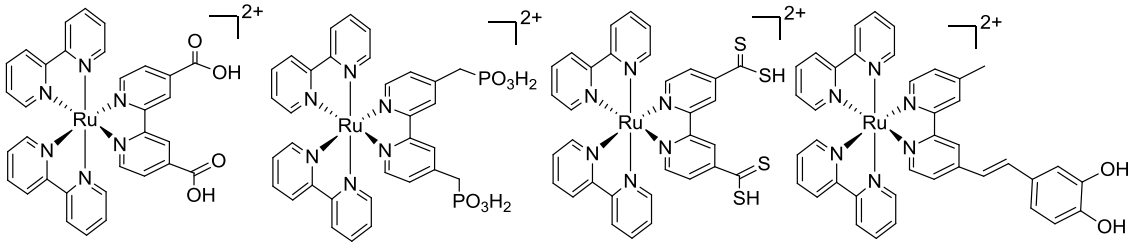

Figure 1.27 Structures of the ruthenium complexes reported by Pellegrin et al.

In this study, they prepared four tris-bipyridine ruthenium complexes substituted by different anchoring groups. In between the different anchoring ligands, they found out how the carboxylic acid having the highest affinity for NiO surface, but certainly not so far from the affinity displayed by methylene phosphonic acid or catechol moieties. However, the presented design doesn't seem ideal for the application in p-type devices because the LUMO which is located on the anchoring ligands is not separated from the NiO surface. Hence electron transfer directionality will be in the opposite direction to that required in a p-type cell. Efficiencies up to 0.02% were achieved, a result close to benchmark coumarin **C343** sensitised cell (0.030%).

In 2012 Ji *et al.*, reported an experimental and computational study of cyclometalated ruthenium complexes of the type $[Ru(N^{\wedge}N)_2(C^{\wedge}N)]^+$ as sensitisers for p-type DSSCs.[44] The cyclometalation ensures that the HOMO is on the anchoring ligand and that the LUMO must be on one of the other ligands hence far from the NiO. Thus charge transfer directionality is away from the NiO surface rather than toward it. These dyes exhibited a large red shift in their absorption bands due to HOMO destabilisation. The anchoring group is a carboxylic acid in *para* to the cyclometalating carbon, which resulted in an efficient hole injection. Also, between the phenyl ring and the carboxylic group, some rigid phenylene linkers have been inserted (Table 1.1). Moving through the series, transient absorption (TA) demonstrated a reduction of the recombination rate. As consequence the efficiency of the cell increased together with the number of spacers, from 0.009% (no spacer) up to 0.051% (two phenyl spacers).

Table 1.1 Cyclometalated sensitisers reported by Ji et al. The arrow indicates the distance between the metal ion and the carboxylic group (estimated by Gaussian 03 calculations).

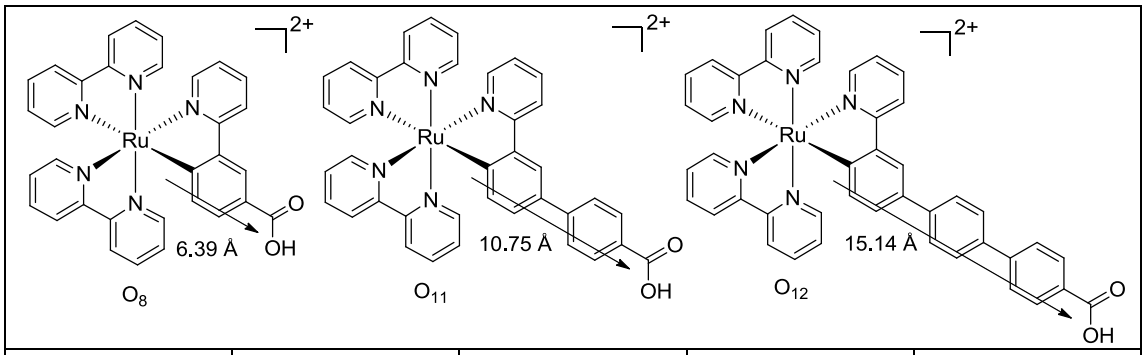

Dye	J_{sc} (mA cm^{-2})	V_{oc} (mV)	FF	η (%)
O8	0.44	63	0.36	0.009
O11	1.16	79	0.36	0.033
O12	1.84	82	0.34	0.051

1.8.2 Cyclometalated Ir(III) complexes as dyes for DSSCs

Despite their main application in light emitting systems, [139] cyclometalated iridium(III) complexes started to be the subject of several studies as chromophores for DSSCs.[98] The main target of these studies has been to red shift the absorption profile of the final iridium complex, modulating the energies of the frontier orbitals together with charge transfer direction control. In Table 1.2 are shown the two first examples of iridium complexes for DSSC, reported in 2006 by Mayo *et al*. [98]

The iridium dye **1.5**, is noteworthy as giving performances very close to those for the ruthenium complex **1.6**. Despite poor device performances, iridium complexes may have some advantages compared to usual ruthenium complexes, such as greater stability and less accessible MC states.

Table 1.2 Complexes reported by Mayo et al and their photoelectrochemical data.

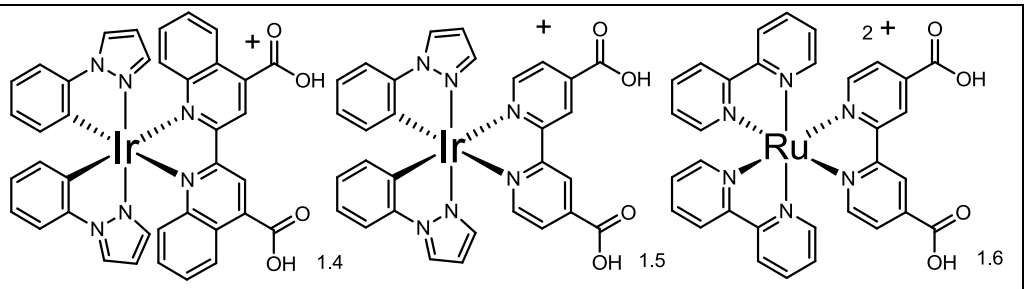

Dye	J_{sc} (mA cm^{-2})	V_{oc} (mV)	FF	η (%)
1.4	1.99	-380	0.66	0.5
1.5	2.24	-438	0.67	0.65
1.6	3.35	-458	0.65	1.0

With the purpose of increasing the separation, Baranoff *et al*. [80]prepared complex **1.7**, which contains a styrenyl spacer between bpy and the anchoring group (Table 1.3). The J_{sc} generated by this complex was very low, however V_{oc} was comparable with those from similar iridium complexes as **1.4** and **1.5** (Table 1.2). Unexpectedly, the use of a "standard" dcb ligand led complex **1.8** to a dramatic enhancement of the efficiency by an order of magnitude, compared to the complex **1.7**.

*Table 1.3 Structure of the dyes **1.7-10** and photoelectrochemical data of devices.*

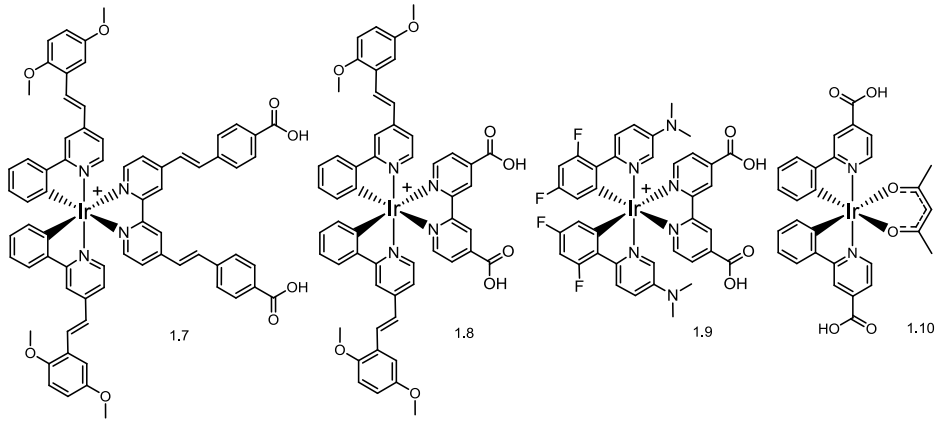

Dye	J_{sc} (mA cm^{-2})	V_{oc} (mV)	FF	η (%)
1.7	0.27	457	0.75	0.09
1.8	2.70	500	0.69	0.94
1.9	2.70	408	0.72	0.79
1.10	4.30	590	0.74	1.87

The insertion of electrowithdrawing fluorine on the phenyl fragment was expected to increase the charge separation, however **1.9** did not result in performances higher than **1.8**. A completely revisited design was presented by Baranoff *et al*. in 2010, [140] in complex **1.10** where the carboxylic groups are *para* to the N-atom in the cyclometalating pyridine fragment and the neutral ancillary ligand has been replaced by an anionic acac ligand. The characteristics reported for **1.10**, to our knowledge, represent the highest reported in the iridium sensitised DSSC field. Compared with complexes **1.7-9**, **1.10** shows ^{3}MLCT/^{3}ILCT rather than ^{3}MLCT/^{3}LLCT character as the LUMO will be located on the pyridyl rings of the C^N ligand. The JV and IPCE data for the complex **1.10** are shown in Figure 1.28.

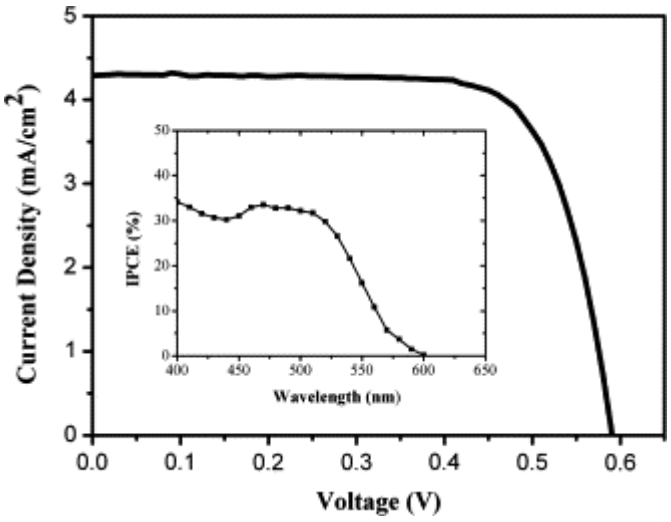

*Figure 1.28 JV curve at full sun for DSSC using **1.10** as a dye. Inset shows the IPCE curve for the device. Reprinted from Ref [80], with permission from Elsevier*

Examples of iridium dyes for p-type DSSCs are even rarer; the first examples were published in 2014 by Gennari *et al.* [43] They reported the synthesis of three cyclometalated iridium complexes whose structures are based on two cyclometalating phenylpyridine ligands bearing methylene phosphonic acid anchoring groups and one bpy based ligand (Figure 1.29)

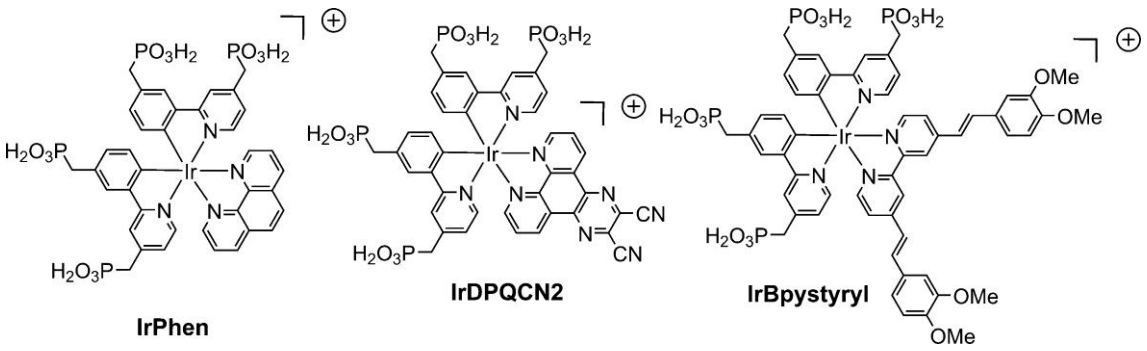

Figure 1.29 Structures of the iridium complexes investigated by Gennari et al.

The choice of phosphonic acid as anchoring group comes by the potential use of these complexes in aqueous dye-sensitized photoelectrosynthetic cells. The reported design led to a good charge separation together with efficiencies up to 0.06%.

The main drawback shown by the iridium sensitisers when compared to ruthenium ones, is mainly their poorly extended IPCE response. Improving the absorption properties of iridium dyes for DSSC is therefore certainly a fundamental goal.

1.8.3 Rhenium tricarbonyl diimine complexes as dyes for DSSCs

The rhenium polypyridyl complexes have received attention because of their high stability and synthetic ease of preparation, enabling them to be widely used as photocatalysts.[141] The $Re(dcb)(CO)_3Cl$ dye, originally published in 1999 by Meyer [72], has been the subject of investigation of electron transfer on TiO_2 by Lian and co-workers.[142] More recently a bpy-pendant cathecol has been applied on rhenium tricabonyl complex and its interfacial electron transfer has been investigated (Figure 1.30). [143] Most of the studies reported in literature about rhenium dyes are more focused on deeply understanding their electron transfer mechanisms rather than quantifying the efficiency of the complexes in their DSSC devices.

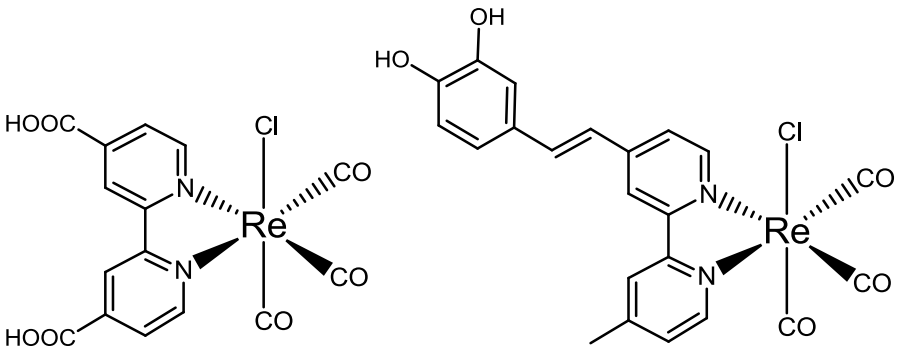

Figure 1.30 Examples of the rhenium complexes used as sensitisers on TiO_2.

As was seen previously for iridium sensitisers, the main drawback of rhenium dyes is related with their limited absorption profile, hence leading to low IPCE and efficiency. However rhenium complexes represent ideal models for studying the mechanisms and interactions on the complex/metal oxide interface.

1.9 Aims and Objectives

Novel sensitisers based on metal polypyridyl complexes are published monthly, and new organic dyes are gaining the upper hand achieving efficiencies higher than 10%.[27, 144, 145 55, 146, 147] Indeed, a "solar" future looks not so utopic anymore.

In order to increase the power conversion efficiency of DSSC devices, a winning strategy is the modification of dye complex ligands with auxiliary chromophoric groups to generate panchromatic dyes.[148-151] By increasing the overall absorption cross section of the dye, one therefore hopes to increase the number of photons that can be utilised for electrical power generation and hence overall cell efficiency.

Cyclometalated iridium complexes, in the DSSC field, represent a nascent dye family.[77, 98, 140] By finding inspiration in the widely studied ruthenium dyes, increasing the molar extinction coefficient of iridium complexes represents a hard but stimulating challenge. The achievement of this goal will significantly improve the IPCE profile resulting in notably conversion efficiencies.[152]

This thesis seeks to further develop and explore chromophoric systems through the synthesis of transition metal complexes (mainly Ir(III)) capable of absorbing photons and injecting them into a metal oxide substrate. All the tuning strategies reported in Chapter 1 have been evaluated becoming the starting point for a judicious selection of ligands and complex architectures. The photophysical and electrochemical properties of the chromophoric systems may then be evaluated, together with a computational investigation and their application in real devices. In this work, these general targets are achieved through the accomplishment of the following aims:

- Building upon the synthetic routes to new ligands pioneered within our group during the PhD project of Dr Baljinder Uppal, the first aim of this project was to realise an array of iridium cyclometalated complexes with aryl-triazole ligands. Aryl triazole ligands are prepared by both CuAAC and Bestmann-Ohira reactions, starting from commercially available arylacetylenes and/or aryl aldehydes. These ligands are easy to make with good yields, their application

as cyclometalating ligands allows the facile tuning of the photophysical properties of the iridium final complexes for DSSC applications.

- The attention toward the development of NiO p-type DSSCs has recently increased thanks to their potential use in tandem DSSC. The tandem cells come from the marriage of a sensitised photocathode with a sensitised photoanode in which ideally their absorption should be complementary. Even if the idea of a tandem device seems futuristic and fascinating, the currents generated by the cell are unfortunately low, mainly influenced by the photocathode. In order to improve the tandem cell performance, it would be essential to design sensitisers able to reduce the recombination rate (picosecond time scale[153]) between holes injected in NiO and reduced dye. Here we present a family of iridium complexes designed to achieve the right electron transfer directionality together with effort to improve absorption in the visible range.
- At present dcb remains the most efficient and widely utilized anchoring ligand for applications in dye sensitised solar cells. The t_{2g}-orbital parentage of the TiO_2 conduction band allows strong bonding interactions with the π*orbitals of the ruthenium bipyridine based excited state through the carboxylic-acid derived surface linkages.

  Following the example of Meyer *et al*., to design a new bipyridine based anchoring ligand (4,5-diazafluoren-9-ylidene) malonic acid (dfm)[137], here we will describe a new bipyridine ligand with carboxylic acid groups connected to the pyridine rings through a triazole ring. This novel anchoring ligand has been applied on Ru, Ir and Re complexes and their performances have been compared with those for analogues dcb complexes.

  Spacers have been successfully used to increase the charge separation and the lack of conductivity through triazole ring may retard the recombination. Conjugated linkers to carboxylic acid functional groups have previously been employed for Ru(II) coordination compounds. [154]
- As already mentioned, the incorporation of iridium(III) photosensitisers (dyes) onto semiconductor surfaces in the context of a DSSC is of particular interest. Despite the potential benefits, we know of only few reports in the literature for iridium-based DSSCs. Gray and co-workers[98] first demonstrated their viability using dcb and dcbq (dcbq = 4,4-dicarboxy-2,2-biquinoline) ancillary ligands to red-shift the absorption spectrum. Low-energy absorption features at ca. 500 nm resulted from ligand-to-ligand charge-transfer (^{1}LLCT) transitions, which contrasts them with ruthenium complexes that absorb primarily from a metal-to-

ligand charge-transfer (^{1}MLCT) state. Using an architecture similar to that of Gray and co-workers[98], Dragonetti and co-workers[77] and Tian and co-workers[155] have each obtained photo-sensitizers absorbing out to 550 nm from the same type of mixed ^{1}MLCT/^{1}LLCT transitions. Finally, Nazeeruddin and co-workers reported six iridium dyes with a maximum η among them of 2.51%.[140] In each of these cases, the absorption profile was not sufficiently red-shifted in order for the dye to act as an efficient harvester of sunlight (i.e. J_{sc} is low), an issue echoed with the iridium photosensitisers used for water splitting.

To maximize the utilization of solar energy through efficient light absorption, the photophysical properties of coumarins can be used and combined together to prepare iridium-coumarin dyes for photovoltaic applications. Based on the work of Takizawa *et al*. in 2012 [152] and Zhao [156, 157] we report two examples of iridium-coumarin dyes for application in both n-type and p-type solar cells.

All complexes will be fully characterised by ^{1}H and ^{13}C NMR spectroscopy, mass spectrometry and the photophysics investigated by UV-vis absorption and fluorescence spectroscopy. Lifetimes of luminescent excited states for these complexes will be determined by time-correlated single-photon counting luminescence spectroscopy. The fabrication and testing of these dyes has been carried out through collaboration with Dr Elizabeth Gibson at Newcastle University.

2 Synthesis and characterization of cyclometalated iridium complexes as chromophores for n-type DSSC

2.1 Introduction

2.1.1 Cyclometalated iridium complexes as DSSC dyes

The choice of moving our research interest to iridium sensitisers comes from several reasons: a) its octahedral coordination allows the introduction of specific ligands in a predictable way; b) the photophysical and the electrochemical properties are tunable and generally predictable; c) the resulting complexes are chemically stable.

As discussed in Chapter 1, ruthenium complexes doubtless represent the lion's share of transition metal based sensitisers. [158] The strength of using these complexes, together with the high IPCE values, is represented by a very efficient injection, almost unity. In this respect, because the injecting state has MLCT character, it is very influenced by the HOMO-LUMO spatial separation. A way to make this separation clear and efficient could be the use of LLCT injecting states. To this end, cyclometalated iridium complexes, normally associated with applications as phosphors in light emitting devices, have been investigated as sensitisers in DSSCs[98] thanks to their intrinsic LLCT states, appealing for frontier orbital separation. Complexes **2.1** and **2.2** (Figure 2.1) have been reported by Dragonetti *et al.* [77] and represent a pioneering example of iridium complexes used as DSSC dyes.

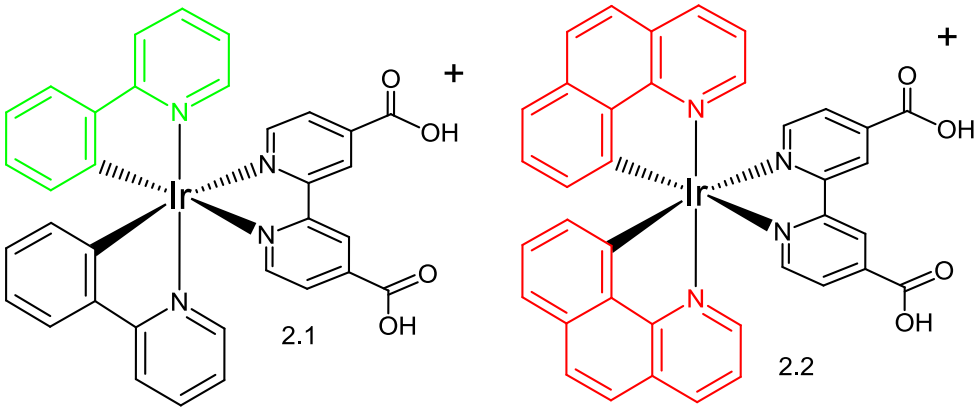

*Figure 2.1 Biscyclometalated phenylpyridine based iridium complexes $[Ir(C^N)_2(dcb)]PF_6$ (C^N= phenylpyridine **2.1**, benzoquinoline **2.2**).*

The excited state directionality should be engineered to allow an efficient electron transfer from the excited dye to the TiO_2 CB via good electronic coupling between the lowest unoccupied molecular orbital (LUMO) of the sensitiser and the 3d orbital of titanium. The HOMO of such biscyclometalated complexes is localized mainly on the phenylpyridyl ligand, because of the carbanionic character of the phenyl ring, whilst the LUMO is bipyridyl ligand in character, yielding the desired directionality of electron transfer for an efficient charge injection and an increased charge separation. Hence,

placement of absorbing and electron donating groups on the aryl ring will therefore be expected to increase the overall photovoltaic performance of these dyes by sensitising electron transfer or regenerating the oxidised dye to prevent back electron transfer.

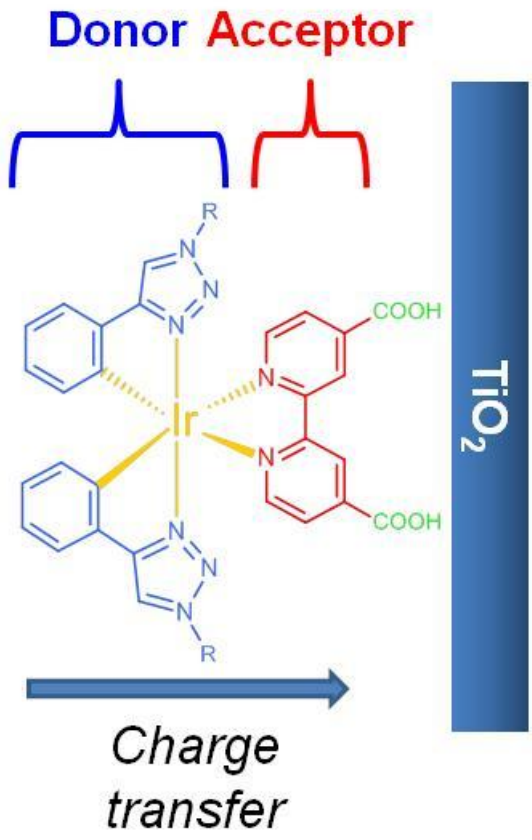

*Figure 2.2 Main design of complexes **AS1-8**, anchoring group (green), donor ligands (blue), metal centre (yellow), acceptor ligand (red).*

The same directionality, together with a controlled stereochemistry was achieved replacing ppy with phenyl-pyrazole as cyclometalating ligand (see complexes **1.4** and **1.5** in Table 1.3). Based on the Elliott group's background, we proceeded to prepare a wide range of triazole ligands by a tandem Bestmann-Ohira/ 'click' reaction (Scheme 2.1)[159] from commercially available aldehydes and explored them as cyclometalating ligands (Table 2.1).

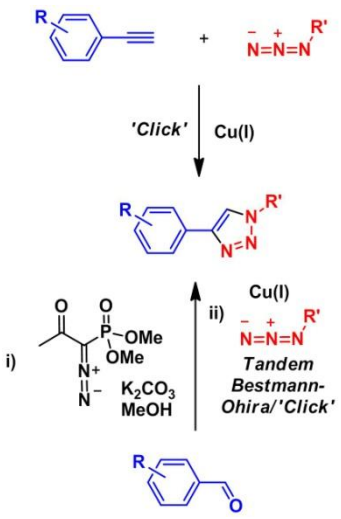

Scheme 2.1 Traditional 'click' chemistry from alkynes and tandem Bestmann-Ohira/ 'click' coupling.

We therefore selected a variety of commercial aryl aldehydes, exploring different substituent groups (nitro and methyl groups) or different conjugated systems (naphthyl or thiophenyl systems) and report the synthesis of their complexes in this chapter.

2.1.2 "Click" chemistry for the synthesis of bidentate C^N donor Ligands

In recent years the coordination chemistry of transition metals has attracted a great deal of attention. This recent explosion within the inorganic chemistry field can be attributed to the interesting photophysical and energy transfer properties of these molecules [86].

There is a great requirement for new and alternative approaches for the preparation of these metal complexes. A coupling reaction which can be used for this purpose must however fulfil certain criteria; it must be tolerant to a variety of functional groups and be highly selective. Furthermore the reaction chosen for this purpose must also give good yields. The copper(I) catalyzed Huisgen [3+2] dipolar cycloaddition between alkynes and azides satisfies these requirements.

The copper-catalyzed alkyne/azide cycloaddition reaction (CuAAC) to form 1,4-disubstituted-1,2,3-triazole ("click" reaction) [160] is highly efficient, and proceeds in very good yields, often greater than 90%, this is primarily due to the thermodynamics for the formation of the triazole. [161] The reaction is also highly selective, and shows a great tolerance to a large number of functional groups, the reaction also proceeds under very

mild reaction conditions, often at room temperature and in a protic solvent mixture including water. [162] As the list suggests this reaction would be an exemplary reaction to be used for the synthesis of coordinating species.

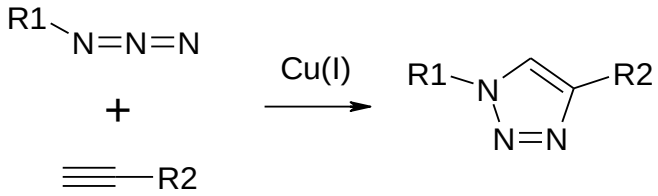

Scheme 2.2 The copper-catalyzed alkyne/azide cycloaddition reaction (CuAAC)

The CuACC reaction has been utilised in a variety of chemical disciplines, which includes the modification of biological macromolecules [163] and polymer chemistry. [164] Also, this reaction has recently attracted the attention of the inorganic community. [165, 166] Some of the most recent work involving this reaction within coordination chemistry has been carried out using this reaction for the preparation of ligand-metal complexes. The reaction has also been used to modify the outer sphere of transition metal complexes,[167] appending a phosphorescent iridium complex to a polymeric support, [168] and ferrocene groups to an organic dendrimer. [169]

An easy, versatile way to get alkynes is given by the Seyferth-Gilbert homologation.

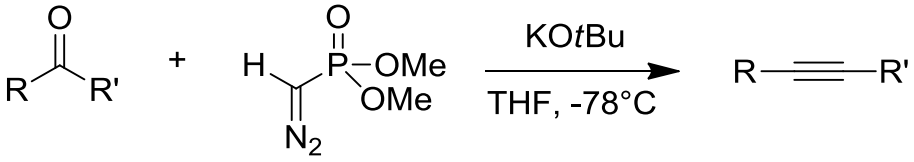

Scheme 2.3 General reaction scheme for The Seyferth-Gilbert Homologation

The Seyferth-Gilbert Homologation is a base-promoted reaction which provides a synthesis of alkynes, specifically reacting dimethyl (diazomethyl)phosphonate with aldehydes and aryl ketones at low temperatures. The Bestmann-Ohira reaction (B.O., Scheme 2.1) is a useful modification of the Seyferth-Gilbert homologation, using dimethyl(1-diazo-2-oxopropyl)phosphonate (Bestmann-Ohira reagent), which methanolysis to form the reactive dimethyl(diazomethyl)phosphonate *in situ.* [159] The B.O. reaction allows the conversion of substrates such as enolizable aldehydes, which generally would tend to undergo aldol condensation under the Seyferth-Gilbert conditions,[170] also the BO reaction can be carried out with a greater variety

functional groups present, and in mild reaction conditions (MeOH, K_2CO_3, room temperature).

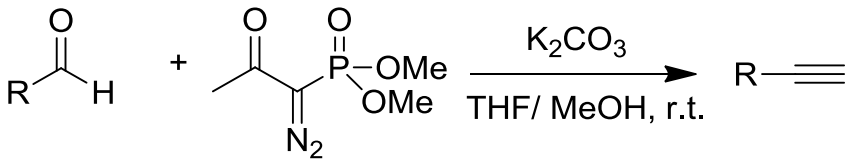

Scheme 2.4 General scheme for Ohira-Bestmann reaction

The decision to explore cyclometalated aryl-triazole ligands comes from their successful previous use as cyclometalating ligands for iridium complexes for OLED applications. [171] A number of groups have explored the use of 4-phenyl-1,2,3-triazoles[171] [172] as precursors for cyclometalating ligands. Schubert[171] showed that heating 4-phenyl-1,2,3-triazole with $IrCl_3.3H_2O$ in ethoxyethanol to reflux temperature, resulted in the formation of a biscyclometalated chloride-bridged dimer. The dimers where treated with a range of different neutral and anion bidentate ancillary ligands (e.g. bpy, acetylacetonate (acac) and picolinate (pic)) resulting in monomeric complexes (Figure 2.3) in excellent yields. [171] The optical-electronic properties for the complexes were studied and it was shown that emission colour-tuning could be easily achieved through changing the ancillary ligand. Using similar conditions De Cola and co-workers have prepared and characterised iridium dimers bearing 4-(2,4-difluorophenyl)-1,2,3-triazolyl)pyridine (dfptz),[173] however crystallographic analysis showed that this is not a dichloro-bridged dimer but a dimer in which one of the 1,2,3-triazole units acts as a bridging moiety. The authors were able to successfully cleave the dimer and access the monomeric complexes e.g. $[Ir(dfptz)_2(bpy)]^+$. The complexes reported showed absorption features similar to those previously reported for other $Ir(ppy)_2$ type complexes, with strong π-π* transitions in the near UV region localised on the dfptz ligand (~260 nm) and on the triazole (~300 nm) and weaker MLCT bands at lower energies between 350-450nm. The complexes with the fluorinated phenyl ring exhibit more intense absorption bands and display intense unstructured emission bands. Polymer light-emitting diode (PLEDs) devices were fabricated with these complexes and it was found that the electroluminescent spectra for the new devices were almost identical to those of the complex in isolation, with no emission from the host polymer matrix. This shows that efficient energy transfer from the host to the guest iridium complex occurs.

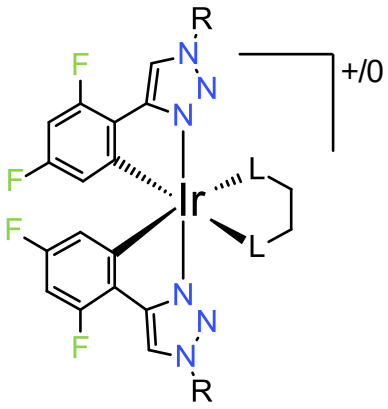

Figure 2.3 Molecular structure of $[Ir(dfptz)_2(L\hat{}L)]^{+/0}$ (L^L = bpy, $acac^-$, pic^-; R = benzyl)

2.2 Aryl-triazole ligand synthesis

A range of aryl triazole ligand precursors were made by both CuACC and BO reactions. Ligands **2a**, **2b**, **2d**, **2e**, **2f**, shown in Table 2.1, were synthesised using a slightly modified version of a pre-existing method,[174] while the reagent itself was prepared from dimethyl 2-oxopropylphosphonate. Ligands **2c**, **2g**, **2h** were synthesised by the alkyne route (Scheme 2.1).These ligands were initially made in conjunction with Mr Levon Mentz who worked under my supervision.

Ligands **2g-h** where prepared in a one-pot CuAAC synthetic procedure (Scheme 2.1) starting from the corresponding propyl halide and alkyne. The starting propyl azide was prepared *in situ* from corresponding propyl bromide by nucleophilic substitution with a slight excess of sodium azide stirring in dimethylsulfoxide at room temperature for 2 hours. Upon completion of the substitution reaction, the remainder of the starting material required for the CuAAC was added to the reaction; a slight excess of the alkyne was added in the presence of a catalytic quantity of $CuSO_4$, sodium ascorbate and 2,6-lutidine. The products were isolated by simple filtration of the reaction mixture and were further purified by recrystallisation from dichloromethane and hexane.

Ligand **2c** was prepared from isolated benzyl azide. Benzyl azide was prepared by reaction of benzyl bromide with an excess of sodium azide in dimethylsulfoxide. Upon completion, the reaction was quenched with water, and the azide extracted into diethyl ether. Benzyl azide was stored at -4°C and used in subsequent reactions. The benzyl triazole was formed by reaction of the azide with an excess of phenyl acetylene in the presence of one equivalent of $CuSO_4$ and two equivalents of sodium ascorbate in THF and water. After stirring at room temperature for 30 minutes, isolation of the product was achieved by partitioning between dichloromethane and aqueous ammonia to

remove copper. Purification of the ligand was achieved by recrystallisation from dichloromethane and hexane.

Ligands **2a-b** and **2d-f** where prepared in a one-pot BO synthetic procedure (Scheme 2.1) starting from the corresponding aldehydes. The starting alkynes were prepared *in situ* from corresponding aldehydes by reaction with BO reagent, in presence of K_2CO_3, in THF/MeOH mixture at room temperature for 24 hours. Upon completion of the alkyne formation, the pre-isolated benzylazide was added in the presence of a catalytic quantity of $CuSO_4$ and sodium ascorbate, stirring at room temperature for further 24hours. The products were isolated by water/EtOAc extraction and then purified by column chromatography. All ligands were isolated in moderate to good yields

Ligands **2a-h** have been fully characterised using ^{1}H and ^{13}C NMR spectroscopy and mass spectrometry. The ^{1}H NMR spectra for the free ligands show a distinct diagnostic signal for the C-H proton of the triazole ring (Figure 3.1). These appear as singlet resonances over the range of 7.3-8.5 ppm. These signals are characterised by nOe interaction in their two dimensional NOESY spectra with the *ortho*-protons of the 4-aryl substituent and the α-protons of the 1-benzyl group or 1-alkyl group, therefore confirming the 1,4-regiochemistry of the 1,2,3-triazole. Successful synthesis of **2a-h** was also confirmed using FT-IR spectroscopy where the lack of the azide and acetylene stretching modes at around 2100 to 2150 cm^{-1} indicated that no starting materials were present and that the reactions had gone to completion.

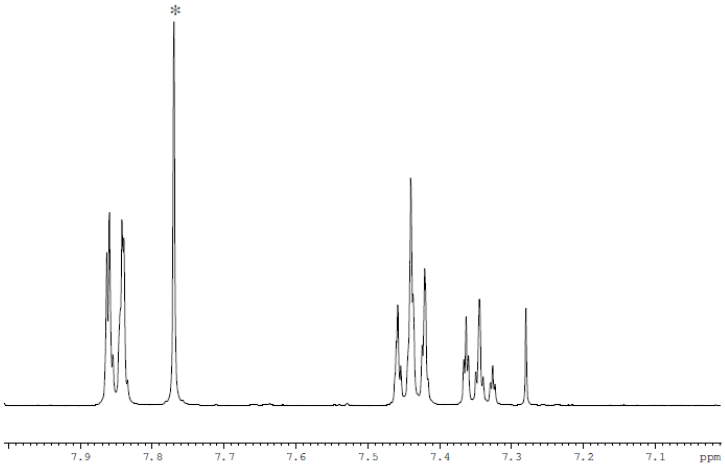

*Figure 2.4 Aromatic region of the ^{1}H NMR spectrum of ligand **2h** ($CDCl_3$). *CH proton of the triazole ring.*

Table 2.1 Ligand precursor synthesis

	Aryl synthon	Product	%yield
2a	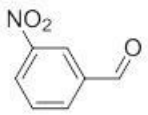	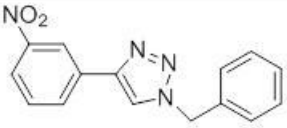	85
2b	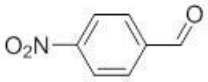	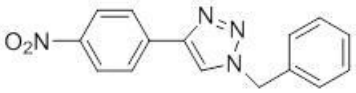	94
2c	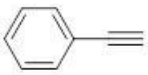	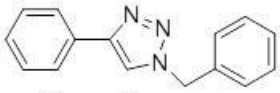	45
2d	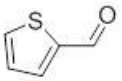	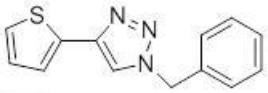	76
2e	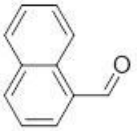	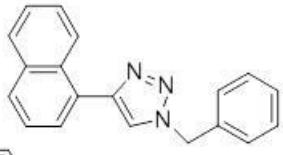	75
2f	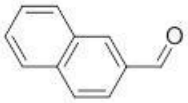	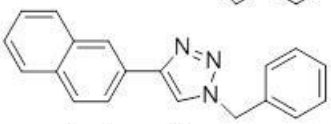	58
2g	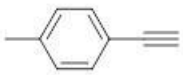	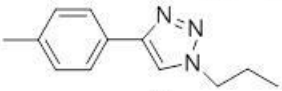	64
2h	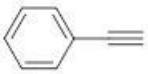	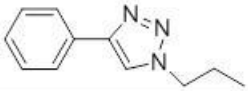	71

The use of different aryl fragments led to a good tunability of the electronic properties of the final products, corresponding to a HOMO energy tunability of the final iridium complexes. Also, the combination of the high energy triazole π system with the electron withdrawing dcb ligand leads to an optimal HOMO-LUMO directionality.

All the tabled ligands prepared by a tandem Bestmann-Ohira/'Click' coupling and standard CuAAC (Table 2.1) have been used to realize biscyclometalated complexes (Figure 2.5) according to Scheme 2.5.

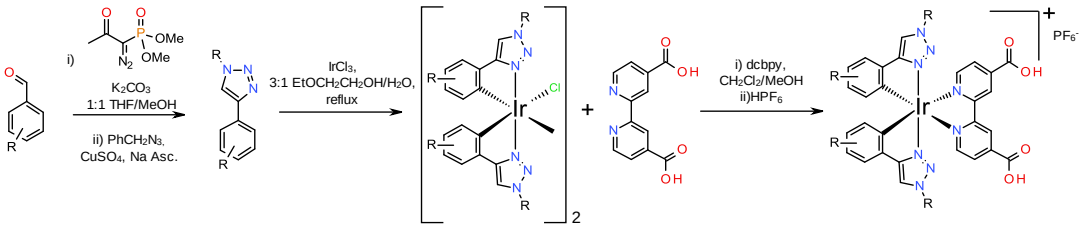

Scheme 2.5 Synthesis of triazole ligand precursors and their cyclometalated Ir(III) dcbpy complexes ***AS1-8****.*

2.3 Synthesis and characterization of Ir complexes AS1-8

As shown in Scheme 2.5 the standard synthesis of cyclometalated iridium complexes are based upon the formation of the iridium (III) chlorobridged dimer. Typically $IrCl_3 \cdot 3H_2O$ was dissolved in 2-ethoxyethanol:H_2O (3:1) and the solution was degassed with nitrogen at 80 °C for 20 minutes, then 2 equivalents of cyclometalating ligand (Table 2.1) was added and the mixture heated to reflux temperature at 135 °C for 4 hours. The crude dimer was filtered under vacuum and dissolved in DCM and hexane was added. The precipitate was filtered and washed with hexane and used without any further purification.

For the preparation of the final complexes, a solution of 2,2'-bipyridine-4,4'-dicarboxylic acid (0.1 mmol) and TBAOH 1M (0.2 cm^3) in methanol was added to a solution of chloro-bridged dimer complex (0.05 mmol) in a mixture of CH_2Cl_2-MeOH (2:1 v/v) and heated at reflux under a nitrogen atmosphere. After 6 hours, the solution was cooled to room temperature. The solution was evaporated to dryness under reduced pressure and the solid was dissolved in a minimal amount of methanol and HPF_6 was added to precipitate the product. The solution was concentrated and the solid was filtered over a porous glass frit, washed with water and ether and then dried. The product was purified by column chromatography on silica to provide the desired product. The products were recrystalised from acetonitrile and ether to yield from yellow to dark red solids in modest yields. The structure of the complexes are described in Figure 2.5

The known phenylpyridine complex $[Ir(dcbpy)(ppy)_2]PF_6$ (**2.1**, Figure 2.1) were also prepared for comparison. The complexes $[Ir(dcbpy)(\mathbf{2a\text{-}2h})_2]PF_6$ (**AS1-8**) have been fully characterised using ^1H and ^{13}C NMR spectroscopy and mass spectrometry.

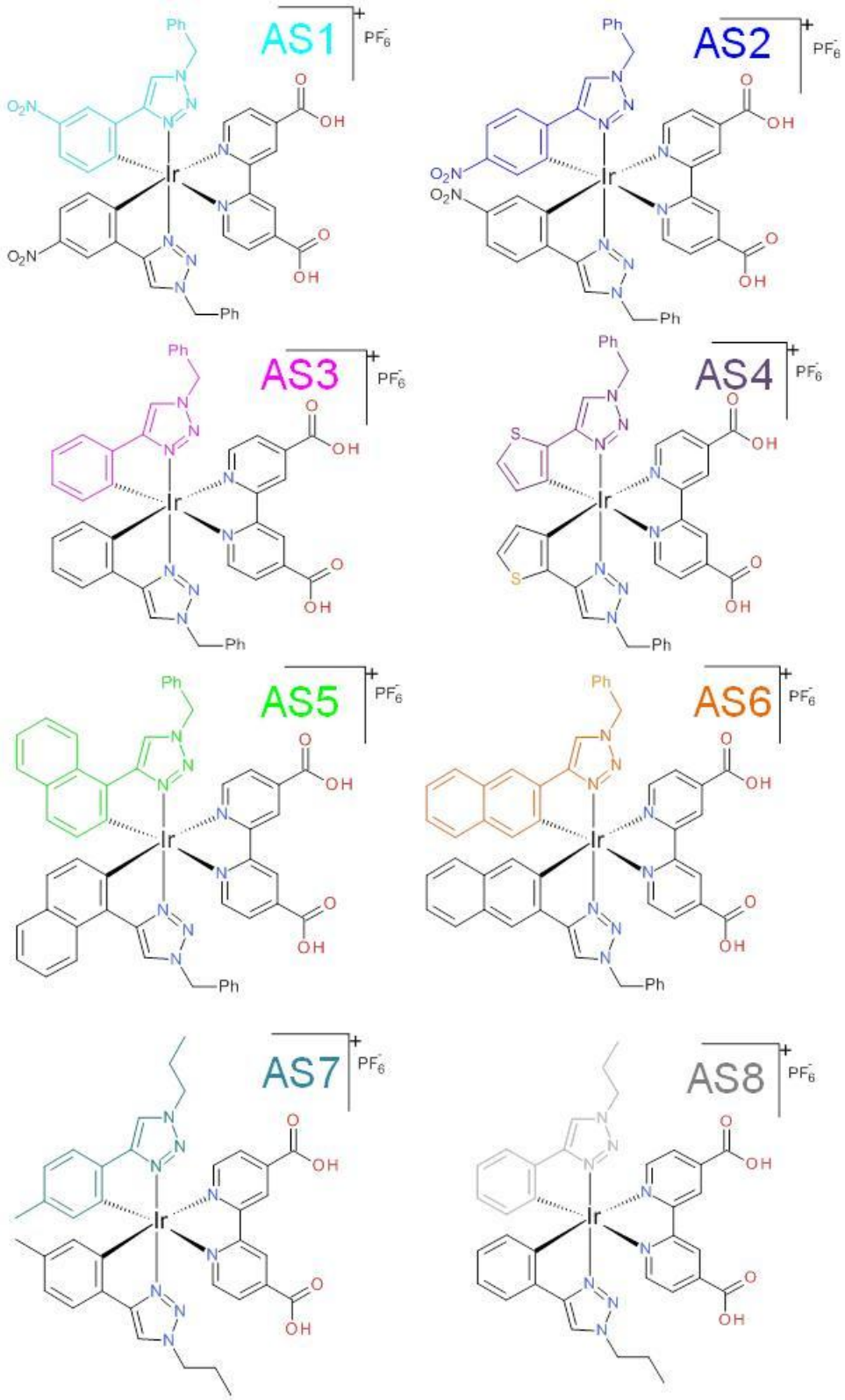

*Figure 2.5 Iridium biscyclometalated complexes synthesised **AS1-8**.*

The ^{1}H NMR spectra of **AS1-8** complexes clearly show 3 signals between 8-10 ppm, for the coordinated 4,4'-substituted-bipyridine (♦ Figure 2.6) and a distinct diagnostic

signal for the C-H proton of the triazole ring (▼Figure 2.6). These appear as singlet resonances over the range of ppm 7.5-8.6. The metalated aryl rings showed a single set of resonances as consequence of the C_2 symmetry of the $Ir(C^N)_2$ fragment, the number of signals is reduced by one (in comparison with the free ligand) due to the metalation (▲Figure 2.6).

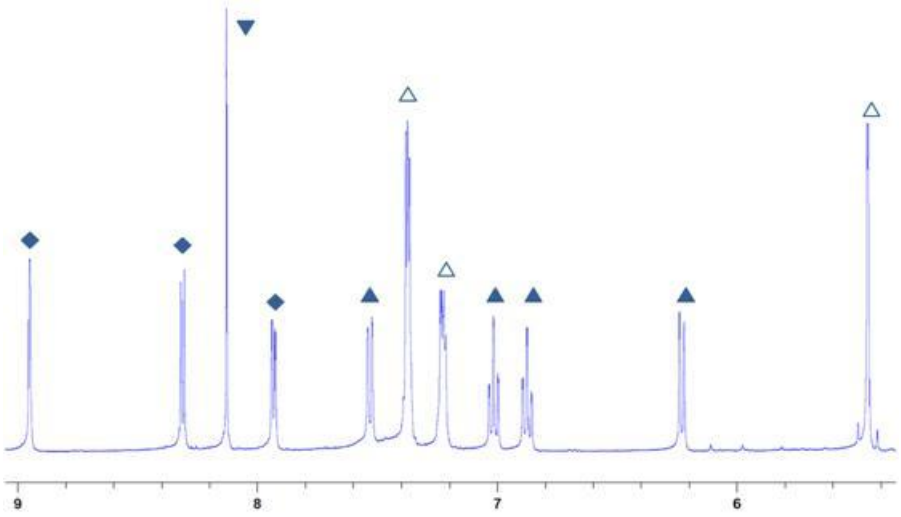

*Figure 2.6 Aromatic region of the ^1H NMR spectrum of complex **AS3** (d-ACN). ▼ proton of the triazole ring; ♦ protons of the dcb ligand; ▲ protons of phenyl cyclometalated ring; ∆ protons of the benzyl fragment.*

2.4 Photophysical properties

UV-visible absorption spectra of complexes **AS1-8** along with those of $Ir(dcbpy)(ppy)_2]PF_6$ where recorded in aerated acetonitrile and are shown in Figure 2.7. UV-visible absorption spectra that were obtained for complexes **AS1-8** are basically very similar to each other as can be seen in Figure 2.7. Photophysical data are summarised in Table 2.2. Luminescence lifetimes were not recorded due to lack of a lifetime spectrometer.

*Table 2.2 Summarised photophysical absorption and emission data for complexes **AS1-8**.*

Complex	Absorption λ / nm (ε)	Emission λ_{max} / nm
AS1	222 (48515), 265 (39888), 322 (18388), 361 (14168) 467 (1326)	554
AS2	274 (8364), 322 (4905), 405 (1196)	568
AS3	234 (80103), 293 (27775), 365 (7770), 483 (1399)	647
AS4	269 (30063), 490 (1115)	548
AS5	238 (123073), 259 (101194), 362 (19066), 494 (2059)	671
AS6	246 (130496), 354 (13268), 484 (2163)	661
AS7	225 (118523), 302 (32537), 367 (9108), 478 (1774)	647
AS8	222 (109381), 294 (33800), 370 (9200), 495 (1620)	647
2.1	253 (88830), 372 (17866), 507 (1794)	601

The absorption spectra of these compounds show intense bands in the ultraviolet region between 200 and 300 nm (Table 2.2). These bands are assigned to spin-allowed π-π* ligand-centred (LC) transitions. This assignment was made on assessment of closely related metal complexes in the literature. [105, 175, 176] Two types of charge transfer transitions can be distinguished between 300 and 600nm: at shorter wavelengths bands of moderate intensity assigned to ^{1}MLCT/^{1}LLCT transitions and transitions with much weaker intensity at longer wavelengths tentatively assigned to ^{3}MLCT. [103]

Looking at the data reported in Table 2.2, the complexes with electronwithdrawing group on the aryl ring show a blue-shifted profile, consistent with the stabilization of the HOMO (Figure 2.10).

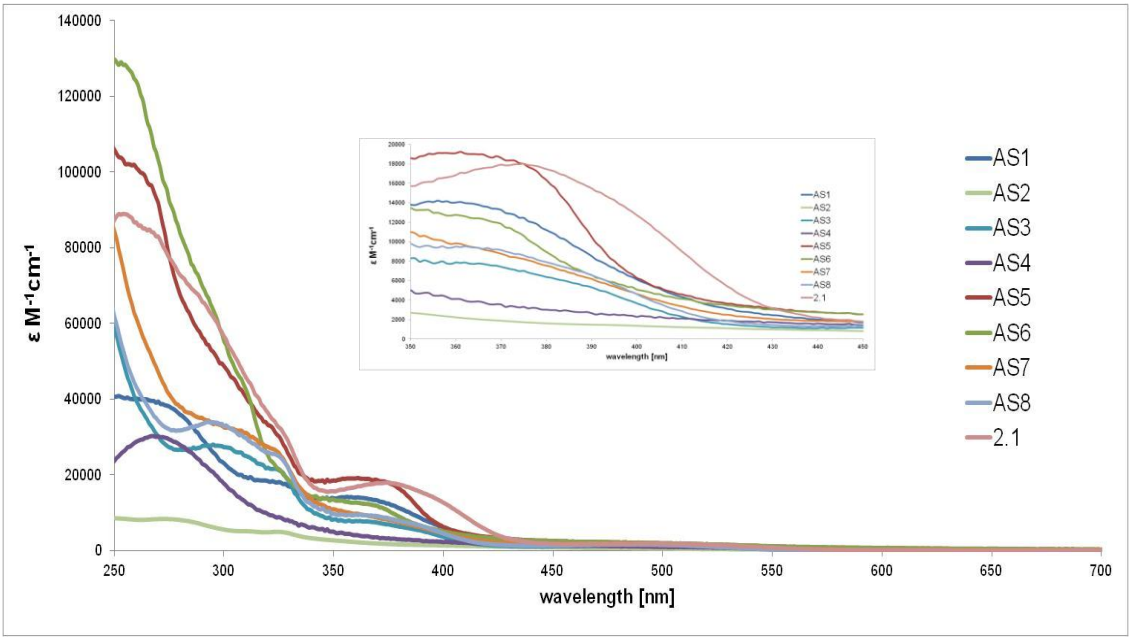

*Figure 2.7 Absorption spectra of **AS1-8** dyes in acetonitrile.*

As shown in the zoomed graph in Figure 2.7, the absorption coefficients of these dyes, in the visible range, is below 2000 $M^{-1}cm^{-1}$. This value unfortunately confirms the light harvesting limits of cyclometalated iridium complexes.

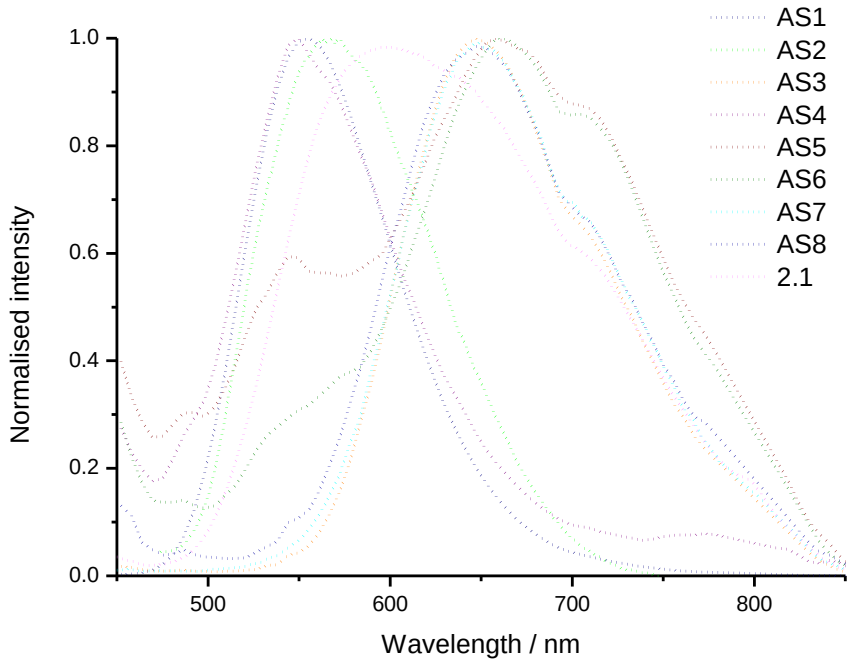

*Figure 2.8 Normalised emission spectra for the eight aryl-triazole complexes **AS1-8** in aerated acetonitrile (excited at 400 nm).*

All complexes were found to emit in acetonitrile solutions at room temperature (Table 2.2) and the emission spectra are shown in Figure 2.8. The emission maxima of complexes **AS1**, **AS2** and **AS4** are around 560nm, blue shifted relative to the other complexes, due to the electrowithdrawing effect of nitro groups and thiophene ring leading to a HOMO stabilization, following the HOMO-LUMO Δ trend in Table 2.3 and in agreement with Figure 2.10.[175] These bands are assigned to phosphorescent emission from mixed triplet metal-to-ligand charge-transfer/ligand-to-ligand charge-transfer (^{3}MLCT/^{3}LLCT) excited states. Complexes **AS3** and **AS5-8** show a similar emission profiles around 660nm, showing that the electron donating methyl and larger naphthyl π system don't have that much tuning effect when compared to simple phenyl-tryazole ligand.

2.5 DFT and TD-DFT Characterization

In order to more fully understand the electronic structure and photophysical properties and to aid in the design of new sensitisers we conducted density functional theory (DFT) modelling of complexes prepared in this project. In particular geometry optimisation and frontier orbital patterns and time-dependent DFT calculations for UV-visible absorption spectra simulation have been carried out.

Geometries of all complexes were optimised at the B3LYP level of theory. Stuttgart-Dresden relativistic small core ECP was used for iridium and 6-311G* basis sets were used for all other atoms. TD-DFT calculations on optimised structures in CH_3CN using the COSMO solvation model, built into the NWChem software package, were used to obtain the electronic spectra and molecular orbital energy levels. The benzyl ($-CH_2$-Ph) groups and the propyl groups have been approximated to methyl groups in order to simplify the calculations, for this reason complexes **AS3** and **AS8** are represented and calculated using the same geometry.

Graphical plots of the frontier orbitals of the complexes are shown in Figure 2.9, with the comparative energies of the molecular orbitals for the complexes plotted in Figure 2.10.

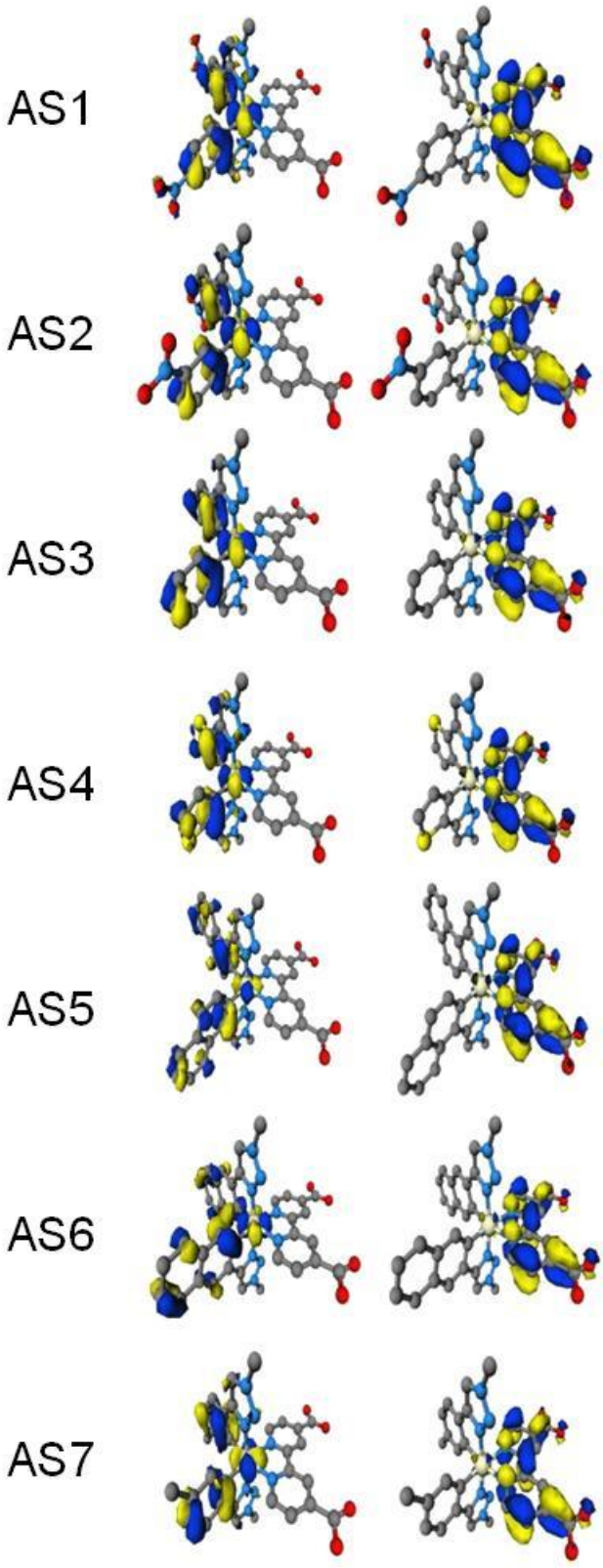

*Figure 2.9 Optimised ground state geometries for complexes **AS1-8**, HOMO density on the left, LUMO on the right.*

In the designed n-type dyes, the LUMO distribution is well located along π system of the dcbpy ligand involving the nitrogen, the carbon and partially the oxygen atoms. The iridium d-orbitals together with the phenyl ring orbitals of the triazole ligands, contribute to the HOMO density. The LUMO localised on the anchoring ligand, makes the electronic distribution on these complexes, ideal for their electron injection into the titanium oxide electrode in a DSSC. On the other side, the HOMO is localised away from the carboxylic groups will therefore avoid the electron-hole recombination.

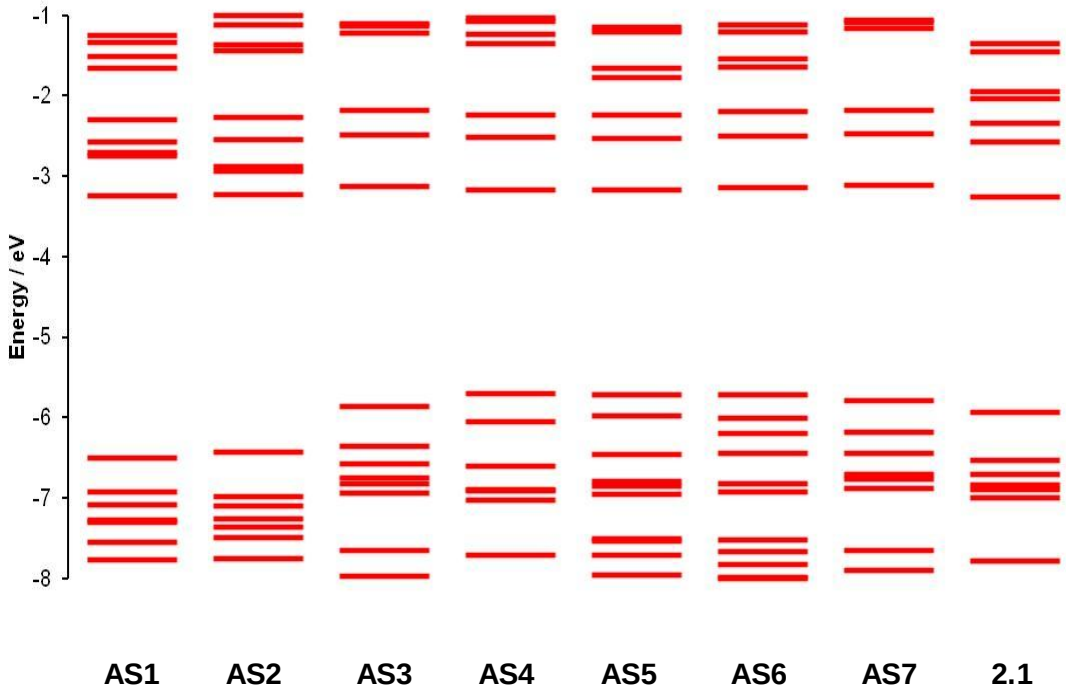

Figure 2.10 Energy level diagram for the frontier molecular orbitals of the complexes ***AS1-7*** *plus* ***2.1****.*

The calculated energy levels of **AS1-8** complexes show that the dcb dominated LUMO lies at about -3.2 eV without any significant change across the series as would be expected. This is due to the coordination of the same dcb ancillary ligand in all complexes. The HOMO energies lie between -5.94 and -5.71 except for complexes **AS1-2** which include a nitro group on the phenyl ring, underlining its electron withdrawing effect. In fact those two complexes show a substantial stabilization of their HOMO energies compared with that of the **2.1** benchmark (Table 2.3), whereas the HOMO energies of complexes **AS4-7**, containing phenyl and naphthyl fragments, are slightly destabilized thereby narrowing the HOMO-LUMO gap (Table 2.3).

Looking at the Δ values in Table 2.3, **AS1-2** have the highest HOMO-LUMO gap, this perfectly match with the corresponding blue shifted absorption maxima reported for those complexes in Table 2.2.

*Table 2.3 HOMO and LUMO energy values for complexes **AS1-7** and **2.1***

Dye	HOMO [eV]	LUMO [eV]	Δ [eV]
AS1	-6.51	-3.25	3.26
AS2	-6.43	-3.23	3.21
AS3	-5.86	-3.12	2.74
AS4	-5.71	-3.17	2.53
AS5	-5.73	-3.17	2.55
AS6	-5.72	-3.14	2.59
AS7	-5.79	-3.12	2.68
2.1	-5.94	-3.25	2.69

Time-dependent DFT (TD-DFT) calculations were carried out on the optimised geometries of each complex in order to determine vertical excitation energies. Simulated absorption spectra overlaid with experimental spectra are shown in Figure 2.11. From TDDFT analysis, the predicted transitions correlate well with the experimental spectra. The excitations to the S_1 state, for all complexes are primarily HOMO→LUMO in character, however, they are of low oscillator strength and will therefore contribute little to the absorption spectra. According with Table 2.4, the S_1 transition for complexes **AS1-2** (containing electronwithdrawing groups) takes place below 500 nm, whereas the S_1 for all the other complexes, occurs above 590 nm. The blue shifted S_1 transition wavelengths for **AS1-2**, are reflected in their blue shifted absorption profiles. The major transitions observed for all complexes between 350 and 400 nm are primarily of ^{1}MLCT character.

All the complexes presented in this chapter all have transitions in common in the range of 290-311 nm, always with oscillator strength higher than 0.20 resulting like the most probable transition and assigned as LC in character (Table 2.4). Together with this main transition, complexes **AS3-7** show also a significant peak across 400nm with a

strong MLCT/LLCT character (Table 2.4). Complexes **AS1-2** present a more elaborated transition profiles.

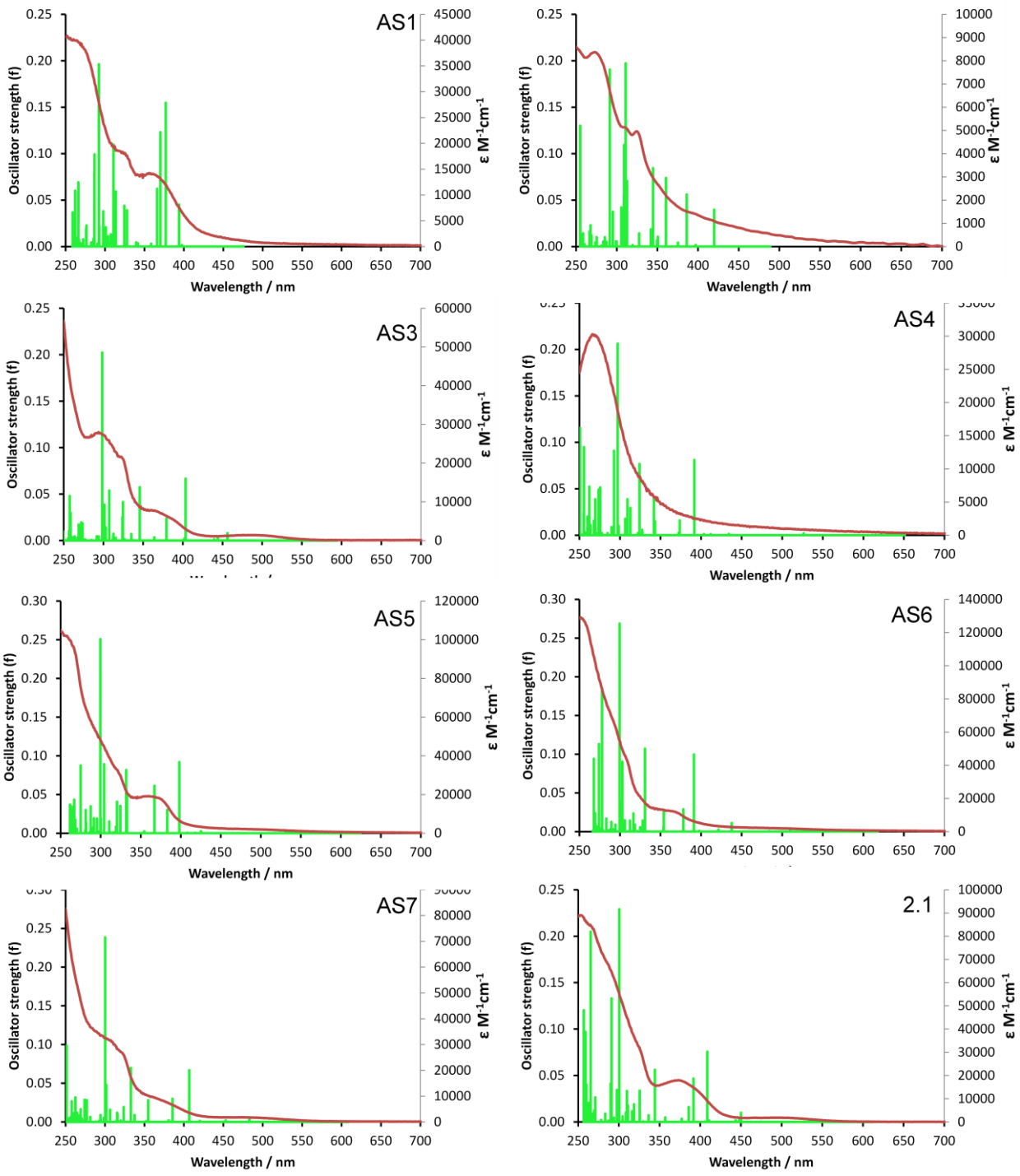

*Figure 2.11 TDDFT calculated absorption spectra for complexes **AS1-8** and **2.1** with experimental spectra overlaid.*

Table 2.4 Selected energies (eV), Oscillator Strength (f), wavelength (nm) and compositions of vertical excitations from TDDFT calculations.

Complex	Transition	Energy	λ	*f*	Composition	Character
AS1	S_1	2.607	476	0.00046	HOMO→ LUMO 99%	MLCT
	S_3	3.147	394	0.05	HOMO-1→ LUMO 94%	MLCT/LLCT
	S_4	3.288	377	0.15	HOMO →LUMO+1 96%	MLCT/ILCT
	S_5	3.349	370	0.12	HOMO-3 →LUMO 30%	MLCT
					HOMO →LUMO+2 38%	MLCT/ILCT
					HOMO →LUMO+3 26%	MLCT/LLCT
	S_6	3.386	366	0.06	HOMO →LUMO+2 23%	MLCT/ILCT
					HOMO →LUMO+3 68%	MLCT/LLCT
AS2	S_1	2.537	488	0.00016	HOMO→ LUMO 99%	MLCT
	S_2	2.954	420	0.04	HOMO→ LUMO+1 96%	MLCT/LLCT
	S_5	3.211	386	0.06	HOMO-1→ LUMO 94%	MLCT/LLCT
	S_7	3.438	361	0.07	HOMO-3 →LUMO 86%	MLCT
	S_{11}	3.599	345	0.08	HOMO-1 →LUMO+2 81%	MLCT/ILCT
AS3	S_1	2.086	594	0.00017	HOMO →LUMO 99%	MLCT
	S_5	3.072	404	0.07	HOMO-3 →LUMO 86%	MLCT/LLCT
	S_8	3.268	379	0.02	HOMO-5 →LUMO 84%	MLCT/LLCT
	S_{10}	3.586	346	0.06	HOMO-2 →LUMO+1 86%	MLCT/LLCT
AS4	S_1	1.905	650	0.00018	HOMO→LUMO 99%	MLCT
	S_8	3.165	392	0.08	HOMO-5 →LUMO 18%	MLCT/LLCT
					HOMO-3 →LUMO 75%	MLCT/LLCT
	S_{12}	3.627	342	0.04	HOMO →LUMO+3 84%	MLCT/ILCT
	S_{15}	3.828	324	0.08	HOMO →LUMO+4 12%	MLCT/ILCT
					HOMO-4 →LUMO+1 77%	MLCT
AS5	S_1	1.985	624	0.00029	HOMO →LUMO 98%	MLCT
	S_8	3.113	398	0.09	HOMO-5 →LUMO 32%	MLCT/LLCT
					HOMO-3 →LUMO 62%	MLCT/LLCT
	S_9	3.237	383	0.03	HOMO-5 →LUMO 60%	MLCT/LLCT
					HOMO-3 →LUMO 34%	MLCT/LLCT
	S_{11}	3.378	367	0.06	HOMO →LUMO+3	MLCT/LLCT
	S_{14}	3.724	333	0.05	HOMO-1 →LUMO+3	ILCT
	S_{15}	3.736	332	0.08	HOMO-4 →LUMO+1	MLCT
AS6	S_1	2.007	618	0.00005	HOMO →LUMO 96%	MLCT
	S_9	3.169	391	0.10	HOMO-5 →LUMO 84%	MLCT
	S_{16}	3.749	331	0.11	HOMO-4 →LUMO+1 92%	MLCT
AS7	S_1	2.038	608	0.0002	HOMO →LUMO 98%	MLCT
	S_7	3.047	407	0.07	HOMO-3 →LUMO 86%	MLCT/LLCT
	S_8	3.216	385	0.03	HOMO-5 →LUMO 82%	MLCT/LLCT

	S_{10}	3.493	355	0.28	HOMO-2 →LUMO+1 86%	MLCT/LLCT
	S_{13}	3.725	333	0.07	HOMO-4 →LUMO+1 90%	MLCT/LLCT
2.1	S_1	2.024	612	0.00036	HOMO →LUMO 99%	MLCT
	S_6	3.033	409	0.08	HOMO-3 →LUMO 84%	MLCT/LLCT
	S_8	3.166	392	0.05	HOMO →LUMO+3 96%	MLCT/ILCT
	S_{12}	3.602	344	0.06	HOMO-4 →LUMO+1 12%	MLCT/LLCT
					HOMO-2 →LUMO+1 81%	MLCT/LLCT

2.6 Photoelectrochemical measurements

Initial photoelectrochemical experiments were performed in sandwich-type two-electrode cells. A dye coated TiO_2 film was used as working electrode (see Section 1.4). After an overnight acetonitrile dye bath, the sensitised anodes showed a pale yellow to orange coloration, indicating the accomplished sensitization.

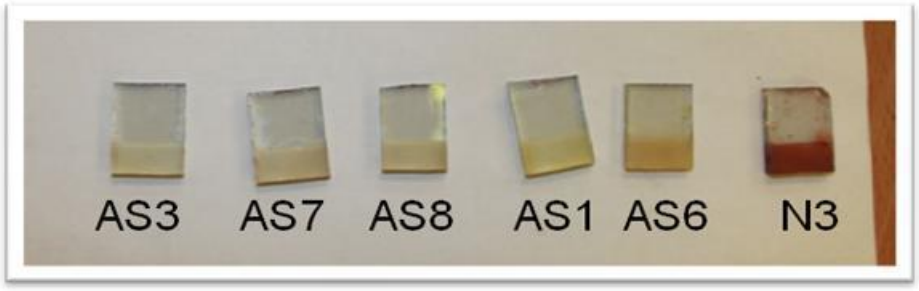

Figure 2.12 TiO_2 electrodes after immersion in dye bath.

Platinic FTO glass was used as counter electrodes and 0.05M I_2/0.7M LiI in acetonitrile:valeronitrile 9:1 as the electrolyte. The irradiation source for the photocurrent was a 20W lamp. The tested solar cells were masked to a working area of 0.25 cm^2. Voltage-current characteristic were performed on a simple digital multimeter. The photochemical properties of dyes sensitized TiO_2 electrodes under irradiation are listed Table 2.5:

Table 2.5 Performance parameters of dye-sensitised solar cells.

Dye	**J_{sc} [mA cm^{-2}]**	**V_{oc} [V]**
N3	1.22	0.328
AS6	0.082	0.200
AS8	0.132	0.137

AS7	0.094	0.140
AS3	0.090	0.125
AS1	0.015	0.039

The assembled cells characterization under irradiation generated a weak but significant current and voltage. Absorption coefficients of the iridium complexes are much lower than for **N3**, hence the difference in J_{sc} values reported in Table 2.5. Considering the quite unrefined experimental conditions, the results in Table 2.5 were promising overall.

After this preliminary and promising test. We were able to repeat these experiments under simulated AM 1.5G illumination thanks to a collaboration with Dr Elizabeth Gibson (University of Nottingham/ Newcastle University).

The dye coated film was realised using a commercial titanium oxide paste, platinic FTO glass was used as counter electrodes and a solution of 0.4 M 1-butyl-3-methyl-imidazolium iodide, 0.03 M I_2 and 0.3 M LiI in acetonitrile:valeronitrile 9:1 as electrolyte. the cell was thermally sealed before the measurement.

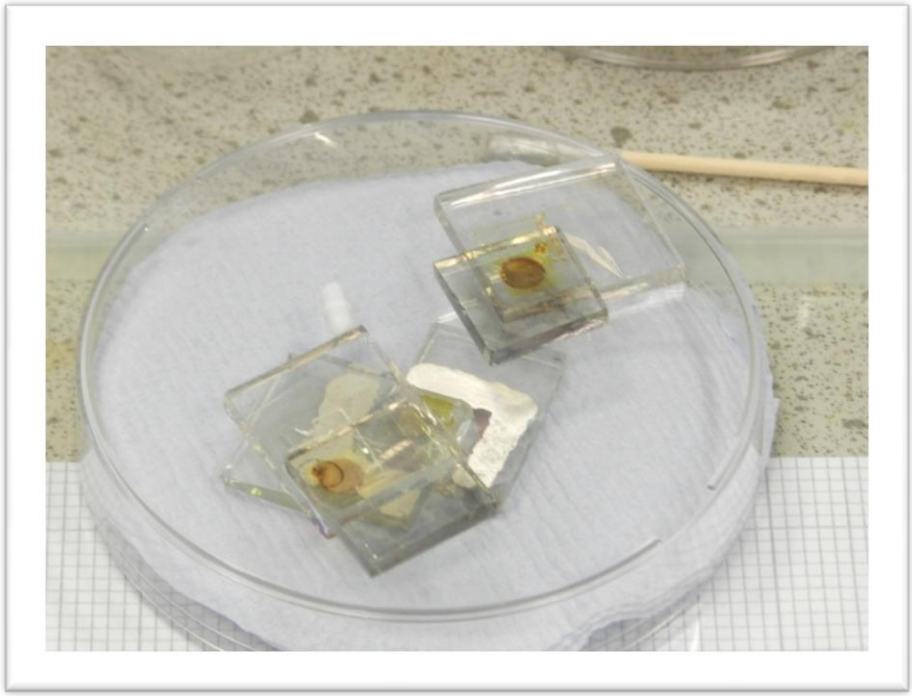

Figure 2.13 Solar cells realized and tested at University of Nottingham.

Photovoltaic measurements were performed on AM 1.5 solar simulator (100mW cm^{-2}). The incident light was calibrated by using a reference Si photodiode. JV curves were obtained by applying an external bias to the cells and measuring the generated photocurrent with a Keithley digital meter.

Main photovoltaic parameters are listed in Table 2.6. The overall conversion efficiencies η were derived from the equation: $\eta = J_{sc} \times V_{oc} \times FF$, where J_{sc} is the short circuit current density, V_{oc} the open circuit voltage, and FF the fill factor. Figure 2.14 shows the photocurrent-voltage curves of DSSCs based on the new dyes.

Table 2.6 Photovoltaic parameters of tested dyes.

Dye	J_{SC} (mA cm^{-2})	V_{OC} (V)	FF	η %
AS1	1.13	0.43	0.70	0.34
AS2	0.74	0.42	0.64	0.20
AS5	0.76	0.52	0.64	0.25
AS6	0.51	0.49	0.66	0.16
AS7	1.92	0.43	0.61	0.50
AS8	0.92	0.40	0.65	0.24
2.1	0.88	0.55	0.59	0.29
N719	4.14	0.43	0.62	1.10

As was not unexpected, the obtained photovoltaic efficiencies are low (see Table 2.6) due to the relatively weak absorption bands of the reported complexes. The best result is achieved by tolyl complex **AS7** with an efficiency of 0.5%, nearly double that of the $[Ir(dcbpy)(ppy)_2]PF_6$ benchmark complex under the same condition. Also, **AS5-6** achieved the highest open circuit voltage (≈0.5 V), this might suggest a longer electron lifetime,[177] due to their steric hindrance, hence a higher electron density on the TiO_2 surface. **AS8**, despite its structural similarity with **AS7**, achieved a poor efficiency of 0.24%, the origin of which is not clear at present.The low efficiencies for complexes **AS2**, **AS5** and **AS6** are attributed to their low solubility and hence a low dye loading. Surprisely, **AS1** reported the second highest efficiency after **AS7**; this demonstrates how not only a red shifted absorption profile but also an adequate HOMO level is

fundamental in order to efficiently regenerate the oxidized dye. Complexes **AS3** and **AS4** haven't been tested, **AS3** because of its total similarity with **AS8** and **AS4** because of its very low solubility

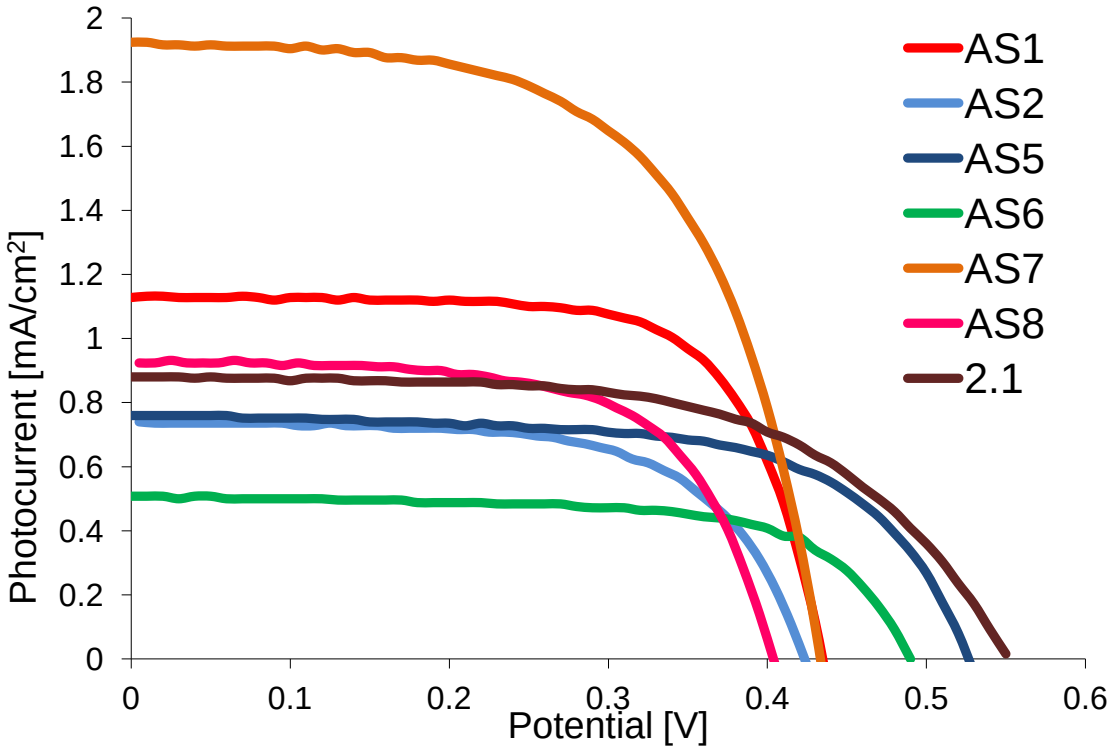

*Figure 2.14 Current-Voltage curves DSSC constructed using iridium complexes **AS1-8***

2.7 Conclusions

We have prepared and characterized eight new iridium (III)-based dyes with various aryltriazole cyclometalating ligands and dcb as an anchoring ligand. In line with expectations, the use of these phenyltriazole ligands led to a good spatial charge transfer directionality. The application of these complexes in real DSSC devices showed a reasonable photoelectrical response, considering their limited optical absorption profile, with efficiencies up to 0.5%. In future, the optimization of each single part of the device will definitely take to higher performances, for example the addition of a $TiCl_4$ blocking layer together with the use of cobalt-based electrolyte could prevent the recombination of the injected electron with the electrolyte (Equation 7) leading to higher efficiency results.[20, 25, 30] The methodology reported here provides a potential route for facile tuning of photophysical and photovoltaic properties of these dyes with greater ease than for existing ruthenium based systems. The results provide a promising basis for the design of new dyes. The versatility of CuAAC/B.O. synthesis

should allow for similar ligand design for inclusion of moieties with increased light absorption properties and lead to dyes with greater light harvesting properties and greater DSSC efficiencies.

3 Synthesis and characterization of cyclometalated iridium complexes as chromophores for p-type DSSC

3.1 Introduction

In a p-type DSSC the hole is injected from the lower SOMO of the excited dye into the NiO valence band and is followed by electron transfer from the upper SOMO to the redox shuttle thereby regenerating the dye. Because the electron flow is in opposition to a n-type cell, the design of the dye has to be different to the one shown in section 1.6. Iridium cyclometalated complexes are interesting in this regard, as they have intrinsic CT character. They also offer tunability of the ligands for further optimization. Iridium dyes as photosensitisers have recently been reported for p-type DSSCs, but with modest results.[43] To match with this inverted mechanism, we designed an array of $Ir(ppy)_2(bpy)$-based complexes with the anchoring groups placed on the cyclometalating ligand, rather than the ancillary ligand, combined with a set of diimine-based acceptor ligands (Figure 3.1).

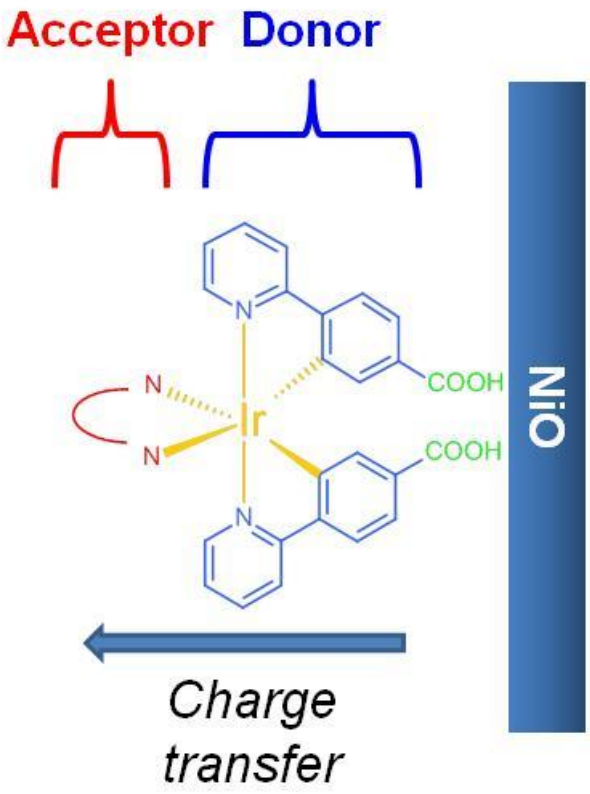

*Figure 3.1 Main design of complexes **AS9-15**, anchoring group (green), donor ligands (blue), metal centre (yellow), acceptor ligand (red).*

As reported in literature[178] for the $[Ir(ppy)_2(bpy)]^+$ architecture the HOMO is distributed on the ppy ligands whereas the LUMO is on the bpy ligand. For this reason the presence of carboxylic acid on the phenyl ring will ensure the ideal charge directionality

for the designed dyes relative to the electrode surface. This kind of design allows a total control on the stereochemistry of the final complex together with a good tunability of the photophysycal properties, leading to an ideal charge separation. The most efficient p-type DSSCs have been fabricated using a mesoporous NiO cathode. Although improvements have been measured, [179] these cells are plagued with low efficiency values, partly due to rapid (ps timescale) recombination of the semiconductor hole with the reduced dye.[179] To overcome this fundamental obstacle in the p-type system, work has been focused on increasing the lifetime of the reduced dye and semiconductor hole. Previous work has shown an increase in lifetime with chromophores that localize the excited electron farther away from the semiconductor surface (Figure 1.28).[180, 181, 182] Significantly greater charge separation can be achieved in dyes with charge transfer (CT) character, the longest being with weakly coupled, separate donor and acceptor units (Figure 3.2). The latter have been long-lived enough to allow the use of redox couples other than I_3^-/I^-,[183, 184] most notably cobalt polypyridine complexes that have recently given breakthrough results in TiO_2 DSSCs[20, 27] and could then allow extension from p-type to tandem cells with Co(III/II) electrolytes.[40]

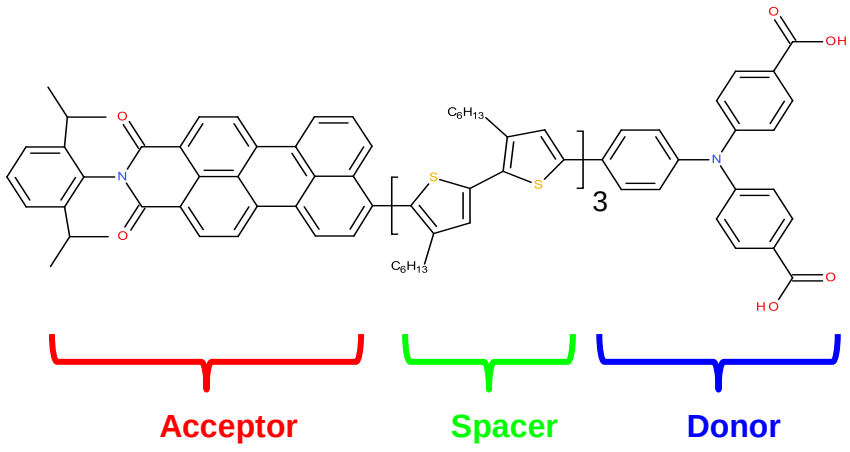

*Figure 3.2 Dye **PMI-6T-TPA** exhibits the highest efficiency (1.3%) in a p-type solar cell in 2013.*

As described for our complexes, the design of a PMI-6T-TPA dye comes mainly from the need to prevent the recombination of the injected hole with the excited electron together with a reasonable absorption in the visible light spectrum. The perylene unit acts as electron acceptor unit, the triphenyl amine unit is a good electron donor fragment and to connect donor-acceptor units and modulate their separation, thiophene linkers have been used.

In this chapter six ligands have been applied as ancillary ligand for complexes **AS9-15** (Figure 3.3); bipyridine and phenanthroline (**2a** and **2b**) as polypyridyl standard ligands; dppz dipyrido[3,2-a:20-30-c]-phenazine (**2c**), complexes including dppz ligands are known to possess low-lying ^{3}MLCT excited states localized on the π* orbitals of the bpy proximal fragment (^{3}MLCTprox) and phenazine distal fragment (^{3}MLCTdis) to the metal centre [185]; 4-nitro-bipyridine and 4,4'-dinitro-bipyridine (**2d** and **2e**) where the presence of electron withdrawing groups on the pyridyl ring can help the charge separation and red-shift the UV-vis absorption; BIAN [bis(arylimino)acenaphthene] (**2f** and **2g**) has been used as ancillary ligand for $[Ir(C^N)_2(N^N)]^+$ complexes because of its ability to absorb well into the red part of the visible spectrum leading to the synthesis of panchromatic complexes.[186]

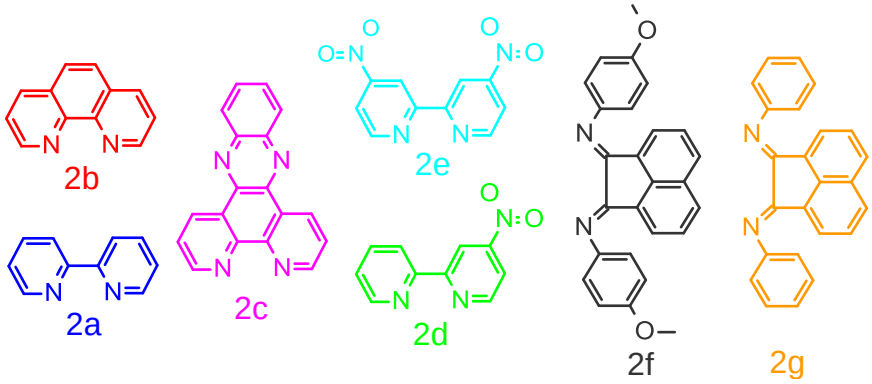

Figure 3.3 Ancillary ligands used for p-type complexes synthesis; (2a) phenantroline; (2b) bipyridine; (2c) dipyrido[3,2-a:20-30-c]-phenazine; (2d) 4-nitrobipyridine; (2e) 4,4'-dinitrobipyridine; (2f) N,N'-bis(4-methoxyphenylimino)acenaphthene; (2g) N,N'-bis(phenylimino)acenaphthene

3.2 General procedure for the synthesis of complexes AS9-15

The cyclometalating ligand precursor used for these complexes has been prepared by oxidizing tolylpyridine to the corresponding pyridylbenzoic acid with $KMnO_4$. The cyclometalated complexes **AS9-15** were prepared using a two-step procedure that is depicted in Scheme 3.1. [77] Iridium (III) chloride and the 4-(2-pyridyl)benzoic acid ligand were combined in ethoxyethanol/water (3:1) and heated to reflux. We originally were working with the ester (ethyl(4-(2-pyridyl))benzoate) and tried de-esterification after formation of the final complex, this proved unnecessary even if leading to higher yields.

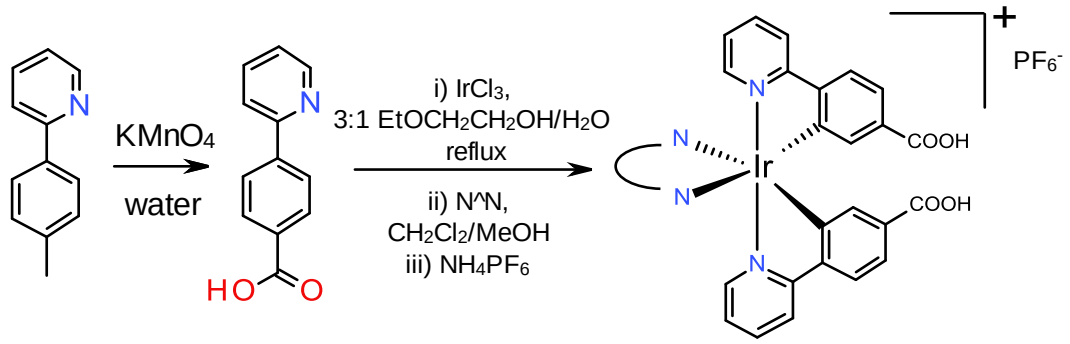

Scheme 3.1 Synthetic route of complexes ***AS9-15***

The reaction mixtures are observed to change from dark red to bright orange within 15 to 30 minutes once the reaction has reached the point of reflux. To ensure complete consumption of the metal salt, the reactions were heated for four hours and then allowed to cool to room temperature. The crude dimer solution [Ir(4-(2-pyridyl)benzoic acid)$_2$Cl]$_2$ was reduced under vacuum to a minimal volume and recrystallised from DCM/Hexane, collected by filtration and was used without purification or characterisation. The dimer was then reacted with the corresponding ancillary ligands (**2a-g**) and NH_4PF_6 in dichloromethane/methanol.

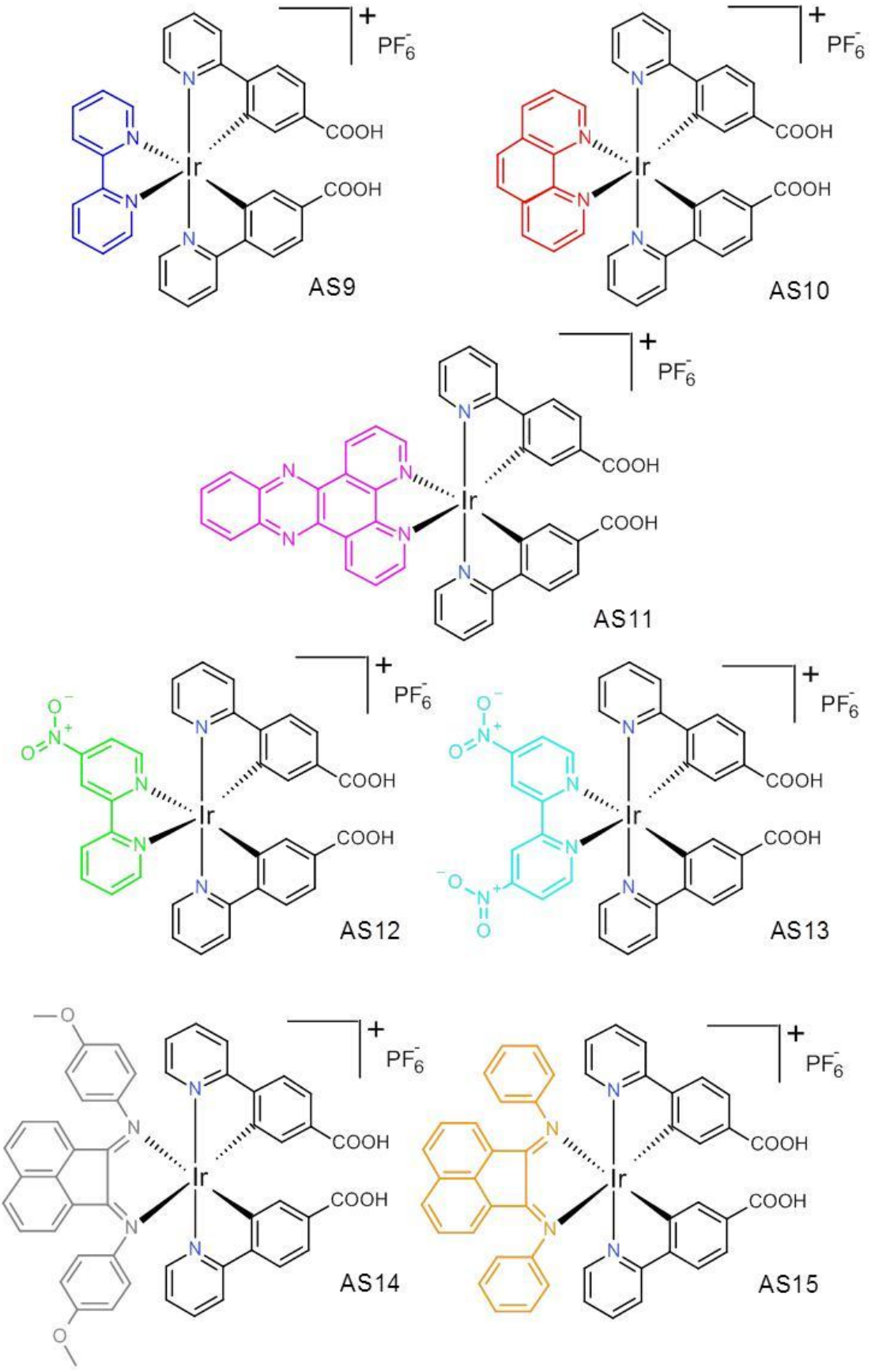

*Figure 3.4 Structure of iridium biscyclometalated complexes synthesised (**AS9-15**).*

The product was purified by column chromatography on silica to provide the desired product. The products were recrystallised from acetonitrile and ether to yield from yellow to dark red solids in modest yields. The complexes [Ir(pyba)(**2a-g**)$_2$]PF_6 **AS9-15** have been fully characterised using ^{1}H and ^{13}C NMR spectroscopy and mass spectrometry.

The cyclometalation of pyba ligand is easily proved by ^{1}H NMR spectroscopy. The corresponding complexes show the loss of one proton, in the aryl fragment, hence a number of signals reduced by one (in comparison with the free pyba) together with a reasonable shift to higher field by ≈0.5ppm for the signals corresponding to the protons next to the coordinated carbon (first peak C from the right in Figure 3.5) and to the coordinated nitrogen (first peak B from the left in Figure 3.5).

In the ^{1}H NMR spectra of **AS9-12** and **AS14-15** complexes, the metalated cyclometalated ligand shows a single set of resonances as consequence of the C_2 symmetry of the Ir(C^N)$_2$ fragment (B and C in Figure 3.5). The peaks distribution for the coordinated diamine ligands shows that half of the ligand is in an unique NMR enviroment, reflecting their symmetry. Complex **AS13** is the only asymmetric complex due to the unsimmetrical NO_2-bpy ligand, for this reason all its protons have a unique resonance.

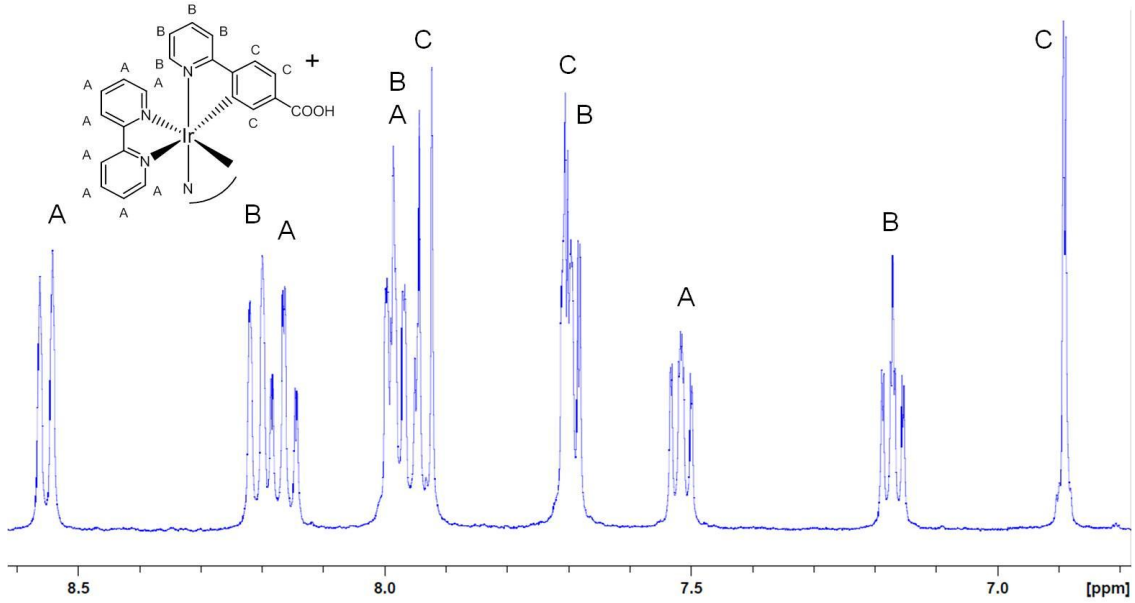

*Figure 3.5 Aromatic region of the ^{1}H NMR spectrum of complex **AS9** (d-ACN). A) protons of the bpy rings; B) protons of the pyridyl ring; C) protons of phenyl cyclometalated ring.*

3.3 Photophysical properties.

UV-visible absorption spectra were recorded for all complexes in aerated acetonitrile solutions at room temperature and are presented in Figure 3.6.

The absorption spectra of these compounds show intense bands in the ultraviolet region between 200 and 300 nm (Table 3.1). These bands are assigned to spin-allowed π-π* ligand-centred (LC) transitions. This assignment was made on assessment of closely related metal complexes in the literature. [105, 175, 176] Two types of charge transfer transitions can be distinguished between 300 and 600 nm: at shorter wavelengths, bands of moderate intensity assigned to ^{1}MLCT/^{1}LLCT transitions and transitions with much weaker intensity at longer wavelengths tentatively assigned to ^{3}MLCT. [103]

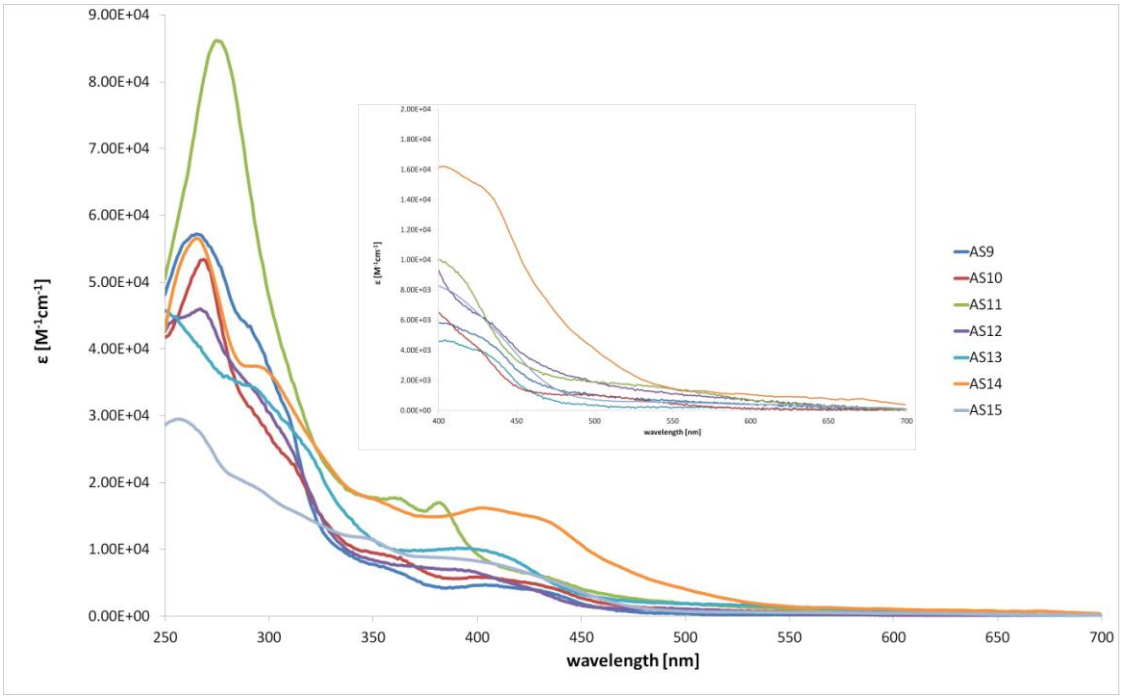

Figure 3.6 UV-vis absorption spectra for cyclometalated iridium complexes ***AS9-15***

Looking at the values reported in Table 3.1 the profile of **AS9** and **AS10** look really similar in terms of wavelengths and extinction coefficient except for a shoulder at 289 nm presented for **AS9** and attributed to bpy centred transition. However their absorption in the visible is limited to a weak band (ε_{410nm} ≈4200 $M^{-1}\cdot cm^{-1}$) about 410 nm. The absorption profile of **AS11** is dominated by a strong transition at 274 nm, due to ppz transition, plus a structure band at 433 nm. Complexes **AS12** and **AS13** have similar profile and, as expected, the presence of two EWGs which helps to enhance the

absorption of **AS13**, (ε_{390nm} ≈10000 $M^{-1}\cdot cm^{-1}$ for **AS13** *vs* 6800 $M^{-1}\cdot cm^{-1}$ for **AS12**). Complex **AS14** has clearly the strongest absorption in the visible range, for the family presented in this chapter with a strong band across 430nm followed by a tail beyond 550nm. BIAN has been used previously by Zysman-Colman *et al* [186] as panchromatic ligand, able to shift into the red and near-IR the absorption of the complexed metal. The observed red shift is due to the greatly stabilized π* LUMO localised on the conjugated Ar-BIAN, red shifted confirmed by TD-DFT calculations in Figure 3.11. The absorption profile of complex **AS15** is clearly affected by the absence of the MeO groups on the phenyl rings, hence the complex solubility is dramatically reduced and its absorption profile is not as extended and as intense (ε_{401nm} ≈8100 $M^{-1}\cdot cm^{-1}$) as for **AS14**.

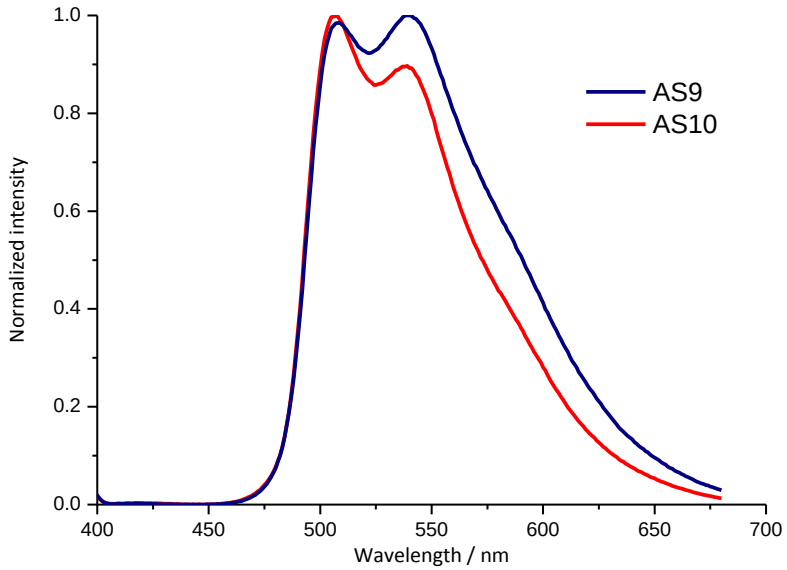

*Figure 3.7 Normalised emission spectra for cyclometalated iridium complexes **AS9-10**, in aerated acetonitrile (excited at 350 nm).*

Complexes **AS9** and **AS10** exhibit intense structured emission bands, with vibronic progression, with maxima at 508 nm and 535 nm assigned as arising from phosphorescent emission from ^{3}MLCT/^{3}ILCT states. Due to the carboxylic acid EWGs, placed on the pyba ligands it is proposed that the excited electron is located in the emissive excited state on the pyridyl rings of the pyba instead of the bpy as in $[Ir(ppy)_2(bpy)]^+$. All the other complexes are essentially non-emissive, due to their electronwithdrawing groups or fragments on the ancillary ligands, suggesting instead transitions from ^{3}MLCT/^{3}LLCT states. Normalised emission spectra are presented in

Figure 3.7

Luminescence lifetimes were also determined in aerated acetonitrile with a value of ≈140 ns for both **AS9** and **AS10**, consistent with phosphorescent emission from a triplet state.

*Table 3.1 Summarised photophysical data for complexes **AS9-15** at room temperature in aerated acetonitrile.*

Complex	λ^{abs}/ nm	λ_{max}^{em}/ nm	τ/ ns
AS9	265 (57200), 289 (43400), 356 (7933), 417 (4250)	508, 535	142 ±1 (75%); 71 ±1 (25%)
AS10	267 (53300), 306 (24300), 354 (7390), 405 (4600)	505, 536	140 ±1 (85%); 68 ±3 (15%)
AS11	274 (86202), 362 (17538), 381 (16936), 433 (5380)	-	-
AS12	267 (46014), 302 (28981), 391 (6871)	-	-
AS13	253 (47529), 291 (34300), 390 (10000)	-	-
AS14	265 (56517), 295 (37402), 402 (16210), 431 (14514)	-	-
AS15	256 (29463), 295 (19024), 347 (11653), 401 (8139)	-	-

3.4 Electrochemistry.

Cyclic voltammetry were recorded in N_2 satured ACN with 0.1 M $TBAPF_6$ as supporting electrolyte. Values are versus Ag/AgCl (Fc/Fc^+ vs Ag/AgCl = 0.41 V).

*Table 3.2 Summarised electrochemical data for complexes **AS9-14** at room temperature acetonitrile.*

$E_{1/2}$/V vs Ag/AgCl (ΔE_p/mV)			
Dye	E_{ox}	E_{red}	ΔE_p
AS9	1.44	-1.38[a]	98
AS10	1.43	-1.35[a]	112
AS11	1.48[a]	-1.33	-
AS12	1.51	-0.38[a]	88
AS13	1.57[b]	-0.31[a]	-
AS14	1.42[b]	-0.65	-

[a] *– irreversible.*

[b] *- quasireversible*

The first reversible or quasi reversible (except for **AS11**) oxidation waves for **AS9-14**, corresponding to the one-electron Ir^{III}/Ir^{IV} couple, occur in the range between +1.43 and +1.60 V, consistent with the expectation of delocalization of the HOMO on the pyridylbenzoic acid. The first reduction waves for all complexes well describe the nature of the ancillary ligand, where the LUMO lies. **AS9-10** present a quasi-reversible reduction peak at -1.38 V and -1.34 V respectively, in line with the value reported for $[Ir(ppy)_2(bpy)]^+$ of -1.14 V *vs* NHE. [187] **AS11** shows a first irreversible reduction peak at -1.41 V followed by a broad and structured wave, similar to the reduction profile for $[Ir(ppy)_2(dppz)]^+$. [188] A second dominant oxidation peak at +2 V has been recorded for **AS11**, it was speculatively assigned to the oxidation of the dppz fragment. [189] Complexes **AS12-13**, present a first irreversible reduction peak at -0.38 and -0.31 V tentatively assigned to NO_2 reduction,[190] followed by a more intense peak ≈ -1.4 V. **AS14** reflects the profile of $[Ir(ppy)_2(BIAN)]^+$,[187] with a reversible reduction peak at -0.66 V (-0.47 *vs* NHE for the ppy analogue) centred on the BIAN ligand and significantly anodically shifted compared to that of the other complexes, attributed to the increased conjugation imparted by BIAN.

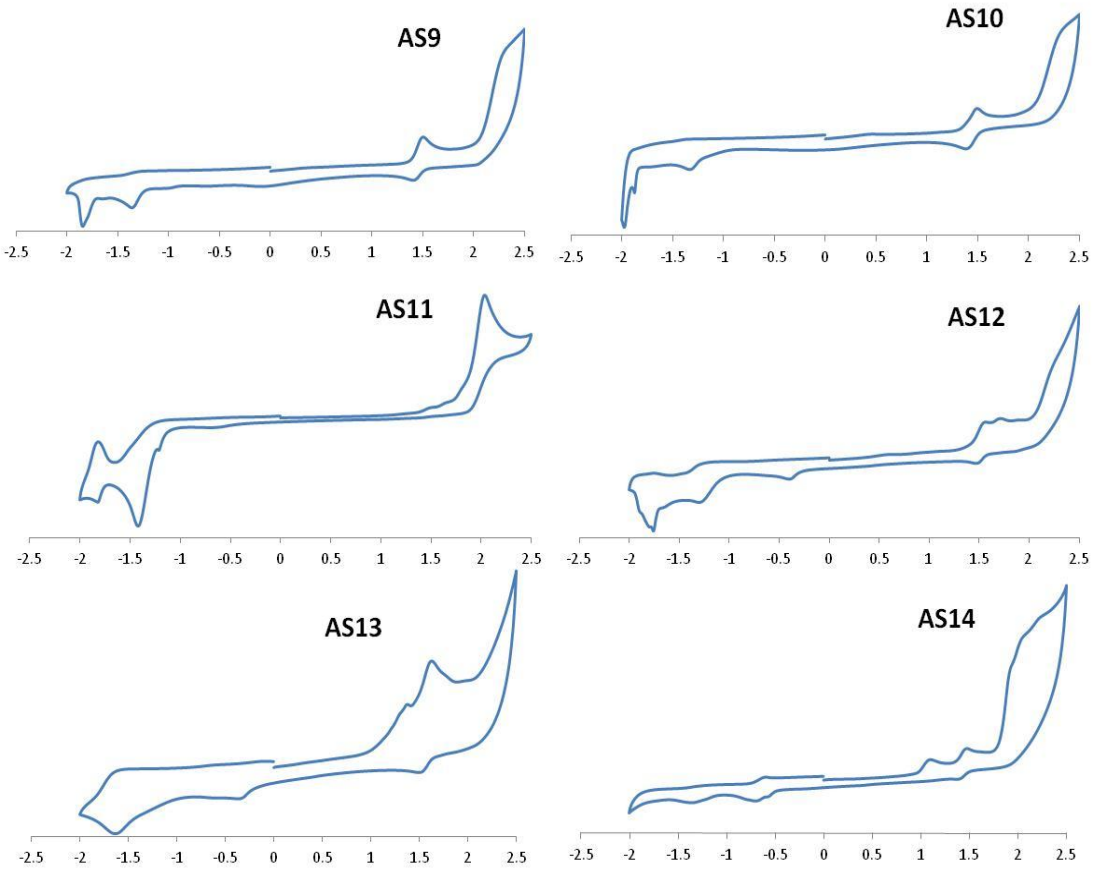

*Figure 3.8 Cyclic Voltammograms for complexes **AS9-14** recorded in ACN.*

3.5 DFT and TDDFT Calculations.

To aid in our understanding of the photophysical properties of the complexes prepared we carried out gas-phase density functional theory (DFT) calculations. Geometries of all complexes were optimised by DFT methods at the B3LYP level of theory. Stuttgart-Dresden relativistic small core ECP was used for iridium and 6-311G* basis sets were used for all other atoms. TD-DFT calculations on optimised structures in CH_3CN by using the COSMO solvation model built into the NWChem software package were used to obtain the electronic spectra. Molecular orbital energies were determined for these ground state geometries and graphical plots are shown in Figure 3.10, a plot of comparative energies of the molecular orbitals for each complex is shown in Figure 3.9.

The results reveal that the LUMO is predominantly localised on the diimine ancillary ligands and that the HOMO orbitals are delocalised amidst the metal centre and the pyridilbenzoic acid ligand, which will facilitate hole injection into the NiO electrode.

Looking at the orbital distribution on complex **AS11**, it is interesting to note that for the dppz ligand the LUMO is localised on the pyrazine rather than on the bpy-like part of the ligand which should lead to increased charge separation.

In complexes **AS12-13**, the nitro groups, on the bpy ligand, strongly stabilise the LUMO (by more than 1eV in comparison with **AS9**) and partially the HOMO too. In fact the LUMO is delocalised on the nitro groups/bpy for **AS13** and on the nitro-pyridine fragment for **AS12**, as consequence of its asymmetry.

*Table 3.3 HOMO and LUMO energy values for complexes **AS9-15***

Dye	HOMO [eV]	LUMO [eV]	Δ [eV]
AS9	-6.04	-2.63	3.41
AS10	-6.05	-2.65	3.40
AS11	-6.07	-3.09	2.50
AS12	-6.16	-3.66	2.37
AS13	-6.26	-3.90	2.97
AS14	-5.94	-3.30	2.64
AS15	-6.02	-3.39	2.63

Despite the emissive state for **AS9-10** being ^{3}MLCT/^{3}ILCT in character, the ground state LUMO for these complexes is on the diimine ligand. This indicates that the order of excited states doesn't necessarily follow the order of the ground state orbitals associated with them.

In Figure 3.9 the energy levels of the frontier orbitals are shown. The calculated HOMO levels remain relatively unchanged as would be expected for the consistency of the pyba ligand; however, the LUMO energy level change sensibly across the series (Table 3.3).

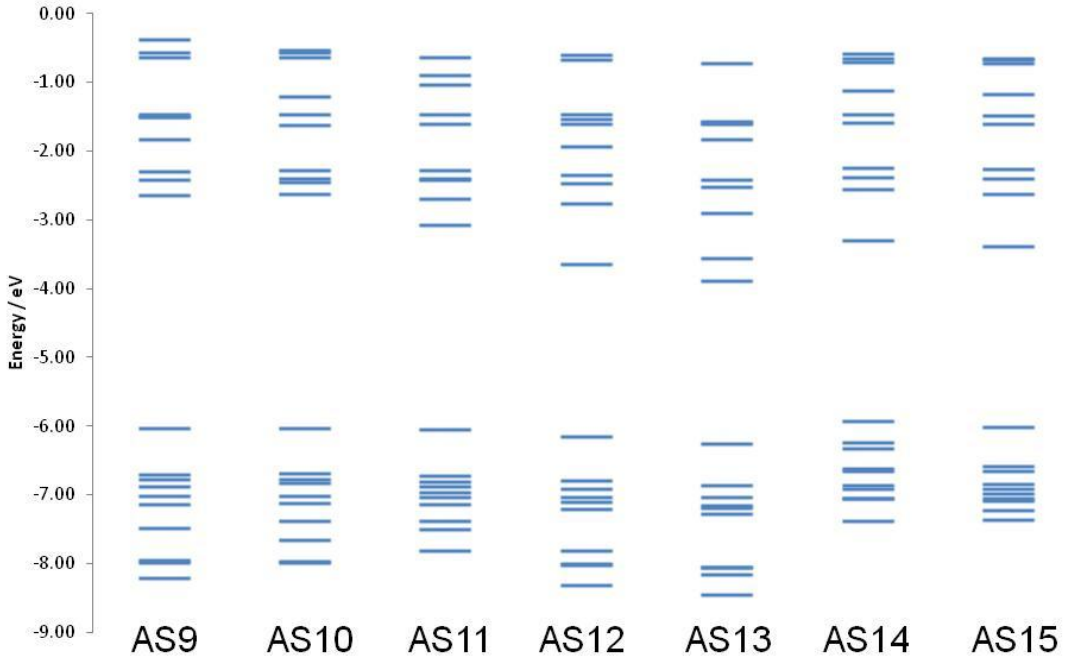

*Figure 3.9 Molecular orbital energy level diagram for complexes **AS9-15***

The calculated energy levels of **AS9-15** complexes showed as the HOMO level value is about -6.2 eV without any significant change across the series. The introduction of electron withdrawing substituents on the bipyridyl skeleton, as nitro group, leads to an energy stabilization of the LUMO relative to those of complexes **AS9** and **AS10** by more than 0.4 eV. For **AS12**, LUMO is dominated by the nitrated ring of the bpy. The computational data obtained for complexes **AS14** and **AS15** are in line with those shown by Zysman-Colman *et al*[186, 187] for $[Ir(ppy)_2(BIAN)]PF_6$ and $[Ir(ppy)_2(MeOBIAN)]PF_6$. In particular the HOMO is localized on the BIAN fragment and the LUMO on the ppy ligands and the reported HOMO-LUMO gaps are about 2.61 eV vs the 2.63 eV reported in Table 3.3.

AS9

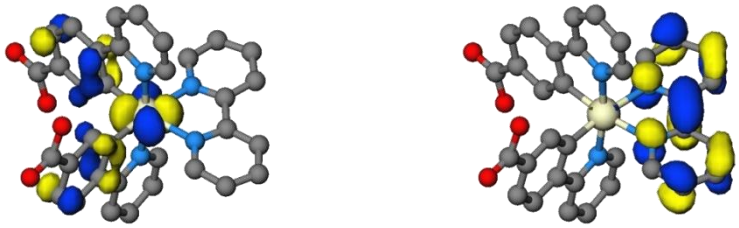

AS10

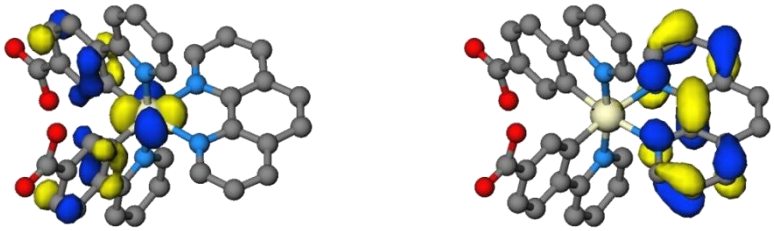

AS11

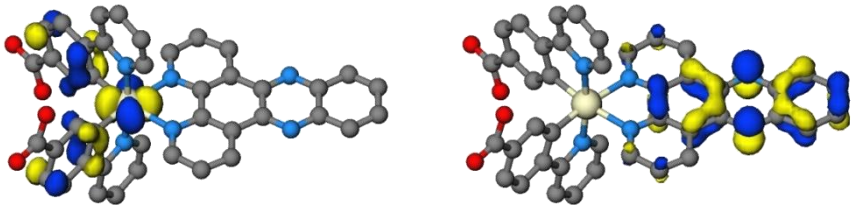

AS12

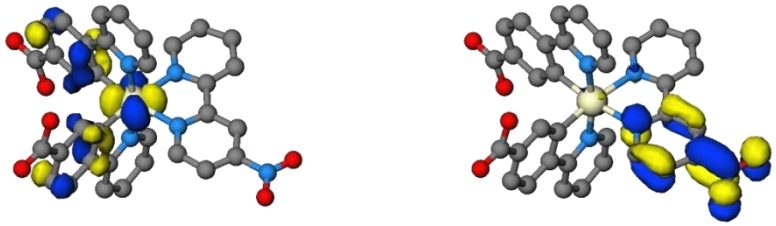

AS13

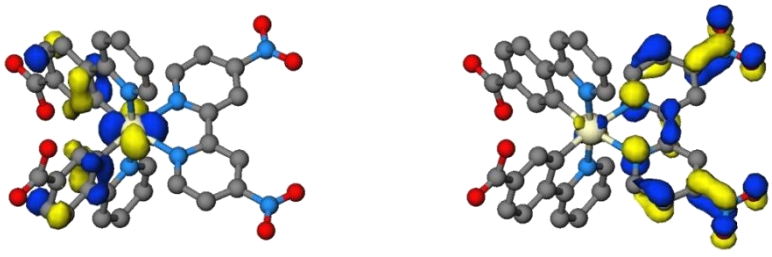

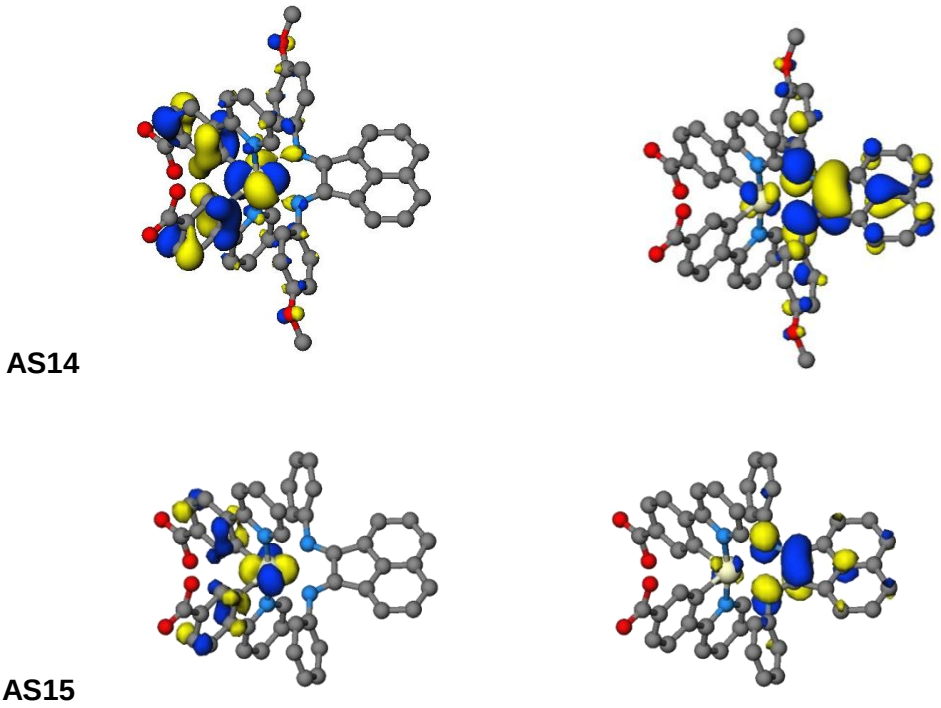

*Figure 3.10 Plots of HOMO (left) and LUMO (right) orbitals of complexes **AS9-15***

The spatial distribution of the HOMO and LUMO are thus perfectly set to promote charge transfer directionality away from the NiO surface and minimize the recombination. The HOMO localised on the anchoring ligand, makes the electronic distribution on these complexes, ideal for their hole injection on nickel oxide. On the other side, the LUMO localised away from the carboxylic groups will avoid the electron-hole recombination. For **AS9-10**, even though the experimental emission spectra show pyba→py e^- directionality, the intended direction is still not far as expected.

Time-dependent DFT (TD-DFT) calculations were carried out on the optimised ground state geometries of each complex in order to determine vertical excitation energies. From TDDFT analysis (Figure 3.11), the predicted transitions correlate well with the experimental spectra.

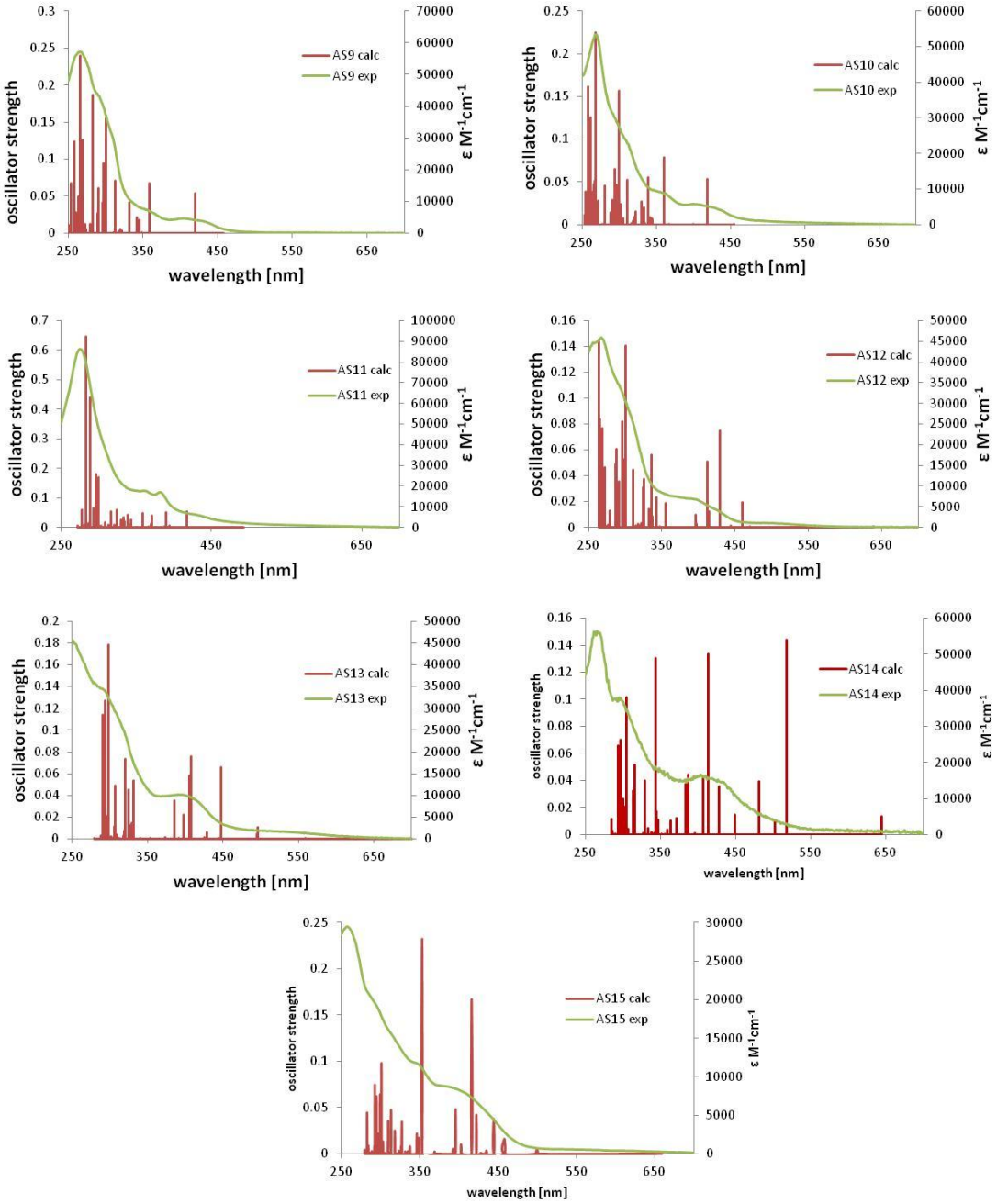

*Figure 3.11 TDDFT calculated absorption spectra for complexes **AS9-15** with experimental spectra overlaid*

The excitations to the S_1 state all complexes are primarily HOMO→LUMO in character, however, they are of low oscillator strength and will therefore contribute little to the observed absorption spectra. According with Table 3.4, the S_1 transition for complexes **AS9-11** takes place below 500 nm, whereas the S_1 for all the other complexes, occurs above 630 nm. The S_1 state for the NO_2-complex **AS13** is lower in energy than that for BIAN-complexes **AS14-15**, however they present an increased ε for those S_1 transitions that lead to increased light absorption at longer wavelengths. The major

transitions observed for all complexes between 350 and 500 nm are primarily of ^{1}MLCT character (Table 3.4), with generally CT from Ir/aryl to ancillary ligand. Below 300 nm most of the transitions are LC in character, for example **AS11** shows a transition at 283 nm with a high oscillator strength which is ILCT in character with CT from the distal dppz (phenazine) to the proximal (bpy). Only **AS14** shows a strong transition beyond 450nm MLCT/ILCT in character, with a substantial contribution of the MeO-BIAN fragment.

Table 3.4 Selected energies (eV), Oscillator Strength (f), wavelength (nm) and compositions of vertical excitations from TDDFT calculations.

Complex	Transition	Energy	λ	*f*	Composition	Character
AS9	S_1	2.708	458	0.00021	HOMO→LUMO 99%	MLCT
	S_2	2.952	420	0.05	HOMO→LUMO+1 96%	MLCT/ILCT
	S_5	3.463	358	0.07	HOMO-3→LUMO 19%	MLCT
					HOMO-1→LUMO 75%	MLCT/LLCT
	S_8	3.627	342	0.02	HOMO-3→LUMO 54%	MLCT
					HOMO-1→LUMO 17%	MLCT/LLCT
					HOMO-1→LUMO+1 17%	MLCT/ILCT
AS10	S_1	2.727	454	0.00026	HOMO→LUMO 98%	MLCT
	S_2	2.958	419	0.05	HOMO→LUMO+2 94%	MLCT/ILCT
	S_6	3.442	360	0.08	HOMO-3→LUMO 16%	MLCT/LLCT
					HOMO-1→LUMO 72%	MLCT/LLCT
	S_{10}	3.659	339	0.05	HOMO-2→LUMO+2 21%	MLCT
					HOMO-1→LUMO+1 59%	MLCT/LLCT
AS11	S_1	2.515	492	0.00029	HOMO→LUMO 88%	MLCT
	S_3	2.971	417	0.05	HOMO→LUMO+2 94%	MLCT/ILCT
	S_6	3.185	389	0.05	HOMO-3→LUMO 15%	MLCT/LLCT
					HOMO-1→LUMO 67%	MLCT/LLCT
	S_9	3.347	370	0.04	HOMO-3→LUMO72%	MLCT
					HOMO-1→LUMO 21%	MLCT/LLCT
	S_{12}	3.463	358	0.05	HOMO-1→LUMO+1 81%	MLCT/LLCT
	S_{14}	3.613	343	0.03	HOMO-3→LUMO+1 73%	MLCT/LLCT
					HOMO-1→LUMO+112%	MLCT/LLCT
AS12	S_1	1.941	638	0.00084	HOMO→LUMO 96%	MLCT
	S_5	2.889	429	0.07	HOMO-3→LUMO 88%	MLCT
	S_7	3.008	412	0.05	HOMO→LUMO+2 92%	MLCT/ILCT
	S_{13}	3.625	342	0.02	HOMO-6→LUMO 39%	ILCT
					HOMO-3→LUMO+1 25%	MLCT
					HOMO-1→LUMO+1 21%	MLCT
	S_{15}	3.698	335	0.06	HOMO-6→LUMO 42%	ILCT
					HOMO-3→LUMO+1 46%	MLCT

AS13	S_1	1.768	701	0.00038	HOMO→LUMO 98%	MLCT
	S_5	2.767	448	0.07	HOMO-3→LUMO 86%	MLCT
	S_{10}	3.039	408	0.08	HOMO-5→LUMO 17%	MLCT
					HOMO-2→LUMO+1 72%	MLCT
	S_{11}	3.057	406	0.06	HOMO→LUMO+3 96%	MLCT/ILCT
	S_{14}	3.216	386	0.03	HOMO-4→LUMO+1 79%	MLCT
					HOMO→LUMO+4 11%	MLCT/ILCT
AS14	S_1	1.923	644	0.013	HOMO→LUMO 94%	MLCT/LLCT
	S_2	2.392	518	0.14	HOMO-1→LUMO 92%	MLCT/ILCT
	S_4	2.573	481	0.04	HOMO-4→LUMO 88%	MLCT/LLCT
	S_7	2.894	428	0.03	HOMO→LUMO+3 92%	ILCT/MLCT
	S_9	2.996	413	0.13	HOMO-5→LUMO 52%	MLCT/LLCT
					HOMO→LUMO+3 25%	ILCT/MLCT
					HOMO→LUMO+1 13%	LLCT/MLCT
	S_{10}	3.043	407	0.04	HOMO→LUMO+3 68%	ILCT/MLCT
					HOMO-5→LUMO 18%	MLCT/LLCT
					HOMO→LUMO+1 5%	LLCT/MLCT
	S_{12}	3.203	387	0.04	HOMO-1→LUMO+1 73%	ILCT/MLCT
					HOMO-8→LUMO 17%	MLCT/ILCT
	S_{14}	3.236	383	0.03	HOMO-8→LUMO 73%	MLCT/ILCT
					HOMO-1→LUMO+1 20%	ILCT/MLCT
	S_{22}	3.602	344	0.13	HOMO-4→LUMO+1 68%	MLCT/LLCT
					HOMO-11→LUMO 17%	MLCT/LLCT
	S_{29}	3.770	328	0.04	HOMO-3→LUMO+3 70%	ILCT/MLCT
					HOMO-5→LUMO+3 16%	ILCT/MLCT
					HOMO-8→LUMO+3 6%	MLCT/LLCT
	S_{32}	3.925	315	0.05	HOMO-5→LUMO+3 70%	ILCT/MLCT
					HOMO-3→LUMO+3 16%	ILCT/MLCT
	S_{36}	4.072	304	0.1	HOMO-6→LUMO+2 72%	ILCT/MLCT
					HOMO-1→LUMO+4 11%	LLCT/MLCT
AS15	S_1	1.878	660	0.00097	HOMO→LUMO 98%	MLCT
	S_4	2.786	445	0.04	HOMO-6→LUMO 15%	MLCT
					HOMO-5→LUMO 65%	MLCT/ILCT
					HOMO-1→LUMO 15%	MLCT/ILCT
	S_7	2.932	423	0.04	HOMO→LUMO+2 96%	MLCT/ILCT
	S_8	2.976	417	0.17	HOMO-4→LUMO 68%	MLCT/LLCT
					HOMO→LUMO+2 14%	MLCT/ILCT
	S_{11}	3.128	396	0.05	HOMO-8→LUMO 84%	MLCT/ILCT
	S_{15}	3.505	354	0.23	HOMO-1→LUMO+1 88%	MLCT/ILCT

3.6 Anchoring test

To verify the binding of the new ligand to the electrode, adsorption tests on NiO have been carried out. Nickel oxide electrodes were left overnight in acetonitrile dye bath solution of **AS14**.

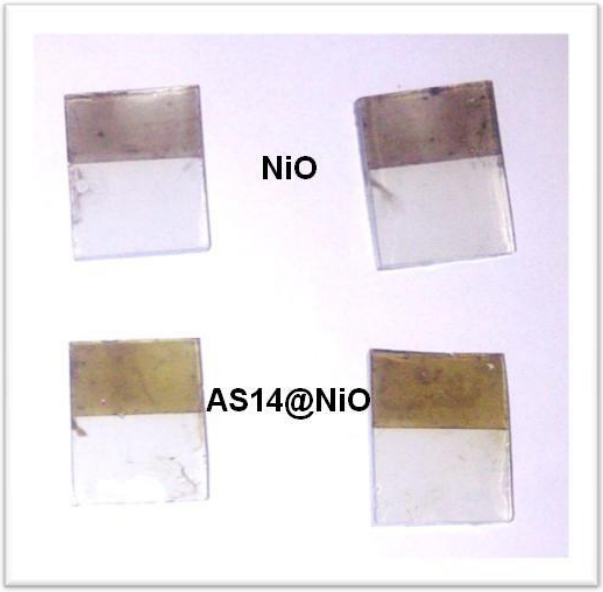

Figure 3.12 NiO electrodes after immersion in dye bath.

The resulting electrodes look clearly of a different colour demonstarting succeful dye loading (Figure 3.12). The absorption spectrum of the sensitised electrode has been compared with the pure nickel oxide one (Figure 3.12).

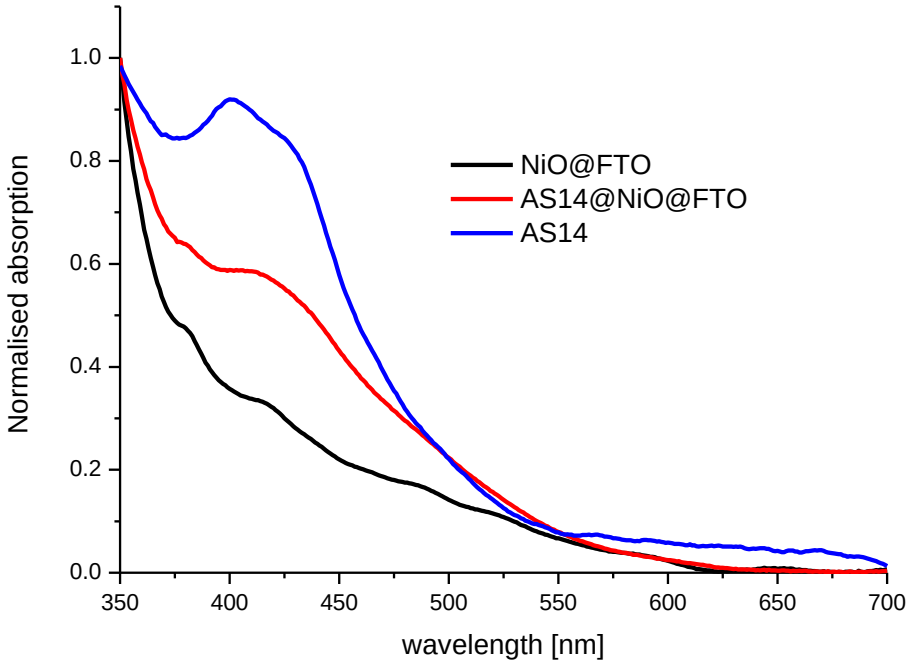

Figure 3.13 Normalised absorption spectra of NiO electrode compared with NiO-dye electrode.

The increased light absorption between 400-550 nm, for AS14@NiO@FTO, clearly matches the absorption profile of **AS14** complex in solution (Table 3.1).

3.7 Photoelectrochemical measurements

After this preliminary test, thanks again to Dr Elizabeth Gibson, the presented complexes were applied in real p-type devices. Complex **AS15** was not tested because of its low solubility.

The dye coated film was realised using a NiO suspension with triblock co-polymer, platinic FTO glass was used as counter electrodes and a solution of 0.1 M I_2 and 1.0 M LiI in acetonitrile as electrolyte. The cell was thermally sealed before the measurement. Photovoltaic measurements were performed on AM 1.5 solar simulator (100 mW cm^{-2}). The incident light was calibrated by using a Si photodiode reference. JV curves were obtained by applying an external bias to the cells and measuring the generated photocurrent with a Keithley digital meter.

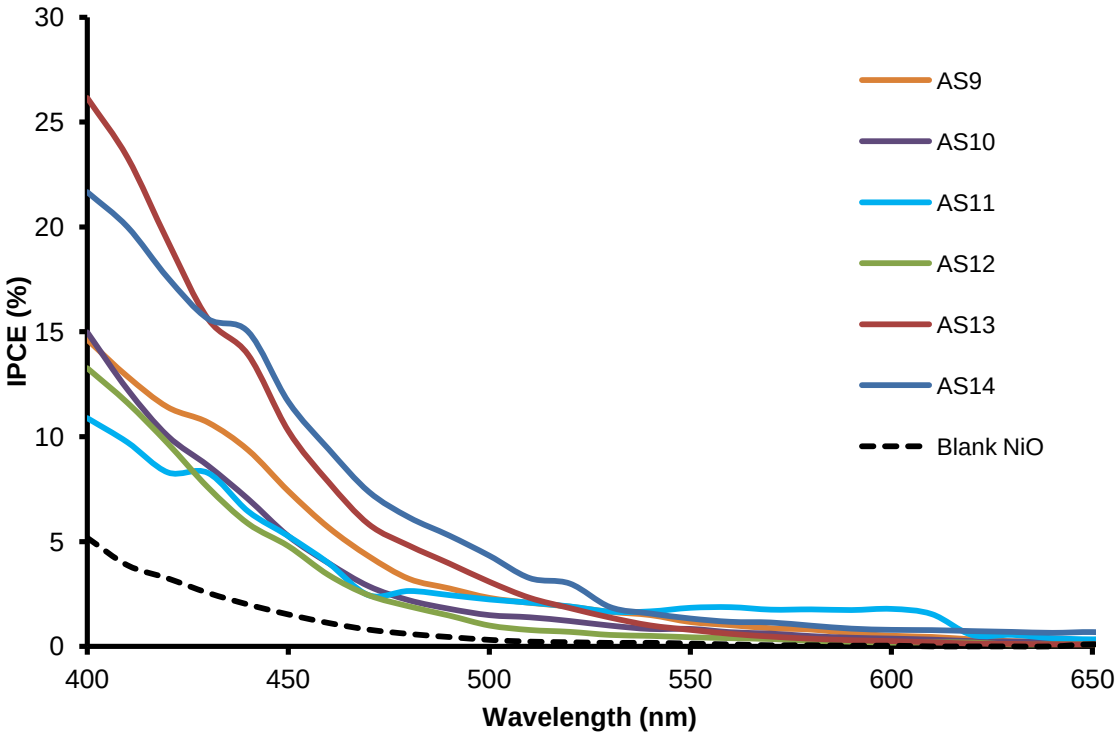

*Figure 3.14 IPCE curves for p-type cells sensitised using iridium complexes **AS9-14***

Figure 3.14 reports the IPCE data for complexes **AS9-14**, which are all in excess the NiO IPCE profile; this suggests an efficient dye loading on the nickel oxide. The IPCE values are between 10 and 25% and their profiles reflect the trend of the corresponding absorption spectra. Unfortunately the presented dyes have their main absorption peaks at or below ≈400 nm, so the IPCE profiles look like the tail of those absorption spectra. Only **AS13-14**, which present the highest extinction coeffincients in the visible, show a reasonable IPCE, hence this has been confirmed by the efficiency measurements reported in Figure 3.15 and by the values reported in Table 3.5 .

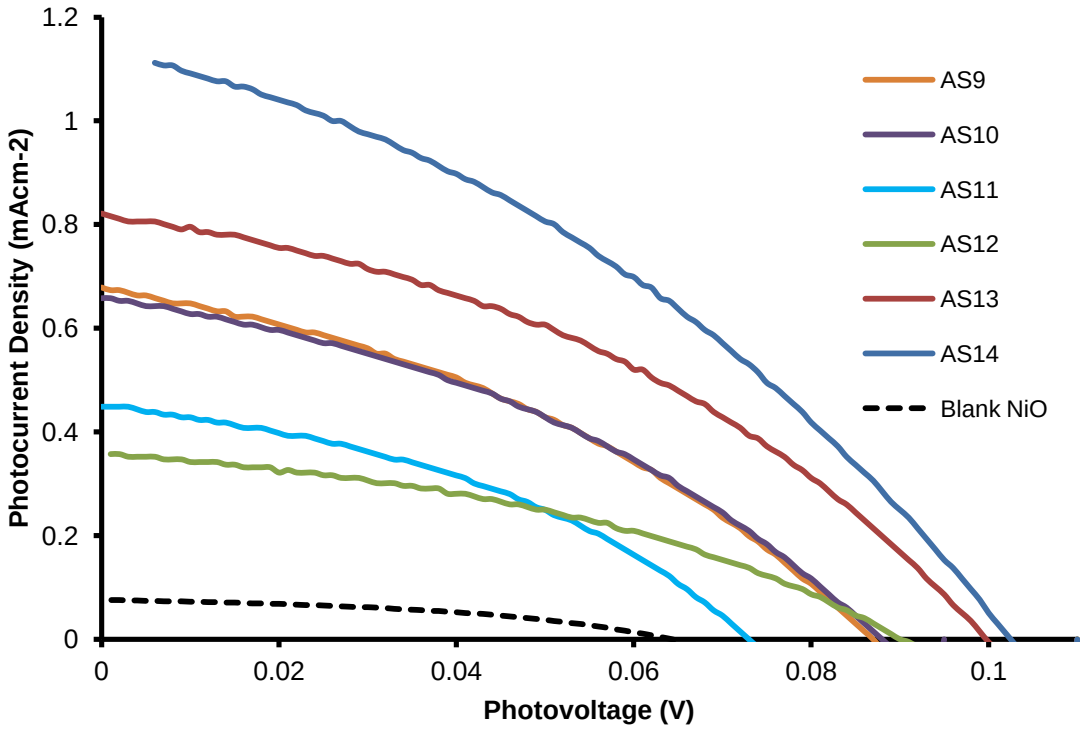

Figure 3.15 Current-Voltage curves for p-type cells sensitised using iridium complexes ***AS9-14***

All the applied complexes, under irradiation, were able to generate a photocurrent. However both IPCE and JV values for **AS11** and **AS12** were strongly affected by their low solubility, achieving the lowest photocurrent conversion. As expected from their very similar structures, **AS9** and **AS10** showed nearly identical results in terms of IPCE and efficiency. Complexes **AS13** and **AS14** showed reasonable efficiencies of 0.032% and 0.043% respectively. The reason is attributable to their enhanced absorption in the visible spectrum, leading to the highest IPCE and JV values observed for this set of complexes.

Table 3.5 Photovoltaic parameters of tested dyes.

Dye	J_{sc} ($mAcm^{-2}$)	V_{oc} (V)	V_{max} (V)	J_{max} ($mAcm^{-2}$)	FF (%)	η (%)
AS9	0.68	0.09	0.05	0.41	36.6	0.022
AS10	0.66	0.09	0.05	0.41	37.6	0.022
AS11	0.45	0.07	0.05	0.26	38.1	0.013
AS12	0.36	0.09	0.06	0.22	40.1	0.013
AS13	0.82	0.10	0.06	0.54	38.7	0.032
AS14	1.12	0.10	0.06	0.68	36.8	0.043

3.8 Conclusions.

We have synthesised and characterised, by ^{1}H and ^{13}C NMR spectroscopy, mass spectrometry and investigated the photophysics by UV-vis absorption and emission spectroscopy, seven new iridium(III) dyes with various ancillary ligands. Computational calculations were fundamental tools in the design new complexes and in the prediction and explanation of their proprieties. Diimine complexes show good tuning of absorption wavelengths and HOMO-LUMO gap, and thanks to their design, these complexes show spatial charge transfer directionality together with energy levels in accordance with their intended application in p-DSSC. The use of these complexes (Figure 3.13 and Figure 3.4) as sensitizers in DSSC devices has been preliminary investigated. All tested complexes achieved modest efficiencies, however **AS13** and **AS14** show reasonable efficiencies of 0.032% and 0.043% respectively, especially if related to those reported for iridium complexes by Gennari *et al* [43]. The methodology here reported will allow for facile tuning of photophysical and photovoltaic properties and produce dyes with greater ease than existing ruthenium based systems. Results are nevertheless encouraging for the development of a new generation of p-type dyes based on this general design. Future research will focus on improving on these initial studies and increasing the light absorbing properties of these dyes together with the substitution of the triiodide/iodide electrolyte for a one-electron, outer sphere redox couple such as cobalt polypyridyl complexes, in order to relieve the constraint that the complexities of the iodine-based system impose on the energetic requirements of the dye. [191]

4 Design and synthesis of a novel triazole carboxylic acid anchoring ligand

4.1 Introduction

Over thirty years ago, Goodenough [192] and co-workers reported the use of 4,4′-dicarboxy-2,2′-bipyridine, dcb, as an ambidentate ligand for coordination to Ru (II) and metal oxide semiconductors. Strong electronic coupling between the metal-to-ligand charge transfer (MLCT) excited states of dcb-containing Ru compounds and TiO_2 has been inferred from femtosecond transient absorption spectroscopy, and the rate constants extracted from such data are in the order of <25 fs.[193]

In 2012, Meyer *et al*, reported the design of a new bipyridine based anchoring ligand (4,5-diazafluoren-9-ylidene) malonic acid (dfm)[137], together with the corresponding $[Ru(bpy)_2(dfm)]^+$ complex.

Theoretical calculations indicate that a coplanar arrangement of the carboxyl and the pyridine ring is most optimal for excited state injection; the interfacial electronic interactions decrease markedly when the carboxyl group becomes orthogonal to the pyridine ring[194]. This suggests that ultrafast injection occurs from those excited states where the carboxyl and pyridine ring are coplanar, and slower injection from those that deviate from planarity.

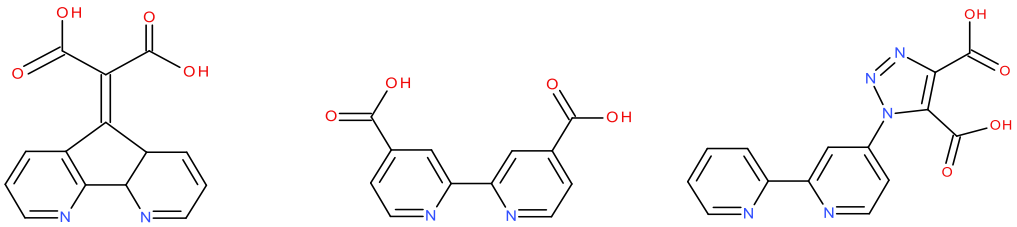

Figure 4.1 Bipyridine-based anchoring ligands.

The anchoring group determines the binding energy of the dye with metal oxide (largely affecting its long-term stability) and the electron/hole injection rate (through mediating the charge transfer from the chromophore to the semiconductor) and can also modulate the injection energy by altering the energy of the dye's excited state. [195]

To this day dcb remains the most efficient and widely utilised ligand for applications in dye sensitised solar cells. In order to enhance power conversion efficiencies of DSSCs, it is imperative to design novel sensitisers that exhibit an enhanced molar absorptivity in combination with a red-shifted absorption band compared to standard dyes. Extension of the p-conjugation of the ancillary ligand and/or the anchoring ligand can improve the spectral response of corresponding metal-based sensitisers, as showed by Mishra *et al*.[196]

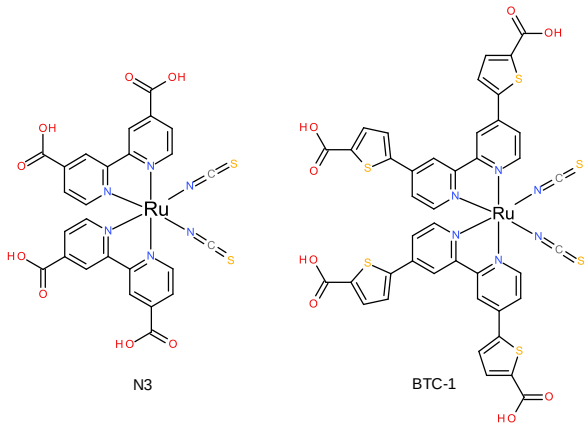

Figure 4.2 Structure of ruthenium (II) ***N3*** *and* ***BTC-1*** *dyes.* [196]

In the complex **BCT-1**, shown in Figure 4.2, the distance between the bpy and the anchoring group has been extended by the introduction of a thiophene unit spacer. The effect on the complex absorptions is a red shifted and enhanced profile for **BTC-1** (ε_{563} 23200 $M^{-1}cm^{-1}$ *vs* ε_{535} 13500 $M^{-1}cm^{-1}$ for **N3**) yielding to an enhancement of an overall conversion efficiency of 6.1% compared with the 4.8% achieved using **N3** dye.

In order to design a new anchoring ligand, considering the reasons above, we applied again “click” chemistry but this time using it as a bridge between the anchoring carboxylate groups and the bpy core of the anchoring ligand. Azido-bipyridine has been reacted with diethyl acetylenedicarboxylate (DADC) to yield 1-[2,2′-bipyridine-4-yl]triazole-4,5-bis(ethylcarboxylate) (detzbpy), followed by a hydrolysis reaction to obtain the novel ligand 1-[2,2′-bipyridine-4-yl]triazole-4,5-dicarboxylic acid (dctzbpy).

This new ligand combines synthetic advantages with applicative needs. More specifically it is readily accessible through a favourable cycloaddition reaction; it posses a π extended system and two carboxylates to ensure a good surface binding; whilst the 1,2,3-triazole moiety isn’t conducting [197, 198], it might insulate the bpy fragment from the metal oxide after electron injection, impeding the recombination.

This ligand has been reacted with Ru(II), Re(I) and Ir(III) precursor complexes, to yield new dyes, which have been analysed and compared with their analogous dcb complexes. In this chapter is reported the synthesis, characterization, photophysical study and photovoltaic application of these new complexes.

4.2 Synthesis

The above mentioned ligand, dctzbpy, has been prepared by a multistep synthesis as described in Scheme 4.1.

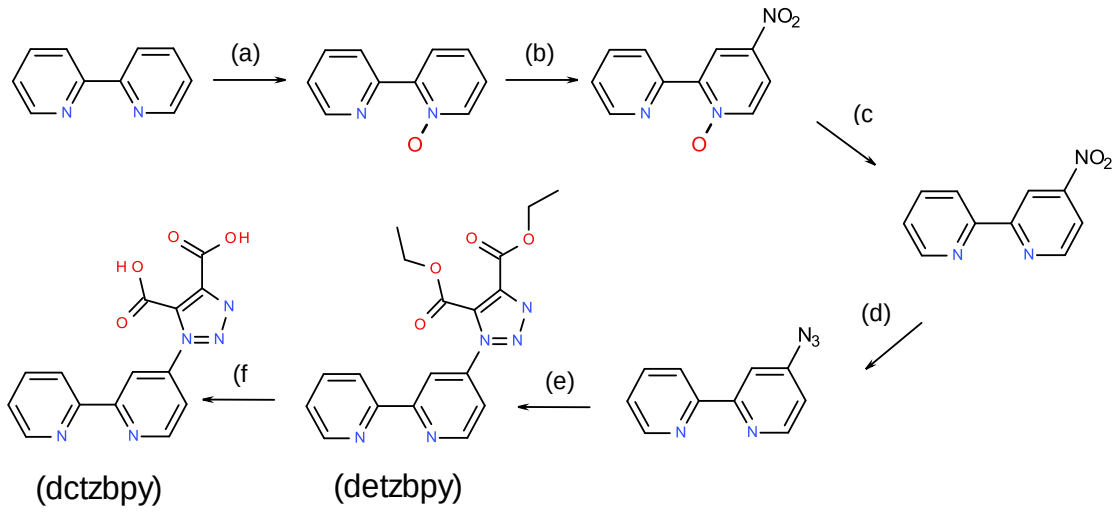

Scheme 4.1 Synthetic route to target ligand: (a) mCPBA, DCM (b) HNO_3, H_2SO_4 (c) PCl_3 (d) NaN_3, DMF (e) DADC, toluene (f) KOH/HCl

Firstly commercially available 2,2'-bipyridyl is converted into the mono-*N*-oxide by treatment with *meta*-chloroperoxybenzoic acid (mCPBA) in dichloromethane. This is then converted in to the 4-nitro derivative under standard nitration conditions using concentrated nitric acid in concentrated sulphuric acid. The oxide protecting group is then removed by heating to reflux temperature with phosphorus trichloride, after which the compound is reacted with excess sodium azide, giving the very useful synthon for "click" reactions, 4-azido-bpy.[166] The conversion of the nitro group into an azide has been confirmed by IR spectroscopy where the azide stretch showed a characteristic peak at 2100 cm^{-1}. The azide then undergoes a cycloaddition reaction with diethyl acetylenedicarboxylate (DADC) in heated to reflux temperature toluene. The reaction between the azido-bpy and the diethyl acetylenedicarboxylate is thermally driven and doesn't require the addition of copper as a catalyst. Thanks to the symmetry of the acetylene this only gives one product. The cycloaddittion has been confirmed by IR spectroscopy with the disappearance of the azide peak and the appearance of new CO stretching peaks. The carboxylate ester groups then undergo hydrolysis to the corresponding carboxylic acids in heated to reflux temperature dilute KOH before neutralisation with HCl.

The ^{1}H NMR spectrum of the product shows seven unique environments for the protons on the bpy system, four for the unsubstituted ring (A in Figure 4.3) and three for the substituted one (B in Figure 4.3), plus two different sets of signals for the ethyl groups of the carboxylate ester moieties.

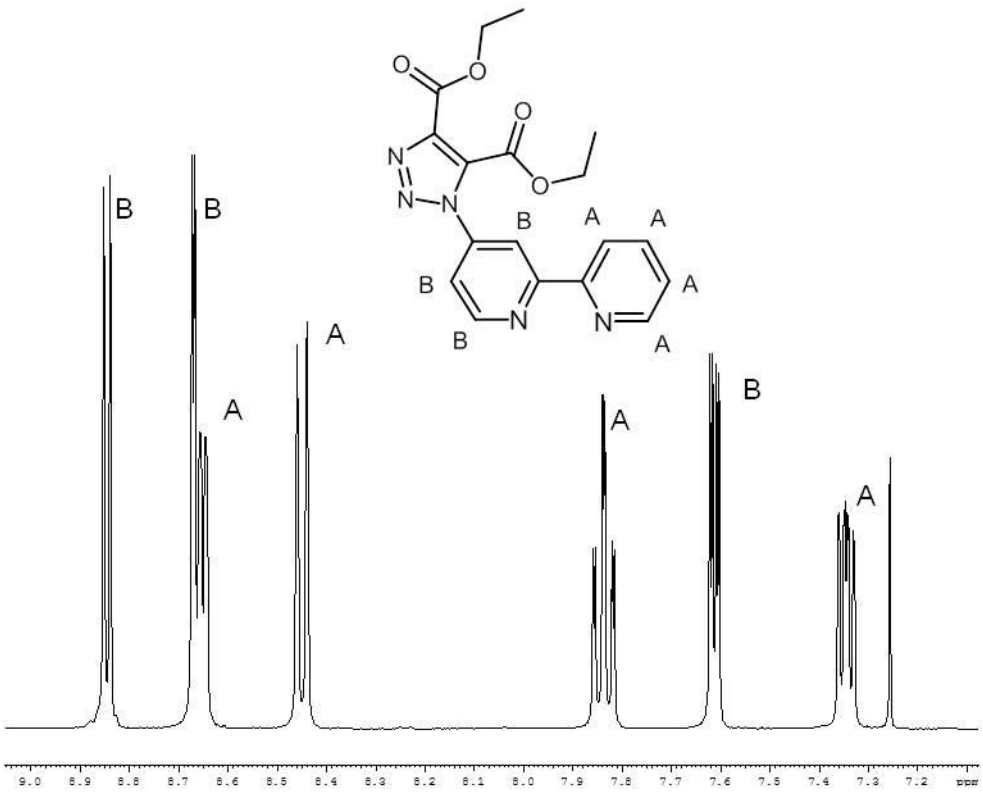

Figure 4.3 Aromatic region of the ^{1}H NMR spectrum of detzbpy ($CDCl_3$), A- protons assigned to unsubstituted ring, B- protons assigned to substituted ring.

4.3 Complexes synthesis

The detzbpy ligand then underwent reaction with $[Ru(bpy)_2Cl_2]$, $[Ir(ppy)_2Cl]_2$, $[Re(CO)_5Cl]$ to yield the complexes $[Ru(bpy)_2(detzbpy)]^{2+}$, $[Ir(ppy)_2(detzbpy)]^{+}$, $[Re(CO)_3(detzbpy)Cl]$, these complexes have been fully characterized by ^{1}H and ^{13}C NMR spectroscopy and HRMS spectrometry. The esterified complexes were then hydrolysed by KOH/HCl to obtain complexes **AS16**, **AS17** and **AS18** respectively, despite the evidence of the hydrolysis by ^{1}H NMR spectroscopy, it was not possible to obtain a MS characterization by ESI or MALDI, speculatively attribute to the fragmentation of the dctzbpy fragment. The corresponding dcb complexes $[Ru(bpy)_2(dcb)]^{2+}$ (**4.1**), $[Ir(ppy)_2(dcb)]^{+}$ (**4.2**), $Re(CO)_3(dcb)Cl$ (**4.3**) were also prepared by analogous methods for comparison.

As a consequence of dctzbpy coordination, all $[Ru(bpy)_2]$ and $[Ir(ppy)_2]$ of the metal precursor complexes lose their original C_2 type symmetry turning to C_1 symmetry. Hence each bpy and ppy proton has a unique environment. For the reason above, the ^1H NMR spectra of **AS16** and **AS17** show two different set of signals for each bpy and ppy ligands respectively, making their assignment very difficult because of the overlap of signals. Complex **AS18** shows only the dctzbpy signals, shifted in comparison with the free ligand to higher field (≈0.1ppm), especially for resonances relative to H_{C6} now shifted to 8.95 and 9.66 ppm respectively (DMSO-d_6).

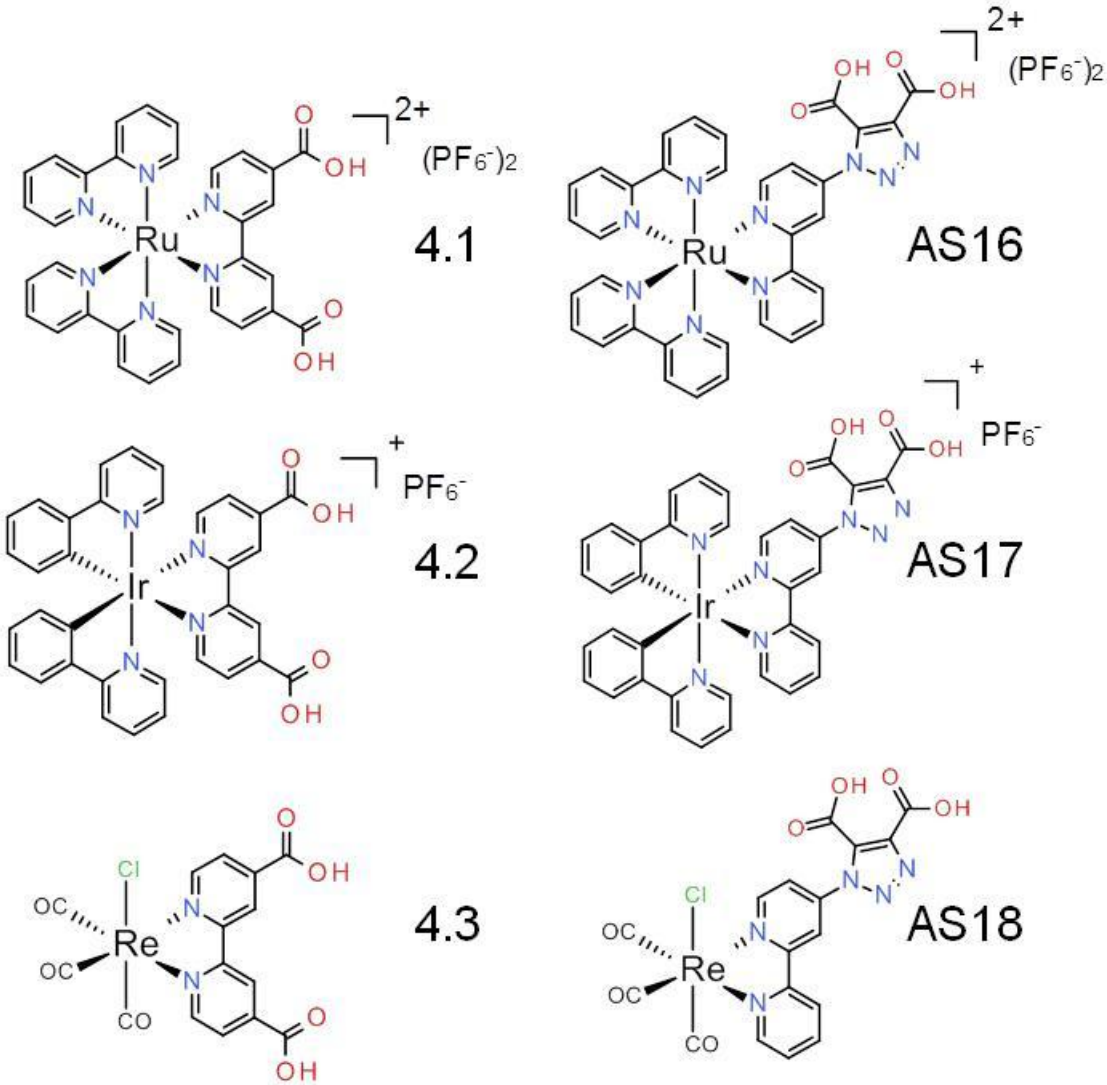

*Figure 4.4 Structures of complexes **AS16-18** compared with their dcb analogues **4.1-3**.*

4.4 Photophysical characterization

UV-visible absorption spectra were recorded for all complexes in acetonitrile solutions at room temperature and are presented in Figure 4.5 and summarised data are listed in Table 4.1.

*Table 4.1 Summarised photophysical data for complexes **AS16-18** and their dcb analogues **4.1-3** at room temperature in acetonitrile.*

Complex	λ^{abs}/ nm (ε)	λ_{max}^{em}/ nm	τ/ ns
4.1	245 (21923), 287 (44481), 308 (26079), 357 (7836), 430 (8807), 475 (9880)	682	37 ±6
4.2	256 (30778), 289 (24016), 377 (6905)	689	32 ±1
4.3	252 (10289), 303 (8202), 413 (1826)	725	41 ±4 (62%); 9 ±0.2 (38%)
AS16	242 (15624), 287 (30138), 424 (4642), 456 (5719)	638	34 ±4 (80%); 2 ±0.1 (20%)
AS17	255 (44311), 301 (23330), 364 (7771), 415 (1914)	590	16 ±1 (28%); 3 ±0.05 (72%)
AS18	254 (20204), 297 (15317), 397 (3815)	553	51 ±1 (98%); 4 ±0.3 (2%)

The comparison between the dcb complexes and their dctzbpy analogues shows similar absorption profiles with a slight blue shifting for complexes **AS16-18**. The ruthenium complexes (**4.1** and **AS16**) show a strong band at 300 nm attributed to π-π* LC transitions together with modest (ε≈ 5000-10000 M^{-1} cm^{-1}) ^{1}MLCT bands above 400 nm. The dcb complex has an enhanced red shifted profile related to the dctzbpy complex, showing a peak at 475 nm and the 453 nm respectively. The iridium complexes (**4.2** and **AS17**) bands are structured as described before for similar complexes, that possess a π-π* LC transitions, in the UV region and a weaker ^{1}MLCT transition in the visible region, with a tailed peak at 377 nm for **4.2** and 415 nm for **AS17**. Both **4.3** and **AS18** absorb weakly above 320 nm, ε_{413}=1826 M^{-1} cm^{-1} for the dcb complex (profile influenced by its low solubility) and ε_{397}=3815 M^{-1} cm^{-1} for the dctzbpy

complex. The blue-shifted absorption bands in the spectra of the dctzbpy complexes demonstrate that the LUMO is likely to be higher in energy than that for dcb and so the $tz(COOH)_2$ group is obviously much less electron withdrawing than the two COOH groups attached directly to the bpy core as in dcb. Nevertheless, the LUMO is correctly positioned with reference to the TiO_2 Fermi level for charge injection. We would therefore predict that **AS16-18** would produce functional DSSCs.

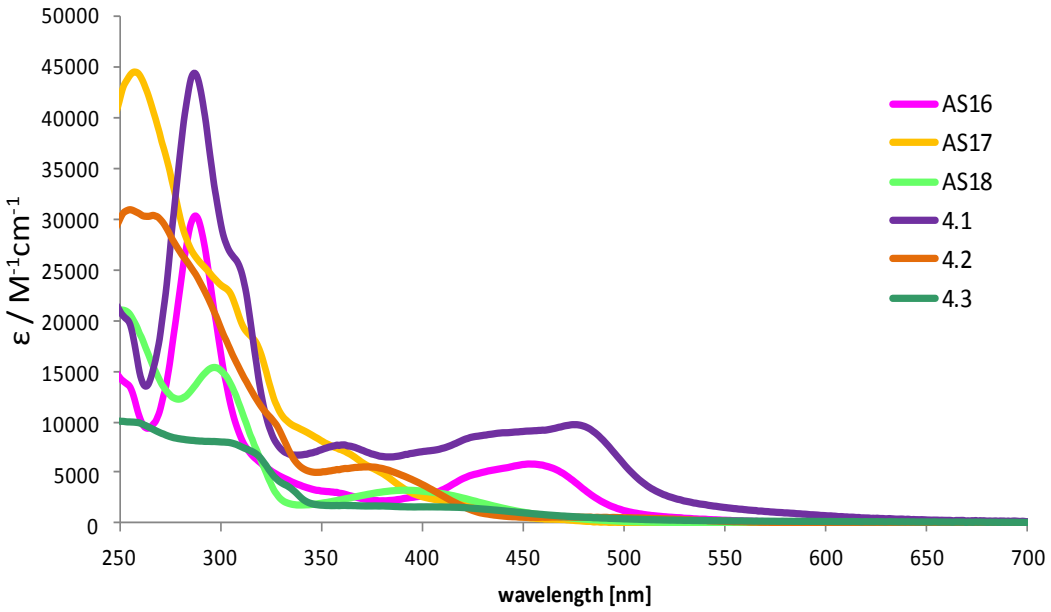

*Figure 4.5 UV-vis absorption spectra for cyclometalated iridium complexes **AS15-17** and **4.1-3***

AS16-18 complexes show broad bands emission similarly blue-shift of relative to their dcb analogues, between 550 and 650 nm, with life times between 16-51 ns. This again demonstrates the higher energy of LUMO of the dctzbpy ligand relative to that of dcb and hence a destabilization of ^{3}MLCT T_1 states in these complexes.

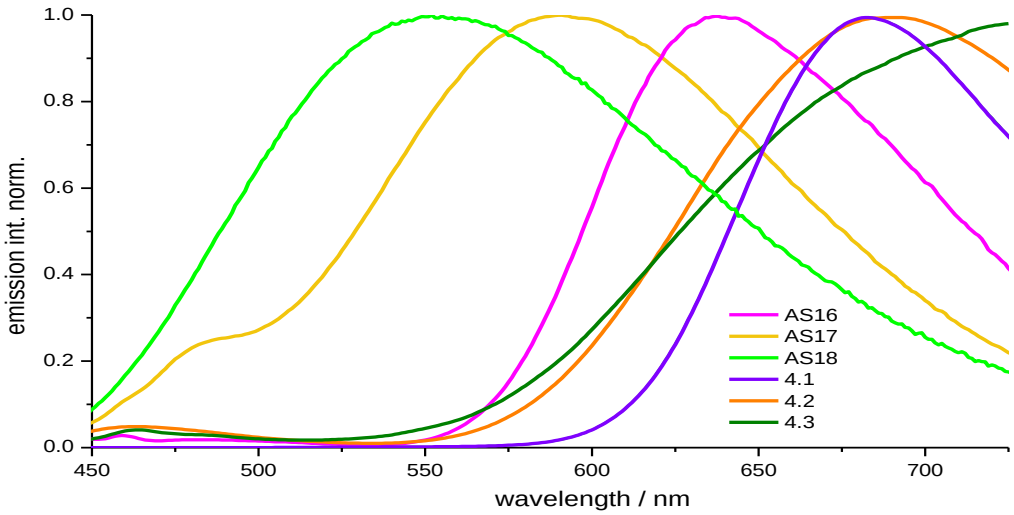

*Figure 4.6 Normalized emission spectra for complexes **AS16-18** and **4.1-3,** in aerated acetonitrile (excited at 400 nm).*

4.5 Electrochemistry.

Cyclic voltammetry were recorded in N_2 satured ACN with 0.1 M $TBAClO_4$ as supporting electrolyte. Values are versus $Ag/AgNO_3$ (Fc/Fc^+ vs $Ag/AgNO_3$ = 0.58 V).

*Table 4.2 Summarised electrochemical data for complexes **4.1-3** and **AS16-18** at room temperature acetonitrile.*

$E_{1/2}$/V vs $Ag/AgNO_3$ (ΔE_p/mV)			
Dye	E_{ox}	E_{red}	ΔE_p
4.1	1.57	-0.65[a]	110
4.2	1.52	-0.61	80
4.3	1.14[a]	-0.64	-
AS16	1.48	-0.53[a]	80
AS17	1.41	-0.48[a]	80
AS18	1.12[a]	-0.69	-

[a] *– irreversible.*

The cyclic voltammetry for homoleptic Ru complexes such as $[Ru(bpy)_3]^{2+}$ [199] shows and oxidation peak for Ru^{II}/Ru^{III} together with three reduction peaks corresponding to the three bpy ligands. In the same way, complexes **4.1** and **AS16** present a first reversible oxidation peak at 1.57 and 1.48 v respectively, the anodic wave reveals a

first irreversible peak at -0.65 and -0.53 V respectively, assigned to the dctzbpy reduction, followed by two furthers reversible reduction peaks assigned to the bpy ligands. The first reversible oxidation waves for **4.2** and **AS17**, corresponding to the one-electron Ir^{III}/Ir^{IV} couple, occur at 1.52 and1.41 V; the first reduction waves present a quasi-reversible reduction peak at -0.61 V and -0.48 V respectively. Complexes **4.3** and **AS18** are characterised by an oxidation peak at 1.14 and 1.12 V respectively, unusually negatively shifted when compared to other $Re(CO)_3(bpy)Cl$-based complexes. [200] They also present a reversible reduction peak at -0.64 and -0.69 V.

Summarising, the first reversible (except for the two ruthenium complexes) reduction waves for **4.1-3** and **AS16-18**, corresponding to the reduction of dcb and dctzbpy respectively, occur in the range between -0.65-(-0.61) for dcb and -0.69-(-0.48) for dctzbpy, consistent with the expectation of delocalization of the LUMO on those ligands.

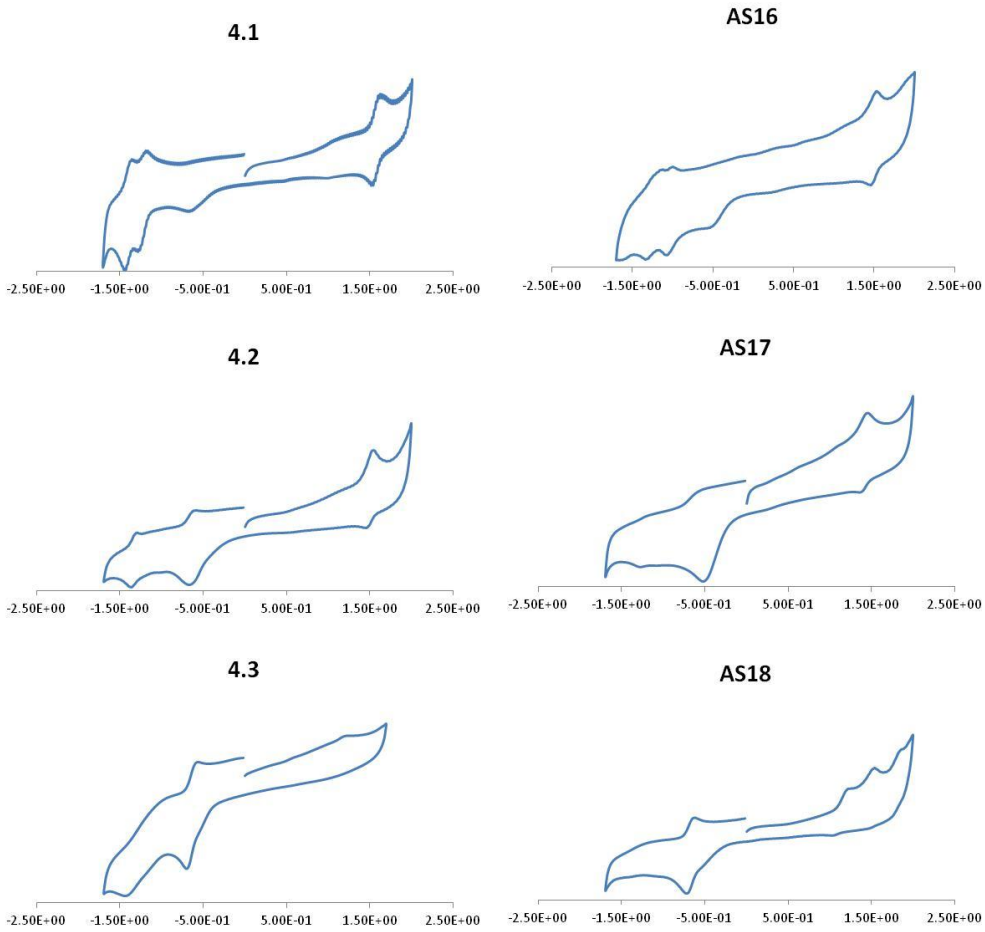

*Figure 4.7. Cyclic Voltammograms for complexes **4.1-3** and **AS16-18** recorded in 0.1 M Bu_4PF_6/ACN solution.*

4.6 DFT and TD-DFT Calculations.

To further rationalise the photophysical properties of complexes **AS16-18** and **4.1-3**, DFT calculations were carried out. Geometries of all complexes were optimised by DFT methods at the B3LYP level of theory. Stuttgart-Dresden relativistic small core ECP was used for the metals and 6-311G* basis sets were used for all other atoms. TD-DFT calculations on optimised structures in CH_3CN by using the COSMO solvation model built into the NWChem software package were used to obtain electronic spectra. Plots of the HOMO and LUMO orbitals of **AS16-18** and **4.1-3** are shown in Figure 4.8 with energies summarised in Table 4.3.

In the designed dyes, the HOMO is predominantly metal d-orbital in character but for the iridium and rhenium complexes there is additional π-aryl and Cl ligand character respectively. The LUMO is located on the dcb and dctzbpy ligands, favouring electron injection into the metal oxide electrode. For the dcb ligands, the carboxylates have an appreciable involvement in the LUMO, whereas for the dctzbpy there is a minor contribution from the triazole, but very little from the carboxylates groups. This is consistent with what we infer from UV-visible absorption and emission data, that triazole biscarboxylate moiety is less electron withdrawing than the two carboxylates directly bonded to the bpy core in dcb and thus the dctzbpy LUMO is higher in energy than that of dcb.

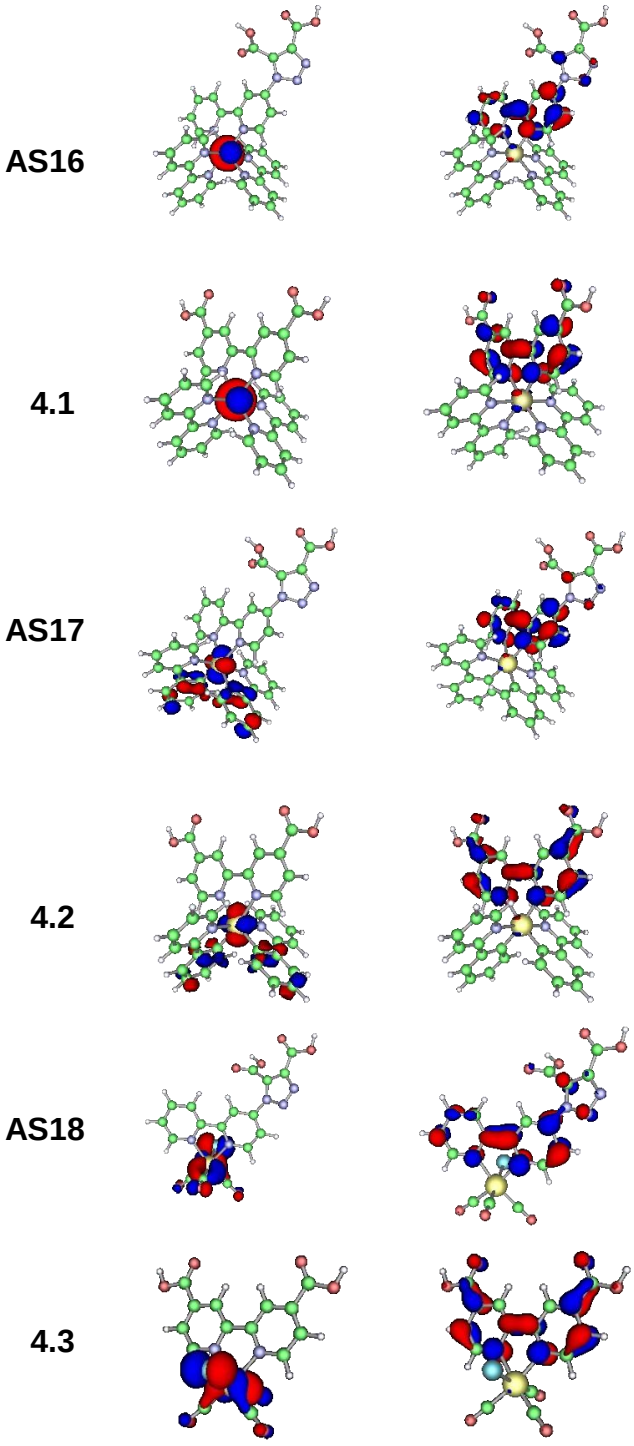

Figure 4.8 Molecular orbital energy level diagram for complexes **AS16-18** and **4.1-3**

Figure 4.8 shows the comparison between dctzbpy and dcb complex molecular orbital energies. In agreement with UV-visible and emission data there is a slight destabilization of both HOMO and LUMO, to a greater extent for the latter, for **AS16-18**

relative to those of their dcb analogues. Thus the HOMO-LUMO gaps for the dctzbpy complexes are an average of 0.12 eV larger than 4.1-3. The reason for the shift in energy for the different metal pairs is due to the different charge on the final complexes (0 for the rhenium, +1 for the iridium, +2 for the ruthenium).

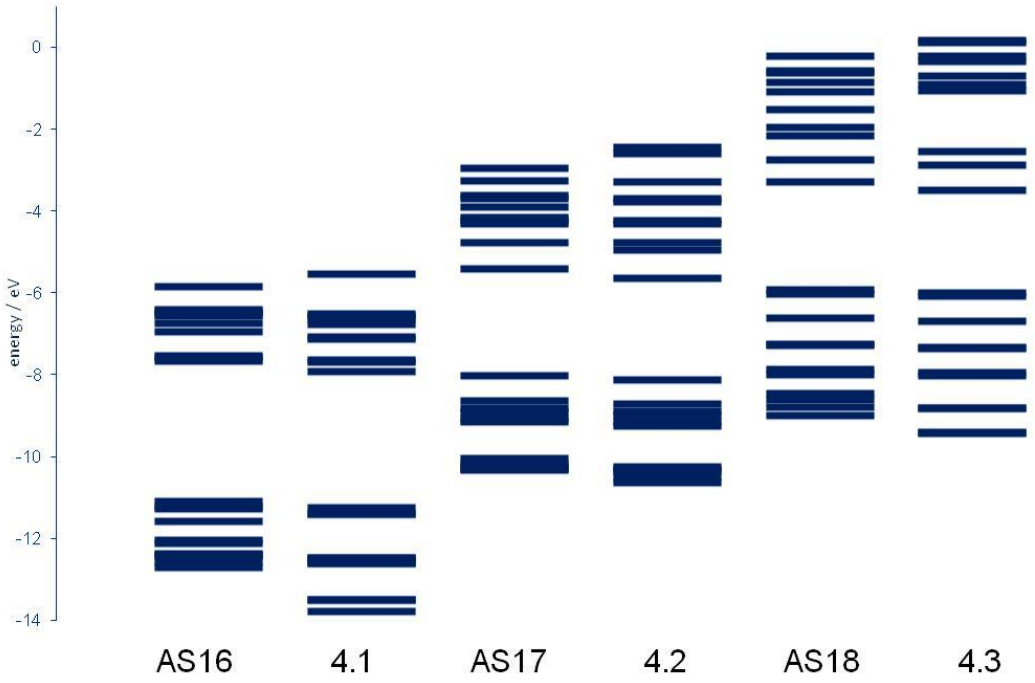

*Figure 4.9 Molecular orbital energy level diagram for complexes **AS16-18** and **4.1-3***

*Table 4.3 HOMO and LUMO energy values for complexes **AS16-18** and **4.1-3***

Dye	HOMO [eV]	LUMO [eV]	Δ [eV]
4.1	-11.26	-7.92	3.33
AS16	-11.10	-7.68	3.42
4.2	-8.13	-5.65	2.48
AS17	-8.04	-5.41	2.63
4.3	-6.00	-3.51	2.49
AS18	-5.94	-3.30	2.63

Time-dependent DFT (TD-DFT) calculations were carried out on the optimised ground state geometries of each complex in order to determine vertical excitation energies.

From TDDFT analysis, the predicted transitions correlate well with the experimental spectra.

Simulated absorption spectra overlaid with experimental spectra are shown in Figure 4.10. The excitations to the S_1 state of all complexes are primarily HOMO→LUMO in character, however, they are of low oscillator strength and will therefore contribute little to the observed absorption spectra. As expected looking at the HOMO-LUMO gaps reported in Table 4.3, the dcb complexes present a smaller gap than for dctzbpy complexes, hence their S_1 transitions occur at higher wavelengths. S_1 transitions for the two iridium complexes are the most red shifted, above 560 nm, however their oscillator strength is one order of magnitude lower than that for the two ruthenium and rhenium complexes; the latter show S1 transition higher in energy, below 514 nm, confirmed by their blue shifted absorption profiles. The major transitions observed for all complexes between 350 and 550 nm are primarily of ^{1}MLCT character. For the two ruthenium complexes **AS16** and **4.1**, the d-orbitals are always involved leading to pure ^{1}MLCT transitions (Table 4.4), in particular **AS16** presents two dominating transitions at 452 and 412 respectively, involving from HOMO-2 to LUMO+2, MLCT in character. The iridium complexes **AS17** and **4.2**, as for similar complexes showed in Chapters 2 and 3, present transitions with a mix of ^{1}MLCT/LLCT character, with few significant transitions in the visible. **AS17** shows one transition at 421 nm (mainly HOMO-1→LUMO) and two at 393 and 394 nm (MLCT/LLCT and MLCT/ILCT in character respectively). Complexes **AS18** and **4.3** show mixed MLCT/LLCT above 300 nm and LC transition below. Specifically **AS18** exhibits a strong transition at 443 nm with a composition of HOMO-1→LUMO, ^{1}MLCT in character.

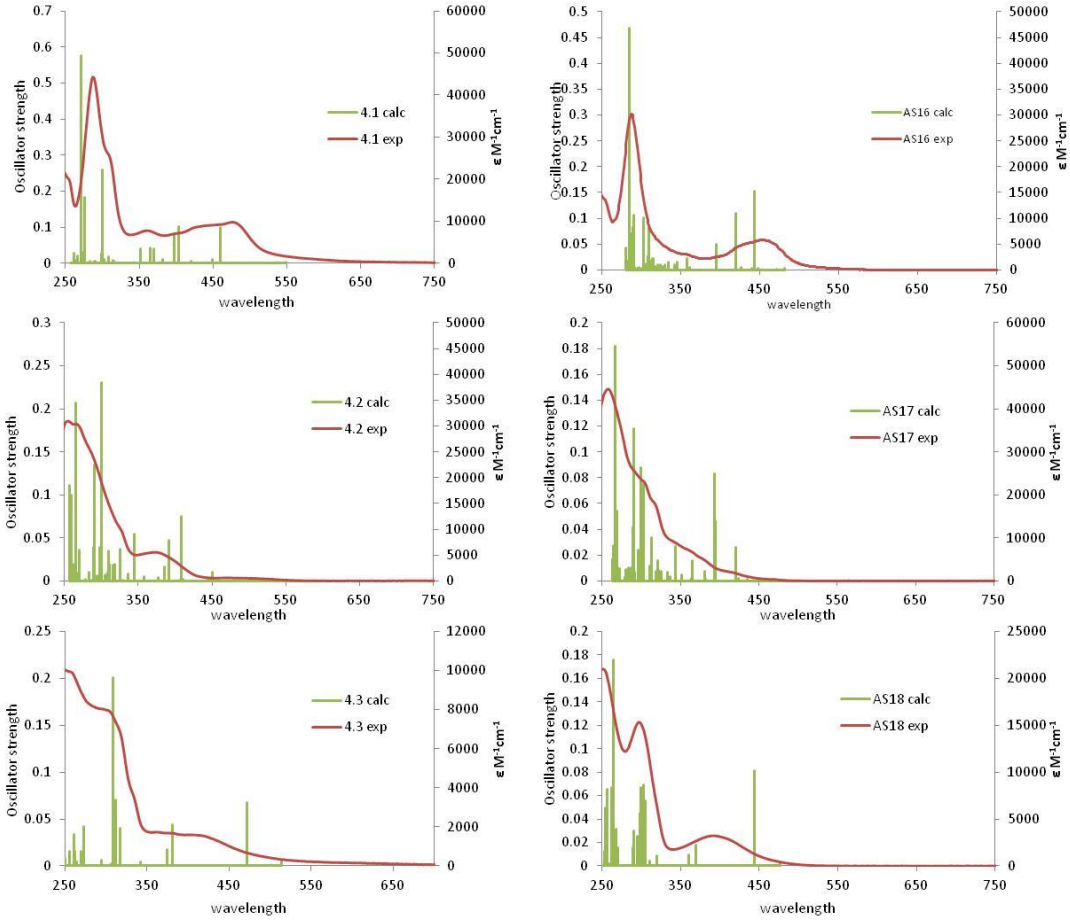

*Figure 4.10 TDDFT calculated absorption spectra for complexes **AS16-18** and **4.1-3** with experimental spectra overlaid*

Table 4.4 Selected energies (eV), Oscillator Strength (f), wavelength (nm) and compositions of vertical excitations from TDDFT calculations.

Complex	Transition	Energy	λ	*f*	Composition	Character
AS16	S_1	2.364	524	0.00362	HOMO→LUMO 90%	MLCT
	S_5	2.743	452	0.15	HOMO-1→LUMO 54%	MLCT
					HOMO-1→LUMO+1 27%	MLCT
	S_8	3.004	412	0.11	HOMO-2→LUMO+1 49%	MLCT
					HOMO-1→LUMO+2 36%	MLCT
					HOMO-1→LUMO+1 7%	MLCT
	S_9	3.105	399	0.05	HOMO→LUMO+3 54%	MLCT
					HOMO-2→LUMO+2 21%	MLCT
					HOMO-1→LUMO+2 8%	MLCT
	S_{11}	3.296	376	0.02	HOMO-1→LUMO+3 68%	MLCT
					HOMO-2→LUMO+3 21%	MLCT
AS17	S_1	2.199	563	0.00061	HOMO→LUMO 96%	MLCT/LLCT
	S_4	2.947	421	0.03	HOMO-1→LUMO 68%	MLCT/LLCT
					HOMO-2→LUMO 21%	MLCT/LLCT
	S_5	3.144	394	0.05	HOMO→LUMO+2 92%	MLCT/ILCT

	S_6	3.152	393	0.08	HOMO-3→LUMO 81%	MLCT/LLCT
	S_9	3.399	365	0.02	HOMO-5→LUMO 88%	MLCT/LLCT
	S_{12}	3.611	343	0.03	HOMO-4→LUMO+1 12%	MLCT/LLCT
					HOMO-2→LUMO+1 77%	MLCT/LLCT
AS18	S_1	2.599	476	0.0037	HOMO→LUMO 96%	MLCT/LLCT
	S_2	2.796	443	0.08	HOMO-1→LUMO 96%	MLCT/LLCT
	S_4	3.360	369	0.02	HOMO→LUMO+1 94%	LLCT/MLCT
	S_9	4.062	305	0.05	HOMO-3→LUMO 38%	ILCT
					HOMO-5→LUMO 28%	LLCT/MLCT
					HOMO-4→LUMO 20%	LLCT/MLCT
4.1	S_1	2.257	549	0.00345	HOMO→LUMO 96%	MLCT
	S_3	2.697	460	0.10	HOMO-2→LUMO 81%	MLCT
	S_5	2.769	448	0.01	HOMO→LUMO+2 90%	MLCT
	S_8	3.077	403	0.10	HOMO-2→LUMO +2 47%	MLCT
					HOMO-1→LUMO+1 49%	MLCT
	S_9	3.119	397	0.08	HOMO→LUMO+3 56%	MLCT
					HOMO-1→LUMO+2 30%	MLCT
	S_{10}	3.250	382	0.10	HOMO-1→LUMO+4 54%	MLCT
					HOMO-2→LUMO+2 6%	MLCT
					HOMO-1→LUMO+2 23%	MLCT
					HOMO→LUMO+3 10%	MLCT
	S_{12}	3.349		0.04	HOMO-2→LUMO+3 72%	MLCT
					HOMO→LUMO+4 21%	MLCT
	S_{13}	3.398	365	0.04	HOMO-1→LUMO+3 36%	MLCT
					HOMO→LUMO+3 21%	MLCT
					HOMO-1→LUMO+2 12%	MLCT
	S_{15}	3.527	352	0.04	HOMO-2→LUMO+4 87%	MLCT
4.2	S_1	2.024	612	0.00036	HOMO→LUMO 99%	MLCT/LLCT
	S_6	3.033	409	0.08	HOMO-3→LUMO 84%	MLCT/LLCT
	S_8	3.166	392	0.05	HOMO→LUMO+3 86%	MLCT/ILCT
	S_{12}	3.602	344	0.06	HOMO-4→LUMO+1 12%	MLCT/LLCT
					HOMO-2→LUMO+1 81%	MLCT/LLCT
4.3	S_1	2.411	514	0.00525	HOMO→LUMO 99%	MLCT/LLCT
	S_2	2.631	471	0.07	HOMO-1→LUMO 96%	MLCT/LLCT
	S_4	3.253	381	0.04	HOMO→LUMO+1 96%	MLCT/LLCT
	S_5	3.311	374	0.02	HOMO-1→LUMO+1 96%	MLCT/LLCT
	S_9	3.905	318	0.04	HOMO-5→LUMO 49%	LLCT/MLCT
					HOMO-3→LUMO 47%	ILCT
	S_{10}	3.977	312	0.07	HOMO-4→LUMO 94%	LLCT

4.7 Anchoring test

To verify the electrode binding of the new ligand absorption tests on TiO_2 were carried out. Titanium oxide electrodes were left in **AS16** and **AS17** in acetonitrile dye bath solutions overnight.

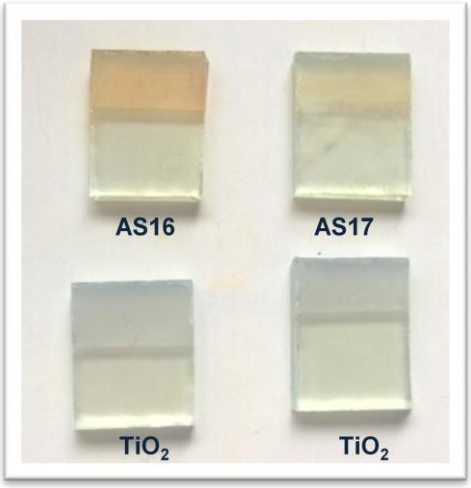

Figure 4.11 Comparison between TiO_2 and TiO_2-dye electrodes.

The resulting electrodes looked clearly coloured showing adsorption of the dye. The absorption spectrum of the sensitised electrode has been compared with the pure titanium oxide blank (Figure 4.11).

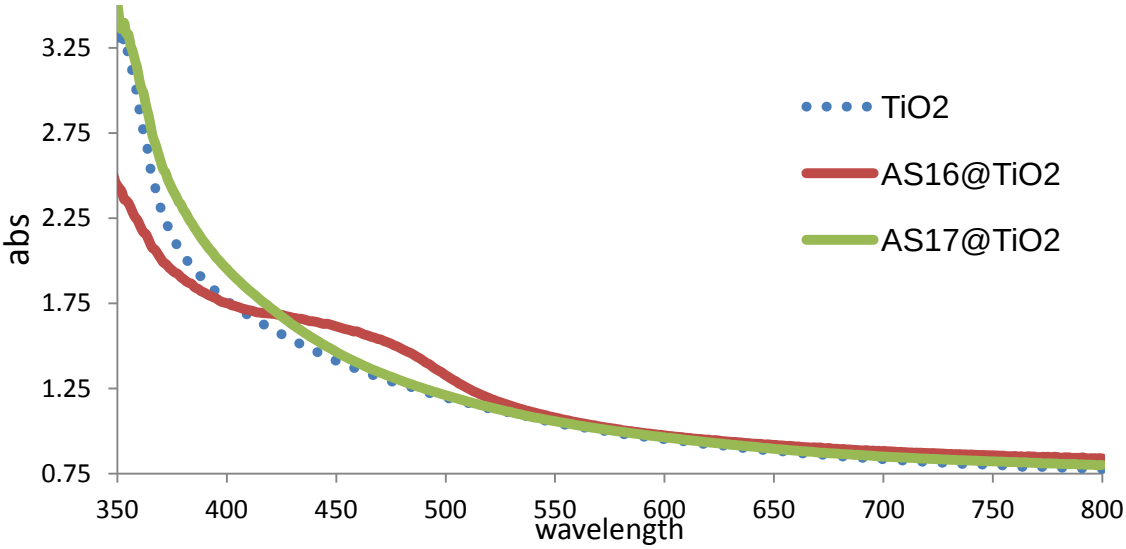

*Figure 4.12 Absorption spectra of TiO_2 electrode compared with TiO_2-**AS16** and TiO_2-**AS17** electrodes.*

The increased light absorptions between below 400nm and between 450-500 nm, for adsorbed dyes on TiO_2, match the absorption profile of **AS16** and **AS17** complexes in solution (Table 4.1 and Figure 4.5).

4.8 Photoelectrochemical measurements

Solar cells fabricated using the new dyes were tested under AM 1.5G illumination at Newcastle University through collaboration with the group of Dr Elizabeth Gibson.

The dye coated film was realised using a commercial titanium oxide paste. Platinic FTO glass was used as the counter electrode and a solution of 0.5 M TBP, 0.015 M I_2, 0.6 M TBAI and 0.1 M GuSCN in acetonitrile as electrolyte. The cell was thermally sealed before taking measurements.

Photovoltaic measurements were performed on AM 1.5 solar simulator (100mW cm^{-2}). The incident light was calibrated by using a Si photodiode reference. JV curves were obtained by applying an external bias to the cells and measuring the generated photocurrent with a Keithley digital meter.

Main photovoltaic parameters are listed in Table 4.5. The overall conversion efficiencies η were derived from the equation: $\eta = J_{sc} \times V_{oc} \times FF$, where J_{sc} is the short circuit current density, V_{oc} the open circuit voltage, and FF the fill factor. Figure 4.14 shows the photocurrent-voltage curves of DSSCs based on the new dyes.

*Table 4.5 Photovoltaic parameters of tested dyes **AS16-18** and **4.1-3** with **N719** as benchmark.*

Dye	V_{oc} (V)	J_{sc} ($mAcm^{-2}$)	FF (%)	η (%)
4.1	0.48	0.81	57	0.222
4.2	0.59	0.55	71	0.233
4.3	0.53	0.08	69	0.029
AS16	0.61	0.35	72	0.154
AS17	0.51	0.12	78	0.048
AS18	0.5	0.09	75	0.034
N719	0.65	6.53	55	2.369

As was not unexpected, the obtained photovoltaic efficiencies for complexes **AS16-18** are lower than their dcb analogues (see Table 4.5). The reasons of this gap are probably attributable to their lower extinction coefficients and more blue-shifted absorption maxima. As shown in Figure 4.9, the LUMO energy for **AS16-18** are destabilised in comparison with those for complexes **4.1-3** and might imply weaker electron injection efficiency to titanium oxide conducting band. All the IPCE values that result are below 10% in the visible region. This is due to a combination of poor absorption in the visible range (as for the iridium and rhenium dyes) and low solubility so a poor dye loading (as for **4.1**, **4.3** and **AS17**). The IPCE profiles reflect the absorption profiles of the corresponding dyes. Both **AS16** and **4.1** have an absorption band between 450-470 nm, the same bands are present in their respectively IPCE curves. All the other complexes have absorption maxima between 370 and 420 nm so their IPCE curves show only the tail of these bands. The IPCE analysis highlights how important it is for a dye to possess a strong absorption in the visible in order to get a high device efficiency. Indeed dyes **AS16**, **4.1** and **4.2** have the highest IPCE values together with the highest efficiencies, η (see Table 4.5. and Figure 4.13).

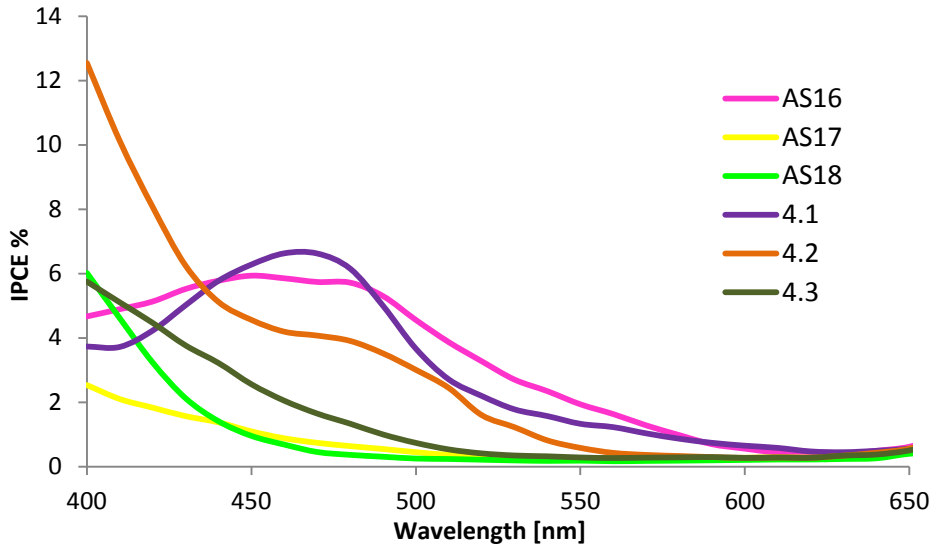

*Figure 4.13 IPCE curves for n-type cells sensitised using complexes **AS16-18** and **4.1-3***

JV and IPCE curves are fundamental tools in order to test the photocurrent efficiency of a dye, however those measurements are not enough to fully understand the deep electronic kinetics between metal oxide-dye-electrolyte. The best result for the three new complexes is achieved for complex **AS16** with an efficiency of 0.15 % (**N719** in the same conditions achieved the 2.37%). Also, **AS16** achieved the highest open circuit

voltage (0.61 V), this might suggest a longer electron lifetime[177], hence a higher electron density on the TiO_2 surface. The efficiency for **AS17** resulted dramatically and unpredictably lower related to the dcb analogue. The rhenium complexes **AS18** and **4.3** showed very similar J_{sc}, V_{oc} and η values.

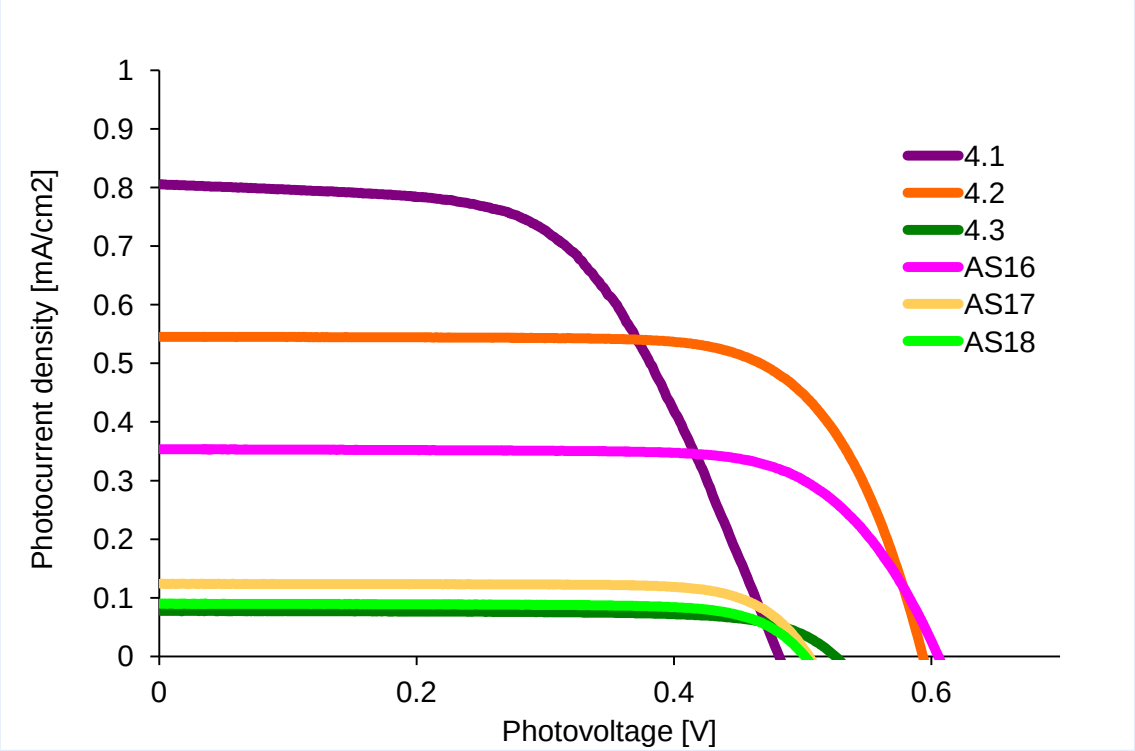

*Figure 4.14 Current-Voltage curves DSSC constructed using complexes **AS16-18** and **4.1-3***

4.9 Conclusions

We have designed and synthesized a new anchoring ligand, 1-[2,2′-bipyridine-4-yl]-1,2,3-triazole-4,5-dicarboxylic acid, and its ruthenium, iridium and rhenium complexes.

All complexes and ligands have been fully characterised by ^{1}H and ^{13}C NMR spectroscopy, mass spectrometry and the photophysics investigated by UV-vis absorption and emission spectroscopy. This class of sensitizers containing triazole in the anchoring site has not been previously reported.

New Ru, Ir and Re-based dyes, **AS16-18** respectively, have been compared with their dcb analogues using computational calculations and photophysical investigation. The novel complexes showed similar photophysical and electronic properties than their dcb analogues. Their photophysic together with their orbitals analysis suggested a suitable

application as dyes for solar cells. However, the application of **AS16-18** DSSCs did result in modest efficiencies, generally lower than for the dcb complexes. The reasons might be attributable to destabilization of the LUMO, then a worse coupling with TiO_2 conduction band, together with lower and more blue shifted absorption profiles.

Despite the low efficiencies of the final complexes, the ligand we designed and described in this chapter, successfully achieved its anchoring function. Further investigation by transient spectroscopy will definitely shed light on the electron injection and electron recombination rates, between the dye and the metal oxide.

In future, this novel anchoring ligand could be used to realise new dyes for p-type solar cells, using the design donor-metal-acceptor, reported in Chapter 3, together with electron withdrawing acceptor ligands.

5 The use of coumarins as ligands for iridium complexes

5.1 Introduction

Transition metal complexes are suitable as photosensitisers for several reasons: they show broad absorption bands due to metal-to-ligand charge transfer; the excited-states of the complexes have long lifetimes and oxidized states chemically stable.

Organic dyes such as 9-phenylxanthene dyes (e.g. rose bengal, fluorescein, and rhodamine B) were also used as photosensitisers for DSSCs in early studies.[201] Recently, construction of nanocrystalline DSSCs based on organic-dye photosensitisers has been reported. [41, 53] Organic dyes have several advantages as photosensitisers for DSSCs: (1) they have larger absorption coefficients (attributed to an intramolecular π-π* transition) than metal-complex photosensitisers (which are due to MLCT absorption), and these large coefficients lead to efficient light-harvesting properties; (2) the variety in their structures provides possibilities for molecular design, e.g., the introduction of substituents, and thus allows for easy control of their absorption spectra; (3) there are no concerns about element abundance, because organic dyes do not contain noble metals such as ruthenium. However, organic dyes have several disadvantages as photosensitisers. First, the emission lifetimes of their excited states are generally shorter than those of metal complexes (e.g. 0.4-5 ns) thus reducing the efficiency of charge injection. [202] Second, organic dyes have relatively sharp absorption bands in the visible region, which is disadvantage for the light harvesting of solar light, rather than panchromatic absorption which can be achieved in metal complexes. A very promising class of organic dyes for photovoltaic applications is constituted by 2H-chromen-2-one derivates, better known as coumarins.

Coumarin is a fragrant organic chemical compound in the benzopyrone chemical class and is a colourless crystalline substance in its standard state. It is a natural substance found in many plants. Substituted coumarins are widely used in pigment industries because they have low molecular weight, are water soluble and are UV-excitable dyes.

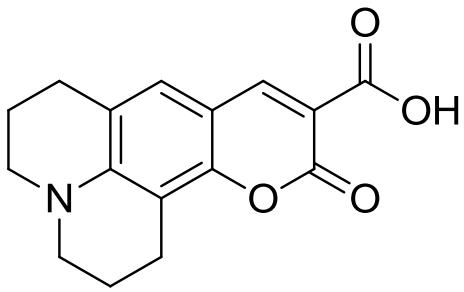

Figure 5.1 Structure of commercially available Coumarin ***343***

Coumarin dyes have been applied in DSSCs [179, 203], e.g., coumarin **343** (Figure 5.1), and are good organic-dye photosensitisers for injecting electrons efficiently into the conduction band of semiconductors. The efficiency for nanocrystalline DSSCs based on the **C343** dye (0.9%)[203], however, are lower than the efficiencies of DSSCs based on Ru-complex photosensitisers, owing to the former's lack of absorption in the visible region. Therefore, the absorption spectra of organic dyes must be broadened and red-shifted for highly efficient solar-cell performance in terms of harvesting sunlight.

5.1.1 Coumarin dyes and their use in cyclometalating and ancillary ligands.

The development of Ir(III) complexes for applications in visible-light harvesting or as molecular probes is still in its early age for a number of reasons: (1) The excitation wavelengths of typical cyclometalated Ir(III) complexes are in the UV or blue region, and their absorption is weak in the visible region ($\varepsilon \approx 5000\ M^{-1}cm^{-1}$).[204-206] This poor light-harvesting ability is a great disadvantage for many of their potential applications in photovoltaics, photocatalysis, or molecular probes.[204, 205] (2) The supramolecular photochemistry of Ir(III) complexes to optimize their photophysical properties is underdeveloped; for example, the triplet excited states of Ir(III) complexes have never been rationally tuned to access the long-lived excited states (the typical lifetime of cyclometalated Ir(III) complexes is usually less than 5.0 μs).[206] Long-lived triplet excited states are significant for applications in photovoltaics, photocatalysis, molecular sensing, and so on. To maximize the utilization of solar energy through efficient light absorption, the photophysical properties of coumarins can be used and combined together to synthesise iridium-coumarin dyes for photovoltaic applications.

In order to tackle the aforementioned challenges, Zhao *et al.* reported a set of iridium, ruthenium and rhenium complexes with imidazolphenanthrolin-7-diethylamino-2-oxo-2H-chromene as ancillary ligand, with application in triplet-triplet-annihilation based upconversion, because of its long-lived coumarin centred ^{3}IL excited state.[112, 156, 207]

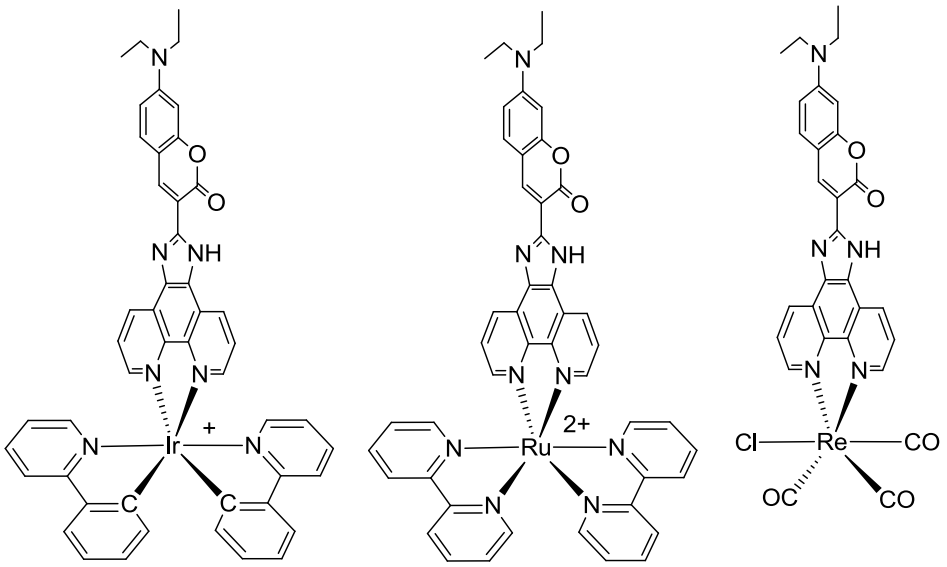

Figure 5.2 Metal-coumarin dyads reported by Zhao et al.[112, 207, 208]

They obtained weakly phosphorescent or even no phosphorescent transition metal complexes that can be used as triplet sensitizers for TTA upconversion.

In 2012 Takizawa *et al*.,[152] reported a set of 4 iridium complexes with coumarin C6 as cyclometalating ligand, having a strong absorbance in the visible range and applying them for visible-light-driven hydrogen generation displaying turnover numbers up to 700, using $[Co(bpy)_3]Cl_2$ as catalyst. [209] The reported complexes, shown in Figure 5.3, recorded impressive ε values higher than 80000 M^{-1} cm^{-1} at 480 nm.

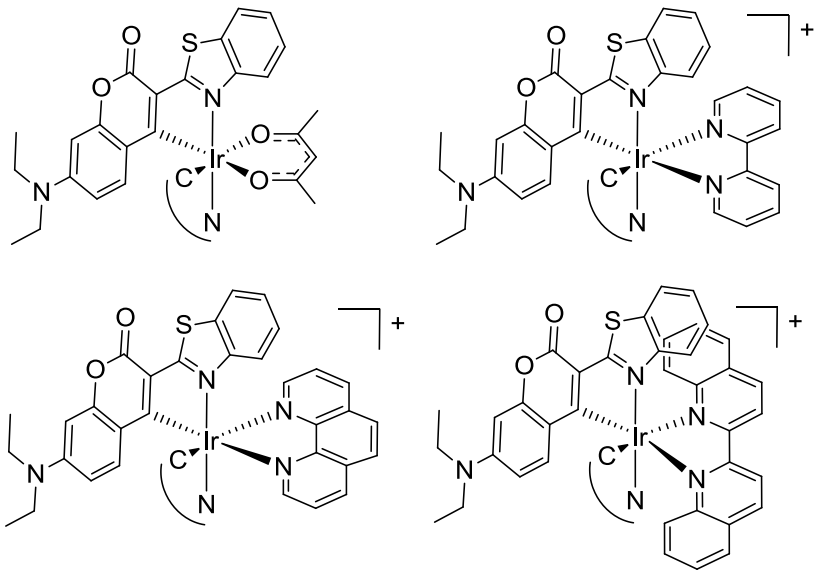

*Figure 5.3 Chemical structures of Ir coumarin **C6** complexes reported by Takizawa et al.*[152]

Based on the reported works, we devised visible-light-harvesting cyclometalated Ir(III)–coumarin molecular arrays, which show intense absorption of visible light, one belonging to p-type dyes family (**AS20**) and another belonging to n-type one (**AS19**).

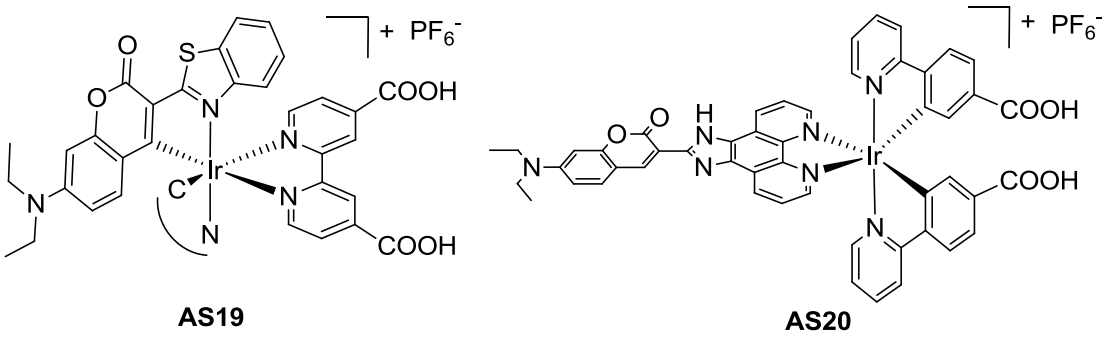

*Figure 5.4 Structure of **AS19** (left) and **AS20** (right)*

In **AS19**, the coumarin augments the light absorbing properties of the iridium cyclometalate framework allowing strong light absorption with longer lifetime through access to triplet excited states.

P-type cells are commonly known for showing a rapid (ps timescale) recombination rate of the semiconductor hole with the reduced dye.[179] To overcome this fundamental obstacle in the p-type system we designed **AS20**, in order to have a coumarin centred ^{3}IL state with no charge separation (Scheme 5.1 2)), rather than having a typical charge separated excited state common in the design of most DSSC sensitisers (Scheme 5.1 1)), trying to achieve higher efficiencies by avoiding recombination.

1) $\text{NiO-S} \xrightarrow{h\nu} \text{NiO-S*} \rightarrow \text{NiO}^+\text{-S}^- \xrightarrow{M+/M^\circ} \text{NiO}^+\text{-S}$

2) $\text{NiO-S-C} \xrightarrow{h\nu} \text{NiO-S*-C} \rightarrow \text{NiO-S-C*} \xrightarrow{M+/M^\circ} \text{NiO-S-C}^+ \rightarrow \text{NiO}^+\text{-S-C}$

Scheme 5.1 1) standard NiO-Sensitiser (NiO-S) charge separation 2) unconventional NiO-Sensitiser-Coumarin (NiO-S-C) excitation; M+/M° represents the redox mediator.

5.2 Synthesis of coumarin-incorporated iridium complexes

Based on the work of Takizawa *et al,*[152] we used coumarin C6 as cyclometalating ligand together with dcb as ancillary ligand to design a n-type iridium-based dye able to strongly absorb in the visible range. The synthetic steps are the standard reported in Chapter 2. The main difference was in the solvent used to split the dimer with the deeb ligand, where the usual DCM:MeOH mixture was replaced by ethoxyethanol. Probably

due to the steric hindrance of the coumarin-iridium dimer, a high boiling point solvent was needed to drive the reaction to the product. The esterified complexes were then hydrolysed to obtain the final product **AS19**.

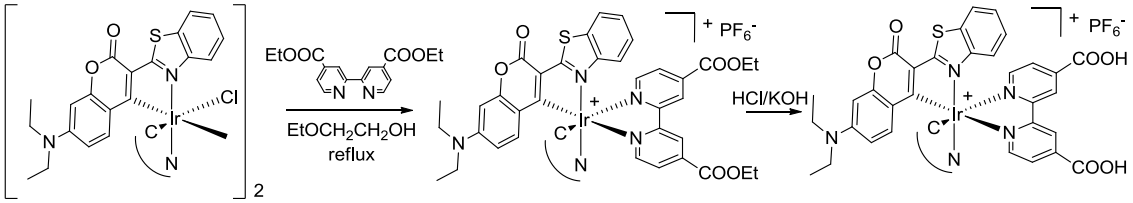

*Scheme 5.2 Synthetic route to target complex **AS19.***

For **AS19** crystals were obtained and analysed by X-Ray diffraction (Figure 5.5). Unfortunately the diffraction data were of insufficient quality for publication, however they confirmed the proposed structure with the expected *trans* arrangement of benzothiazole.

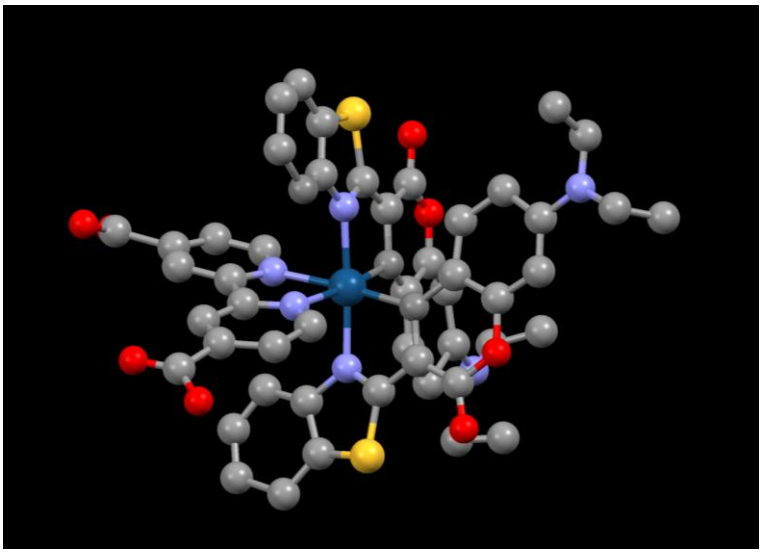

*Figure 5.5 X-ray structure for **AS19***

The ^{1}H NMR spectrum for **AS19** is similar to those discussed in Chapter 2, in fact the metalated coumarin rings showed a single set of resonances as consequence of the C_2 symmetry of the Ir(C^N)$_2$ fragment, the number of signals is reduced by one (in comparison with the free ligand) due to the metalation.

Following the design proposed in Chapter 3, an imidazole appended coumarin unit was incorporated into a Ir(III) complex **AS20** (Figure 5.4) to enhance its UV/vis absorption profile and create a ligand centred excited state. The phenathroimidazocoumarin has been synthesised as reported in literature[208], in other words the chromene unit has been condensed together with the phenanthroline dione. The final coumarin ligand has

been used as ancillary ligand together with pyba as cyclomatalating/anchoring ligand as described previously in Chapter 3. NMR characterization for **AS20** was problematic because of its low solubility; a mixture of $CD_3OD/CDCl_3$ was needed to obtain a ^1H NMR spectrum. This shows a single set of resonances for the $Ir(C^N)_2$ fragment, suggesting a free rotation around the single bond between the imidazol and the chromene fragments, hence an averaged C_2 symmetry of the whole complex.

5.3 Photophysical characterization

UV-visible absorption spectra were recorded for all complexes in acetonitrile solutions at room temperature and are presented in Figure 5.6. The intensity of the profile of **AS20** has to been considered underestimated due to the low solubility of the complex.

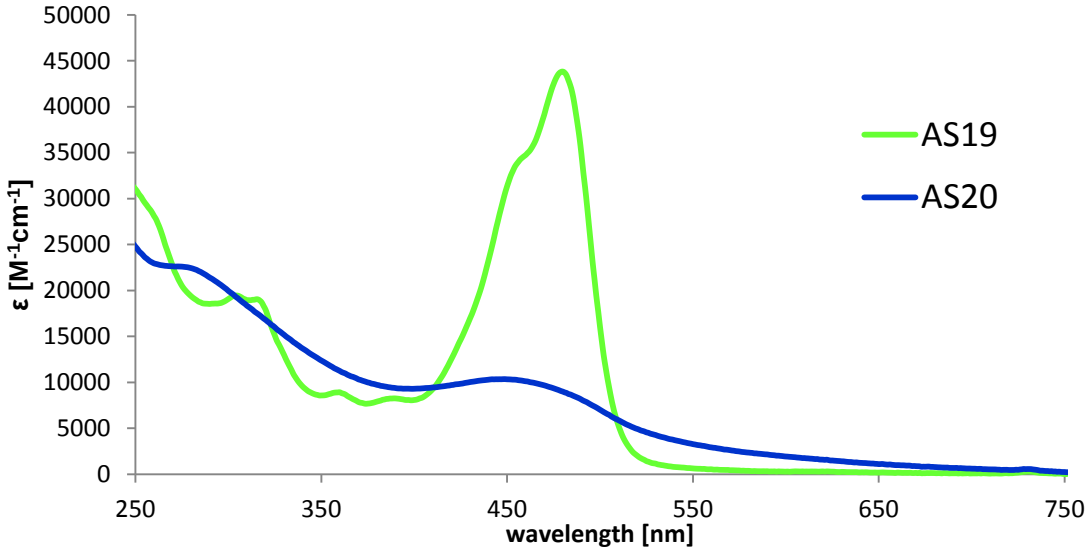

*Figure 5.6 UV-vis absorption spectra for cyclometalated iridium complexes **AS19-20***

The photophysical data for the complexes are listed in Table 5.1. The UV/vis absorption spectra of **AS19-20** show bands between 250-320 nm together with strong absorption in the visible region (400-600 nm), attributed mainly to the absorption of the coumarin unit. Importantly, the molar absorptivity for these complexes (beyond 450 nm) is much higher than that for all the novel complexes reported in this thesis (see Table 2.2, Table 3.1 and Table 4.1 for comparison). Specifically, the molar extinction coefficient of **AS19** reaches 43800 $M^{-1}cm^{-1}$ at 480 nm, which is an unprecedentedly high value relative to those of other reported Ir-based dyes for DSSC, demonstrating the visible-light-harvesting effect of the coumarin unit. The enhanced absorptivity of **AS19** is presumably due to the combined effects of spin-allowed intraligand π-π*

transition in the coumarin ligand, metal to ligand CT and/or ligand-to-ligand CT related to the diimine ligands.

Emission spectra for complex **AS20** have been recorded in both aerated and deaereted acetonitrile in order to better understand the nature of their emission bands. At room temperature complex **AS19** was non-emissive.

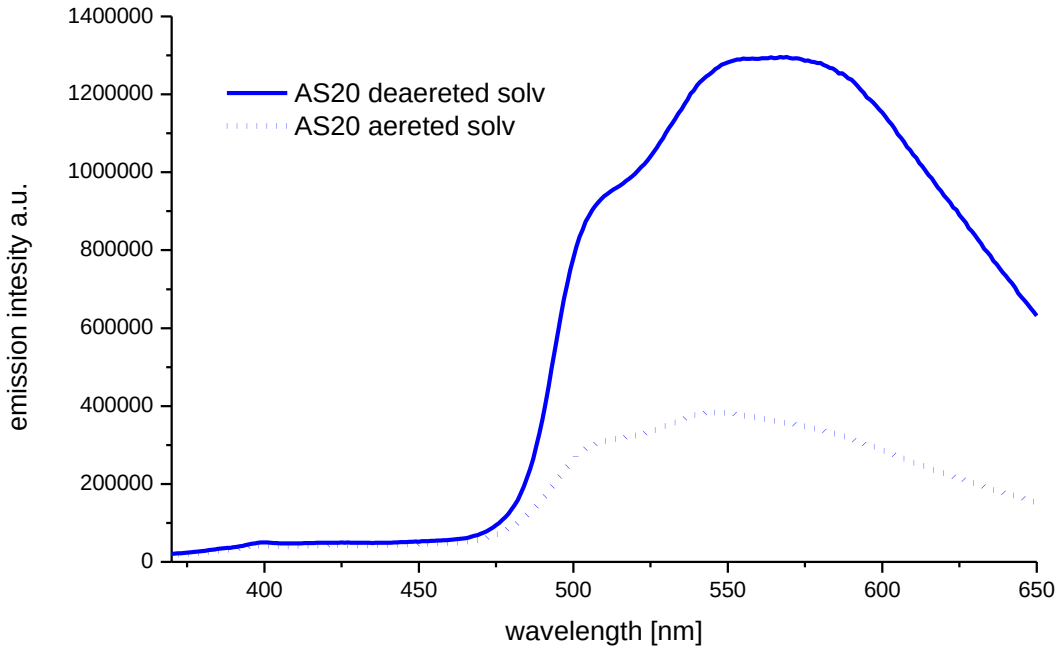

*Figure 5.7 Emission spectra for complex **AS20** in aerated and deaereted acetonitrile, excited at 350 nm.*

Complex **AS20** exhibited a phosphorescent emission bands at 511 and 563 nm, suggesting that emission is due to the ^{3}IL excited states localized on the coumarin ligand[208]. The presence of oxygen quenches the emission of **AS20** to one third of its value in deaereted solvent, thus demonstrating triplet based emission, probably from a mixed MLCT/ coumarin-ILCT excited state.

*Table 5.1 Summarised photophysical data for complexes **AS19-20** at room temperature in aereted acetonitrile.*

Complex	λ^{abs}/ nm	λ_{max}^{em}/ nm	τ/ ns
AS19	245 (31955), 314 (18998), 452 (32959), 480 (43826)	-	-
AS20	243 (26181), 280 (22386), 450 (10348)	511, 563	24 ±1 (62%); 3 ±0.1 (38%)

5.4 Electrochemistry.

Cyclic voltammetry were recorded in N_2 satured ACN with 0.1 M $TBAClO_4$ as supporting electrolyte, values are versus $Ag/AgNO_3$ (Fc/Fc^+ *vs* $Ag/AgNO_3$ = 0.58 V).

Table 5.2 *Summarised electrochemical data for complexes* ***AS19-20*** *at room temperature acetonitrile.*

$E_{1/2}$/V vs $Ag/AgNO_3$ (ΔE_p/mV)			
Dye	E_{ox}	E_{red}	ΔE_p
AS19	1.27	-0.69	60
AS20	1.30[a]	-0.51	-

[a] *– irreversible*

The first oxidation waves for **AS19-20**, corresponding to the one-electron Ir^{III}/Ir^{IV} couple, occur at +1.27 and +1.30 V respectively. The reversible oxidation potential for **AS19** is in line with that reported for $[Ir(C6)_2(bpy)]^+$ (0.68 V *vs* ferrocene) [152] as consequence of **C6** cyclometalation and lower by 250 mV than the first E_{ox} for $[Ir(ppy)_2(dcb)]^+$ (Table 4.2), whereas the first reduction peak matchs with the E_{red} values reported in Chapter 4 for dcb (centred LUMO) complexes **4.1-3**.

AS20, despite its low solubility, exhibits an irreversible oxidation peak and a reversible reduction peak at -0.51 V, tentatively assigned to the coumarin ligand and significantly anodically shifted compared to the reduction peak of **AS9-10** (bpy and phen analogues), attributed to the increased conjugation imparted by the ancillary ligand of **AS20**.

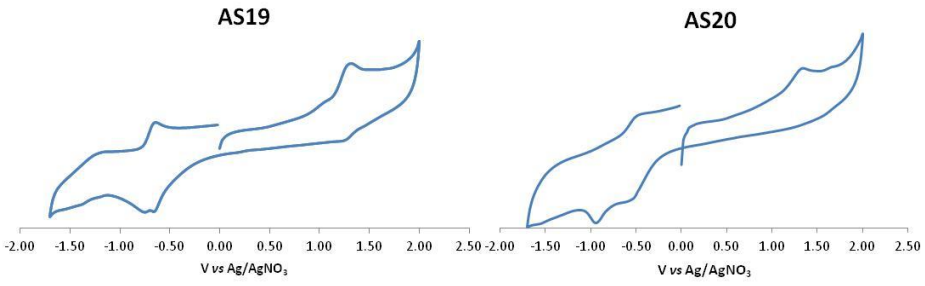

Figure 5.8. *Cyclic voltammograms for complexes* ***AS19-20*** *recorded in ACN.*

5.5 DFT and TDDFT Calculations.

To aid in our understanding of the photophysical properties of the complexes prepared we carried out gas-phase density functional theory (DFT) calculations. Geometries of both complexes were optimised by DFT methods at the B3LYP level of theory. Stuttgart-Dresden relativistic small core ECP was used for iridium and 6-311G* basis sets were used for all other atoms. TD-DFT calculations on optimised structures in CH_3CN by using the COSMO solvation model built into the NWChem software package were used to obtain the electronic spectra. Molecular orbital energies were determined for these ground state geometries and graphical plots of the frontier orbitals are shown in Figure 5.9. A plot of comparative energies of the molecular orbitals for each complex is shown in Figure 5.10.

The HOMO-LUMO distribution for complex **AS19**, is similar to that seen already for complexes in Chapter 2, where the HOMO lies on the cyclometalating ligands (here coumarin **C6**) and the LUMO is localised on the dcb ligand. However, contrary to complexes reported in Chapter 2, in **AS19** orbital localization, there is no metal involvment untill the HOMO-2 orbital. Complex **AS20**, as shown by **AS9-10**, has the LUMO on the bpy fragment whereas the HOMO is interestingly on the coumarin. This implies that both pyba ligands and the iridium centre are not involved in frontier molecular orbitals for **AS20**.

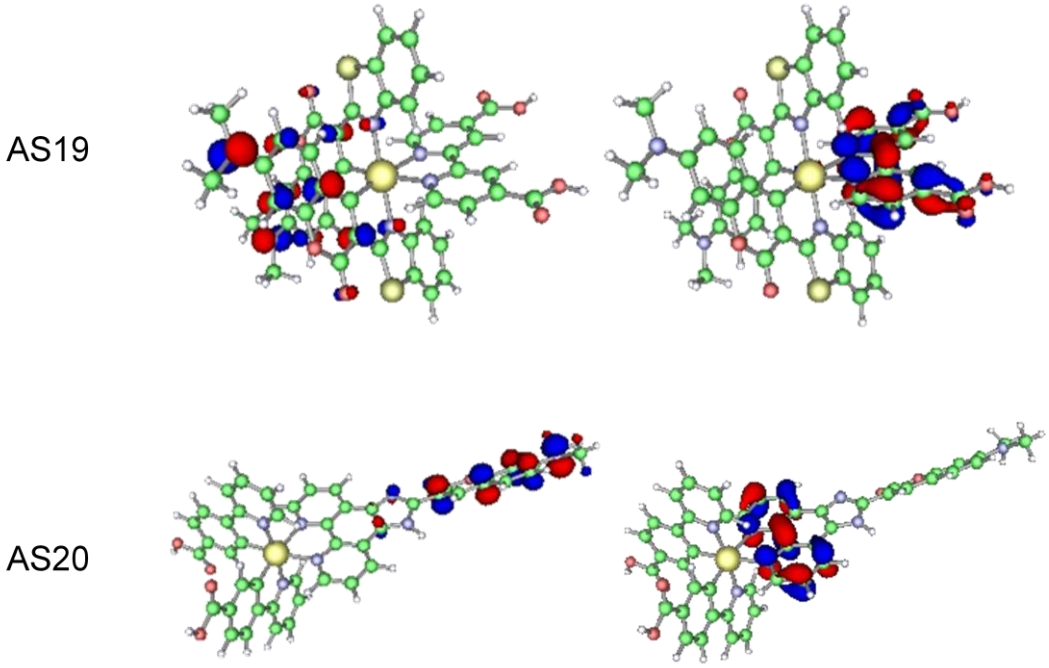

*Figure 5.9 HOMO (left) and LUMO (right) plots complexes **AS19-20***

Comparing the energies of the frontier orbitals for **AS19** and **AS20** with those respectively reported in Table 2.3 and Table 3.3, it emerges how the LUMO for **AS19** is more stable than the average values for **AS1-7** by ≈0.3 eV and the HOMO is inside the reported range. For **AS20**, even if the cyclometalating ligand is the same used in **AS9-15**, its HOMO is less stable than the average value for **AS9-15** by ≈0.3 eV, expected considering its different orbital localization; **AS20** LUMO value is very close to those for **AS9** (-2.63 eV) and **AS10** (-2.65 eV), as expected considering that the LUMO is delocalized on the same bpy fragment for all three complexes.

*Table 5.3 HOMO and LUMO energy values for complexes **AS19-20***

Dye	HOMO [eV]	LUMO [eV]	Δ [eV]
AS19	-5.74	-3.46	2.27
AS20	-5.61	-2.62	2.99

Interestingly, the Δ HOMO-LUMO gap for **AS19** (2.27 eV) is the smallest calculated between the complexes presented in this thesis, leading S_1 to take place at very low energy (672 nm according to Table 5.4), and generally to a more red shifted absorption profile.

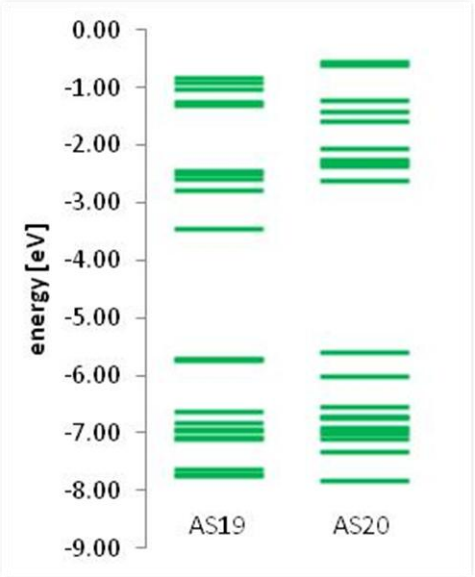

*Figure 5.10 Molecular orbital energy level diagram for complexes **AS19-20***

Time-dependent DFT (TD-DFT) calculations were carried out on the optimised ground state geometries of each complex in order to determine vertical excitation energies. The TD-DFT calculations for complexes **AS19-20** resulted in overestimated energies for transitions as shown in Figure 5.11.

Simulated absorption spectra overlaid with experimental spectra are shown in Figure 5.11. The excitation to S_1 state of complex **AS19** is LLCT in character, taking place from HOMO-1 (coumarin **C6** centred) to LUMO (dcb centred) at 672 nm with a very low oscillator strength. The transition profile for **AS19** is dominated by two main transitions at 423 and 429 nm respectively, assigned to a combination of ILCT and LLCT.

For complex **AS20,** S_1 is ILCT in character and primarily HOMO→LUMO, presenting an unprecedented high oscillator strength of 0.08 at 473 nm (usually S_1 has O.S. one or more orders of magnitude smaller). Even **AS20** shows two main transitions at 385 and 418 nm respectively, however they are mainly ILCT in character.

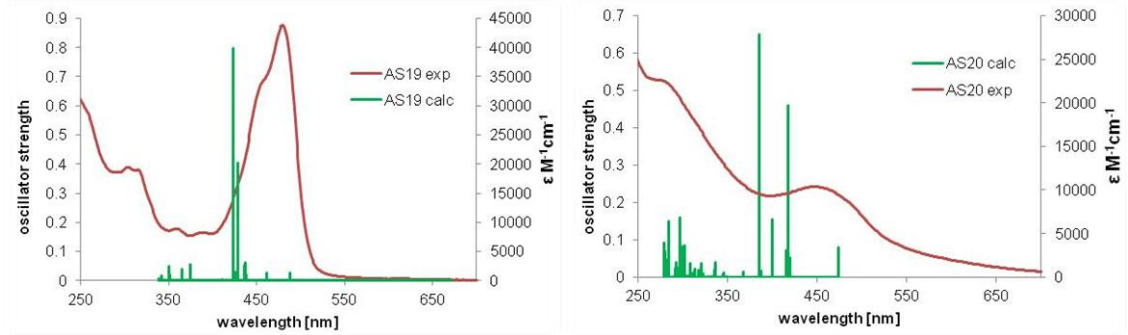

*Figure 5.11 TDDFT calculated absorption spectra for complexes **AS19-20** with experimental spectra overlaid*

Table 5.4 Selected energies (eV), Oscillator Strength (f), wavelength (nm) and compositions of vertical excitations from TDDFT calculations.

Complex	Transition	Energy	λ	*f*	Composition	Character
AS19	S_1	1.845	672	0.00052	HOMO-1→LUMO 92%	LLCT
	S_4	2.542	488	0.03	HOMO→LUMO+1 81%	LLCT
	S_6	2.689	461	0.03	HOMO-1→LUMO+2 53%	ILCT/LLCT
					HOMO→LUMO+3 33%	ILCT/LLCT
					HOMO→LUMO+2 6%	ILCT/LLCT
	S_7	2.689	461	0.03	HOMO→LUMO+2 54%	ILCT/LLCT
					HOMO-1→LUMO+3 31%	ILCT/LLCT

					HOMO-1→LUMO+2 6%	ILCT/LLCT
	S_9	2.835	437	0.06	HOMO→LUMO+4 42%	LLCT
					HOMO-1→LUMO+3 25%	ILCT/LLCT
					HOMO→LUMO+2 18%	ILCT/LLCT
					HOMO-3→LUMO+1 9%	MLCT/LLCT
	S_{10}	2.840	437	0.05	HOMO-1→LUMO+4 65%	LLCT
					HOMO→LUMO+3 17%	ILCT/LLCT
					HOMO-1→LUMO+2 14%	ILCT/LLCT
	S_{11}	2.889	429	0.40	HOMO→LUMO+4 46%	LLCT
					HOMO-1→LUMO+2 35%	ILCT/LLCT
					HOMO→LUMO+2 12%	ILCT/LLCT
	S_{12}	2.910	426	0.03	HOMO-4→LUMO 92%	MLCT/LLCT
	S_{13}	2.931	423	0.79	HOMO→LUMO+3 42%	ILCT/LLCT
					HOMO-1→LUMO+4 28%	LLCT
					HOMO-1→LUMO+2 18%	ILCT/LLCT
	S_{17}	3.307	375	0.06	HOMO-2→LUMO+1 92%	MLCT/LLCT
	S_{18}	3.390	366	0.04	HOMO-2→LUMO+2 86%	MLCT/LLCT
	S_{21}	3.542	350	0.05	HOMO-2→LUMO+3 74%	MLCT/LLCT
					HOMO-10→LUMO 11%	MLCT/LLCT
AS20	S_1	2.620	473	0.08	HOMO→LUMO 96%	ILCT
	S_3	2.957	419	0.05	HOMO-1→LUMO+1 94%	MLCT/ILCT
	S_4	2.967	418	0.46	HOMO→LUMO+2 70%	ILCT
					HOMO→LUMO+1 22%	LLCT
	S_5	2.985	415	0.07	HOMO→LUMO+1 75%	LLCT
					HOMO→LUMO+2 20%	ILCT
	S_7	3.105	399	0.15	HOMO→LUMO+2 96%	ILCT
	S_9	3.223	385	0.65	HOMO→LUMO+4 86%	LLCT
	S_{16}	3.684	337	0.04	HOMO-2→LUMO+2 29%	MLCT/ILCT
					HOMO-2→LUMO+3 22%	MLCT/LLCT
					HOMO-4→LUMO+1 10%	MLCT/ILCT
					HOMO-4→LUMO+3 6%	MLCT/ILCT
	S_{24}	3.875	320	0.03	HOMO-4→LUMO+2 46%	MLCT/LLCT
					HOMO-4→LUMO+3 21%	MLCT/ILCT
					HOMO-4→LUMO+4 22%	MLCT/LLCT

The DFT and TD-DFT analysis confirmed a lowest excited state without charge separation (HOMO→LUMO, both ligand centred) for **AS20**, matching with the intended design.

5.6 Photoelectrochemical measurements

Solar cells fabricated using the new dyes were tested under AM 1.5G illumination at Newcastle University through collaboration with the group of Dr Elizabeth Gibson.

Complex **AS19** has been tested under the same condition reported in Section 4.7. Both **AS19** and **AS20** have been tested on NiO using the condition reported in Section 3.7

*Table 5.5 Photovoltaic parameters of tested dyes **AS19-20**.*

Dye	V_{oc} (V)	J_{sc} (mAcm^{-2})	FF (%)	η (%)
AS19$_{@TiO_2}$	0.553	1.71	59	0.56
AS19$_{@NiO}$	0.104	0.45	42	0.020
AS20$_{@NiO}$	0.096	0.40	40	0.015
N719$_{@TiO_2}$	0.65	6.53	55	2.369

The sensitization of TiO_2 with **AS19** resulted in an efficiency value of 0.56% and IPCE value about 28%. Despite the starting purpose to test **AS19** in a n-type cell, the reported encouraging values moved us to test it on NiO in a p-type cell as well as **AS20**. On NiO, **AS19** and **AS20** achieved 0.02% and 0.015% respectively value in line with those reported for complexes **AS9-14** in Table 3.5.

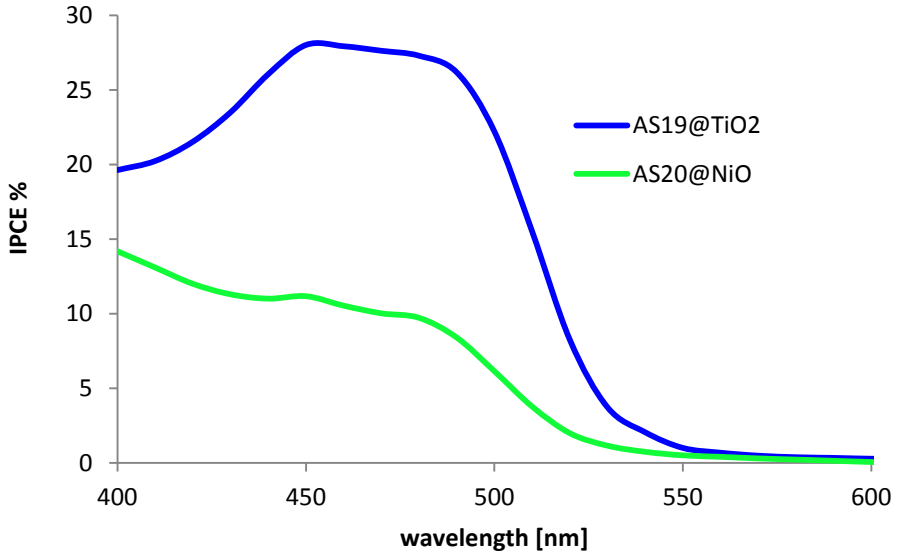

*Figure 5.12 IPCE curve for n-type cell sensitised using complex **AS19** and p-type cell sensitised using complex **AS20***

The IPCE profiles for both dyes reflect their absorption maxima in the visible between 450-500 nm, corresponding to the absorption of the coumarin units presents in the complexes.

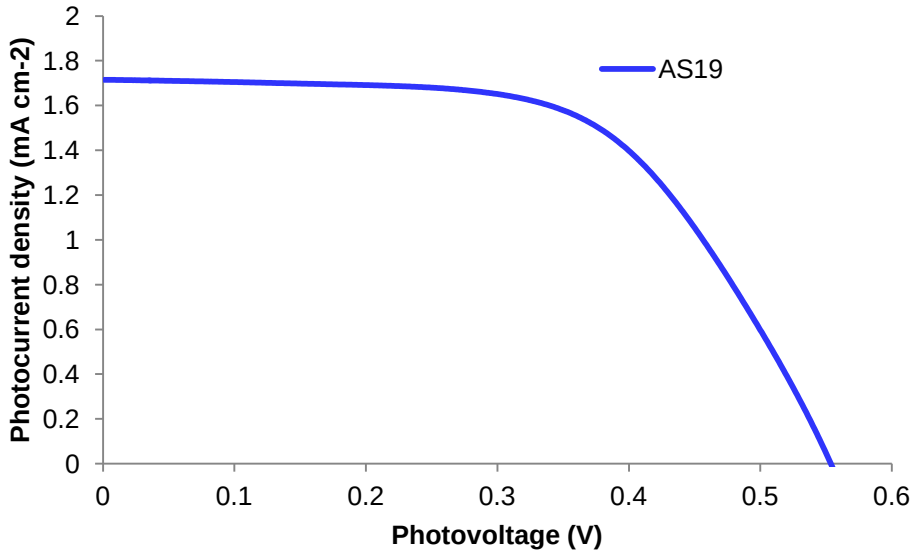

*Figure 5.13 Current-Voltage curve DSSC constructed using complex **AS19**.*

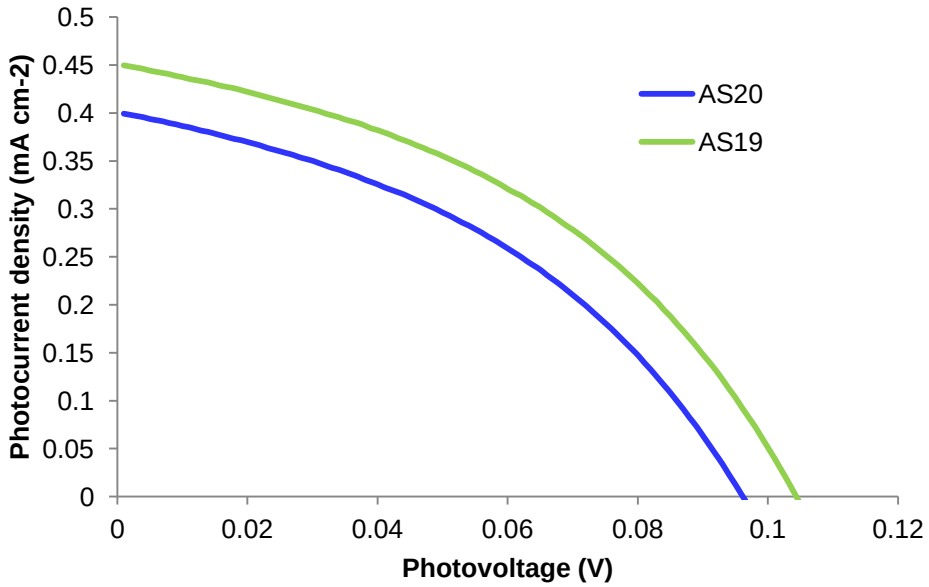

*Figure 5.14 Current-Voltage curves DSSC constructed using complexes **AS19-20***

5.7 Conclusion

The good results obtained with **AS19** on both NiO and TiO_2, demonstrate how a good dye design, together with a high absorption profile in the visible, are fundamental requirements for gaining good device efficiencies. To our knowledge, the value of 0.56% for **AS19** is one of the 5 highest efficiencies for iridium based dyes in the literature. [77, 98, 140] We tried to better understand the potential efficiency that this dye could achieve in optimised cells conditions referring to ruthenium benchmark efficiencies, from there it's interesting to note how the ratio between **N719** and **AS19** efficiencies here reported is 4.2, same ratio between **N719** and the iridium complexes reported by Dragonetti *et al.* is 23.3, also the ratio between complex **4.1** and **AS19** efficiencies is 0.4, whereas the same ratio for iridium complexes reported by Baranoff *et al.* is 1.5; a lower ruthenium/iridium complex efficiency ratio is indicative of the significant perfomances achieved by **AS19**. **AS20** didn't achieve the expected efficiency ascribable to its low solubility, hence low dye loading, low IPCE and JV curves. Designing 3-imidazole-chromene based ligands and cyclometalate them on iridium centre, could open the door to a new class of coumarin-iridium complexes able to strongly absorb above 500 nm, suitable for photovoltaic and photoelectrochemical devices, such as DSSC and LEC.[210]

6 General Conclusions &Outlook

6.1 General conclusion

Through our work with iridium dcb complexes we have shown that CuAAC/B.O. synthesis is a useful tool to design new aryltriazol ligands providing potential routes for facile tuning of photophysical and photovoltaic properties of the final complex. The new $[Ir(aryltriazole)_2(dcb)]^+$ complexes showed a good spatial charge transfer directionality and their application in real DSSC devices showed a reasonable photoelectrical response, considering their limited optical absorption profile, with efficiencies up to 0.5%. The inclusion of moieties with increased light absorption properties will lead to the synthesis of dyes with greater light harvesting properties and greater DSSC efficiencies.

We have demonstrated how nowadays computational chemistry is fundamental in order to design new complexes and to predict and explain their proprieties. The choice of pyridylbenzoic acid as cyclometalating ligand, together with diimine ancillary ligands, led to design a novel family of iridium dyes for p-type cells. These $[Ir(pyba)_2(N\text{^}N)]^+$ complexes showed spatial charge transfer directionality together with energy levels in accordance with their intended application in p-DSSC's. Some of the tested complexes achieved reasonable efficiencies representing an encouraging starting point for the development of a new generation of iridium p-type dyes.

In a marriage of "click" chemistry and the design of a new anchoring ligand to apply in transition metal complexes, we have designed and synthesized the novel 1-[2,2′-bipyridine-4-yl]-1,2,3-triazole-4,5-dicarboxylic acid, and its ruthenium, iridium and rhenium complexes. The purpose of this new ligand was to avoid the recombination of the injected electron without altering the charge transfer directionality inside the final complex. New Ru(II), Ir(III) and Re(I)-based dyes have been compared with their dcb analogues using computational calculations and photophysical investigations, showing similar photophysical and electronic properties to their dcb analogues. However, their application in DSSCs did result in modest efficiencies.

We have integrated coumarin units in iridium complexes in order to realise strongly absorbing dyes. We successfully achieved this aim, using coumarin C6 as cyclometalating ligand and imidazolphenanthrolinchromene as ancillary ligand, synthesising the corresponding iridium-coumarin complexes and applying them in both n-type and p-type cells. The results achieved showed a way forward to make iridium complexes competitive with ruthenium complexes in photovoltaic field.

6.2 Future work

Cyclometalated iridium complexes, in the DSSC field, represent a nascent dye family [77, 98, 140] and the efficiencies reported in Chapter 2, 3 and 5 definitely demonstrate the suitability of iridium complexes for photovolatic applications. It has been an exciting challenge for us to design new dyes with increased molar extinction coefficient to enhance their light harvesting properties, which significantly would improve the short-circuit current resulting in useful power conversion efficiencies.[152]

The efficiencies achieved and reported in this thesis for our novel dyes can absolutely be enhanced by a systematic optimization of each single part of the solar cell device, for example with the use of cobalt-based electrolyte, or with multiple MO_x layers.

The use of these phenyltriazole ligands in Chapter 2 led to the birth of iridium complexes with good spatial charge transfer directionality. Our work with CuAAC/B.O. synthesis, thanks to its versatility, has been preliminarily extended by using a formylphenylpyridine cyclometalating ligand, so we were able to synthesise the complex $[Ir(fppy)_2dcb]PF_6$ (**AS21**). Looking at complex **AS21** in Figure 6.1, the aldehyde groups could be easily converted to acetylenes by the Bestmann-Ohira reaction providing a CuAAC synthon for further derivatization. This building block approach using CuAAC coupling of ferrocenyl or thiophenyl groups will then yield a new range of DSSC sensitizer complexes.

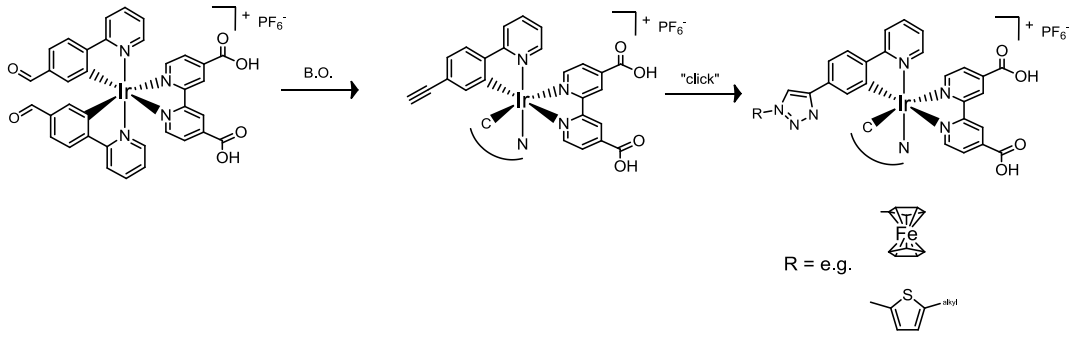

*Figure 6.1 Functionalization of aldehyde group in **AS21***

Chapter 3 revealed how the pyridylbenzoic acid might be an ideal candidate as anchoring ligand in a p-type dye design. Further work with our iridium pyba complexes can be explored. The choice of ancillary ligands with more electron withdrawing groups or extended conjugation will lead to a longer charge separation together with red shifted absorption profiles, hence a higher efficiency on NiO devices. Also, the design of the presented dyes makes them potentially suitable for the application in water splitting cells. There has been increasing interest in the development of a sunlight-

driven catalytic system able to generate hydrogen through reduction of H_2O because this process is a potential solution for the current limitations in the processes of green, sustainable solar energy conversion and storage.[211] One desirable approach for the chemical utilisation of solar energy is a molecular water photolysis system that mimics the natural system. This photolysis is a very complex process that involves multiple sequential photoinduced electron-transfer reactions. The utilisation of visible light to initiate reactions generally requires the use of a photoactive and redox-active chromophore that serves as a photosensitiser (PS); this PS must be capable of collecting and converting photon energy and is subject to the thermodynamic limit of the electron transfer reaction in conjunction with a suitable water-reduction catalyst (WRC). In this respect, emissive transition metal complexes, particularly d^6 species such as ruthenium (II), are well suited for this remarkable utility because they possess tuneable long-lived metal-to-ligand charge transfer states with sufficient energy to undergo favourable catalytic transformations. Among these species, cyclometalated iridium complexes emerged as a highly attractive alternative because of their high efficiency for solar light-to-energy conversion schemes. [212-214]

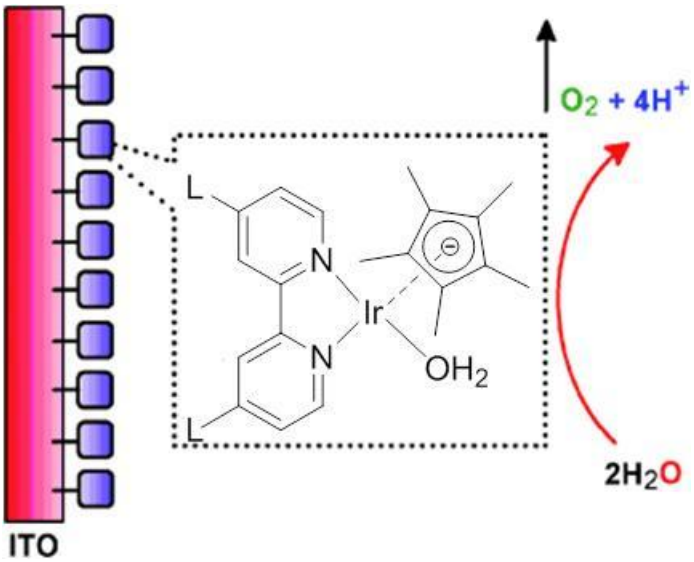

Figure 6.2. Schematic representation of the immobilized $[(L_2bpy)Ir(III)Cp\text{-}(OH_2)]^{2+}$ on ITO for electrochemical water oxidation.[213]

AS9-10, combining the presence of an anchoring group with an appreciable life time,[215] have been preliminarily used in water splitting cells by the aforementioned Gibson group.

Despite its mediocre effects on metal based dyes, the novel 1-[2,2′-bipyridine-4-yl]-1,2,3-triazole-4,5-dicarboxylic acid presented in Chapter 4 could be redesigned as anchoring ligand for p-type dyes. In fact, the destabilization of both HOMO and LUMO for dctzbpy complexes related to their dcb analogues, might well match with NiO bands. Also the blue shifted absorption profile of dctzbpy complexes could be easily moved to lower energies with the addition of electron withdrawing groups on the non-anchoring ligands, getting the double effect of red shifting the absorption profile and moving away the electrons from the anchoring sites. In addition, the use of a triazole based anchoring ligand could be useful in a p-type system because the 1,2,3-triazole moiety isn't conducting [197, 198], then it might insulate the bpy fragment from the metal oxide after charge injection, impeding or slowing down the recombination.

Combining the photophysical properties of coumarin together with the electronic and synthetic characteristics of iridium complexes in Chapter 5, certainly provides the basis for the birth of a new generation of dyes with potential applications in DSSCs, water splitting, catalysts,[212-215] OLEDs [216] and other photoelectrochemical devices. [80]

A very useful approach would be to extend the conjugation of the coumarin ligand, red shifting its absorption profile hence enhancing its light harvesting properties. At present, the 3-(diethylamino)-7-oxo-7H-benzo[4,5]-imidazo[1,2-a]chromeno[3,2-c]pyridine-6-carbonitrile dye (chromene 3) and the 3-(diethylamino)-7-imino-7H-benzo-[4,5]imidazo[1,2-a]chromeno[3,2-c]pyridine-6-carbonitrile dye (chromene 13) are utilized in colouring plastics and synthetic fibers. Their trade names are Solvent Red 197 and Solvent Red 196, respectively, being widely used for industrial coloring engineering plastics and as luminescent probes. [217] Only recently these dyes have been studied and well characterised from the photophysical and computational point of view [218] , reporting remarkable $\varepsilon_{\approx 508nm}$ values (61000 and 51000 M^{-1} cm^{-1} respectively). Their strong absorbance together with their coumarin-imidazole based structure would make them ideal as cyclometalating ligands for $[Ir(C\hat{}N)_2(dcb)]^+$ complexes (Figure 6.3).

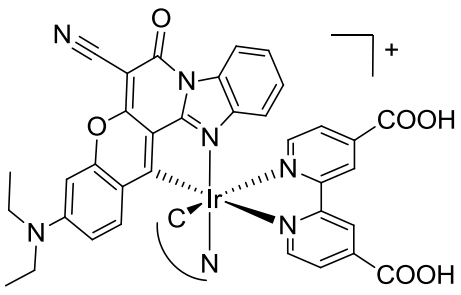

Figure 6.3 Potential iridium coumarin complex as high absorbing dye.

7 Experimental

7.1 General characterization methods

Reagents and solvents were purchased from Aldrich chemical company and Acros Organics and used as supplied, $[Ru(bpy)_2Cl_2]$ [219], $[Ir(ppy)_2Cl]_2$ [77], $[Ru(bpy)_2(dcb)](PF_6)_2$ **4.1**[138], $[Ir(ppy)_2(dcb)](PF_6)$ **4.2** [77], $[Re(dcb)(CO_3)Cl]$ **4.3** [75], $[Ir(C6)_2Cl]_2$ [152] were all prepared according to literature procedures. All the compounds synthesised in this thesis were characterized by ^1H NMR and ^{13}C NMR spectrometry; spectra were obtained on a Bruker Advance 400 MHz instrument. Mass spectrometry data were collected on a Bruker MicroTOF-Q instrument and Agilent 6210 TOF MS. UV-visible absorption spectra were recorded on an Agilent Cary 60 UV-vis spectrophotometer and corrected emission spectra were recorded on a Horiba Fluoromax-4 spectrofluorometer equipped with a 150 W ozone free xenon arc lamp. Lifetime data were recorded following 405 nm excitation with an EPL 405 picosecond pulsed diode laser (Edinburgh Instruments), using time correlated single photon counting (TCC900 plug-in PC card for fast photon counting). Lifetimes were obtained by tail fit on the data obtained, and quality of fit judged by minimization of reduced chi-squared and residuals squared. Infrared spectra were recorded on a Nicolet 380 FT-IR spectrometer.

7.2 Electrochemistry.

To characterise the electrochemical properties of the reported complexes, cyclic voltammetry (CV) has been used. The voltammograms in Chapter 3 were conducted on an Electrochemical Analyzer potentiostat model PGStation101 Metrohm workstation. The three electrode cell consisted of a Ag/AgCl electrode, used as the pseudoreference electrode; a glassy-carbon electrode, used for the working electrode and a Pt electrode, used as the counter electrode. Tetra(n-butyl)ammoniumhexafluorophosphate ($TBAPF_6$; ca. 0.1 M in ACN) was used as the supporting electrolyte. The voltage was measured between the working electrode and the reference electrode and the current was measured between the working electrode and the counter electrode. The data were then plotted as current *vs* voltage. The ferrocenium/ferrocene (Fc^+/Fc) redox couple was used as standard (0.41 V vs Ag/AgCl). The redox potentials are reported relative to a (Ag/AgCl) electrode using the Fc^+/Fc couple as a reference.

The voltammograms in Chapter 4-5 were conducted using three electrode cell, consisted of a $Ag/AgNO_3$ electrode, used as the pseudoreference electrode; a glassy-carbon electrode, used for the working electrode and a Pt electrode, used as the

counter electrode. Tetra(n-butyl)ammoniumperchlorate ($TBAClO_4$; ca. 0.1 M in ACN) was used as the supporting electrolyte. The voltage was measured between the working electrode and the reference electrode and the current was measured between the working electrode and the counter electrode. The data were then plotted as current *vs* voltage. The ferrocenium/ferrocene (Fc^+/Fc) redox couple was used as standard (0.58 V vs $Ag/AgNO_3$). The redox potentials are reported relative to a ($Ag/AgNO_3$) electrode using the Fc^+/Fc couple as a reference.

7.3 Density Functional Theory Calculations.

DFT calculations were carried out using the NWChem 6.3 software package. [220] B3LYP hybrid functional (20% Hartree–Fock) method has been used for calculations,[221] Stuttgart relativistic small core ECP[222] for transition metals and 6-311G* basis sets for all other atoms. Molecular geometries and molecular orbitals pictures were realised using the ccp1 graphical software. For all the studied complexes, the ground state geometries were first optimized and molecular orbital energies determined. TD-DFT calculations on optimised structures in CH_3CN by using the COSMO solvation model, built in NWChem software, were used to obtain the electronic spectra and molecular orbital energy levels.

In order to confirm the reliability of the computational calculations reported in this thesis, the computed bond lengths for three random iridium complexes have been compared with some examples of crystal structure for iridium cyclometalated complexes reported in literature (Table 7.1). [178, 214]

Table 7.1 Comparison of calculated bond lengths in iridium cyclometalated complexes with experimental crystallographic data for similar complexes.

Complex	Ir-$N_{(C^N)}$ [Å]	Ir-$C_{(C^N)}$ [Å]	Ir-$N_{(N^N)}$ [Å]	$C_{(C^N)}$-Ir-$N_{(C^N')}$ [°]
AS2	2.06	2.05	2.19	93.8
AS12	2.10	2.03	2.21	94.9
AS19	2.11	2.06	2.22	101.1

$[Ir(dfppy)_2(btz)]^+$ [178]	2.04	2.00	2.15	92.6
$[Ir(bt)_2(dcb)]^+$ [214]	2.05	2.06	2.13	93.7

The data reported in Table 7.1 showed a slightly overestimation on calculated distances and angle in respect to the crystallographic data, however the structures obtained with the used functional and basis set definitely represent good models for structural and photophysical investigation.

7.4 Preparation of dye-sensitized nanocrystalline MO_x electrodes

In order to carry out the preliminary cell test in Sessions 2.6 and 4.7, titanium oxide electrodes were prepared as follows. TiO_2 colloidal dispersion was made employing commercial TiO_2 powder (Aldrich, 99.7% anatase, particles size <25 nm). To 0.750 g of powder 1 mL of HNO_3 0.1M was added. To this suspension 30 mg of PEG8000 and 2 drops of Triton-X100 were added. The solution was sonicated for 2h and stirred overnight. Films of nanocrystalline TiO_2 colloidal on FTO glass (TEC 15, Solaronix) were prepared by sliding a glass rod over the conductive side of the glass. Sintering was carried out at 450°C for 30 minutes. The films were then dipped into a 0.3 mM dye solution in ethanol for 12h at 60°C. The dye coated TiO_2 film, as working electrode, was placed on top of an FTO glass as counter electrode. The latter was made with solvent-assisted drop-casting technique, spreading a H_2PtCl_6 (5 mM) isopropanol solution onto FTO glass, and heating the resulting film at 500 °C for half an hour. The redox electrolyte was introduced into the inter-electrode space by capillary force.

Nanostructured NiO films used anchoring test in Session 3.6 were prepared as follows: 4.75 g (0.020 mol) $NiCl_2$,$6H_2O$ (Merck) was dissolved in 100 mL deionised water, and 45 mL of a 1.0M NaOH solution was added under strong stirring. A green $Ni(OH)_2$ precipitate formed immediately. After settling overnight, the clear supernatant was removed and the precipitate (~70 mL) was dialyzed against deionised water. Next, the suspension was concentrated using a rotary evaporator until it was visibly viscous. A small amount of acetic acid (10 drops of 1.75M acetic acid) and up to 30% ethanol were added to improve spreading and drying characteristics. The sol was spread using a glass rod on conducting FTO glass (TEC 15, Solaronix), which was masked by adhesive tape (Scotch Magic, 40 µm thickness). The film was dried in air and fired at

300-320 °C for 15 min in a hot air stream. [223] Pt-electrodes were made as described above.

For the measurements at University of Nottingham (Chapter 2), FTO glass was used as current collector (TCO30-8, 3 mm thick glass substrate with a 8 Ω/sq fluorine doped tin oxide coating on one face), which was cut into 1.5x1.5 cm size by using a diamond glasscutter. To prepare the DSSC working electrodes, the FTO glass was first cleaned with ethanol. After drying, they were immersed into a 40 mM aqueous $TiCl_4$ (877 µL in 200 mL of water) solution at 70° C for 30 minutes and washed with pure water and ethanol and dried. Then the plates were cleaned in a boiling acetone bath for 15 minutes, followed by a bath of 0.1M HCl in ethanol for 10 minutes and again in a boiling acetone bath. A layer of nanocrystalline TiO_2 paste (Solaronix Ti-Nanoxide D) was coated on the FTO glass plates by doctor blade technique, using a round mask (5 mm diameter, 0.2 cm^2 area) made by adhesive tape (3M Magic). The film was dried for 5 minutes on a hotplate and a second layer of TiO_2 was deposited as before. The films were sintered at 450° C for 30 minutes. After cooling to 80 °C, the TiO_2 electrodes were immersed into a 0.5 mM dye solution in a mixture of ethanol/tert-buthanol 4:1 and kept at 45 °C overnight in the dark. To prepare the counter electrode, a hole was drilled in the FTO glass (TCO30-8, 3 mm thick glass substrate with an 8 Ω/sq fluorine doped tin oxide coating on one side). The perforated plate was washed with water and cleaned by a boiling acetone bath for 15 minutes. After drying, the Pt catalyst was deposited on the FTO glass by doctor blade coating with 10µL/cm^2 of H_2PtCl_6 solution (5 mM isopropanol solution), air dried and heated at 400°C for 15 minutes. The dye-covered TiO_2 electrodes, previously washed with acetonitrile, and Pt-counter electrodes were assembled into a sandwich-type cell and sealed with a hot-melt gasket of 60 µm thickness made of Surlyn on a heating stage. Then, the hole in the back of the counter electrode was covered with a hot-melt ionomer film. A hole was made in the hot-melt ionomer film with a needle. A drop of the electrolyte, a solution of 0.4 M 1-butyl-3-methyl-imidazolium iodide, 0.03 M I_2 and 0.3 M LiI in acetonitrile:valeronitrile 9:1, was introduced through the predrilled hole in the counter electrode, which was sealed afterward. The edge of the FTO was painted with a silver conductive painting.
NiO electrodes (Chapter 3 and 5) were made by applying the precursor solution described in previous literature[224] onto conducting glass substrates (Pilkington TEC15, sheet resistance 15 Ω/sq) by doctor blade using Scotch tape as a spacer (0.25 cm^2 active area), followed by sintering in a NaberthermB150 oven at 450 °C for 30 min. The NiO electrodes were soaked in an acetonitrile solution of the dye (0.3 mM) for 16 h at room temperature. The dyed NiO electrode was assembled face-to-face with a

platinized counter electrode (Pilkington TEC8, sheet resistance 8 Ω/sq) using a 30 μm thick thermoplastic frame (Surlyn 1702). The electrolyte, containing LiI (1.0 M) and I_2 (0.1 M) in acetonitrile, was introduced through the predrilled hole in the counter electrode, which was sealed afterward.

For the measurements at Newcastle University (Chapter 4 and 5), FTO glass was used as current collector (TCO30-10, 3 mm thick glass substrate with a 10 Ω/sq fluorine doped tin oxide coating on one side), which was cut into 1.5x1.5 cm size by using a diamond glasscutter. To prepare the DSSC working electrodes, the FTO glass was first cleaned with ethanol. After dried they were immersed into a 40 mM aqueous $TiCl_4$ (877 μL in 200 mL of water) solution at 70 °C for 30 minutes and washed with pure water and ethanol and dried. A layer of nanocrystalline TiO_2 paste (Solaronix Ti-Nanoxide SP-T) was coated on the FTO glass plates by doctor blade technique, using a round mask (5 mm diameter, 0.25 cm^2 area) made by adhesive tape (3M Magic). The film was dried for 5 minutes on a hotplate and a second layer of TiO_2 was deposited as before. The films were sintered at 450° C for 30 minutes. After cooling to 80 °C, the TiO_2 electrodes were immersed into a 0.5 mM acetonitrile dye solution overnight. To prepare the counter electrode, a hole was drilled in the FTO glass (TCO30-8, 3 mm thick glass substrate with an 8 Ω/sq fluorine doped tin oxide coating on one side). The perforated plate was washed with water and cleaned by a boiling acetone bath for 15 minutes. After drying, the Pt catalyst was deposited on the FTO glass by doctor blade coating with 10μL/cm^2 of H_2PtCl_6 solution (5 mM isopropanol solution), air dried and heated at 400°C for 15 minutes. The dye-covered TiO_2 electrodes, previously washed with ethanol, and Pt-counter electrodes were assembled into a sandwich-type cell and sealed with a hot-melt gasket of 60 μm thickness made of Surlyn on a heating stage. Then, the hole in the back of the counter electrode was covered with a hot-melt ionomer film. A hole was made in the hot-melt ionomer film with a needle. A drop of the electrolyte, 0.5 M TBP, 0.015 M I_2, 0.6 M TBAI and 0.1 M GuSCN in acetonitrile, was introduced through the predrilled hole in the counter electrode, which was sealed afterwards.

7.5 Synthesis of Bestmann-Ohira reagent [159]

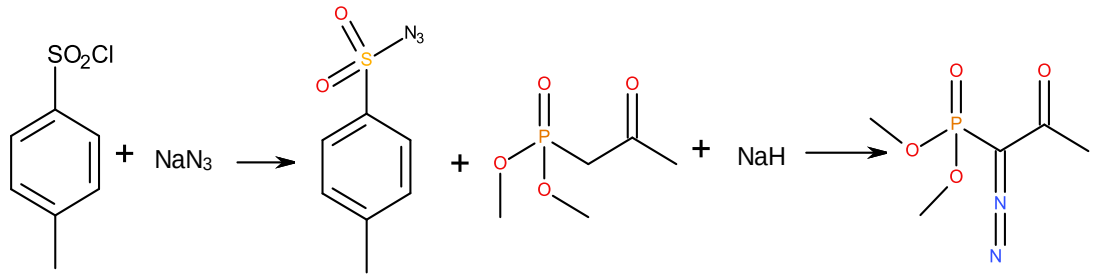

NaN_3 (21 mmol) and p-toluene sulphonyl chloride (21 mmol) were dissolved in 1:1 acetone/water (120 mL) and stirred at 0°C for 2 hours. The resulting solution was concentrated to 20 mL and the product was extracted into diethyl ether (3x60 mL). It was then dried over $MgSO_4$ and concentrated to 20 mL. NaH 60% in mineral oil (0.86 g) was washed with *n*-hexane to give oil-free NaH (21 mmol) which was dissolved in THF (50 mL) and cooled at 0°C. Dimethyl-2-oxopropylphosphonate was dissolved in THF (50 mL) and the solution was added drop-wise to the hydride solution. The mixture was stirred at 0 °C for 1 hour. The ethereal solution of tosyl azide was added to the other solution and stirred at 0 °C for 15 minutes. This was then filtered and purified by column chromatography (PE:EtOAc 1:1). (2.9 g, yield 72%)

^{1}H NMR (400 MHz, $CDCl_3$) δ: 3.80 (s, 3H, OCH_3); 3.77 (s, 3H, OCH_3); 2.21 (s, 3H, CH_3).

7.6 Synthesis of 4,4'-dicarboxy-2,2'-bipyridine[225]

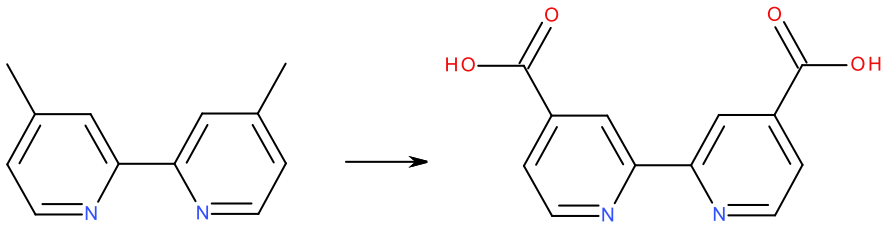

To a stirring solution, put in an oil bath, of sulphuric acid (95% 25 mL), 1.0 g (4.1 mmol) of 4,4'-dimethyl-2,2'-bipyridine was added. With efficient stirring, 4.8 g (48 mmol) of chromium trioxide (in powder) was then added in very small portions. After the chromium trioxide was added, the reaction was stirred at 40 °C for 3h. The deep green reaction mixture was poured into 160 mL of ice water overnight and filtered. The solid was washed with water until the filtrate was colourless and allowed to dry. The resulting light yellow solid was then further purified dissolving it in 34 mL of 50% nitric acid and heating to reflux temperature for 4 hours. This solution was poured over 200 mL of ice water. The precipitate was filtered, washed with water (5 * 10 mL), then acetone (2 * 10 mL) and allowed to dry overnight giving a fine white solid. (1 g, yield 75%)

^{1}H NMR (400 MHz, $CDCl_3$) δ: 8.93 (dd, ^{3}J =4.85, ^{4}J = 0.87; 2H, Py-*H*); 8.86-8.85 (m, 2H, Py-*H*); 7.92 (dd, ^{3}J = 5.05, ^{4}J = 1.75; 2H, Py-*H*).

7.7 Synthesis of Diethyl-4,4'-dicarboxylate-2,2'-bipyridine

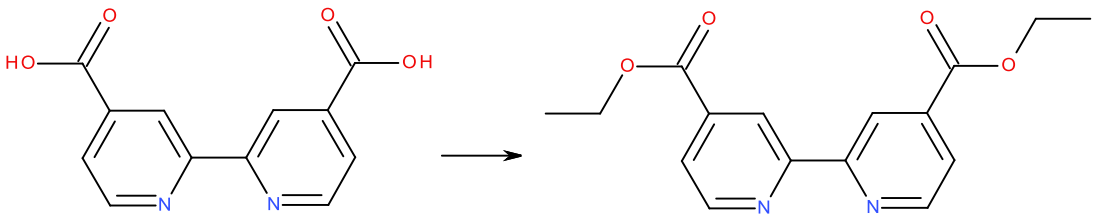

A solution of 0.84 g. (0.0034 mol) of 2,2'-bipyridine-4,4'-dicarboxylic acid in a mixture of 10.5 mL of sulphuric acid (95%) and 22.5 mL of absolute ethanol was heated to reflux temperature for 15 h. and was then cooled and poured on 160 mL of ice. Neutralization with 25% aqueous sodium hydroxide caused precipitation of a white solid. The latter was collected by filtration, washed thoroughly with water and allowed to dry. The product was recrystallized from 95% ethanol yielding a white solid. (0.84 g, yield 82%)

^{1}H NMR (400 MHz, DMSO-d_6) δ: 8.96 (dd, ^{3}J = 5.01, ^{4}J = 0.74; 2H, Py-*H*); 8.85 (s, 2H, Py-*H*); 7.96 (dd, ^{3}J = 4.87, ^{4}J = 1.59; 2H, Py-*H*); 4.42 (q, ^{3}J = 7.32, 4H, C*H*$_2$CH$_3$); 1.38 (t, ^{3}J = 7.32, 6H, CH$_2$C*H*$_3$).

7.8 Synthesis of 1-benzyl-4-(3-nitrophenyl)-1,2,3-triazole (2a)

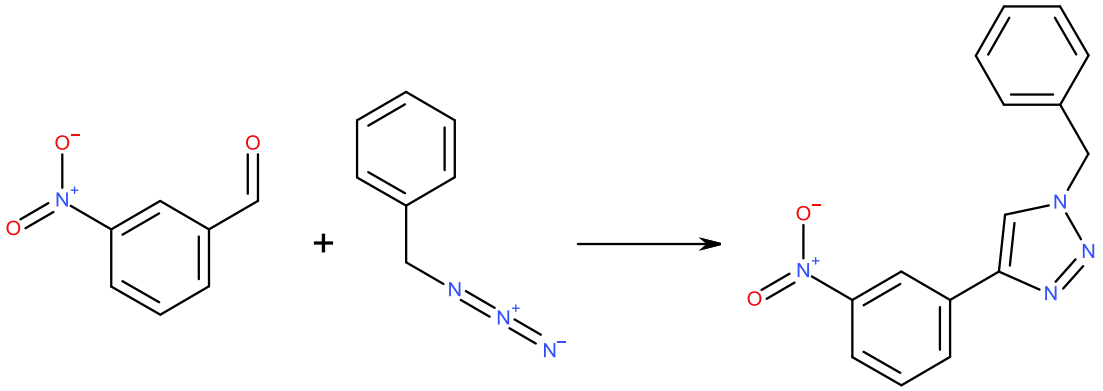

3-nitroaldehyde (2.5 mmol), Bestmann-Ohira reagent (5 mmol), and K_2CO_3 (7.5 mmol) were dissolved in 1:1 MeOH:THF (5 mL). The reaction mixture was stirred at room temperature for 24 h and monitored by TLC (silica, 2% MeOH in DCM). $CuSO_4 \cdot 5H_20$ (4.5 mmol), sodium ascorbate (1 mmol) and benzyl azide (2.5 mmol) were added, and the reaction mixture was stirred for a further 24 h and monitored by TLC. The solvent was removed in vacuo and the remaining residue was dissolved in EtOAc (25 mL) and H_2O (25 mL). The aqueous layer was washed with EtOAc (5x20 mL). The combined organics were washed with saturated NH_4Cl (30 mL) and saturated brine (30 mL) then dried with $MgSO_4$. The solvent was removed to leave the crude product which was purified by column chromatography (silica, 2% MeOH in DCM). (Yield 93%)

^{1}H NMR (400 MHz, $CDCl_3$) δ: 8.48 (s, 1H, Ph-*H*), 8.15 (d, ^3J = 7.7, 1H, Ph-*H*), 8.09 (d, ^3J = 8.2, 1H, Ph-*H*), 7.74 (s, 1H, Tz-*H*), 7.52 (t, ^3J = 8, 1H, Ph-*H*), 7.34 (d, ^3J = 6.4, 3H, CH_2-Ph-*H*), 7.27 (d, ^3J = 7.6, 2H, CH_2-Ph-*H*), 5.54 (s, 2H, C*H*$_2$-Ph).

^{13}C {^{1}H} NMR (400 MHz, $CDCl_3$) δ: 148.6, 146.1, 134.2, 132.3, 131.5, 129.9, 129.3, 129.1, 128.2, 122.8, 120.5, 120.4, 54.5

MS (ESI) *m/z* calcd 280.28 $C_{15}H_{12}N_4O_2$, found 303.085 $(M+Na)^+$

7.9 Synthesis of 1-benzyl-4-(4-nitrophenyl)-1,2,3-triazole (2b)

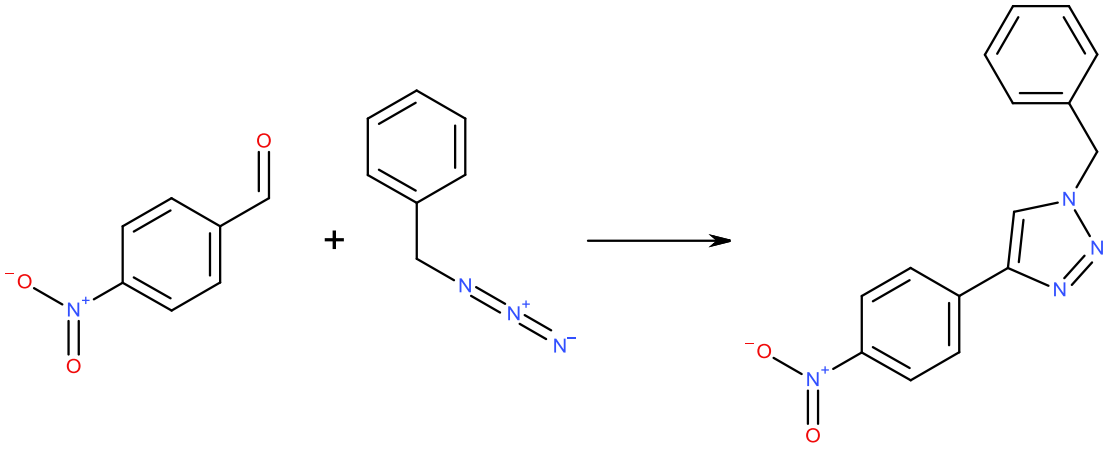

4-nitroaldehyde (5 mmol), Bestmann-Ohira reagent (5 mmol), and K_2CO_3 (7.5 mmol) were dissolved in 1:1 MeOH:THF (5 mL). The reaction mixture was stirred at room temperature for 24 h and monitored by TLC. $CuSO_4 \cdot 5H_20$ (4.5 mmol), sodium ascorbate (1 mmol) and benzyl azide (2.5 mmol) were added, and the reaction mixture was stirred for a further 24 h and monitored by TLC (silica, 2% MeOH in DCM). The solvent was removed in vacuo and the remaining residue was dissolved in EtOAc (25 mL) and H_2O (25 mL). The aqueous layer was washed with EtOAc (5x20 mL). The combined organics were washed with saturated NH_4Cl (30 mL) and saturated brine (30 mL) then dried with $MgSO_4$. The solvent was removed to leave the crude product which was purified by column chromatography (silica, 2% MeOH in DCM). (Yield 85%)

^{1}H NMR (400 MHz, $CDCl_3$) δ: 8.19 (dd, ^3J = 7.0, ^4J = 1.9; 2H, Ph-*H*), 7.90 (dd, ^3J = 7.0, ^4J = 1.9; 2H, Ph-*H*), 7.73 (s, 1H, Tz-*H*), 7.32-7.35 (m, 3H, CH_2-Ph-*H*), 7.25-7.28 (m, 2H, CH_2-Ph-*H*), 5.54 (s, 2H, C*H*$_2$-Ph).

^{13}C {^{1}H} NMR (400 MHz, $CDCl_3$) δ: 147.3, 146.1, 136.8, 134.2, 129.3, 129.1, 128.2, 126.1, 124.3, 121.0, 54.5.

MS (ESI) *m/z* calcd 280.28 $C_{15}H_{12}N_4O_2$, found 303.3080 $(M+Na)^+$

7.10 Synthesis of 1-benzyl-4-(phenyl)-1,2,3-triazole (2c)

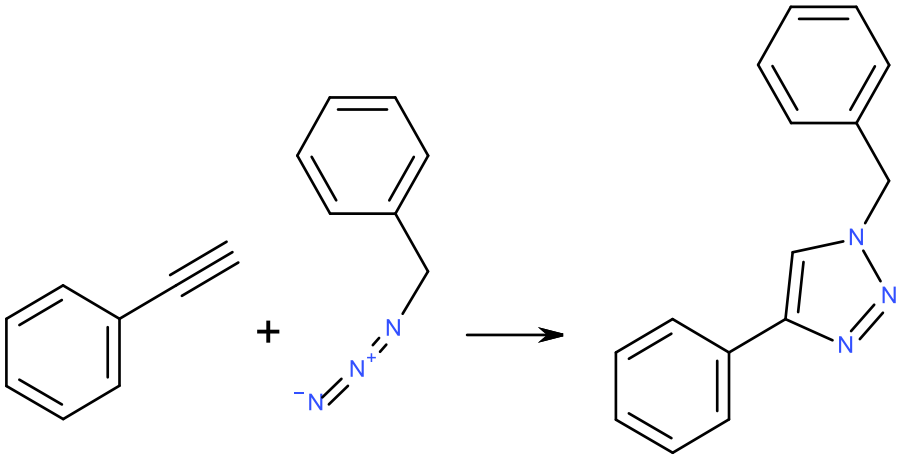

Bromomethylbenzene (0.88 mL, 11 mmol), one crystal of KI and NaN_3 (0.61 g, 9.38 mmol) were dissolved in dimethyl sulfoxide (15 mL). The reaction mixture was stirred at room temperature for 2 h and monitored by TLC. Aqueous $CuSO_4 \cdot 5H_2O$ solution (35 mg, 0.14 mmol), water (7 mL), phenylacetylene (1.2 mL, 11 mmol), 1M aqueous sodium ascorbate solution (1.2 mL, 1.2 mmol) and 2,6-lutidine (1.28 mL, 11 mmol) were added, and the reaction mixture was stirred for a further 12 h and monitored by TLC. 25 mL of water were added to the reaction mixture and the resulting solid was filtered off. The solid was then washed with water (25 mL) and dilute ammonia (25 mL), dried under vacuum and washed with petroleum ether (40-60 °C). (Yield 48%)

^{1}H NMR (400 MHz, $CDCl_3$) δ: 7.82 (d, ^3J = 7.26, 2H, Ph-*H*); 7.68 (s, 1H, Tz-*H*), 7.45-7.30 (m, 8H, Ph-*H*&CH_2-Ph-*H*); 5.98 (s, 2H, C*H*$_2$-Ph).

^{13}C {^{1}H} NMR (400 MHz, $CDCl_3$) δ: 148.3; 134.7; 130.6; 129.2; 128.9; 128.3; 128.1; 125.8; 119.6; 54.3.

HRMS (ESI) *m/z* calcd 235.1109 $C_{15}H_{13}N_3$, found 258.09938 $(M+Na)^+$

7.11 Synthesis of 1-benzyl-4-(2-thienyl)-1,2,3-triazole (2d)

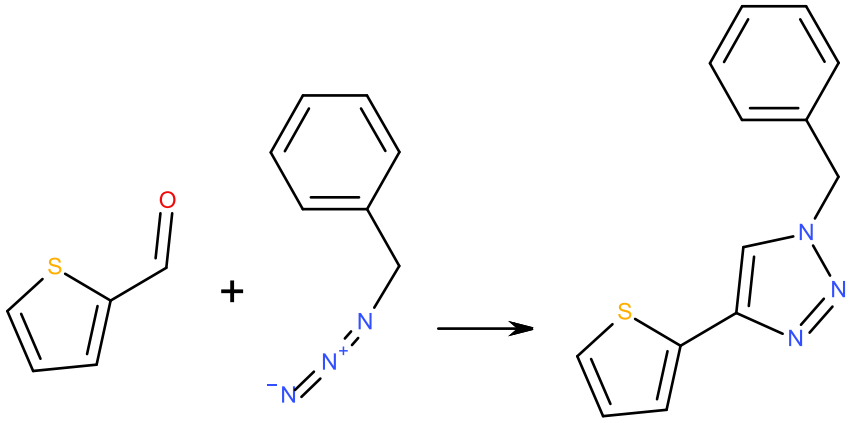

2-Thienylaldehyde (2.5 mmol), Bestmann-Ohira reagent (5 mmol), and K_2CO_3 (7.5 mmol) were dissolved in 1:1 MeOH:THF (5 mL). The reaction mixture was stirred at room temperature for 24 h and monitored by TLC. $CuSO_4 \cdot 5H_20$ (4.5 mmol), sodium ascorbate (1 mmol) and benzyl azide (2.5 mmol) were added, and the reaction mixture was stirred for a further 24 h and monitored by TLC. The solvent was removed in vacuo and the remaining residue was dissolved in EtOAc (25 mL) and H_2O (25 mL). The aqueous layer was washed with EtOAc (5x20 mL). The combined organics were washed with saturated NH_4Cl (30 mL) and saturated brine (30 mL) then dried with $MgSO_4$. The solvent was removed to leave the crude product which was purified by column chromatography (silica, 2% MeOH in DCM). (Yield 76%)

^{1}H NMR (400 MHz, $CDCl_3$) δ: 7.50 (s, 1H, Tz-*H*), 7.29-7.34 (m, 3H, H_{Bn}), 7.26 (dd, ^3J = 3.6, ^4J = 1.0, 1H, Th-*H*), 7.23 (dd, ^3J = 7.3, ^4J = 2.4, 2H, CH_2-Ph-*H*), 7.20 (dd, ^3J = 5.1, ^4J = 1.04, 1H, Th-*H*), 6.97 (dd, ^3J = 5.0, ^4J = 3.6, 1H, Th-*H*), 5.48 (s, 2H, C*H*$_2$-Ph).

^{13}C {^{1}H} NMR (400MHz, $CDCl_3$) δ: 143.3, 134.5, 132.9, 129.2, 128.9, 128.1, 127.6, 125.1, 124.2, 119.0, 54.2.

MS (ESI) *m/z* calcd 241.31 $C_{13}H_{11}N_3S$, found 242.07 $(M+H)^+$

7.12 Synthesis of 1-benzyl-4-(1-naphtyl)triazole (2e)

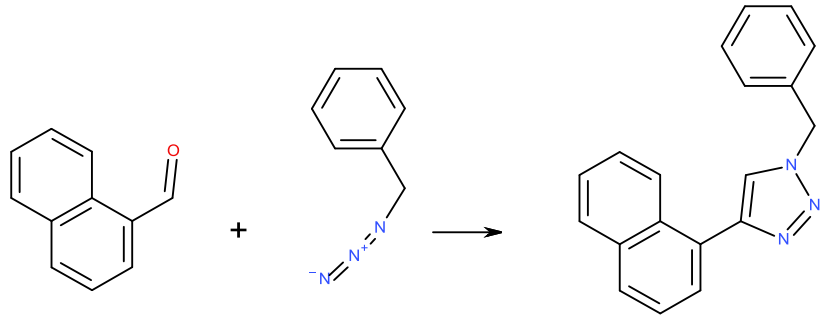

1-Naphtylaldehyde (2.5 mmol), Bestmann-Ohira reagent (5 mmol), and K_2CO_3 (7.5 mmol) were dissolved in 1:1 MeOH:THF (5 mL). The reaction mixture was stirred at room temperature for 24 h and monitored by TLC. $CuSO_4 \cdot 5H_20$ (4.5 mmol), sodium ascorbate (1 mmol) and benzyl azide (2.5 mmol) were added, and the reaction mixture was stirred for a further 24 h and monitored by TLC. The solvent was removed in vacuo and the remaining residue was dissolved in EtOAc (25 mL) and H_2O (25 mL). The aqueous layer was washed with EtOAc (5x20 mL). The combined organics were washed with saturated NH_4Cl (30 mL) and saturated brine (30 mL) then dried with $MgSO_4$. The solvent was removed to leave the crude product which was purified by column chromatography (silica, 2% MeOH in DCM). (Yield 75%)

^{1}H NMR (400 MHz, $CDCl_3$) δ: 8.26-8.31 (m, 1H, Nph-*H*), 7.76-7.82 (m, 2H, Nph-*H*), 7.64 (s, 1H, Tz-*H*), 7.60 (dd, ^3J = 7.14, ^4J = 1.08, 1H, Nph-*H*), 7.39-7.45 (m, 3H, Nph-*H*), 7.26-7.35 (m, 5H, CH_2-Ph-*H*), 5.56 (s, 2H, CH_2-Ph).

^{13}C {^{1}H} NMR (400MHz, $CDCl_3$) δ: 147.4, 134.7, 133.9, 131.1, 129.2, 129.0, 128.9, 128.5, 128.2, 128.0, 127.2, 126.7, 126.0, 125.4, 125.3, 122.5, 54.4.

MS (ESI) *m/z* calcd 285.34 $C_{19}H_{15}N_3$, found 308.11 $(M+Na)^+$

7.13 Synthesis of 1-benzyl-4-(2-naphtyl)-1,2,3-triazole (2f)

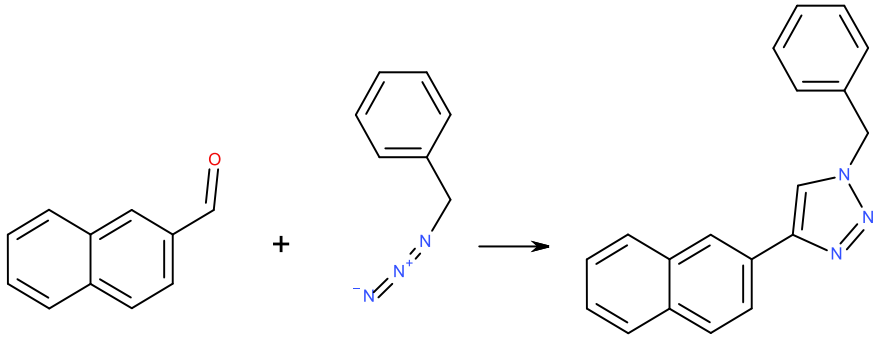

2-Naphtylaldehyde (2.5 mmol), Bestmann-Ohira reagent (5 mmol), and K_2CO_3 (7.5 mmol) were dissolved in 1:1 MeOH:THF (5 mL). The reaction mixture was stirred at room temperature for 24 h and monitored by TLC. $CuSO_4 \cdot 5H_20$ (4.5 mmol), sodium ascorbate (1 mmol) and benzyl azide (2.5 mmol) were added, and the reaction mixture was stirred for a further 24 h and monitored by TLC. The solvent was removed in vacuo and the remaining residue was dissolved in EtOAc (25 mL) and H_2O (25 mL). The aqueous layer was washed with EtOAc (5x20 mL). The combined organics were washed with saturated NH_4Cl (30 mL) and saturated brine (30 mL) then dried with $MgSO_4$. The solvent was removed to leave the crude product which was purified by column chromatography (silica, 2% MeOH in DCM). (Yield 58%)

^{1}H NMR (400 MHz, $CDCl_3$) δ: 8.24 (s, 1H, Nph-*H*), 7.74-7.84 (m, 4H, Nph-*H*), 7.70 (s, 1H, Tz-*H*), 7.40 (d, ^3J = 3.52, 2H, CH_2-Ph-*H*), 7.32 (m, 3H, CH_2-Ph-*H*), 7.27 (dd, ^3J = 7.52, ^4J = 2.16, 2H, Nph-*H*), 5.53(s, 2H, C*H*$_2$-Ph).

^{13}C {^{1}H} NMR (400MHz, $CDCl_3$) δ: 54.3, 123.8, 124.4, 126.1, 126.4, 127.8, 127.9, 128.2, 128.2, 128.6, 128.9, 129.2, 133.2, 133.5, 134.7, 148.3.

MS (ESI) *m/z* calcd 285.34 $C_{19}H_{15}N_3$, found 308.11 $(M+Na)^+$

7.14 Synthesis of 4-(*p*-tolyl)-1-propyl-1,2,3-triazole (2g)

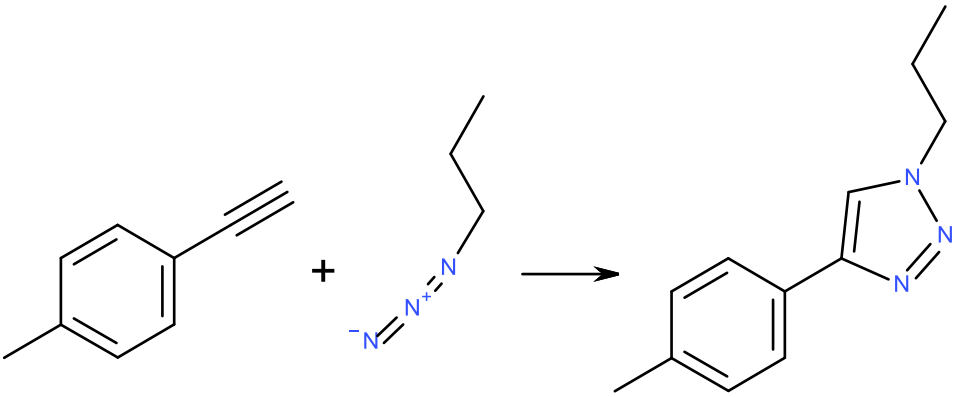

1-Bromopropane (1 mL, 11 mmol), one crystal of KI and NaN_3 (0.61 g, 9.38 mmol) were dissolved in dimethyl sulfoxide (15 mL). The reaction mixture was stirred at room temperature for 2 h and monitored by TLC. Aqueous $CuSO_4 \cdot 5H_2O$ solution (35 mg, 0.14 mmol), water (7 mL), *p*-tolylacetylene (1.39 mL, 11 mmol), 1M aqueous sodium ascorbate solution (1.2 mL, 1.2 mmol) and 2,6-lutidine (1.28 mL, 11 mmol) were added, and the reaction mixture was stirred for a further 12 h and monitored by TLC. 25 mL of water were added to the reaction mixture and the resulting solid was filtered off. The solid was then washed with water (25 mL) and dilute ammonia (25 mL), dried under vacuum and washed with petroleum ether (40-60 °C). (Yield 66 %)

^{1}H NMR (400 MHz, $CDCl_3$) δ: 7.75 (s, 1H, Tz-*H*); 7.73 (d, ^3J = 7.9, 2H, Ph-*H*); 7.25 (d, ^3J = 7.9, 2H, Ph-*H*); 4.38 (t, ^3J = 7.1, 2H, C*H*$_2$-CH$_2$-CH$_3$); 2.40 (s, 3H, Ph-C*H*$_3$); 1.99 (sex, ^3J = 7.3, 2H, CH$_2$-C*H*$_2$-CH$_3$); 1.00 (t, ^3J = 7.5, 3H, CH$_2$-CH$_2$-C*H*$_3$).

^{13}C {^{1}H} NMR (400 MHz, $CDCl_3$) δ: 147.9; 138.0; 129.6; 128.0; 125.7; 119.2; 52.1; 23.9; 21.4; 11.2.

HRMS (ESI) calcd: 201.27 $C_{12}N_3H_{15}$, found: 224.115713 $(M+Na)^+$

7.15 Synthesis of 4-phenyl-1-propyl-1,2,3-triazole (2h)

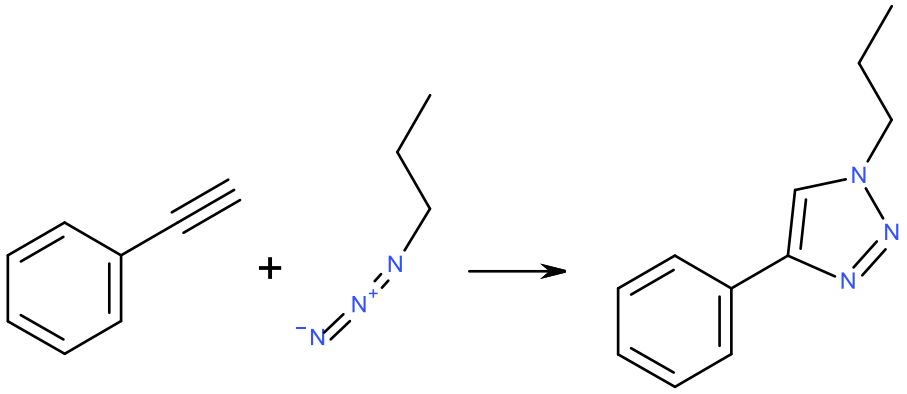

1-Bromopropane (1 mL, 11 mmol), one crystal of KI and NaN_3 (0.61 g, 9.38 mmol) were dissolved in dimethyl sulfoxide (15 mL). The reaction mixture was stirred at room temperature for 2 h and monitored by TLC. Aqueous $CuSO_4 \cdot 5H_2O$ solution (35 mg, 0.14 mmol), water (7 mL), phenylacetylene (1.2 mL, 11 mmol), 1M aqueous sodium ascorbate solution (1.2 mL, 1.2 mmol) and 2,6-lutidine (1.28 mL, 11 mmol) were added, and the reaction mixture was stirred for a further 12 h and monitored by TLC. 25 mL of water were added to the reaction mixture and the resulting solid was filtered off. The solid was then washed with water (25 mL) and dilute ammonia (25 mL), dried under vacuum and washed with petroleum ether (40-60 °C). (Yield 69%)

^{1}H NMR (400 MHz, $CDCl_3$) δ: 7.85 (d, ^3J = 4.2, 2H, Ph-*H*); 7.77 (s, 1H, Tz-*H*); 7.44 (t, ^3J = 7.5, 2H, Ph-*H*); 7.34 (t, ^3J = 7.4, 1H, Ph-*H*); 4.38 (t, ^3J = 7.2, 2H, C*H*$_2$-CH_2-CH_3); 1.99 (sex, ^3J = 7.3, 2H, CH_2-C*H*$_2$-CH_3); 1.00 (t, ^3J = 7.6, 3H, CH_2-CH_2-C*H*$_3$).

^{13}C {^{1}H} NMR (400 MHz, $CDCl_3$) δ: 147.8; 130.8; 128.9; 128.2; 125.8; 119.6; 52.1; 23.9; 11.2.

HRMS (ESI) *m/z* calcd: 187.1109 $C_{11}N_3H_{13}$ found 210.100285 $(M+Na)^+$.

7.16 Synthesis of N,N'-bis(4-methoxyphenylimino)acenaphthene (4-MeOPh-BIAN) [186]

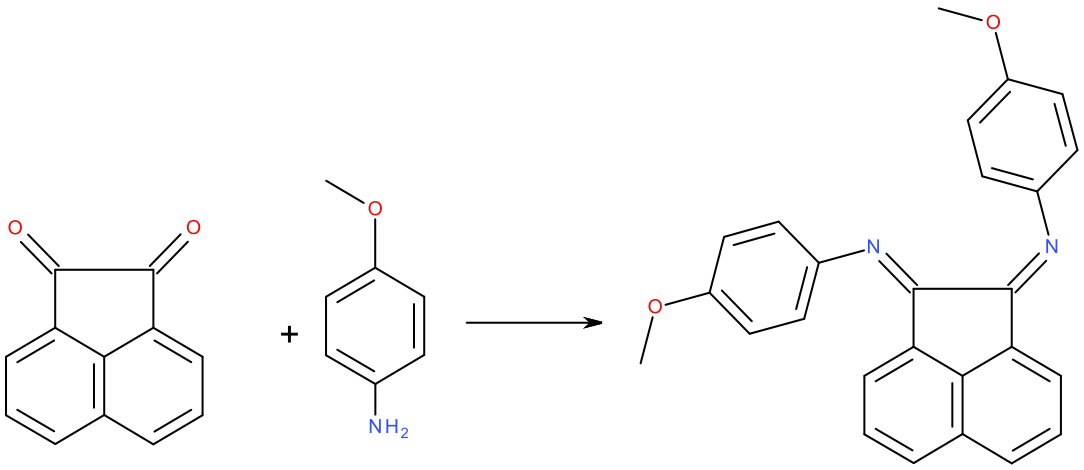

An oven dried double-necked round-bottom flask was charged with acenaphthenequinone (0.50 g, 2.75 mmol) and anhydrous $ZnCl_2$ (1.0 g, 7.4 mmol) under an atmosphere of nitrogen. A mixture of glacial acetic acid (20 mL) / toluene (6 mL) was added to the flask and the solution was heated to 60 °C for 5 min. Once a yellow suspension was observed, p-anisidine (0.78 g, 6.3 mmol) was added and the solution heated to 120 °C for 1 h. During this time, the colour of the reaction mixture changed from yellow to red and back to yellow again. The mixture was then filtered hot through a Buckner funnel and washed with acetic acid (2 x 10 mL) and Et_2O (2 x 20 mL) to obtain a yellow coloured zinc chloride complex. Then, the zinc chloride complex was suspended in 40 mL of CH_2Cl_2 and to this was added 20 mL of aqueous sodium oxalate (0.453 g, 3.38 mmol). The mixture was physically agitated for 5 min. The organic phase was separated and washed with water (2 x 20 mL) and then dried over $MgSO_4$. The solution was concentrated in vacuum. The red oil was further dried under reduced pressure to obtain 0.440 g of red solid. (Yield 41%)

^{1}H NMR (400 MHz, $CDCl_3$) δ: 7.88 (d, ^3J = 8.2, 2H, Ar-*H*), 7.39 (t, ^3J = 7.8, 2H, Ar-*H*), 7.10 (d, ^3J = 8.5, 4H, Ar-*H*), 7.03 (t, ^3J = 3.4, 4H, Ar-*H*), 7.01 (d, ^3J = 8.4, 2H, Ar-*H*), 3.89 (s, 6H, O-C*H*$_3$).

7.17 Synthesis of N,N'-bis(phenylimino)acenaphthene (Ph-BIAN)[186]

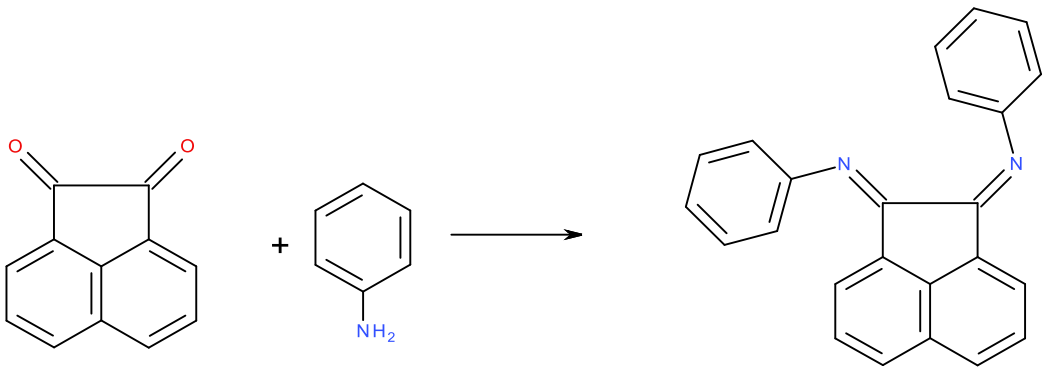

An oven dried double-necked round-bottom flask was charged with acenaphthenequinone (0.50 g, 2.75 mmol) and anhydrous $ZnCl_2$ (1.0 g, 7.4 mmol) under an atmosphere of nitrogen. A mixture of glacial acetic acid (20 mL) / toluene (6 mL) was added to the flask and the solution was heated to 60 °C for 5 min. Once a yellow suspension was observed, aniline (0.58 g, 6.3 mmol) was added and the solution heated to 120 °C for 1 h. The mixture was then filtered hot through a Buckner funnel and washed with acetic acid (2 x 10 mL) and Et_2O (2 x 20 mL) to obtain a yellow coloured zinc chloride complex. Then, the zinc chloride complex was suspended in 40 mL of CH_2Cl_2 and to this was added 20 mL of aqueous sodium oxalate (0.453 g, 3.38 mmol). The mixture was physically agitated for 5 min. The organic phase was separated and washed with water (2 x 20 mL) and then dried over $MgSO_4$. The solution was concentrated in vacuum. (Yield 52%)

^{1}H NMR (400 MHz, $CDCl_3$) δ: 7.81 (d, ^3J = 8.05, 2H, Ar-*H*), 7.40 (t, ^3J = 8.05, 4H, Ar-*H*), 7.29 (t, ^3J = 8.05, 2H, Ar-*H*), 7.19 (t, ^3J = 7.43, 2H, Ar-*H*), 7.05 (d, ^3J = 8.05, 4H, Ar-*H*), 6.75 (d, ^3J = 7.43, 2H, Ar-*H*).

7.18 Synthesis of 1,10-phenanthroline-5,6-dione.[226]

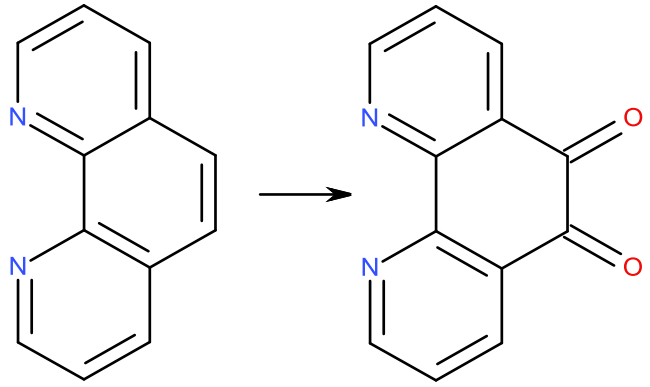

An ice cold mixture of concentrated H_2SO_4 (40 mL) and HNO_3 (20 mL) was added to 4.0 g of 1,10-phenanthroline and 4.0 g of KBr. The mixture was heated at reflux temperature for 3 h. The hot yellow solution was poured over 500 mL of ice and neutralized carefully with NaOH until neutral to slightly acidic pH. The product was extracted with $CHCl_3$, dried with Na_2SO_4 and the solvent was removed. The resulting solid was purified further by crystallization from ethanol. (4.5 g, yield 96%)

^{1}H NMR (400 MHz, $CDCl_3$) δ: 9.15 (dd, ^3J = 4.75, 1.86, 2H, Ar-*H*); 8.53 (dd, ^3J = 7.82, ^4J = 1.86, 2H, Ar-*H*); 7.61 (dd, ^3J = 7.91, ^4J = 4.75, 2H, Ar-*H*).

7.19 Synthesis of dipyrido[3,2-a:2',3'-c]phenazine (dppz)[185]

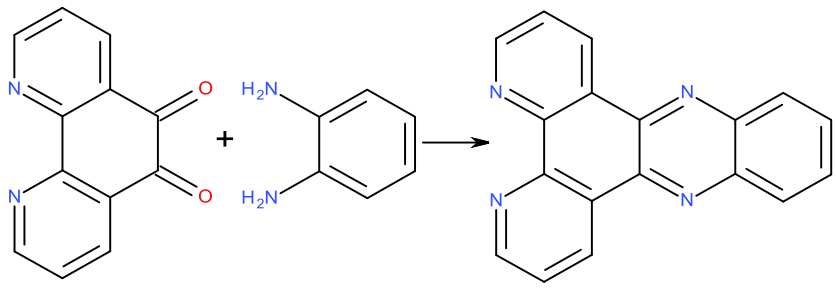

The dione was condensed with 1,2-phenylenediamine to form dipyrido[3,2-a:2',3'-c]phenazine. A mixture of 108.2 mg (0.515 mmol) of 1,10-phenanthroline-5,6-dione in 5 mL ethanol and 106.5 mg (0.986 mmol) in 5 mL of ethanol were heated to reflux temperature for 40 minutes. The solution was cooled to room temperature and left in the refrigerator, after which the yellow solid precipitated. The solid was recrystallized by ethanol-water. (101 mg, yield 43%).

^{1}H NMR (400 MHz, $CDCl_3$) δ: 9.68 (dd, ^{3}J = 8.15, ^{4}J = 1.74, 2H, Ar-*H*); 9.30 (dd, ^{3}J = 4.45, ^{4}J = 1.66, 2H, Ar-*H*); 8.39 (dd, ^{3}J = 6.57, ^{4}J = 3.47, 2H, Ar-*H*); 7.95 (dd, ^{3}J = 6.57, ^{4}J = 3.55, 2H, Ar-*H*); 7.83 (dd, ^{3}J = 8.03, ^{4}J = 4.30, 2H, Ar-*H*).

7.20 Synthesis of 4-(2-pyridyl)benzoic acid (pyba)

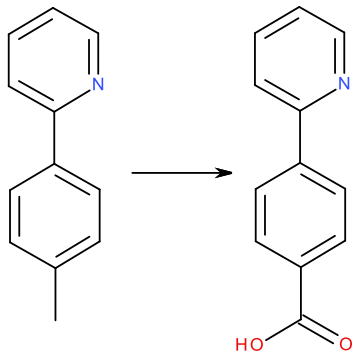

This synthetic procedure was adapted from ref [225]. Tolyl-pyridine was oxidized with $KMnO_4$ as follows: a mixture of tolyl-pyridine (0.514 g) and $KMnO_4$ (1.54 g) in water 50mL was heated at 70°C for 24h. After filtration of the reaction mixture and washing the filtrate with aqueous NaOH (1M 5 mL), the combined water fraction were collected and washed three times with $CHCl_3$ to remove unconverted starting material. The aqueous solution was neutralized with HCl (1M) and concentrated (30 mL). After acidifying to pH 4, the precipitate was collected, washed with ethanol and dried in vacuum yielding a white powder. (Yield 85%)

^{1}H NMR (400 MHz, CD_3OD) δ:8.57 (d, ^3J = 4.46, 1H, Py-*H*); 8.05 (d, ^3J = 8.23, 2H, Ar-*H*); 7.97 (d, ^3J = 8.23, 2H, Ar-*H*); 7.87 (d, ^3J = 3.43, 1H, Py-*H*); 7.37-7.33 (m, 2H, Py-*H*).

^{13}C {^{1}H} NMR (400 MHz, DMSO-d_6): 168.0465, 154.5943, 148.7504, 141.7868, 139.9051, 131.5113, 130.4489, 129.9892, 127.5556, 124.5049, 122.6979

HRMS (ESI) *m/z* calcd 199.0633 for $C_{12}H_9NO_2$, found 200.0706 $(M+H)^+$

7.21 Synthesis of 2,2'-bipyridine-N-oxide[227]

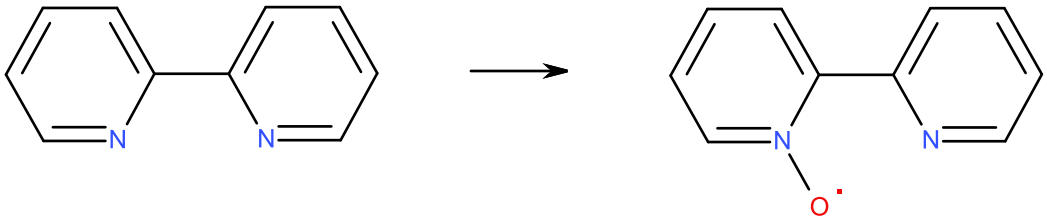

A solution of 2,2'-bipyridyl (7.00 g, 44.82 mmol) in 25 mL of $CHCl_3$, was stirred at 0 °C, for 35 min. A solution of m-chloroperbenzoic acid (84.5%, 9.156 g, 44.8 mmol) in 87 mL of $CHCl_3$, was then added dropwise over 80 min and the mixture allowed to stir at room temperature for 12h. The solution was washed three times with 500 mL portions of 5% Na_2CO_3, dried ($MgSO_4$), and evaporated. The extract was evaporated and the residue placed under vacuum, leading to a hygroscopic solid 2,2'-bipyridine-N-oxide. The Na_2CO_3 washing were extracted four times with 45mL $CHCl_3$ portions. The extract was dried ($MgSO_4$) and evaporated. Filtration of the mixture, evaporation of the filtrate, provided more of the grey-brown 2,2'-bipyridine-N-oxide. (4.27 g, yield 55 %)

^{1}H NMR (400 MHz, $CDCl_3$) δ:8.81 (dt, ^3J = 8.2, ^4J = 1.0, 1H, Py-*H*); 8.64 (dd, ^3J = 4.8, ^4J = 1.0, 1H, Py-*H*); 8.23 (dd, ^3J = 6.5, ^4J = 1.0, 1H, Py-*H*); 8.08 (dd, ^3J = 8.0, ^4J = 2.1, 1H, Py-*H*); 7.74 (dt, ^3J = 7.7, ^4J = 1.7, 1H, Py-*H*); 7.31-7.24 (m, 1H, Py-*H*); 7.19 (dt, ^3J = 6.6, ^4J = 2.2, 1H, Py-*H*).

7.22 Synthesis of 4-nitro-2,2'-bipyridine-N-oxide [227]

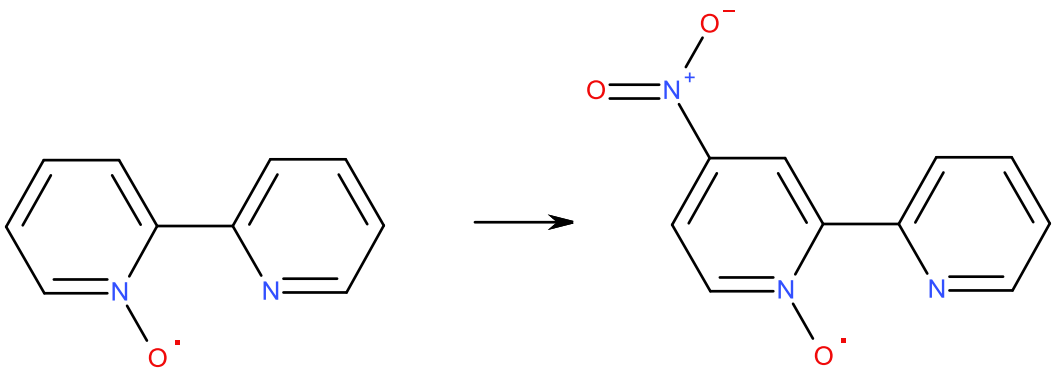

2,2'-Bipyridine-N-oxide (5.00 g, 27.7 mmol) was dissolved in concentrated sulphuric acid (20 mL), whilst in an ice bath. Fuming nitric acid (30 mL) in concentrated sulphuric acid (20 mL) was added to the mixture over 20 minutes with stirring. The mixture was heated at 100 °C for 2 hours. The solution was poured onto ice and the pH was adjusted to 13 with aqueous sodium hydroxide (25% v/v). The orange-brown precipitate was collected by filtration. The filtrate was dissolved in $CHCl_3$ and filtered to remove any 4,4'-dinitro-2,2'-bipyridine. The $CHCl_3$ was then removed under vacuum to yield a pale yellow oil. (4.08 g, yield 65%)

^{1}H NMR (400 MHz, $CDCl_3$) δ:9.18 (d, ^3J = 3.4, 1H, Py-*H*); 8.90 (dt, ^3J = 8.1, ^4J = 0.8, 1H, Py-*H*); 8.81 (dd, ^3J = 4.8, ^4J = 0.9, 1H, Py-*H*); 8.38 (d, ^3J = 7.3, 1H, Py-*H*); 8.09 (dd, ^3J = 7.3, ^4J = 3.3, 1H, Py-*H*); 7.90 (td, ^3J = 7.8, ^4J = 1.7, 1H, Py-*H*); 7.46 (ddd, ^3J = 6.2, ^4J = 4.8, ^5J = 1.22, 1H, Py-*H*).

7.23 Synthesis of 4-nitro-2,2'-bipyridine [227]

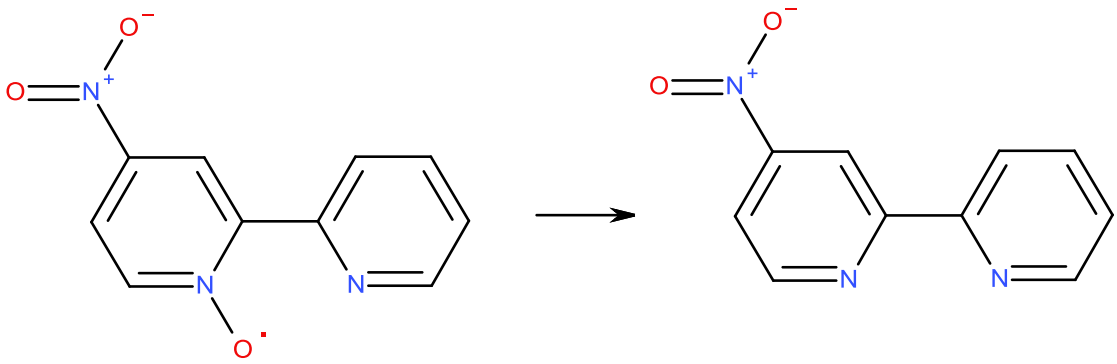

4-Nitro-2,2'-bipyridine-N-oxide (3.00 g, 13.6 mmol) was heated to reflux temperature in PCl_3 (25 mL, 290 mmol) at 75 °C for 21h. The reaction was thrown into 200 mL of ice water. This was then basified to pH 13 with concentrated NaOH and extracted exhaustively with $CHCl_3$. The combined $CHCl_3$, layers were died ($MgSO_4$) and evaporated to yield a pale yellow solid. (1.64 g, yield 49%)

^{1}H NMR (400 MHz, $CDCl_3$) δ:9.18 (d, ^3J = 2.2, 1H, Py-*H*); 8.97 (d, ^3J = 5.3, 1H, Py-*H*); 8.77(d, ^3J = 4.3, 1H, Py-*H*); 8.49 (dt, ^3J = 8.0, ^4J = 0.9, 1H, Py-*H*); 8.04 (dd, ^3J = 5.4, ^4J = 2.2, 1H, Py-*H*); 7.90 (td, ^3J = 7.6, ^4J = 1.8, 1H, Py-*H*); 7.43 (ddd, ^3J = 6.2, ^4J = 4.9, ^5J = 1.2, 1H, Py-*H*).

7.24 Synthesis of 2,2'-bipyridyl-N,N'-dioxide [228]

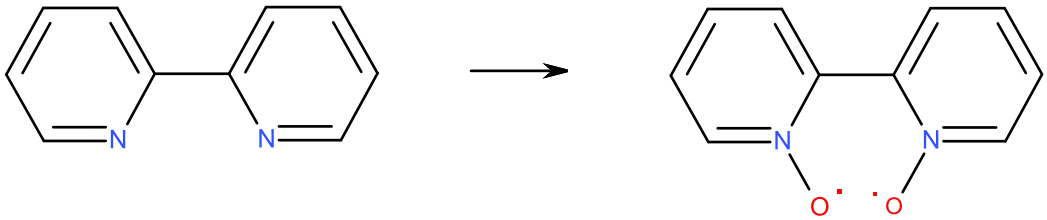

A mixture of 2,2'-bipyridyl (1.57 g, 0.01 mol), hydrogen peroxide (2.04 mL, 30%) and glacial acetic acid (12 mL) was heated at 80 °C for 3 hours. Hydrogen peroxide (1.5 mL, 30%) was added and the heating was continued for a further 4 hours. The pale yellow solution was allowed to cool to room temperature and slowly added to acetone (150 mL). Upon cooling a white solid of 2,2'-bipyridyl-N,N'-dioxide precipitated and was collected by filtration and air dried. (1.09 g, yield 56.3 %)

^{1}H NMR (400 MHz, DMSO-d_6) δ:8.36 (d, ^{3}J = 6.4, 2H, Py-*H*); 8.64 (dd, ^{3}J = 7.8, ^{4}J = 1.8, 2H, Py-*H*); 7.52 (td, ^{3}J = 7.8, ^{4}J = 2.0, 2H, Py-*H*); 7.42 (t, ^{3}J = 7.7, 2H, Py-*H*).

7.25 Synthesis of 4,4'-dinitro-2,2'-bipyridyl-N,N'-dioxide [228]

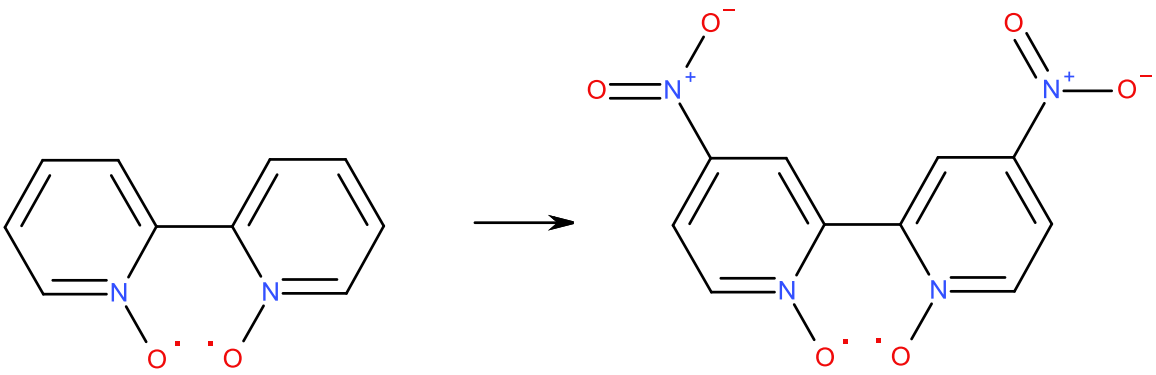

A solution of 2,2'-bipyridyl-N,N'-dioxide (0.56 g, 2.98 mmol) in conc. H_2SO_4 (10 mL) was cooled to 5 °C and then fuming nitric acid (6 mL) was added dropwise. The brown solution was heated at 120 °C for 5 hours under reflux. The reaction mixture was allowed to cool to room temperature and then quenched by pouring it on to an ice-water (50% w/v) solution, which gave a pale yellow precipitate which was collected by filtration and washed several times with water and acetone, and allowed to air dry to yield a pale yellow solid as 4,4'-dinitro-2,2'-bipyridyl-N,N'-dioxide. (0.27g, yield 32 %)

^{1}H NMR (400 MHz, DMSO-d_6) δ:8.70 (d, ^3J = 3.4, 2H, Py-*H*); 8.60 (d, ^3J = 7.2, 2H, Py-*H*); 8.37 (dd, ^3J = 7.2, ^4J = 3.3, 2H, Py-*H*).

7.26 Synthesis of 4,4'-dinitro-2,2'-bipyridyl [228]

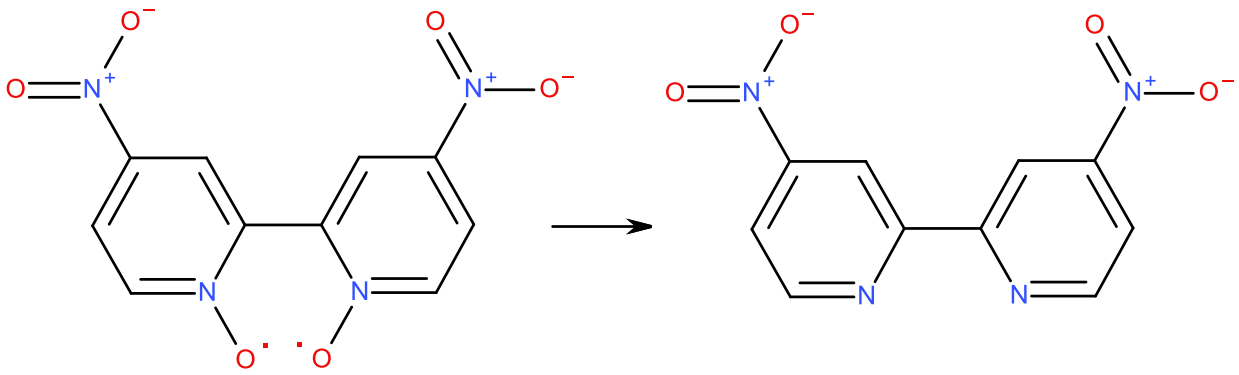

4,4'-Dinitro-2,2'-bipyridyl-N,N-dioxide (3.00 g, 10.8 mmol) was heated to reflucx temperature in PCl_3 (25 mL, 290 mmol) for 21 hours. The reaction was thrown into 200 mL of ice water. This was then basified to pH 13 with concentrated NaOH and extracted exhaustively with $CHCl_3$. The combined $CHCl_3$ layers were dried ($MgSO_4$) and evaporated to give a yellow solid. (2.22 g, yield 83 %)

^{1}H NMR (400 MHz, $CDCl_3$) δ:9.24 (d, ^3J = 2.1, 2H, Py-*H*); 9.06 (d, ^3J = 5.3, 2H, Py-*H*); 8.15 (dd, ^3J = 5.3, ^4J = 2.1, 2H, Py-*H*).

7.27 Synthesis of 4-azido-2,2'-bipyridine [229]

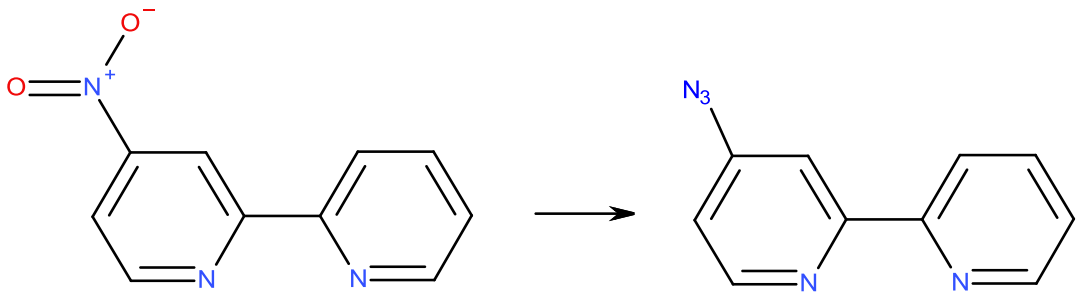

A mixture of 4-nitro-2,2'-bipyridine (1.36 g, 6.76 mmol) and NaN_3 (3.57g, 55.07 mmol) was heated in DMF (60 mL) for 3 hours at 100 °C. The DMF was removed by rotary evaporation and water (60 mL) was added, the mixture was extracted with DCM (4 x 50 mL) and the combined organic phase was dried over $MgSO_4$ and the solvent was removed. 4-azido-2,2'-bipyridine was purified by column chromatography (silica gel, DCM/AcOEt 1:1) to yield a yellow solid (1.07 g, yield 80%)

^{1}H NMR (400 MHz, $CDCl_3$) δ:8.69 (ddd, ^3J = 4.8, ^4J = 1.8, ^5J = 0.9, 1H, Py-*H*); 8.58 (d, ^3J = 5.4, 1H, Py-*H*); 8.40 (dt, ^3J = 7.8, ^4J = 0.9, 1H, Py-*H*); 8.15 (d, ^3J = 2.3, 1H, Py-*H*); 7.83 (td, ^3J = 7.8, ^4J = 1.8, 1H, Py-*H*); 7.34 (ddd, ^3J = 7.5, ^4J = 4.8, ^5J = 1.2, 1H, Py-*H*); 6.94 (dd, ^3J = 5.4, ^4J = 2.3, 1H, Py-*H*).

IR (ATR): 2115 cm^{-1} (azide stretch).

7.28 Synthesis of 1-[2,2′-bipyridine-4-yl]triazole-4,5-ethyldicarboxylate

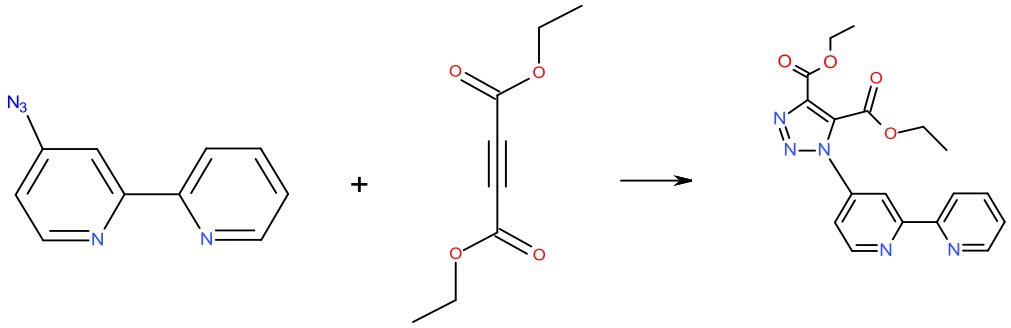

4-Azido-2,2'-bipyridine (0.1 g, 0.51 mmol) and diethyl acetylenedicarboxylate (0.16 g, 0.76 mmol) was dissolved in toluene (15 mL). The solution was allowed to stir at 70°C for 24 h. The solvent was removed under vacuum and the product was recrystallised from DCM and hexane to yield a white solid. (0.175 g, yield 93%)

^{1}H NMR (400 MHz, $CDCl_3$) δ:8.79 (d, ^{3}J = 5.34, 1H, Py-*H*); 8.61 (d, ^{3}J = 2.18, 1H, Py-*H*); 8.59 (d, ^{3}J = 4.51, 1H, Py-*H*); 8.39 (d, ^{3}J = 7.93, 1H, Py-*H*); 7.78 (td, ^{3}J = 7.67, ^{4}J = 1.71, 1H, Py-*H*); 7.55 (dd, ^{3}J = 5.34, ^{4}J = 2.23, 1H, Py-*H*); 7.29 (ddd, ^{3}J = 7.52, ^{4}J = 4.77, ^{5}J = 1.00, 1H, Py-*H*); 4.41 (dd, ^{3}J = 7.21, ^{4}J = 2.40, 4H, C*H*$_2$-CH$_3$); 1.36 (t, ^{3}J = 6.88, 3H, CH$_2$-C*H*$_3$); 1.29 (t, ^{3}J = 7.14, 3H, CH$_2$-C*H*$_3$).

^{13}C {^{1}H} NMR (400 MHz, $CDCl_3$) δ:159.45, 158.90, 158.61, 154.21, 150.91, 149.38, 143.36, 139.38, 137.12, 132.45, 124.69, 121.24, 117.37, 114.59, 63.93, 62.09, 14.20, 13.77.

HRMS (ESI) *m/z* calcd for $C_{18}H_{17}N_5O_4$ 367.1280, found 368.1359 $(M+H)^+$

7.29 Synthesis of 1-[2,2′-bipyridine-4-yl]triazole-4,5-dicarboxylic acid

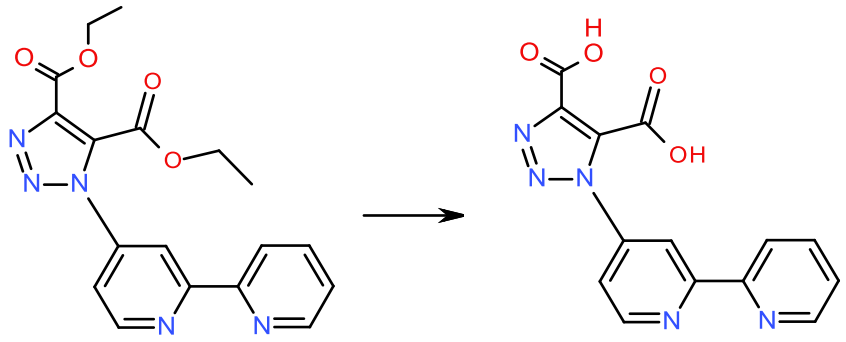

1-[2,2′-bipyridine-4-yl]triazole-4,5-ethyldicarboxylate (0.1 g, 0.51 mmol) was dissolved in 25 mL of NaOH 0.1M and heated to reflux temperature for 4h, after that the solution was neutralised with HCl 2M. A white solid crushed out, collected by filtration and dried under reduced pressure. (Yield 85%)

^{1}H NMR (400 MHz, DMSO-d_6) δ:8.85 (d, ^{3}J = 5.13, 1H, Py-*H*); 8.66 (d, ^{3}J = 4.12, 1H, Py-*H*); 8.45-8.39 (m, 2H, Py-*H*); 8.10 (t, ^{3}J = 7.68, 1H, Py-*H*); 7.68 (d, ^{3}J = 4.16, 1H, Py-*H*); 7.59 (t, ^{3}J = 6.08, 1H, Py-*H*).

^{13}C {^{1}H} NMR (400 MHz, DMSO-d_6) δ:161.99, 158.96, 155.11, 152.73, 150.92, 148.61, 145.85, 140.73, 140.35, 134.61, 126.10, 122.30, 122.13, 118.66.

HRMS (ESI) *m/z* calcd for $C_{14}H_9N_5O_4$ 311.0654, found 310.0582 $(M-H)^-$

7.30 Synthesis of 7-diethylamino-2-oxo-2H-chromene-3-carboxylic acid ethyl ester [230]

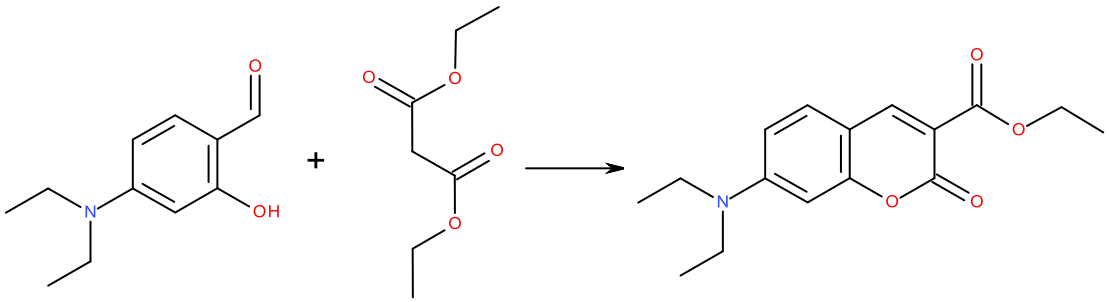

A mixture of 4-diethylamino salicyldehyde (5.05 g, 0.026 mmol), diethylmalonate (4.73 mL, 0.028 mmol) and a catalytic amount of piperidine (1 mL) and Acetic acid (1 mL) in toluene (20 mL) was heated to reflux temperature in a Dean-Stark trap for 72h. The mixture was cooled, and the solvent evaporated. The product was extracted with DCM and purified by column using petroleum ether and ethyl acetate (1:1) as the eluent. Further purification by recrystallisation afforded a yellow crystalline solid. (6.58 g, yield 87%)

^{1}H NMR (400 MHz, $CDCl_3$) δ:8.45 (s, 1H, Ar-*H*), 7.30 (d, ^{3}J = 8.9, 2H, Ar-*H*), 6.55 (dd, ^{3}J = 8.9, ^{4}J = 2.5, 1H, Ar-*H*), 6.40 (d, ^{3}J = 2.5, 1H, Ar-*H*), 4.30 (q, ^{3}J = 7.0, 2H, O-CH_2-CH_3), 3.40 (q, ^{3}J = 7.1, 4H, N-CH_2-CH_3), 1.30 (t, ^{3}J = 7.0, 3H, O-CH_2-CH_3), 1.15 (t, ^{3}J = 7.1, 6H, N-CH_2-CH_3).

7.31 Synthesis of 7-diethylamino-chromene-2-one [230]

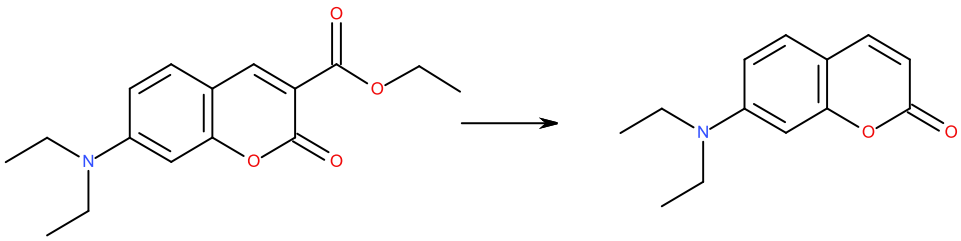

7-diethylamino-coumarin-3-carboxylic acid ethyl ester (4.00 g) in 120 mL of 37% strength HCl and 120 mL of H_2O were heated for 5 hours to boil under reflux. After cooling, a saturated solution of sodium acetate (30 mL) was added and the pH value adjusted to around 4-5 with 45% strength NaOH whilst cooling. Crystalline precipitate was filtered off, washed with H_2O and dried, affording a light yellow solid. (1.98g, yield 65%)

^{1}H NMR (400 MHz, $CDCl_3$) δ:7.54 (d, ^3J = 9.3, 1H, Ar-*H*), 7.25 (d, ^3J = 8.9, 1H, Ar-*H*), 6.58−6.55 (m, 1H, Ar-*H*), 6.48 (d, ^3J = 2.3, 1H, Ar-*H*), 6.04 (d, ^3J = 9.3, 1H, Ar-*H*), 3.43-3.38 (m, 4H, N-C*H*$_2$-CH$_3$), 1.20 (t, ^3J = 7.0, 6H, N-CH$_2$-C*H*$_3$).

7.32 Synthesis of 7-diethylamino-2-oxo-2H-chromene-3-carboxyldehyde 230

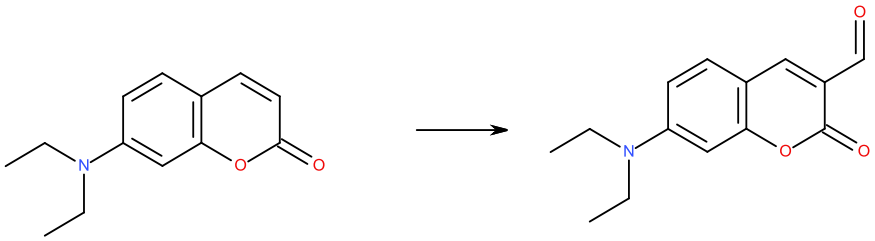

4 mL of dry DMF were added drop wise to 0.4 mL of $POCl_3$, keeping the temperature below 50 °C. The mixture was stirred for 45 minutes at 50 °C under N_2 atmosphere. A suspension of 0.65 g of 7-diethylamino-chromene-2-one in 3 mL of dry DMF was added, and the mixture warmed to 60 °C for 2 hours and poured out onto ice water, then left for another hour. Crystalline precipitate was filtered off, washed with water and dried, affording an orange solid. The product was purified by column chromatography on a solvent gradient of 2%-5% MeOH in DCM. Further purification by recrystallisation, afforded a yellow crystalline solid. (0.42 g, yield 57%)

^{1}H NMR (400 MHz, $CDCl_3$) δ:10.12 (s, 1H, OC-*H*), 8.24 (s, 1H), 7.42 (d, ^3J = 8.8, 1H, Ar-*H*), 6.66-6.63 (m, 1H, Ar-*H*), 6.48 (d, ^3J = 2.0, 1H, Ar-*H*), 3.51-3.45 (m, 4H, N-C*H*$_2$-CH_3), 1.26 (t, ^3J = 7.0, 6H, N-CH_2-C*H*$_3$).

7.33 Synthesis of 3-(imidazo[1,10]phenanthrolin-2-yl)-7-(diethylamino)chromen-2-one [208]

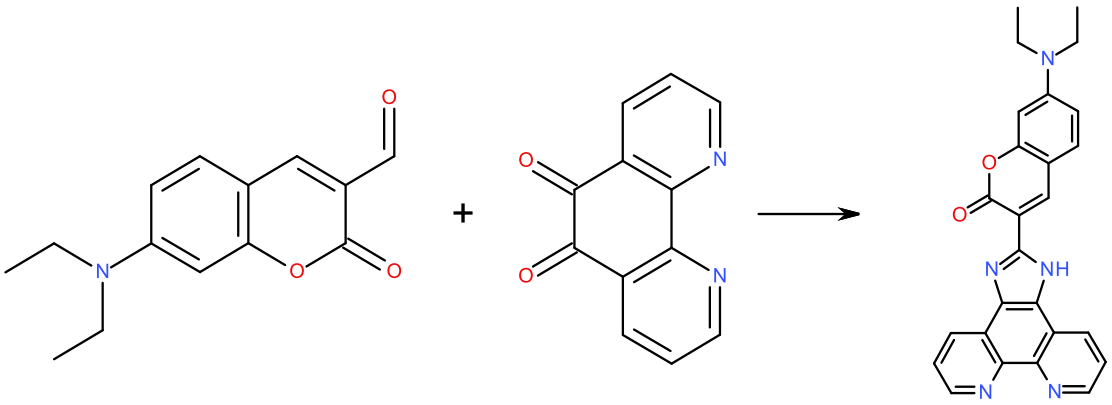

7-Diethylamino-2-oxo-2H-chromene-3-carboxyldehyde (128 mg, 0.68 mmol), 1,10-phenanthroline-5,6-dione (104 mg, 0.5 mmol), and ammonium acetate (805 mg, 11.3 mmol) were dissolved in glacial acetic acid (13 mL). The mixture was heated to reflux for 6 h under N_2 atmosphere. The colour of the mixture turned to orange. After completion of the reaction, the mixture was cooled to room temperature, and concentrated $NH_3 \cdot H_2O$ was added until the pH of the mixture was brought to about 7.0 to give a yellow precipitate. The precipitate was filtered, washed with water, and then dried under vacuum overnight. The crude product was further purified by column chromatography (silica gel, 10% MeOH in DCM). (167 mg, yield: 77%)

^{1}H NMR (400 MHz, $CDCl_3$) δ:9.16 (d, ^3J = 4.2, 2H, Ar-*H*), 8.99 (s, 1H, Ar-*H*), 8.78 (d, ^3J = 5.8, 2H, Ar-*H*), 7.72–7.69 (m, 2H, Ar-*H*), 7.48 (d, ^3J = 8.0, 1H, Ar-*H*), 6.66–6.63 (m, 1H, Ar-*H*), 6.50 (d, ^3J = 2.3, 1H, Ar-*H*), 3.48–3.43 (m, 4H, N-CH_2-CH_3), 1.26 (t, ^3J = 7.0, 6H, N-CH_2-CH_3).

7.34 General synthesis of $[Ir(2a\text{-}h)_2Cl]_2$

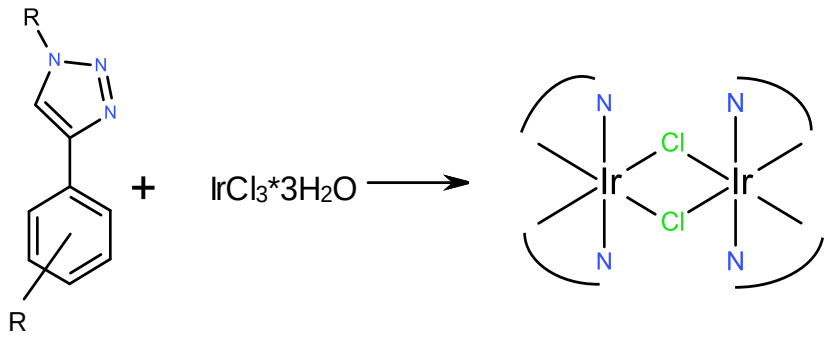

353 mg $IrCl_3{:}3H_2O$ (1 mmol) were dissolved in 35 mL 2-ethoxyethanol:H_2O 3:1 in 2 necked RBF. Degassed with N_2 at 80°C for 20 minutes. 2 equivalents of the corresponding triazole (**2a-h**) were added and heated to reflux temperature for 4 hours. The solution was reduced to a minimum volume under vacuum and recrystallized from DCM/Hexane. The dimers were used without further characterization or purification.

7.35 Synthesis of 2.1 [Ir(phenylpyridine)$_2$(4,4'-dicarboxybipyridine)]PF_6 (2.1) [77]

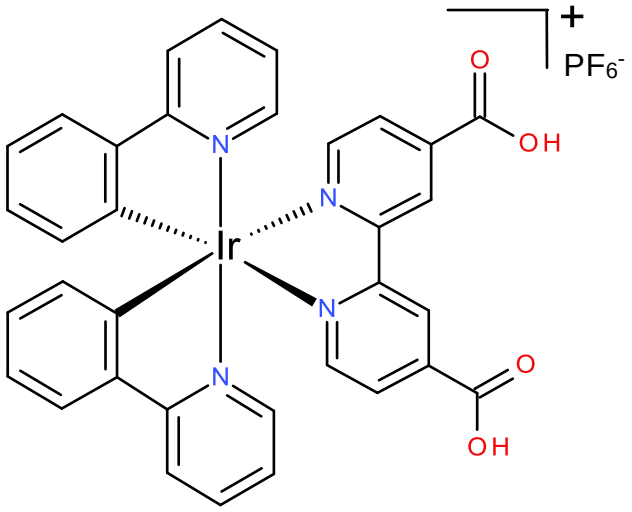

A solution of 2,2'-bipyridine-4,4'-dicarboxylic acid (0.025 g, 0.1 mmol) and TBAOH 1M (0.2 mL) in methanol was added to a solution of $[Ir(ppy)_2(Cl)]_2$ (0.044 g, 0.05 mmol) in a mixture of CH_2Cl_2/MeOH (20 mL, 2:1 v/v) and heated at reflux under nitrogen atmosphere. After 6 hrs, the orange solution was cooled to room temperature. The solution was evaporated to dryness under reduced pressure. The crude solid was dissolved in a minimal amount of methanol and HPF_6 was added to precipitate the product. The solution was concentrated and the solid was filtered over a porous glass frit, washed with water and ether and then dried yielding a red product. The product was recrystallised with acetonitrile/ether. (Yield 58.9%)

^{1}H NMR (400 MHz, CD_3CN) δ:9.06 (s, 2H, Bpy-*H*); 8.19 (d, ^3J = 5.62, 2H, Bpy-*H*); 8.10 (d, ^3J = 8.24, 2H, Ppy-*H*); 7.98 (d, ^3J = 5.62, 2H, Bpy-*H*); 7.88 (t, ^3J = 8.98, 2H, Ppy-*H*); 7.85 (d, ^3J = 8.24, 2H, Ppy-*H*); 7.59 (d, ^3J = 5.62, 2H, Ppy-*H*); 7.09 (t, ^3J = 7.85, 2H, Ppy-*H*); 7.03 (t, ^3J = 6.36, 2H, Ppy-*H*); 6.96 (t, ^3J = 7.48, 2H, Ppy-*H*); 6.29 (d, ^3J = 7.53, 2H, Ppy-*H*).

MS (ESI): *m/z* calcd for $[C_{34}H_{24}IrN_4O_4]^+$ 745.17, found 745.1 (M^+)

7.36 Synthesis of [Ir(1-benzyl-4-(2-nitrophenyl)triazole)$_2$(4,4'-dicarboxybipyridine)]PF_6 (AS1)

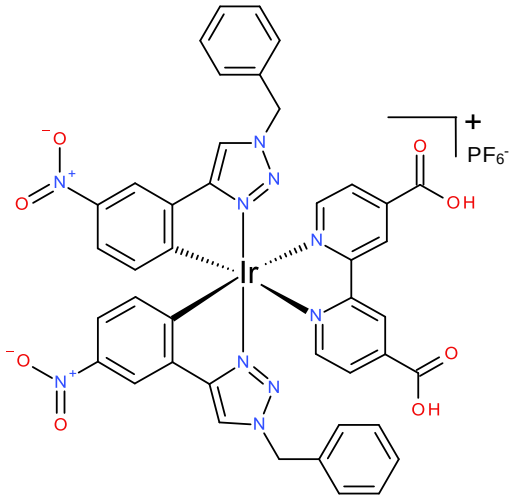

A solution of 2,2'-bipyridine-4,4'-dicarboxylic acid (0.025 g, 0.1 mmol) and TBAOH 1M (0.2 mL) in methanol was added to a solution of [Ir(1-benzyl-4-(2-nitrophenyl)triazole)$_2$(Cl)]$_2$ (0.078 g, 0.05 mmol) in a mixture of CH_2Cl_2/MeOH (20 mL, 2:1 v/v) and heated at reflux under nitrogen atmosphere. After 6 hrs, the yellow/brown solution was cooled to room temperature. The solution was evaporated to dryness under reduced pressure. The crude solid was purified by column on silica eluted with MeCN:H_2O:KNO_3 7:1:0.5. Three main fractions were isolated. The yellow fraction was dried under vacuum, redissolved in acetonitrile and filtered. The solution was dried again and the solid was dissolved in a minimal amount of methanol and HPF_6 was added to precipitate the product. The solution was concentrated and the solid was filtered over a porous glass frit, washed with water and ether and then dried yielding a yellow product. (Yield 8.7%)

^{1}H NMR (400 MHz, CD_3CN) δ:9.00 (s, 2H, Bpy-*H*); 8.44 (s, 2H, Ph-*H*); 8.36 (s, 2H, Tz-*H*); 8.20 (d, ^3J = 5.60, 2H, Bpy-*H*); 7.92 (d, ^3J = 5.39, 2H, Bpy-*H*); 7.71 (d, ^3J = 8.50, 2H, Ph-*H*); 7.41-7.39 (m, 6H, CH_2-Ph-*H*); 7.26 (d, ^3J = 4.48, 4H, CH_2-Ph-*H*); 6.50 (d, ^3J = 8.45, 2H, Ph-*H*); 5.5 (d, ^2J = 4.81, 4H, C*H*$_2$-Ph).

[Low solubility] ^{13}C {^{1}H} NMR (400 MHz, CD_3OD) δ:168.31, 158.30, 156.70, 155.35, 144.80, 137.04, 134.19, 132.69, 128.83, 128.73, 127.86, 126.56, 123.08, 122.32, 116.55, 29.30.

HRMS (ESI) *m/z* calcd for $[C_{42}H_{30}IrN_{10}O_8]^+$ 993.1877, found 993.1831 $(M)^+$

7.37 Synthesis of [Ir(1-benzyl-4-(4-nitrophenyl)triazole)$_2$(4,4'-dicarboxybipyridine)]PF_6 (AS2)

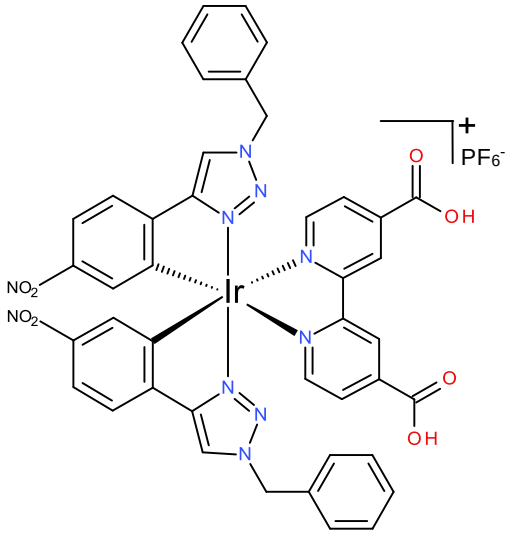

A solution of 2,2'-bipyridine-4,4'-dicarboxylic acid (0.025 g, 0.1 mmol) and TBAOH 1M (0.2 mL) in methanol was added to a solution of [Ir(1-benzyl-4-(4-nitrophenyl)triazole)$_2$(Cl)]$_2$ (0.078 g, 0.05 mmol) in a mixture of CH_2Cl_2/MeOH (20 mL, 2:1 v/v) and heated at reflux under nitrogen atmosphere. After 6 hrs, the yellow/brown solution was cooled to room temperature. The solution was evaporated to dryness under reduced pressure. The crude solid was purified by column on silica eluted with MeCN:H_2O:KNO_3 7:1:0.5. The yellow fraction was dried under vacuum, redissolved in acetonitrile and filtered. The solution was dried again and the solid was dissolved in a minimal amount of methanol and HPF_6 was added to precipitate the product. The solution was concentrated and the solid was filtered over a porous glass frit, washed with water and ether and then dried yielding a dark yellow product. (yield 14.3%)

^{1}H NMR (400 MHz, CD_3OD) δ:8.93 (s, 2H, Bpy-*H*); 8.55 (s, 2H, Tz-*H*); 8.05 (d, ^3J = 5.62, 2H, Bpy-*H*); 7.79 (dd, ^3J = 8.28, ^4J = 2.25, 2H, Ph-*H*); 7.77 (d, ^3J = 5.12, 2H, Bpy-*H*); 7.67 (d, ^3J = 8.37, 2H, Ph-*H*); 7.34-7.26 (m, 6H, CH_2-Ph-*H*); 7.16 (d, ^3J = 6.95, 4H, CH_2-Ph-*H*); 6.94 (d, ^3J = 2.24, 2H, Ph-*H*); 5.52 (dd, ^2J = 2.8, ^3J = 1.5, 4H, C*H*$_2$-Ph).

[Low solubility] ^{13}C {^{1}H} NMR not recorded

HRMS (ESI): *m/z* calcd for $[C_{42}H_{30}IrN_{10}O_8]^+$ 993.1877, found 994.9711 $(M+H)^+$

7.38 Synthesis of [Ir(1-benzyl-4-(phenyl)triazole)$_2$(4,4'-dicarboxybipyridine)]PF_6 (AS3)

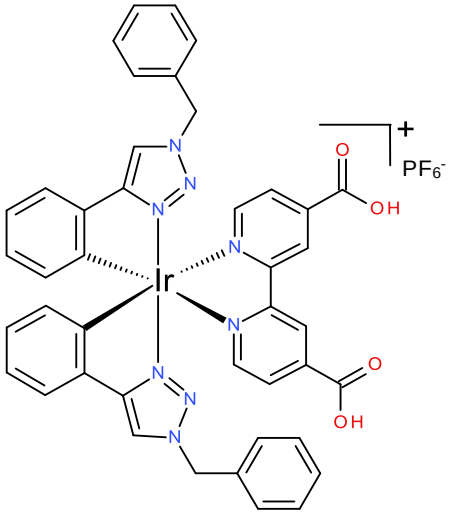

A solution of 2,2'-bipyridine-4,4'-dicarboxylic acid (0.025 g, 0.1 mmol) and TBAOH 1M (0.2 mL) in methanol was added to a solution of [Ir(1-benzyl-4-(phenyl)triazole)$_2$(Cl)]$_2$ (0. 07 g, 0.05 mmol) in a mixture of CH_2Cl_2/MeOH (20 mL, 2:1 v/v) and heated at reflux under nitrogen atmosphere. After 6 hrs, the orange solution was cooled to room temperature. The solution was evaporated to dryness under reduced pressure. The crude solid was purified by column on silica eluted with MeCN:H_2O:KNO_3 7:1:0.5. Three main fractions were isolated. The orange fraction was dried under vacuum, redissolved in acetonitrile and filtered. The solution was dried again and the solid was dissolved in a minimal amount of methanol and HPF_6 was added to precipitate the product. The solution was concentrated and the solid was filtered over a porous glass frit, washed with water and ether and then dried yielding a pale orange product. (yield 24%)

^{1}H NMR (400 MHz, CD_3CN) δ:8.94 (s, 2H, Bpy-*H*); 8.31 (d, ^3J = 5.52, 2H, Bpy-*H*); 8.12 (s, 2H, Tz-*H*); 7.93 (dd, ^3J = 5.57, ^4J = 1.49, 2H, Bpy-*H*); 7.53 (d, ^3J = 7.49, ^4J = 0.96, 2H, Ph-*H*); 7.38-7.36 (m 6H, CH_2-Ph-*H*); 7.23-7.21 (m 4H, CH_2-Ph-*H*); 7.01 (td, ^3J = 7.54, ^4J = 1.01, 2H, Ph-*H*); 6.87 (td, ^3J = 7.48, ^4J = 1.33, 2H, Ph-*H*); 6.22 (d, ^3J = 7.39, 2H, Ph-*H*); 5.45 (d, ^2J = 1.93, 4H, C*H*$_2$-Ph).

^{13}C {^{1}H} NMR (400 MHz, CD_3CN) δ:164.47 157.57 157.50 152.97 145.77 140.71 136.19 134.85 132.85 129.56 129.38 128.98 128.62 127.65 124.10 123.59 123.15 120.60 55.82

MS (ESI): *m/z* calcd for $[C_{42}H_{32}IrN_8O_4]^+$ 905.24, found 905.2 $(M)^+$

7.39 Synthesis of [Ir((1-benzyltriazol-4-yl)-2-thienyl)$_2$ (4,4'-dicarboxybipyridine)]PF_6 (AS4)

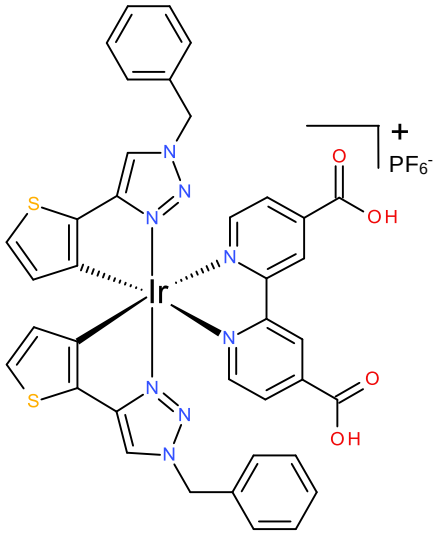

A solution of 2,2'-bipyridine-4,4'-dicarboxylic acid (0.0125 g, 0.05 mmol) and TBAOH 1M (0.1 mL) in methanol was added to a solution [Ir((1-benzyltriazol-4-yl)-(2-thienyl))$_2$Cl]$_2$ (0.043 g, 0.025 mmol) in a mixture of CH_2Cl_2/MeOH (10 mL, 2:1 v/v) and heated at reflux under nitrogen atmosphere. After 6 hrs, the brown solution was cooled to room temperature. The solution was dried and the solid was dissolved in a minimal amount of methanol and HPF_6 was added to precipitate the product. The solution was concentrated and the solid was filtered over a porous glass frit, washed with water and ether and then dried yielding a pale brown product. The product was recrystallised with acetonitrile/ether. It was not possible to purify the complex because of its low solubility. (yield 35%)

^{1}H NMR (400 MHz, CD_3OD) δ:9.05 (s, 2H, Bpy-*H*); 8.30 (d, ^3J = 5.45, 2H, Bpy-*H*); 8.11 (s, 2H, Tz-*H*); 8.04 (d, ^3J = 5.56, 2H, Bpy-*H*); 7.4 (d, ^3J = 4.91, 2H, Th-*H*); 7.35-7.30 (m, 6H, CH_2-Ph-*H*); 7.24 (d, ^3J = 2.76, 4H, CH_2-Ph-*H*); 6.12 (d, ^3J = 4.56, 2H, Th-*H*); 5.53 (d, ^3J = 8.29, 4H, C*H*$_2$-Ph).

[Low solubility] ^{13}C {^{1}H} NMR not recorded

7.40 Synthesis of [Ir(1-benzyl-4-(1-naphthyl)triazole)$_2$(4,4'-dicarboxybipyridine)]PF_6 (AS5)

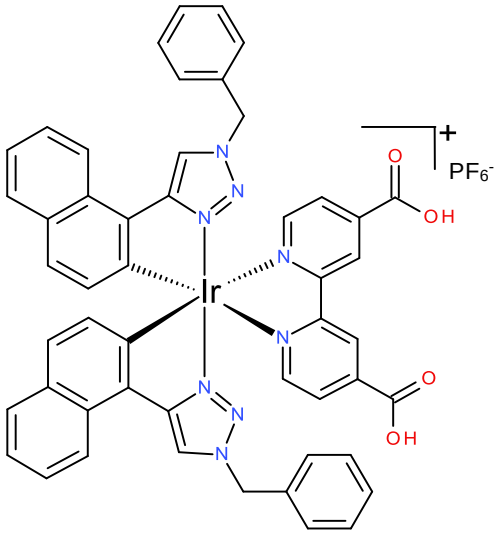

A solution of 2,2'-bipyridine-4,4'-dicarboxylic acid (0.025 g, 0.1 mmol) and TBAOH 1M (0.2 mL) in methanol was added to a solution of [Ir(1-benzyl-4-(1-naphthyl)triazole)$_2$(Cl)]$_2$ (0.080 g, 0.05 mmol) in a mixture of CH_2Cl_2/MeOH (20 mL, 2:1 v/v) and heated at reflux under nitrogen atmosphere. After 6 hrs, the yellow/orange solution was cooled to room temperature. The solution was evaporated to dryness under reduced pressure. The crude solid was purified by column on silica eluted with MeCN:H_2O:KNO_3 7:1:0.5. Three main fractions were isolated. The orange fraction was dried under vacuum, redissolved in acetonitrile and filtered. The solution was dried again and the solid was dissolved in a minimal amount of methanol and HPF_6 was added to precipitate the product. The solution was concentrated and the solid was filtered over a porous glass frit, washed with water and ether and then dried yielding an orange product. (yield 12%)

^{1}H NMR (400 MHz, CD_3CN) δ:8.98 (s, 2H, Bpy-*H*); 8.64 (s, 2H, Tz-*H*); 8.22 (d, ^3J = 5.42, 2H, Bpy-*H*); 8.10 (d, ^3J = 8.46, 2H, Napht-*H*); 7.85 (d, ^3J = 5.64, 2H, Bpy-*H*); 7.81 (d, ^3J = 8.02, 2H, Napht-*H*); 7.56 (t, ^3J = 7.34, 2H, Napht-*H*); 7.40-7.36 (m, 6H, CH_2-Ph-*H*); 7.27 (d, ^3J = 4.68; 4H, CH_2-Ph-*H*); 6.50 (d ^3J = 8.19, 2H, Napht-*H*); 5.56-5.53 (m, 4H, C*H*$_2$-Ph).

^{13}C {^{1}H} NMR (400 MHz, CD_3OD) δ:168.71, 156.88, 156.39, 151.14, 149.83, 148.41, 148.40, 134.84, 131.09, 131.05, 129.43, 129.00, 128.72, 128.48, 127.87, 127.44, 126.41, 126.15, 123.04, 122.72, 121.73, 121.25, 55.00.

MS (ESI): *m/z* calcd for $[C_{50}H_{40}IrN_8O_4]^+$ 1005.28, found 1005.2 $(M)^+$

7.41 Synthesis of [Ir(1-benzyl-4-(2-naphthyl)triazole)$_2$(4,4'-dicarboxybipyridine)]PF_6 (AS6)

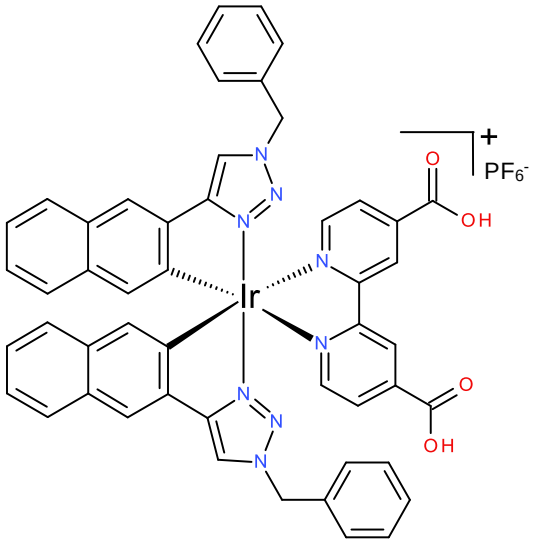

A solution of 2,2'-bipyridine-4,4'-dicarboxylic acid (0.025 g, 0.1 mmol) and TBAOH 1M (0.2 mL) in methanol was added to a solution of [Ir(1-benzyl-4-(2-naphthyl)triazole)$_2$(Cl)]$_2$ (0.080 g, 0.05 mmol) in a mixture of CH_2Cl_2/MeOH (20 mL, 2:1 v/v) and heated at reflux under nitrogen atmosphere. After 6 hrs, the orange solution was cooled to room temperature. The solution was evaporated to dryness under reduced pressure. The crude solid was purified by column on silica eluted with MeCN:H_2O:KNO_3 7:1:0.5. Three main fractions were isolated. The orange fraction was dried under vacuum, redissolved in acetonitrile and filtered. The solution was dried again and the solid was dissolved in a minimal amount of methanol and HPF_6 was added to precipitate the product. The solution was concentrated and the solid was filtered over a porous glass frit with water and ether and then dried yielding a pale orange product. (yield 10%)

^{1}H NMR (400 MHz, CD_3CN) δ:9.00 (s, 2H, Bpy-*H*); 8.44 (d, ^3J = 5.70, 2H, Bpy-*H*); 8.35 (s, 2H, Tz-*H*); 8.07 (s, 2H, Napht-*H*); 7.90 (d, ^3J = 5.49, 2H, Bpy-*H*); 7.75 (d, ^3J = 7.60, 2H, Napht-*H*); 7.45-7.43 (m, 6H, CH_2-Ph-*H*); 7.34-7.32 (m, 10H, Napht-*H*&CH_2-Ph-*H*); 6.56 (s, 2H, Napht-*H*); 5.55-5.53 (m, 4H, C*H*$_2$-Ph).

^{13}C {^{1}H} NMR (400 MHz, DMSO-d_6) δ:165.82, 156.62, 156.20, 150.98, 150.91, 143.20, 136.00, 135.59, 134.00, 130.63, 129.57, 129.46, 129.09, 128.42, 128.18, 127.08, 126.43, 126.08, 124.23, 122.97, 122.28, 121.34, 55.16.

MS (ESI): *m/z* calcd for $[C_{50}H_{40}IrN_8O_4]^+$ 1005.28 found 1005.2 $(M)^+$

7.42 Synthesis of [Ir(1-propyl-4-(tolyl)triazole)$_2$(4,4'-dicarboxybipyridine)]PF_6 (AS7)

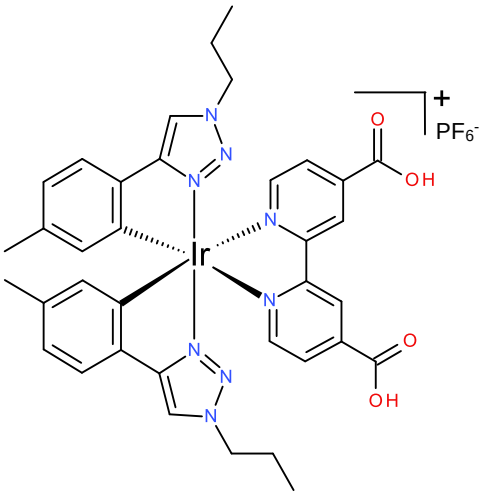

A solution of 2,2'-bipyridine-4,4'-dicarboxylic acid (0.025 g, 0.1 mmol) and TBAOH 1M (0.2 mL) in methanol was added to a solution of [Ir(1-propyl-4-(phenyl)triazole)$_2$(Cl)]$_2$ (0.080 g, 0.05 mmol) in a mixture of CH_2Cl_2/MeOH (20 mL, 2:1 v/v) and heated at reflux under nitrogen atmosphere. After 6 hrs, the orange solution was cooled to room temperature. The crude solid was purified by column on silica eluted with MeCN:H_2O:KNO_3 7:1:0.5. Three main fractions were isolated. The orange fraction was dried under vacuum, redissolved in acetonitrile and filtered. The solution was dried again and the solid was dissolved in a minimal amount of methanol and HPF_6 was added to precipitate the product. The solution was concentrated and the solid was filtered over a porous glass frit, washed with water and ether and then dried yielding a red product. The product was recrystallised with acetonitrile/ether. (yield 26%)

^{1}H NMR (400 MHz, CD_3CN) δ:9.00 (s, 2H, Bpy-*H*); 8.33 (d, ^3J = 5.47, 2H, Bpy-*H*); 8.07 (s, 2H, Tz-*H*); 7.94 (dd, ^3J = 5.61, ^4J = 1.44, 2H, Bpy-*H*); 7.44 (d, ^3J = 7.62, 2H, Ph-*H*); 6.86 (dd, ^3J = 7.77, ^4J = 1.01, 2H, Ph-*H*); 6.07 (s, 2H, Ph-*H*); 4.22 (t, ^3J = 6.89, 4H, CH_2-CH_2-CH_3); 2.15 (s, 6H, Ph-CH_3); 1.83 (sex, ^3J = 7.68, 4H, CH_2-CH_2-CH_3); 0.83 (t, ^3J = 7.52, 6H, CH_2-CH_2-CH_3).

^{13}C {^{1}H} NMR (400 MHz, CD_3CN) δ:164.35, 157.60, 157.07, 153.02, 152.97, 152.63, 145.89, 136.40, 132.88, 128.88, 127.66, 124.10, 123.55, 122.98, 120.35, 53.96, 23.45, 10.47

MS (ESI): *m/z* calcd for $[C_{36}H_{36}IrN_8O_4]^+$ 837.24, found 837.20 $(M)^+$

7.43 Synthesis of [Ir(1-propyl-4-(phenyl)triazole)$_2$(4,4'-dicarboxybipyridine)]PF_6 (AS8)

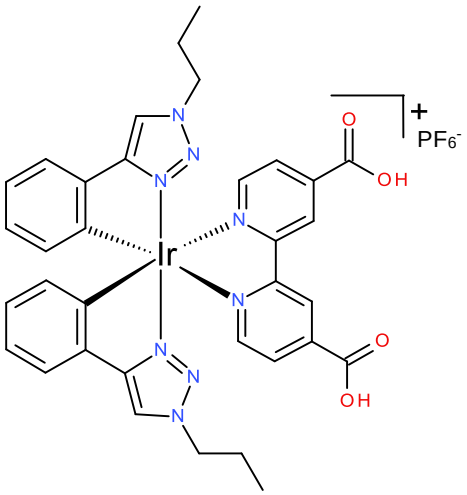

A solution of 2,2'-bipyridine-4,4'-dicarboxylic acid (0.025 g, 0.1 mmol) and TBAOH 1M (0.2 mL) in methanol was added to a solution of [Ir(1-propyl-4-(phenyl)triazole)$_2$(Cl)]$_2$ (0.080 g, 0.05 mmol) in a mixture of CH_2Cl_2/MeOH (20 mL, 2:1 v/v) and heated at reflux under nitrogen atmosphere. After 6 hrs, the orange solution was cooled to room temperature. The crude solid was purified by column on silica eluted with MeCN:H_2O:KNO_3 7:1:0.5. Three main fractions were isolated. The orange fraction was dried under vacuum, redissolved in acetonitrile and filtered. The solution was dried again and the solid was dissolved in a minimal amount of methanol and HPF_6 was added to precipitate the product. The solution was concentrated and the solid was filtered over a porous glass frit, washed with water and ether and then dried yielding a red product. The product was recrystallised with acetonitrile/ether. (yield 15%)

^{1}H NMR (400 MHz, CD_3CN) δ:8.99 (s, 2H, Bpy-*H*); 8.35 (d, ^3J = 5.55, 2H, Bpy-*H*); 8.13 (s, 2H, Tz-*H*); 7.95 (d, ^3J = 5.55, 2H, Bpy-*H*); 7.57 (d, ^3J = 7.49, 2H, Ph-*H*); 7.03 (t, ^3J = 7.31, 2H, Ph-*H*); 6.90 (t, ^3J = 7.48, 2H, Ph-*H*); 6.28 (d, ^3J = 7.42, 2H, Ph-*H*); 4.22 (t, ^3J = 6.91, 4H, CH_2-CH_2-CH_3); 1.83 (sex, ^3J = 7.52, 4H, CH_2-CH_2-CH_3); 0.82 (t, ^3J = 7.28, 6H, CH_2-CH_2-CH_3).

^{13}C {^{1}H} NMR (400 MHz, CD_3CN) δ:164.35, 157.60, 157.07, 152.97, 145.89, 136.40, 132.95, 132.88, 128.88, 127.66, 124.10, 123.55, 122.98, 120.35, 53.96, 23.45, 10.47.

MS (ESI): *m/z* calcd for $[C_{34}H_{32}IrN_8O_4]^+$ 809.21, found 809.20 $(M)^+$

7.44 Synthesis of [Ir(4-(2-pyridyl)benzoic acid)$_2$Cl]$_2$

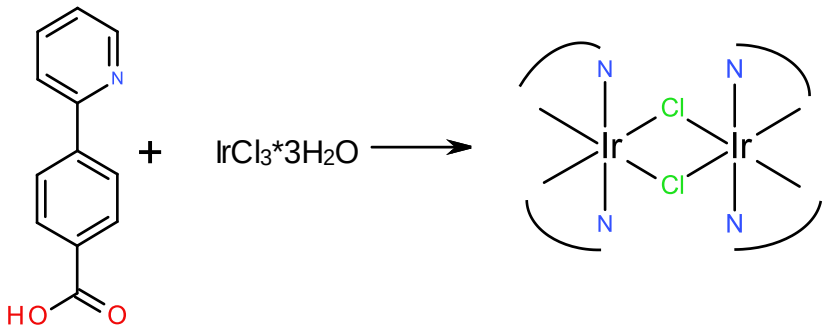

353 mg of $IrCl_3$:3H_2O (1 mmol) were dissolved in 35 mL 2-ethoxyethanol:H_2O 3:1 in 2 necked round bottom flask and degassed with N_2 at 80°C for 20 minutes. 2 equivalents (400 mg) of 4-(2-pyridyl)benzoic acid were added and heated to reflux temperature for 4 hours. The solution was reduced to a minimal volume and recrystallized from DCM/Hexane. The dimer was used without any further characterization or purification.

7.45 Synthesis of [Ir(pyba)$_2$(2,2'-bipyridine)]PF$_6$ (AS9)

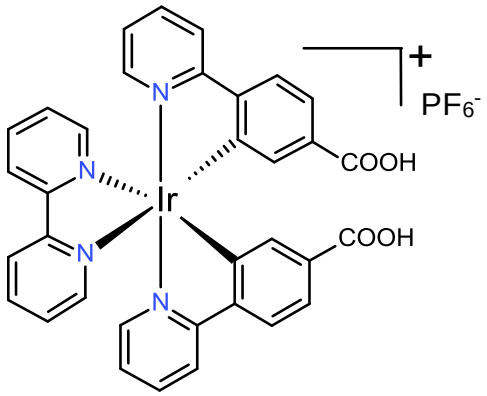

2,2'-bipyridine (0.025 g, 0.16 mmol) was dissolved in DCM:MeOH 2:1 (6 mL) and [Ir(pyba)$_2$(Cl)]$_2$ (0.100 g, 0.08 mmol) was added. The mixture was heated at reflux under nitrogen atmosphere, in the dark. After 6 hrs, the yellow solution was cooled to room temperature. The crude solid was purified by column on silica eluted with MeCN:H_2O:KNO_3 7:1:0.5. The yellow fraction was dried under vacuum, redissolved in acetonitrile and filtered. The solution was dried again and the solid was dissolved in a minimal amount of methanol and NH_4PF_6 (130 mg, 0.9 mmol) was added allowed to stir overnight. The solution was left in the fridge for two hours and then filtered on sintered glass. A yellow powder was collected by filtration. (42 mg, yield 30%)

^{1}H NMR (400 MHz, CD_3CN) δ:8.55 (d, ^3J = 8.36, 2H, Bpy-*H*); 8.20 (d, ^3J = 8.36, 2H, Pyba-*H*); 8.16 (t, ^3J = 6.18, 2H, Bpy-*H*); 8.00-7.94 (m, 4H, Bpy-*H*&Pyba-*H*); 7.93 (d, ^3J = 8.36, 2H, Pyba-*H*); 7.71-7.67 (m, 4H, Pyba-*H*); 7.51 (t, ^3J = 6.84, 2H, Bpy-*H*); 7.17 (t, ^3J = 6.59, 2H, Pyba-*H*); 6.89 (s, 2H, Pyba-*H*).

^{13}C {^{1}H} NMR (400 MHz, CD_3CN): 167.15, 166.58, 156.29, 151.48, 150.21, 149.79, 149.29, 140.14, 139.61, 132.63, 131.29, 129.10, 125.32, 125.30, 125.26, 124.85, 121.70.

MS (ESI) *m/z* calcd for $[C_{34}H_{24}IrN_4O_4]^+$ 745.1426, found 745.1 (M^+).

7.46 Synthesis of [Ir(pyba)$_2$(1,10-phenantroline)]PF$_6$ (AS10)

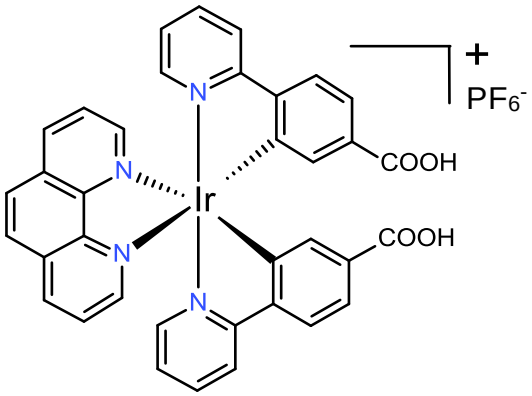

1,10-phenantroline (0.027 g, 0.16 mmol) was dissolved in DCM:MeOH 2:1 (20 cm^3) and [Ir(pyba)$_2$(Cl)]$_2$ (0.100 g, 0.08 mmol) was added. The mixture was heated at reflux under nitrogen atmosphere, in the dark. After 6 hrs, the yellow solution was cooled to room temperature The crude solid was purified by column on silica eluted with MeCN:H_2O:KNO_3 7:1:0.5. The yellow fraction was dried under vacuum, redissolved in acetonitrile and filtered. The solution was dried again and the solid was dissolved in a minimal amount of methanol and NH_4PF_6 (130 mg, 0.9 mmol) was added allowed to stir overnight. The solution was left in the fridge for two hours and then filtered on sintered glass. A yellow powder was collected by filtration. The product was recrystallized from acetonitrile/diethylether to yield a bright yellow microcrystalline powder. (20 mg, yield 13%)

^{1}H NMR (400 MHz, CD_3CN) δ:8.72 (dd, ^3J = 8.23, ^4J = 1.27, 2H, Phen-*H*); 8.31 (dd, ^3J = 8.5, ^4J = 1.27, 2H, Phen-*H*); 8.26 (s, 2H, Phen-*H*); 8.19 (d, ^3J = 8.00, 2H, Pyba-*H*); 7.96 (d, ^3J = 8.23, 2H, Pyba-*H*); 7.90 (td, ^3J = 7.30, ^4J = 1.51, 2H, Phen-*H*); 7.86 (dd, ^3J = 8.24, ^4J = 5.03, 2H, Phen-*H*); 7.72 (dd, ^3J = 8.23, ^4J = 1.62, 2H, Pyba-*H*); 7.51 (dd, ^3J = 5.45, ^4J = 0.70, 2H, Pyba-*H*); 7.00 (td, ^3J = 5.33, ^4J = 1.27, 4H, Pyba-*H*)

^{13}C {^{1}H} NMR (400 MHz, CD_3CN) δ:166.62, 152.12, 150.38, 149.55, 149.29, 147.27, 139.50, 139.31, 132.83, 132.23, 128.86, 127.98, 127.41, 126.65, 125.21, 125.15, 124.92, 121.6.

MS (ESI) *m/z* calcd for $[C_{36}H_{24}IrN_4O_4]^+$ 769.142, found 769.2 (M^+).

7.47 Synthesis of [Ir(pyba)$_2$(2,5-bis(2-pyridyl)pyrazine)]PF$_6$ (AS11)

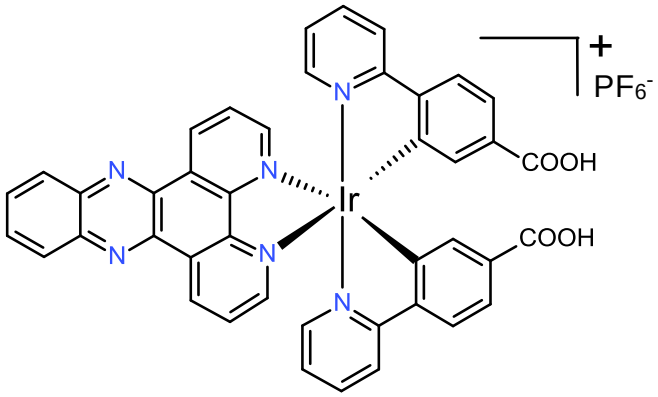

2,5-bis(2-pyridyl)pyrazine (0.043 g, 0.154 mmol) were dissolved in DCM:MeOH 2:1 (6 mL) and [Ir(pyba)$_2$(Cl)]$_2$ (0.100 g, 0.080 mmol) was added. The mixture was heated at reflux under nitrogen atmosphere, in the dark. After 6 hrs, the yellow/brown solution was cooled to room temperature overnight. The solution was evaporated to dryness under reduced pressure. The crude product was purified by silica gel column chromatography using a mixture of chloroform and methanol 1:1 as eluent, followed by a mixture of MeCN:H_2O:KNO_3 7:1:0.5. The main yellow fraction was then dried, redissolved in acetonitrile and filtered. The filtrate was dried and redissolved in a minimum amount of methanol, NH_4PF_6 (130 mg, 0.9 mmol) was added. The solution was left in the fridge overnight. The solution was left in the fridge for two hours and then filtered on sintered glass. A brown powder was collected by filtration. The product was recrystallized from acetonitrile/diethylether to yield a dark yellow powder. (28 mg, yield 17.8 %)

^{1}H NMR (400 MHz, CD_3CN) δ:9.80 (d, ^3J = 8.22, 2H, Dppz-*H*); 8.51-8.47 (m, 2H, Dppz-*H*); 8.41 (d, ^3J = 4.40, 2H, Dppz-*H*); 8.23 (d, ^3J = 8.03, 2H, Pyba-*H*); 8.18-8.14 (m, 2H, Dppz-*H*); 8.04-7.90 (m, 6H, Dppz-*H*&Pyba-*H*); 7.75 (d, ^3J = 8.22, 2H, Pyba-*H*); 7.71 (d, ^3J = 4.97, 2H, Pyba-*H*); 7.05 (t, ^3J = 6.50, 2H, Pyba-*H*); 7.00 (s, 2H, Pyba-*H*).

[Low solubility] ^{13}C {^{1}H} NMR (400 MHz, CD_3CN): 166.05, 152.80, 150.07, 149.61, 148.92, 148.44, 142.80, 139.93, 139.11, 135.38, 132.57, 132.25, 131.34, 129.65, 128.39, 124.77, 124.67, 124.50, 121.16.

MS (ESI) calcd for $[C_{42}H_{26}IrN_6O_4]^+$ 871.1644, found 871.2 (M^+).

7.48 Synthesis of $[Ir(pyba)_2(4\text{-nitro-2,2'-bipyridine})]PF_6$ (AS12)

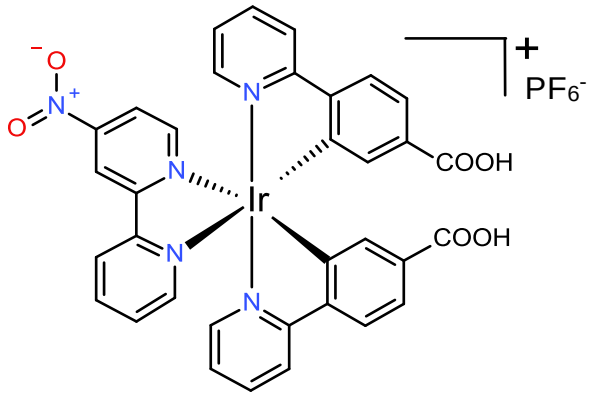

4-nitro-2,2'-bipyridine (0.031 g, 0.16 mmol) was dissolved in DCM:MeOH 2:1 (20 mL) and $[Ir(pyba)_2(Cl)]_2$ (0.100 g, 0.08 mmol) was added. The mixture was heated at reflux under nitrogen atmosphere, in the dark. After 6 hrs, the orange solution was cooled to room temperature. The solution was evaporated to dryness under reduced pressure. The crude product was purified by silica gel column chromatography using acetone as eluent, followed by a mixture of $MeCN:H_2O:KNO_3$ 7:1:0.5. The main gloving fraction was then dried, redissolved in acetonitrile and filtered. The filtrate was dried and redissolved in a minimum amount of methanol, NH_4PF_6 (130mg, 0.9 mmol) was added. The solution was left in the fridge overnight and then filtered on sintered glass. A red powder was collected by filtration. The product was recrystallized from acetonitrile/diethylether to yield an orange powder (28.6 mg, yield 20%)

^{1}H NMR (400 MHz, CD_3CN) δ:9.81 (d, ^3J = 1.88, 1H, Bpy-*H*); 8.77 (d, ^3J = 8.15, 1H, Bpy-*H*); 8.28 (d, ^3J = 5.95, 1H, Bpy-*H*); 8.26-8.20 (m, 3H, Bpy-*H*); 8.10 (dd, ^3J = 5.95, ^4J = 1.88, 1H, Bpy-*H*); 8.04 (d, ^3J = 5.33, 1H, Bpy-*H*); 8.01-7.92 (m, 4H, Pyba-*H*); 7.73-7.66 (m, 4H, Pyba-*H*); 7.60 (t, ^3J = 6.42, 1H, Bpy-*H*); 7.18 (t, ^3J = 6.42, 1H, Pyba-*H*); 7.16 (t, ^3J = 6.58, 1H, Pyba-*H*); 6.89 (d, ^3J = 1.10, 1H, Pyba-*H*); 6.85 (d, ^3J = 1.10, 1H, Pyba-*H*).

[Low solubility] ^{13}C {^{1}H} NMR (400 MHz, CD_3CN) δ:166.58, 165.90, 165.79, 159.63, 154.78, 154.24, 153.78, 151.35, 149.95, 149.79, 148.16, 148.47, 139.91, 139.33, 139.31, 132.14, 131.90, 130.94, 129.69, 126.13, 124.90, 124.84, 124.79, 124.77, 124.66, 124.58, 121.62, 121.31, 118.27.

MS (ESI) calcd for $[C_{34}H_{23}IrN_5O_6]^+$ 790.17, found 790.1 (M^+).

7.49 Synthesis of [Ir(pyba)$_2$(4',4-dinitro-2,2'-bipyridine)]PF$_6$ (AS13)

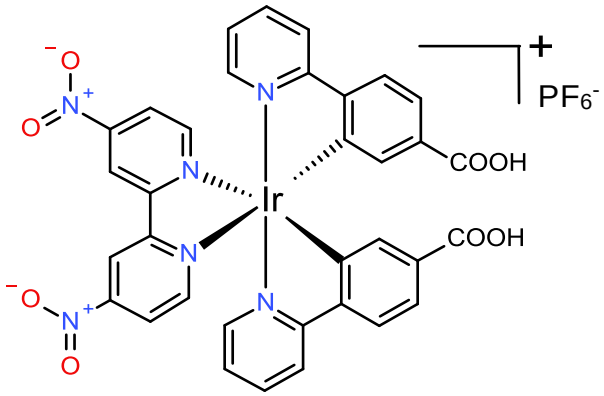

4',4-dinitro-2,2'-bipyridine (0.039 g, 0.16 mmol) was dissolved in DCM:MeOH 2:1 (20 mL) and [Ir(pyba)$_2$(Cl)]$_2$ (0.100 g, 0.08 mmol) was added. The mixture was heated at reflux under nitrogen atmosphere, in the dark. After 6 hrs, the dark orange solution was cooled to room temperature. The solution was evaporated to dryness under reduced pressure. The crude product was purified by silica gel column chromatography using acetone as eluent, followed by a mixture of MeCN:H_2O:KNO_3 7:1:0.5. The main gloving fraction was then dried, redissolved in acetonitrile and filtered. The filtrate was dried and redissolved in a minimum amount of methanol, NH_4PF_6 (130mg 0.9 mmol) was added. The solution was left in the fridge overnight and then filtered on sintered glass. A red powder was collected by filtration. The product was recrystallized from acetonitrile/diethylether to yield a dark red powder (40.3 mg, yield 25%)

^{1}H NMR (400 MHz, CD_3CN) δ:9.43 (s 2H, Bpy-*H*); 8.34 (d, ^3J = 6.03, 2H, Bpy-*H*); 8.23 (d, ^3J = 8.03, 2H, Pyba-*H*); 8.18 (dd, ^3J = 6.03, ^4J = 1.67, 2H, Bpy-*H*); 8.00 (t; ^3J = 8.03, 2H, Pyba-*H*); 7.98-7.95 (m, 2H, Pyba-*H*); 7.73 (d, ^3J = 8.03, 2H, Pyba-*H*); 7.67 (d, ^3J = 5.36, 2H, Pyba-*H*); 7.18 (t, ^3J = 6.19, 2H, Pyba-*H*); 6.85 (s, 2H, Pyba-*H*).

[Low solubility] ^{13}C {^{1}H} NMR (400 MHz, CD_3CN) δ:165.63, 157.76, 157.51, 155.05, 154.17, 154.13, 150.07, 150.04, 139.62, 139.22, 131.92, 131.12, 124.94, 124.92, 122.78, 121.48, 119.56.

MS (ESI) *m/z* calcd for $[C_{34}H_{22}IrN_6O_8]^+$ 835.1128, found 835.1 (M^+).

7.50 Synthesis of [Ir(pyba)$_2$(N,N'-bis(4-methoxyphenylimino)acenaphthene)]PF$_6$ (AS14)

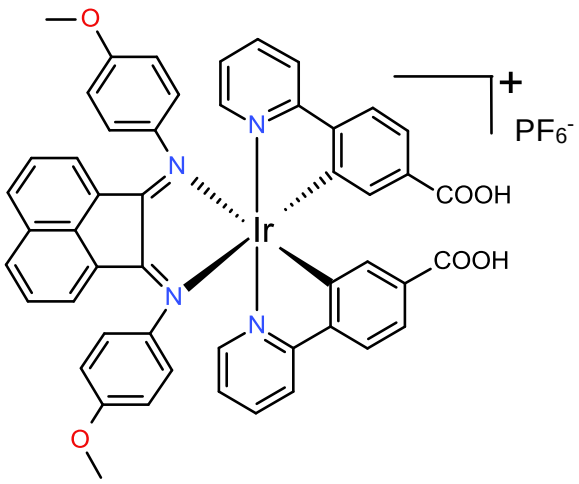

4-MeOPh-BIAN (0.063 g, 0.16mmol) was dissolved in DCM:MeOH 2:1 (6 cm^3) and [Ir(pyba)$_2$(Cl)]$_2$ (0.100 g, 0.08 mmol) was added. The mixture was heated at reflux under nitrogen atmosphere, in the dark. After 6 hrs, the brown solution was cooled to room temperature, and then dried under vacuum. The crude product was purified by silica gel column chromatography using acetone as eluent, followed by a mixture of MeCN:H_2O:KNO_3 7:1:0.5. The main dark fraction was then dried, redissolved in acetonitrile and filtered. The filtrate was dried and redissolved in a minimum amount of methanol, NH_4PF_6 (130 mg, 0.9 mmol) was added. The solution was left in the fridge overnight and then filtered on sintered glass. A brown powder was collected by filtration. The product was recrystallized from acetonitrile/diethylether to yield a brown powder. (35 mg, yield 21%)

^{1}H NMR (400 MHz, CD_3CN) δ: 8.84 (d, ^3J = 5.12 Hz, 2H, Pyba -*H*); 8.31 (d, ^3J = 8.28 Hz, 2H, BIAN-*H*); 8.07-8.01 (m, 4H, Pyba -*H*); 7.60 (t, ^3J = 7.84 Hz, 2H, BIAN-*H*); 7.52 (d, ^3J = 7.68 Hz, 2H, Pyba-*H*); 7.47-7.41 (m, 4H, Pyba-*H*); 7.35 (d, ^3J = 7.56 Hz, 2H, BIAN-*H*); 6.99 (bs, 2H, BIAN-*H*); 6.73 (s, 2H, Pyba-*H*); 6.63 (bs, 4H, BIAN-*H*); 6.11 (bs, 2H, BIAN-*H*); 3.74 (s, 6H, BIAN-C*H*$_3$).

^{13}C {^{1}H} NMR (400 MHz, CD_3CN) δ:173.23, 165.73, 159.33, 151.64, 148.12, 147.63, 139.34, 137.77, 131.92, 131.54, 131.28, 130.27, 128.92, 127.27, 125.12, 124.06, 123.84, 123.80, 120.66, 114.69, 55.34.

MS (ESI) *m/z* calcd for $[C_{50}H_{34}IrN_4O_6]^+$ 981.2264, found 981.2 (M^+).

7.51 Synthesis of [Ir(pyba)$_2$(N,N'-bis(phenylimino)acenaphthene)]PF$_6$ (AS15)

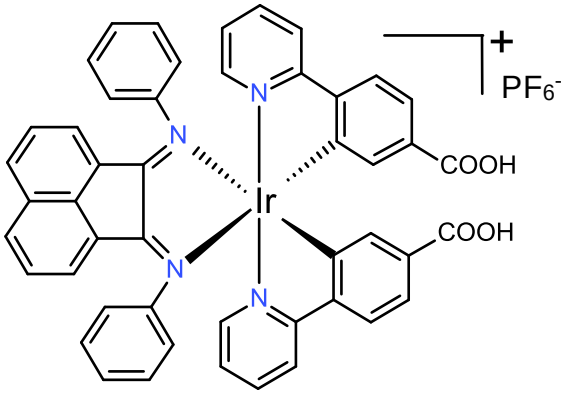

Ph-BIAN (0.054 g, 0.16mmol) was dissolved in DCM:MeOH 2:1 (6 cm^3) and [Ir(pyba)$_2$(Cl)]$_2$ (0.100 g, 0.08 mmol) was added. The mixture was heated at reflux under nitrogen atmosphere, in the dark. After 6 hrs, the dark solution was cooled to room temperature, and then dried under vacuum. The crude product was purified by silica gel column chromatography using acetone as eluent, followed by a mixture of MeCN:H_2O:KNO_3 7:1:0.5. The main gloving fraction was then dried, redissolved in acetonitrile and filtered. The filtrate was dried and redissolved in a minimum amount of methanol, NH_4PF_6 (130 mg, 0.9 mmol) was added. The solution was left in the fridge overnight and then filtered on sintered glass. A green powder was collected by filtration. The product was recrystallized from acetonitrile/diethylether to yield AS15 as a dark green powder. (35 mg, yield 21%)

^{1}H NMR (400 MHz, DMSO-d$_6$) δ:9.06 (d, ^3J = 5.49, 2H, Pyba-*H*); 8.40 (d, ^3J = 8.30, 2H, BIAN-*H*); 8.24 (d, ^3J = 7.60, 2H, Pyba-*H*); 8.18 (d, ^3J = 7.04, 2H, Pyba-*H*); 7.71-7.64 (m, 2H, BIAN-*H*); 7.63-7.53 (m, 4H, Pyba-*H*); 7.30-7.18 (m, 8H, Pyba-*H*&BIAN-*H*); 7.15-7.08 (m, 2H, BIAN-*H*); 7.03-6.95 (m, 2H, BIAN-*H*); 6.53 (d, ^3J = 6.25, 2H, Pyba-*H*); 6.05-5.93 (m, 2H, BIAN-*H*).

[Low solubility] ^{13}C {^{1}H} NMR not recorded

HRMS (ESI) *m/z* calcd for [$C_{48}H_{32}IrN_4O_4$]$^+$ 921.2052, found 921.2204 (M^+)

7.52 Synthesis of $[Ru(bpy)_2(1\text{-}[2,2'\text{-bipyridine-4-yl}]triazole\text{-}4,5\text{-}ethyldicarboxylate)](PF_6)_2$

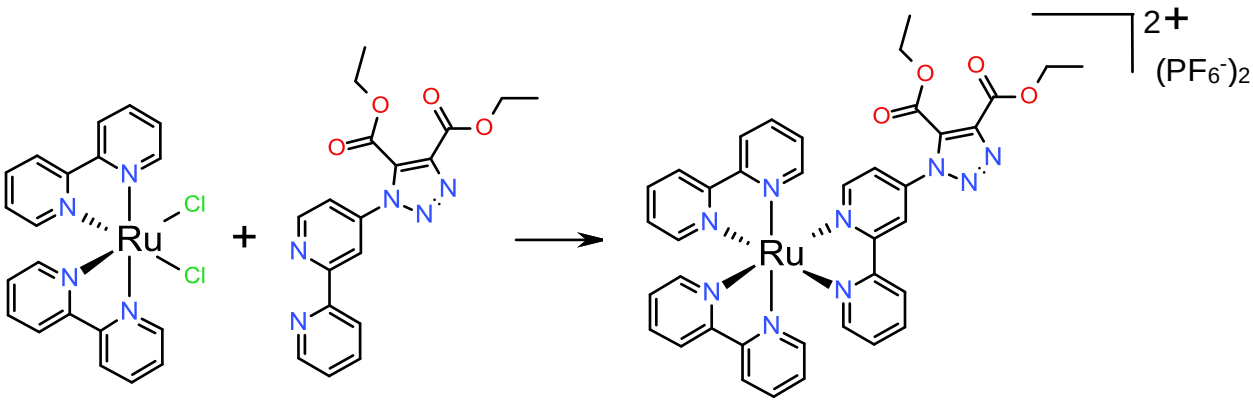

100 mg of $Ru(bpy)_2Cl_2$ were dissolved in EtOH (20 mL) together with 113 mg of dectzbpy. The solution was heated to reflux temperature overnight, under N_2 in the dark. The solvent was removed under reduced pressure and the resulting solid dissolved in MeOH, an excess of NH_4PF_6 was added and an orange crystalline solid was collected by filtration. The solid was columned on silica gel with $MeCN:H_2O:KNO_3$ 7:1:0.5 as eluent. The main gloving fraction was then dried, redissolved in acetonitrile and filtered. The filtrate was dried and redissolved in a minimum amount of methanol, NH_4PF_6 was added, an orange solid crashed and it was collected by filtration. (170 mg, yield 76%)

^{1}H NMR (400 MHz, CD_3CN) δ:8.84 (d, ^3J = 2.02, 1H, Bpy-*H*); 8.59-8.54 (m, 5H, Bpy-*H*); 8.13-8.06 (m, 5H, Bpy-*H*); 7.97 (d, ^3J = 6.15, 1H, Bpy-*H*); 7.84 (d, ^3J = 5.32, 1H, Bpy-*H*); 7.79 (d, ^3J = 5.53, 1H, Bpy-*H*); 7.76-7.70 (m, 3H, Bpy-*H*); 7.56 (dd, ^3J = 6.15, ^3J = 2.20, 1H, Bpy-*H*); 7.49-7.40 (m, 5H, Bpy-*H*); 4.42 (q, ^3J = 7.16, 2H, CH_2-CH_3); 4.31 (q, ^3J = 7.07, 2H, CH_2-CH_3) 1.36 (t, ^3J = 7.12, 3H, CH_2-CH_3); 1.11 (t, ^3J = 7.03, 3H, CH_2-CH_3).

^{13}C {^{1}H} NMR (400 MHz, CD_3CN) δ:159.54; 159.10; 157.74; 156.97, 156.96; 156.93, 156.92; 156.88, 156.87; 156.83; 156.05; 153.52; 152.00; 151.94; 151.91; 151.83; 151.65; 143.10; 140.54, 138.19; 138.10; 138.09; 137.94, 128.41; 127.78; 127.74; 127.70; 127.62; 125.12; 125.08, 124.48; 124.43; 122.04; 119.67; 63.75; 62.25; 13.40; 13.04.

HRMS (ESI) *m/z* calcd for $[C_{38}H_{33}N_9O_4Ru]^{2+}$ 390.5860, found 390.5864 $(M)^{2+}$

7.53 Synthesis of $[Ru(bpy)_2(1\text{-}[2,2'\text{-bipyridine-4-yl}]triazole\text{-}4,5\text{-}dicarboxylic\ acid)](PF_6)_2$ (AS16)

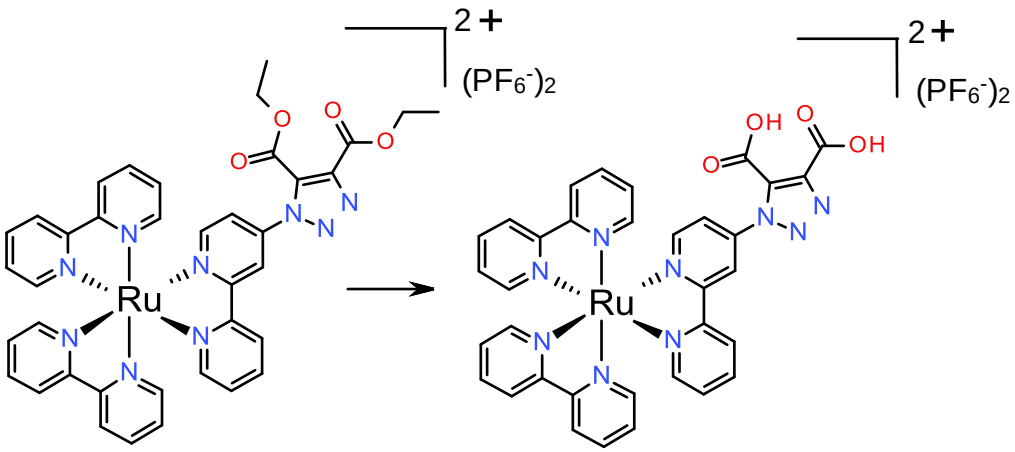

50 mg of $[Ru(bpy)_2(detzbpy)](PF_6)_2$ was dissolved in 8 mL 1M KOH/acetone 1:1 and heated to reflux temperature for 12 hours. After cooling the acetone was removed under vacuum and the solution was neutralised with 1M HCl. The solution was concentrated and a solid crashed out. The solid was collected by filtration, redissolved in a minimal amount of methanol and NH_4PF_6 was added, newly a red solid crashed and it was collected by filtration. (yield 75%)

^{1}H NMR (400 MHz, CD_3CN) δ:8.79 (s, 1H, Bpy-*H*); 8.58-8.49 (m, 5H, Bpy-*H*); 8.16-8.05 (m, 5H, Bpy-*H*); 7.94 (d, ^3J = 5.91, 1H, Bpy-*H*); 7.86-7.72 (m, 5H, Bpy-*H*); 7.64 (d, ^3J = 5.26, 1H, Bpy-*H*); 7.51-7.40 (m, 5H, Bpy-*H*).

^{13}C {^{1}H} NMR (400 MHz, CD_3CN) δ:159.63, 159.21, 157.86, 157.03, 156.99, 156.94, 156.90, 156.88, 156.46, 156.23, 154.69, 152.38, 151.89, 151.86, 151.84, 151.82, 151.81, 151.62, 143.42, 138.68, 138.03, 138.00, 137.96, 128.03, 127.74, 127.72, 127.66, 127.65, 124.75, 124.43, 124.40, 124.31, 121.72, 120.59.

7.54 Synthesis of [Ir(ppy)$_2$(1-[2,2′-bipyridine-4-yl]triazole-4,5-ethyldicarboxylate)]PF$_6$

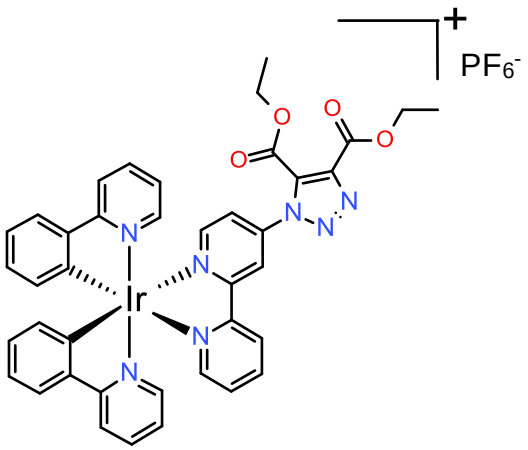

107 mg of [Ir(ppy)$_2$Cl]$_2$ dimer were dissolved in DCM:MeOH 2:1 (12 mL) together with 77 mg of detzbpy and 53 mg of AgPF$_6$. The solution was heated to reflux temperature overnight, under N_2 in the dark. The solvent was removed under reduced pressure and the resulting solid dissolved in DCM and filtered on celite pad. The solvent was removed again and the solid recrystallised from acetonitrile/ether. A pale orange solid was collected by filtration and columned with 10% MeOH in DCM. (yield 74%)

^{1}H NMR (400 MHz, CD_3CN) δ:8.84 (d, ^3J = 1.70, 1H, Bpy-*H*); 8.57 (d, ^3J = 8.04, 1H, Bpy-*H*); 8.23-8.16 (m, 2H, Bpy-*H*); 8.11 (d, ^3J = 8.14, 2H, Ppy-*H*); 8.05 (d, ^3J = 5.78, 1H, Bpy-*H*); 7.89 (t, ^3J = 7.35, 2H, Ppy-*H*); 7.84 (d, ^3J = 7.62, 2H, Ppy-*H*); 7.75 (d, ^3J = 5.52, 1H, Ppy-*H*); 7.70-7.64 (m, 2H, Bpy-*H*); 7.59 (t, ^3J = 6.30, 1H, Bpy-*H*); 7.13-7.05 (m, 4H, Ppy-*H*); 6.99-6.93 (m, 2H, Ppy-*H*); 6.32 (d, ^3J = 7.75, 1H, Ppy-*H*); 6.29 (d, ^3J = 7.63, 1H, Ppy-*H*); 4.45 (q, ^3J = 6.95, 2H, C*H*$_2$-CH$_3$); 4.34 (q, ^3J = 7.10, 2H, C*H*$_2$-CH$_3$); 1.39 (t, ^3J = 7.10, 3H, CH$_2$-C*H*$_3$); 1.13 (t, ^3J = 7.10, 3H, CH$_2$-C*H*$_3$).

^{13}C {^{1}H} NMR (400 MHz, CD_3CN) δ:167.35; 167.24; 159.48; 158.15; 157.72; 154.72; 152.48; 150.99; 149.52; 149.49, 149.43; 144.40; 144.09; 143.97; 140.50; 139.62; 138.78; 138.72; 131.80; 131.59; 131.44; 130.49; 130.44; 129.26; 125.37; 124.98; 124.95; 123.66; 123.54; 123.08; 122.82; 122.76; 120.10; 120.01; 119.98; 63.81; 62.24; 13.39; 12.97.

HRMS (ESI) *m/z* calcd for [$C_{40}H_{33}N_7O_4Ir$]$^+$ 867.2230, found 867.2228 (M^+)

7.55 Synthesis of [Ir(ppy)$_2$(1-[2,2′-bipyridine-4-yl]triazole-4,5-dicarboxylic acid)]PF$_6$ (AS17)

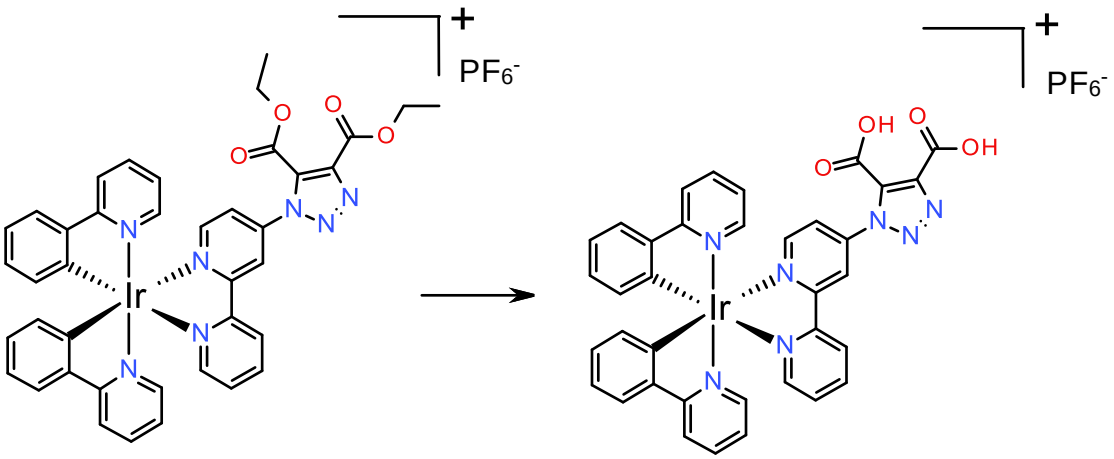

50 mg of [Ir(ppy)$_2$(detzbpy)]PF$_6$ was dissolved in 8 mL 1M KOH/acetone 1:1 and heated to reflux temperature for 12 hours. After cooling the acetone was removed under vacuum and the solution was neutralised with 1M HCl. The solution was concentrated and a solid crashed out. The solid was collected by filtration, redissolved in a minimal amount of methanol and NH_4PF_6 was added, newly a yellow solid crashed and it was collected by filtration. (yield 68%)

^{1}H NMR (400 MHz, CD_3CN) δ: 8.46 (d, ^3J = 6.56 Hz, 1H); 8.11 (td, ^3J = 6.28, ^4J = 1.24 Hz, 1H); 8.07 (t, ^3J = 5.64 Hz, 2H); 8.00 (bs, 1H); 7.97 (dd, ^3J = 4.3, ^4J = 0.8 Hz, 1H); 7.89-7.84 (m, 2H); 7.81 (d, ^3J = 6.08 Hz, 2H); 7.71 (d, ^3J = 4.72 Hz, 1H); 7.65 (d, ^3J = 4.6 Hz, 1H); 7.63 (d, ^3J = 5.16 Hz, 1H); 7.47 (td, ^3J = 5.24, ^4J = 0.72 Hz, 1H); 7.09-7.02 (m, 5H); 6.97-6.9 (m, 3H); 6.31 (dd, ^3J = 6.06, ^4J = 0.6 Hz, 1H); 6.28 (dd, ^3J = 6.04, ^4J = 0.52 Hz, 1H);

^{13}C {^{1}H} NMR (400 MHz, CD_3CN) δ: 167.63, 167.49, 157.16, 156.23, 151.26, 150.45, 149.14, 149.11, 144.28, 144.06, 139.99, 139.88, 139.86, 139.84, 139.21, 139.16, 138.36, 138.33, 131.91, 131.67, 131.65, 131.51, 130.31, 130.27, 130.23, 128.11, 124.82, 124.78, 124.33, 123.4, 123.37, 122.32, 122.3,

7.56 Synthesis of $Re(CO)_3$(1-[2,2′-bipyridine-4-yl]triazole-4,5-ethyldicarboxylate)Cl

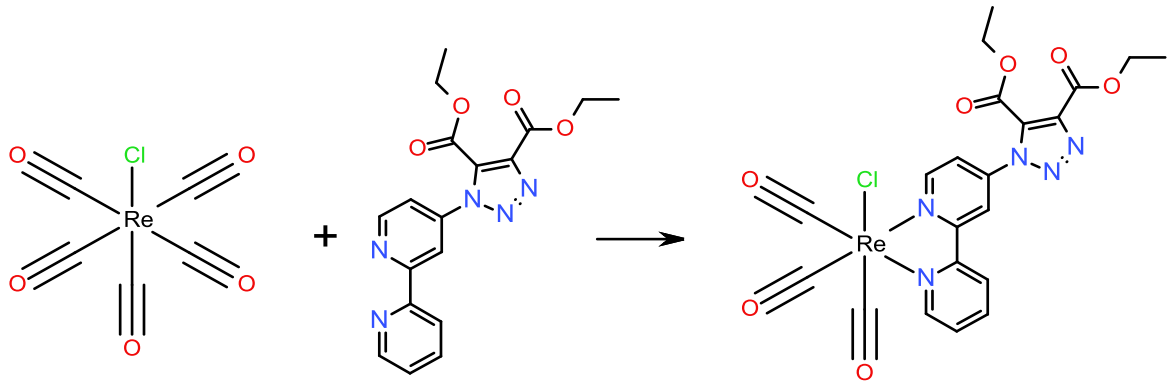

100 mg of $[Re(CO)_5Cl]$ and 113 mg of detzbpy were dissolved in 25 mL of toluene and heated at 70 °C for 12 hours. After cooling the volume was reduced under reduced pressure and a yellow solid crashed out, it was collected by filtration and dried with diethylether. (158 mg yield 84%)

^{1}H NMR (400 MHz, CD_3CN) δ:9.24 (d, ^3J = 5.96, 1H, Bpy-*H*); 9.09 (dd, ^3J = 5.38, ^3J = 0.70, 1H, Bpy-*H*); 8.73 (d, ^3J = 2.10, 1H, Bpy-*H*); 8.47 (d, ^3J = 8.18, 1H, Bpy-*H*); 8.26 (dt, ^3J = 7.95 1.52, 1H, Bpy-*H*); 7.81 (dd, ^3J = 6.08, ^3J = 2.34, 1H, Bpy-*H*); 7.72 (dt, ^3J = 6.49, ^3J = 1.22, 1H, Bpy-*H*); 4.47 (q, ^3J = 7.13, 2H, C*H*$_2$-CH_3); 4.44 (q, ^3J = 7.02, 2H, C*H*$_2$-CH_3); 1.98-1.95 (m, 6H, CH_2-C*H*$_3$).

^{13}C {^{1}H} NMR (400 MHz, CD_3CN) δ: 197.63, 197.47, 189.26, 159.55, 157.96, 157.87, 154.73, 154.65, 153.25, 144.91, 140.59, 140.22, 131.79, 128.29, 124.65, 121.86, 119.36, 63.94, 62.24, 13.40, 13.07.

HRMS (ESI) *m/z* calcd for $C_{21}H_{17}ClN_5O_7Re$ 671.0352, found 689.0694 $(M+NH_4)^+$

7.57 Synthesis of $Re(CO)_3$(1-[2,2′-bipyridine-4-yl]triazole-4,5-dicarboxylic acid)Cl (AS18)

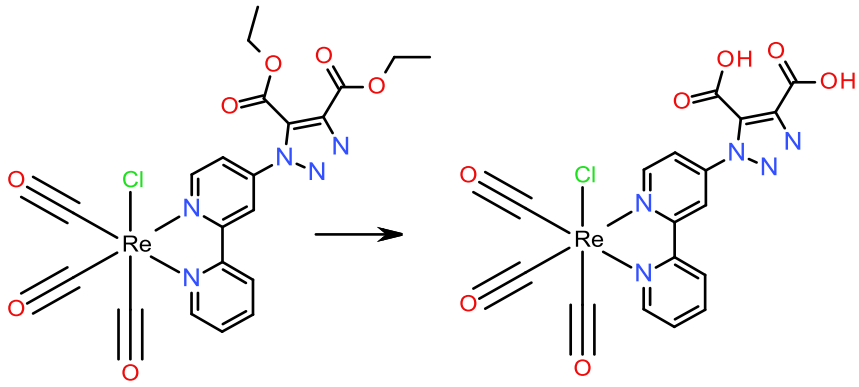

50 mg of $[Re(CO)_3(detzbpy)Cl]$ was dissolved in 8 mL 1M KOH/acetone 1:1 and heated to reflux temperature for 12 hours. After cooling the acetone was removed under vacuum and the solution was neutralised with 1M NaOH. The solution was concentrated and a yellow solid crashed out. The solid was collected by filtration. (yield 67%)

^{1}H NMR (400 MHz, DMSO-d_6) δ:8.95 (d, ^3J = 5.27, 1H, Bpy-*H*); 8.76 (d, ^3J = 4.38, 1H, Bpy-*H*); 8.59 (s, 1H, Bpy-*H*); 8.53 (d, ^3J = 7.89, 1H, Bpy-*H*); 8.14 (t, ^3J = 7.71, 1H, Bpy-*H*); 7.80 (dd, ^3J = 5.43, ^4J = 1.75, 1H, Bpy-*H*); 7.63 (t, ^3J = 5.78, 1H, Bpy-*H*).

[Low solubility] ^{13}C {^{1}H} NMR not recorded

7.58 Synthesis of Iridium(III) bis[3-(2-benzothiazolyl)-7-(diethylamino)-2H-1-benzopyran-2-onato-N',C4]- diethyl-4,4'-dicarboxylate-2,2'-bipyridine

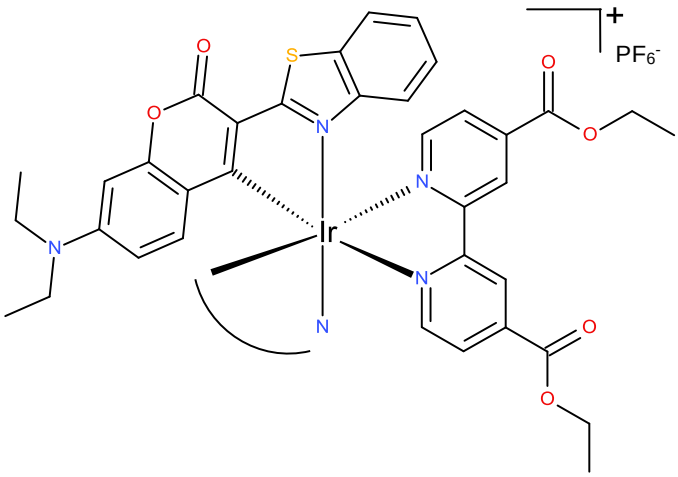

100 mg of dimer $[Ir(C6)_2Cl]_2$ (0.054 mmol) and 41 mg of diethyl 4,4'-dicarboxylate-2,2'-bipyridine (0.134 mmol) in ethoxyethanol (9 mL) was heated at 150 °C for 21 h under nitrogen. The reaction mixture was reduced to a minimum volume, the solid was dissolved in methanol and ammonium hexafluorophosphate (0.060 g, 0.37 mmol) was added. Adding diethyl ether a solid crashed out and it was collected by filtration. The crude product obtained was purified by column chromatography on silica gel (solvent: 10% MeOH in DCM) followed by recrystallization from acetonitrile/ether to yield a orange-red powder. (yield 72%)

^{1}H NMR (400 MHz, CD_3CN) δ: 8.95 (d, ^3J = 5.99, 2H, Bpy-*H*); 8.83 (s, 2H Bpy-*H*); 8.15 (dd, ^3J = 5.99, ^4J = 1.67, 2H Bpy-*H*); 7.95 (d, ^3J = 7.99, 2H, Coum-*H*); 7.27 (t, ^3J = 7.66, 2H, Coum-*H*); 6.99 (t, ^3J = 7.99, 2H, Coum-*H*); 6.46 (d, ^3J = 2.00, 2H, Coum-*H*); 6.07-6.04 (m, 4H, Coum-*H*); 5.93 (d, ^3J = 8.66, 2H, Coum-*H*); 4.45 (q, ^3J = 7.33, 4H, O-CH_2-CH_3); 3.32 (q, ^3J = 6.99, 8H, N-CH_2-CH_3); 1.40 (t, ^3J = 6.66, 6H, O-CH_2-CH_3); 1.04 (t, ^3J = 6.66, 12H, N-CH_2-CH_3).

^{13}C {^{1}H} NMR (400 MHz, CD_3CN) δ:179.80, 178.10, 162.68, 157.49, 156.17, 155.21, 152.86, 152.21, 147.85, 142.21, 132.00, 128.83, 127.70, 124.82, 124.15, 123.76, 121.78, 118.31, 115.68, 109.84, 96.33, 62.92, 44.42, 13.36, 11.72.

HRMS (ESI) *m/z* calcd for $[C_{56}H_{50}N_6O_8S_2Ir]^+$ 1191.2761, found 1191.2929 $(M)^+$

7.59 Synthesis of Iridium(III) bis[3-(2-benzothiazolyl)-7-(diethylamino)-2H-1-benzopyran-2-onato-N',C4]- dicarboxy-2,2'-bipyridine (AS19)

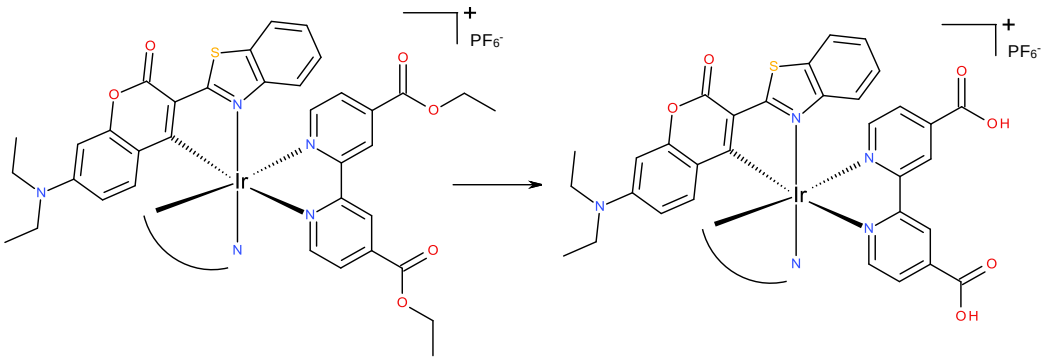

50mg of $[Ir(C6)_2(deeb)](PF_6)$ was dissolved in 8 mL of 1M KOH/acetone 1:1 and heated to reflux temperature for 12 hours. After cooling the acetone was removed under vacuum and the solution was neutralised with 1M NaOH. The solution was concentrated and an orange solid crashed out. The solid was collected by filtration. (yield 68%)

^{1}H NMR (400 MHz, CD_3CN) δ: 8.93 (d, ^3J = 5.67, 2H, Bpy-*H*); 8.82 (s, 2H, Bpy-*H*); 8.14 (d, ^3J = 5.48, 2H, Bpy-*H*); 7.95 (d, ^3J = 8.16, 2H, Coum-*H*); 7.27 (t, ^3J = 7.72, 2H, Coum-*H*); 7.00 (t, ^3J = 7.83, 2H, Coum-*H*); 6.49 (s, 2H, Coum-*H*); 6.07 (s, 4H, Coum-*H*); 5.90 (d, ^3J = 8.28, 2H, Coum-*H*); 3.32 (q, ^3J = 6.93, 8H, CH_2-CH_3); 1.04 (t, ^3J = 7.09, 12H, CH_2-CH_3).

[Low solubility] ^{13}C {^{1}H} NMR not recorded

HRMS (ESI) *m/z* calcd for $[C_{52}H_{42}N_6O_8S_2Ir]^+$ 1133.2134, found 1133.2091 $(M)^+$

7.60 Synthesis of $[Ir(pyba)_2(3\text{-}(imidazo[1,10]phenanthrolin\text{-}2\text{-}yl)\text{-}7\text{-}(diethylamino)chromen\text{-}2\text{-}one)]PF_6$ (AS20)

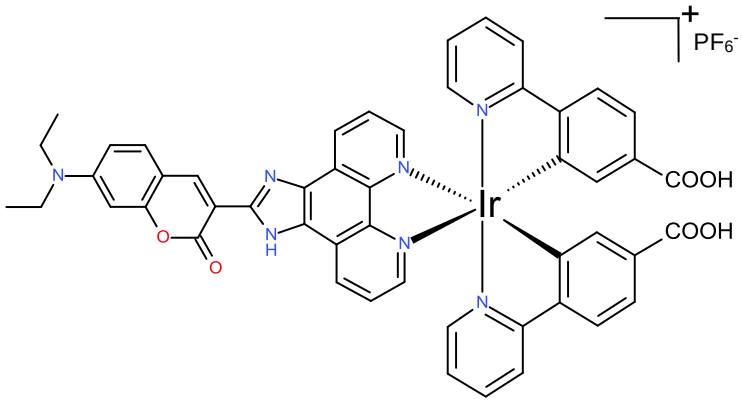

3-(imidazo[1,10]phenanthrolin-2-yl)-7-(diethylamino)chromen-2-one (0.070 g, 0.16mmol) was dissolved in DCM:MeOH 2:1 (6 mL) and $[Ir(pyba)_2(Cl)]_2$ (0.100 g, 0.08 mmol) was added. The mixture was heated at reflux under nitrogen atmosphere, in the dark. After 6 hrs, the yellow/brown solution was cooled to room temperature and dried under vacuum. The crude product was purified by silica gel column chromatography using acetone as eluent, followed by a mixture of $MeCN:H_2O:KNO_3$ 7:1:0.5. The main coloured fraction was then dried, redissolved in acetonitrile and filtered. The filtrate was dried and redissolved in a minimum amount of methanol, NH_4PF_6 (130 mg 0.9 mmol) was added. The solution was left in the fridge overnight. The product was recrystallized from acetonitrile/diethylether to yield a yellow/brown powder. (yield 24%)

^{1}H NMR (400 MHz, $CD_3OD/CDCl_3$ 1/1) δ: 9.27 (d, ^3J = 8.18, 2H, Phen-*H*); 8.91 (s, 1H, Phen-*H*); 8.27-8.20 (m, 2H, Phen-*H*); 8.12 (d, ^3J = 8.08, 2H, Ppy-*H*); 7.92-7.80 (m, 5H, Phen-*H*&Ppy-*H*); 7.73 (d, ^3J = 8.08, 2H, Ppy-*H*); 7.59-7.56 (m, 2H, Phen-*H*); 7.43 (d, ^3J = 5.82, 2H, Ppy-*H*); 7.02 (s, 2H, Ppy-*H*); 6.96 (t, ^3J = 6.47, 2H, Ppy-*H*); 6.78 (dd, ^3J = 9.05, ^4J = 1.94, 1H, Phen-*H*); 6.58 (bs, 1H, Phen-*H*); 3.50 (q, ^3J = 6.93, 4H, CH_2-CH_3); 0.83 (t, ^3J = 6.49, 6H, CH_2-CH_3).

[Low solubility] ^{13}C {^{1}H} NMR not recorded

HRMS (ESI) *m/z* calcd for $[C_{50}H_{37}N_7O_6Ir]^+$ 1022.2406, found 1022.2399 $(M)^+$

8 References

1. *International Energy Outlook*, US Dept of Energy, Washington DC, 2010.
2. A. Ç. Köne and T. Büke, *Renew. Sust. Energ. Rev.*, 2010, **14**, 2906.
3. E. M. Corporation, *The Outlook for Energy: A View to 2040*, http://www.slideshare.net/GemMaRezasmitHa/2015-energyoutlookpresentation.
4. I. McConnell, G. Li and G. W. Brudvig, *Chem. Biol.*, 2010, **17**, 434.
5. N. S. Lewis and D. G. Nocera, *Proc. Natl. Acad. Sci. USA*, 2006, **103**, 15729.
6. M. A.Green, K. Emery, Y. Hishikawa and W. Warta, *Prog. Photovolt. Res. Appl.*, 2010, **18**, 144.
7. M. A. Green, *Prog. Photovolt. Res. Appl.*, 2009, **17**, 183.
8. Eurobserver, *The state of renewable energies in Europe*, 2014.
9. B. O'Regan and M. Grätzel, *Nature*, 1991, **353**, 737.
10. N. R. E. Laboratory, http://www.nrel.gov/ncpv/.
11. A. Hagfeldt, G. Boschloo, L. Sun, L. Kloo and H. Pettersson, *Chem. Rev.*, 2010, **110**, 6595.
12. S. Hore, E. Palomares, H. Smit, N. J. Bakker, P. Comte, P. Liska, K. R. Thampi, J. M. Kroon, A. Hinsch and J. R. Durrant, *J. Mat. Chem.*, 2005, **15**, 347.
13. A. Hagfeldt and M. Gratzel, *Acc. Chem. Res.*, 2000, **33**, 269.
14. C. J. Barbé, F. Arendse, P. Comte, M. Jirousek, F.Lenzmann, V. Shklover and M. Grätzel, *J. Am. Chem. Soc.*, 1997, **80**, 3157.
15. K. D. Benkstein, N. Kopidakis, J. v. d. Lagemaat and A. J.Frank, *J. Phys. Chem. B*, 2003, **107**, 7759.
16. S. Tatay, S. A. Haque, B. O'Regan, J. R. Durrant, W. J. H. Verhees, J. M. Kroon, A. Vidal-Ferran, P. Gavina and E. Palomares, *J. Mat. Chem.*, 2007, **17**, 3037.
17. C. Teng, X. Yang, S. Li, M. Cheng, A. Hagfeldt, L. Wu and L. Sun, *Chem.-Eur. J.*, 2010, **16**, 13127.
18. B. V. Bergeron, A. Marton, G. Oskam and G. J. Meyer, *J. Phys. Chem. B*, 2004, **109**, 937.
19. T. Daeneke, T.-H. Kwon, A. B. Holmes, N. W. Duffy, U. Bach and L. Spiccia, *Nature Chem.*, 2011, **3**, 211.
20. S. A. Sapp, C. M. Elliott, C. Contado, S. Caramori and C. A. Bignozzi, *J. Am. Chem. Soc.*, 2002, **124**, 11215.
21. T. C. Li, A. M. Spokoyny, C. She, O. K. Farha, C. A. Mirkin, T. J. Marks and J. T. Hupp, *J. Am. Chem. Soc.*, 2010, **132**, 4580.
22. H. Tian, X. Jiang, Z. Yu, L. Kloo, A. Hagfeldt and L. Sun, *Angew. Chem. Int. Ed.*, 2010, **49**, 7328.
23. S. Hattor, Y. Wada, S. Yanagida and S. Fukuzumi, *J. Am. Chem. Soc.*, 2005, **127**, 9648.
24. H. Nusbaumer, S. M. Zakeeruddin, J. E. Moser and M. Grätzel, *Chem.-Eur. J.*, 2003, **9**, 3756.
25. S. M. Feldt, P. W. Lohse, F. Kessler, M. K. Nazeeruddin, M. Gratzel, G. Boschloo and A. Hagfeldt, *Phys. Chem. Chem. Phys.*, 2013, **15**, 7087.
26. S. M. Feldt, E. A. Gibson, E. Gabrielsson, L. Sun, G. Boschloo and A. Hagfeldt, *J. Am. Chem. Soc.*, 2010, **132**, 16714.
27. A. Yella, H. W. Lee, H. N. Tsao, C. Yi, A. K. Chandiran, M. K. Nazeeruddin, E. W. Diau, C. Y. Yeh, S. M. Zakeeruddin and M. Gratzel, *Science*, 2011, **334**, 629.
28. D. Zhou, Q. Yu, N. Cai, Y. Bai, Y. Wang and P. Wang, *Energ. Environ. Sci.*, 2011, **4**, 2030.
29. S. M. Feldt, G. Wang, G. Boschloo and A. Hagfeldt, *J. Phys. Chem. C*, 2011, **115**, 21500.
30. J. H. Yum, E. Baranoff, F. Kessler, T. Moehl, S. Ahmad, T. Bessho, A. Marchioro, E. Ghadiri, J. E. Moser, C. Yi, M. K. Nazeeruddin and M. Gratzel, *Nat. Commun.*, 2012, **3**, 631.

31. A. J. Frank, N. Kopidakis and J. V. d. Lagemaat, *Coord.Chem. Rev.*, 2004, **248**, 1165.
32. S. Pelet, J. E. Moser and M. Grätzel, *J. Phys. Chem. B*, 2000, **104**, 1791.
33. Z. Zhang, N. Evans, S. M. Zakeeruddin, R. Humphry-Baker and M. Grätzel, *J. Phys. Chem. C*, 2007, **111**, 398.
34. D. F. Watson and G.J.Meyer, *Coord.Chem. Rev.*, 2004, **248**, 1391.
35. T. N. Murakami and M. Grätzel, *Inorg. Chim. Acta*, 2008, **361**, 572.
36. P. Calandra, G. Calogero, A. Sinopoli and P. G. Gucciardi, *Int. J. Photoenergy*, 2010, **2010**, 1.
37. T. N. Murakami, S. Ito, Q. Wang, M. K. Nazeeruddin, T. Bessho, I. Cesar, P. Liska, R. Humphry-Baker, P. Comte, P. Pechy and M. Grätzel, *J. Electrochem. Soc.*, 2006, **153**, 2255.
38. D. Xiong and W. Chen, *Front. Optoelectron.*, 2012, **5**, 371.
39. G. H. Summers, J.-F. Lefebvre, F. A. Black, E. Stephen Davies, E. A. Gibson, T. Pullerits, C. J. Wood and K. Zidek, *Phys. Chem. Chem. Phys.*, 2016, **18**, 1059.
40. E. A. Gibson, A. L. Smeigh, L. c. Le Pleux, L. Hammarström, F. Odobel, G. Boschloo and A. Hagfeldt, *J. Phys. Chem. C*, 2011, **115**, 9772.
41. S. Powar, T. Daeneke, M. T. Ma, D. Fu, N. W. Duffy, G. Gotz, M. Weidelener, A. Mishra, P. Bauerle, L. Spiccia and U. Bach, *Angew. Chem.*, 2013, **52**, 602.
42. G. Natu, P. Hasin, Z. Huang, Z. Ji, M. He and Y. Wu, *Appl. Mater. Interfaces*, 2012, **4**, 5922.
43. M. Gennari, F. Légalité, L. Zhang, Y. Pellegrin, E. Blart, J. Fortage, A. M. Brown, A. Deronzier, M.-N. Collomb, M. Boujtita, D. Jacquemin, L. Hammarström and F. Odobel, *J. Phys. Chem. Lett.*, 2014, **5**, 2254.
44. Z. Ji, G. Natu, Z. Huang, O. Kokhan, X. Zhang and Y. Wu, *J. Phys. Chem. C*, 2012, **116**, 16854.
45. K. L. Wu, S. T. Ho, C. C. Chou, Y. C. Chang, H. A. Pan, Y. Chi and P. T. Chou, *Angew. Chem. Int. Ed.*, 2012, **51**, 5642.
46. N. Robertson, *Angew. Chem. Int. Ed.*, 2006, **45**, 2338.
47. K. Kalyanasundaram and M. Grätzel, *Coord.Chem. Rev.*, 1998, **177**, 347.
48. S. Altobello, C. A. Bignozzi, S. Caramori, G. Larramona, S. Quici, G. Marzanni and R. Lakhmiri, *J. Photochem. Photobiol., A*, 2004, **166**, 91.
49. G. Calogero, A. Sinopoli, I. Citro, G. Di Marco, V. Petrov, A. M. Diniz, A. J. Parola and F. Pina, *Photochem. Photobiol. Sci.*, 2013, **12**, 883.
50. I. Gillaizeau-Gauthier, F. Odobel, M. Alebbi, R. Argazzi, E. Costa, C. A. Bignozzi, P. Qu and G. J. Meyer, *Inorg. Chem.*, 2001, **40**, 6073.
51. T. J. Meyer, G. J. Meyer, B. W. Pfennig, J. R. Schoonover, C. J. Timpson, J. F. Wall, C. Kobusch, X. Chen and B. M. Peek, *Inorg. Chem.*, 1994, **33**, 3952.
52. A. Vittadini, A. Selloni, F. P. Rotzinger and M. Gratzel, *J. Phys. Chem. B*, 2000, **104**, 1300.
53. A. Mishra, M. K. Fischer and P. Bauerle, *Angew. Chem. Int. Ed.*, 2009, **48**, 2474.
54. Y. Ooyama and Y. Harima, *Eur. J. Org. Chem.*, 2009, 2903.
55. Z. Yao, M. Zhang, H. Wu, L. Yang, R. Li and P. Wang, *J. Am. Chem. Soc.*, 2015, **137**, 3799.
56. G. Calogero, J.-H. Yum, A. Sinopoli, G. Di Marco, M. Grätzel and M. K. Nazeeruddin, *Solar Energy*, 2012, **86**, 1563.
57. A. S. Polo, M. K. Itokazu and N. Y. M. Iha, *Coord.Chem. Rev.*, 2004, **248**, 1343.
58. V. Martinez-Diaz, G. D. L. Torre and T. Torres, *Chem. Commun.*, 2010, **46**, 7090.
59. N. Koumura, Z.-S. Wang, S. Mori, M. Miyashita, E. Suzuki and K. Hara, *J. Am. Chem. Soc.*, 2006, **128**, 14256.
60. J. Luo, M. Xu, R. Li, K.-W. Huang, C. Jiang, Q. Qi, W. Zeng, J. Zhang, C. Chi, P. Wang and J. Wu, *J. Am. Chem. Soc.*, 2014, **136**, 265.

61. D. P. Hagberg, J.-H. Yum, H. Lee, F. D. Angelis, T. Marinado, K. M. Karlsson, R. Humphry-Baker, L. Sun, A. Hagfeldt, M. Grätzel and M. K. Nazeeruddin, *J. Am. Chem. Soc.*, 2008, **130**, 6259.
62. S. Wang, Y. Cui, Y. Dan-oh, C. Kasada, A. Shinpo and K. Hara, *J. Phys. Chem. C*, 2007, **111**, 7224.
63. J.-H. Yum, P. Walter, S. Huber, D. Rentsch, T. Geiger, F. Nuesch, F. De Angelis, M. Gratzel and M. K. Nazeeruddin, *J. Am. Chem. Soc.*, 2007, **129**, 10320.
64. T. Edvinsson, C. Li, N. Pschirer, J. Schöneboom, F. Eickemeyer, R. Sens, G. Boschloo, A. Herrmann, K. Müllen and A. Hagfeldt, *J. Phys. Chem. C*, 2007, **111**, 15137.
65. A. Forneli, M. Planells, M. A. Sarmentero, E. Martinez-Ferrero, B. O'Regan, P. Ballester and E. Palomares, *J. Mat. Chem.*, 2008, **18**, 1652.
66. J. J. Cid, J. H. Yum, S. R. Jang, M. K. Nazeeruddin, E. Martinez-Ferrero, E. Palomares, J. Ko, M. Grätzel and T. Torres, *Angew. Chem. Int. Ed.*, 2007, **46**, 8358.
67. F. G. Gao, A. J. Bard and L. D. Kispert, *J. Photochem. Photobiol. A*, 2000, **130**, 49.
68. G. Calogero, I. Citro, G. Di Marco, S. Armeli Minicante, M. Morabito and G. Genovese, *Spectrochim. Acta A* 2014, **117**, 702.
69. C. A. Bignozzi, R. Argazz and C. J. Kleverlaan, *Chem. Soc. Rev.*, 2000, **29**, 87.
70. M. K. Nazeeruddin, F. De Angelis, S. Fantacci, A. Selloni, G. Viscardi, P. Liska, S. Ito, B. Takeru and M. Gratzel, *J. Am. Chem. Soc.*, 2005, **127**, 16835.
71. A. Islam, H. Sugihara, K. Hara, L. P. Singh, R. Katoh, M. Yanagida, Y. Takahashi, S. Murata, H. Arakawa and G. Fujihashi, *Inorg. Chem.*, 2001, **40**, 5371.
72. G. M. Hasselmann and G. J. Meyer, *J. Phys. Chem.*, 1993, **97**, 11987.
73. S. Altobello, R. Argazzi, S. Caramori, C. Contado, S. Da Fre, P. Rubino, C. Chone, G. Larramona and C. A. Bignozzi, *J. Am. Chem. Soc.*, 2005, **127**, 15342.
74. E. A. M. Geary, L. J. Yellowlees, L. A. Jack, I. D. H. Oswald, S. Parsons, N. Hirata, J. R. Durrant and N. Robertson, *Inorg. Chem.*, 2005, **44**, 242.
75. G. M. Hasselmann and G. J. Meyer, *J. Phys. Chem. B*, 1999, **103**, 7671.
76. E. C. C. T. Bessho, M. Grätzel, A. H. Redondo, C. E. Housecroft, W. Kylberg, M. K. Nazeeruddin, M. Neuburger, S. Schaffner, *Chem. Commun.*, 2008, 3717.
77. C. Dragonetti, A. Valore, A. Colombo, S. Righetto and V. Trifiletti, *Inorg. Chim. Acta*, 2012, **388**, 163.
78. S. Ferrere, *Chem. Mat.*, 2000, **12**, 1083.
79. R. Argazzi, G. Larramona, C. Contado and C. A. Bignozzi, *J. Photochem. Photobiol., A*, 2004, **164**, 15.
80. E. Baranoff, J.-H. Yum, M. Graetzel and M. K. Nazeeruddin, *J. Organomet. Chem.*, 2009, **694**, 2661.
81. A. Juris, V. Balzani, F. Barigelletti, S. Campagna, P. Belser and A. V. Zelewsky, *Coord.Chem. Rev.*, 1988, **84**, 85.
82. J. Heine and K. Muller-Buschbaum, *Chem. Soc. Rev.*, 2013, **42**, 9232.
83. G.A.Crosby, *Acc. Chem. Res.*, 1975, **8**, 231.
84. K. Kalyanasundaram and M. K. Nazeeruddin, *Chem. Phys. Lett.*, 1992, **193**, 292.
85. S. Campagna, F. Puntoriero, F. Nastasi, G. Bergamini and V. Balzani, *Top. Curr. Chem.*, 2007, **280**, 117.
86. V. Balzani, G. Bergamini, F. Marchion and P. Ceroni, *Coord.Chem. Rev.*, 2006, **250**, 1254.
87. V. Balzani, A. Juris, M. Venturi, S. Campagna and S. Serroni, *Chem. Rev.*, 1996, **96**, 759.

88. M. Maestri, N. Armaroli, V. Balzani, E. C. Constable and A. M. W. C. Thompson, *Inorg. Chem.*, 1995, **34**, 2759.
89. K. W. Lee, J. D. Slinker, A. A. Gorodetsky, S. Flores-Torres, H. D. Abruna, P. L. Houston and G. G. Malliaras, *Phys. Chem. Chem. Phys.*, 2003, **5**, 2706.
90. K. Kalyanasundaram, *Photochemistry of Polypyridine and Porphyrin Complexes*, Academic Press edn., 1992.
91. P. A. Anderson, G. F. Strouse, J. A. Treadway, F. R. Keene and T. J. Meyer, *Inorg. Chem.*, 1994, **33**, 3863.
92. C. E. Welby, S. Grkinic, A. Zahid, B. S. Uppal, E. A. Gibson, C. R. Rice and P. I. P. Elliott, *Dalton Trans.*, 2012, **41**, 7637.
93. Y. Ohsawa, S. Sprouse, K. A. King, M. K. D. Armond, K. W. Hanck and R. J. Watts, *J. Phys. Chem.*, 1987, **91**, 1047.
94. F. O. Garces, K. A. King and R. J. Watts, *Inorg. Chem.*, 1988, **27**, 3464.
95. F. Xu, H. U. Kim, J.-H. Kim, B. J. Jung, A. C. Grimsdale and D.-H. Hwang, *Prog. Pol. Sci.*, 2015, **47**, 92.
96. J. Tang, *Front. Optoelectr.*, 2015, **8**, 239.
97. K. Hasan, A. K. Bansal, I. D. Samuel, C. Roldan-Carmona, H. J. Bolink and E. Zysman-Colman, *Sci. Rep.*, 2015, **5**, 12325.
98. E. I. Mayo, K. Kilsa, T. Tirrell, P. I. Djurovich, A. Tamayo, M. E. Thompson, N. S. Lewis and H. B. Gray, *Photochem. Photobiol. Sci.*, 2006, **5**, 871.
99. A. B. Tamayo, B. D. Alleyne, P. I. Djurovich, S. Lamansky, I. Tsyba, N. N. Ho, R. Bau and M. E. Thompson, *J. Am. Chem. Soc.*, 2003, **125**, 7377.
100. H. Wang, Q. Liao, H. Fu, Y. Zeng, Z. Jiang, J. Ma and J. Yao, *J. Mat. Chem.*, 2009, **19**, 89.
101. P.J.Hay, *J. Phys. Chem. A*, 2002, **106**, 1634.
102. K. A. King and R. J. Watts, *J. Am. Chem. Soc.*, 1987, **109**, 1589.
103. C.-H. Yang, S.-W. Li, Y. Chi, Y.-M. Cheng, Y.-S. Yeh, P.-T. Chou, G.-H. Lee, C.-H. Wang and C.-F. Shu, *Inorg. Chem.*, 2005, **44**, 7770.
104. B. J. Coe and S. J. Glenwright, *Coord.Chem. Rev.*, 2000, **203**, 5.
105. A. B. Tamayo, S. Garon, T. Sajoto, P. I. Djurovich, I. M. Tsyba, R. Bau and M. E. Thompson, *Inorg. Chem.*, 2005, **44**, 8723.
106. G. Zhou, W.-Y. Wong, B. Yao, Z. Xie and L. Wang, *Angew. Chem. Int. Ed.*, 2007, **46**, 1149.
107. C.-L. Ho, W.-Y. Wong, Z.-Q. Gao, C.-H. Chen, K.-W. Cheah, B. Yao, Z. Xie, Q. Wang, D. Ma, L. Wang, X.-M. Yu, H.-S. Kwok and Z. Lin, *Adv. Funct. Mat.*, 2008, **18**, 319.
108. K. Dedeian, P. I. Djurovich, F. O. Garces, C. Carlson and R. J. Watts, *Inorg. Chem.*, 1991, **30**, 1685.
109. Y. You and S. Y. Park, *J. Am. Chem. Soc.*, 2005, **127**, 12438.
110. E. Portenkirchner, E. Kianfar, N. S. Sariciftci and G. Knor, *ChemSusChem*, 2014, **7**, 1347.
111. A. W.-T. Choi, C.-S. Poon, H.-W. Liu, H.-K. Cheng and K. K.-W. Lo, *N. J. Chem.*, 2013, **37**, 1711.
112. X. Yi, J. Zhao, W. Wu, D. Huang, S. Ji and J. Sun, *Dalton Trans.*, 2012, **41**, 8931.
113. S. Clede, F. Lambert, C. Sandt, Z. Gueroui, M. Refregiers, M. A. Plamont, P. Dumas, A. Vessieres and C. Policar, *Chem. Commun.*, 2012, **48**, 7729.
114. L. Zhao, H. Odaka, H. Ono, S. Kajimoto, K. Hatanaka, J. Hobley and H. Fukumura, *Photochem. Photobio. Sci.*, 2005, **4**, 113.
115. L. Yang, A.-M. Ren, J.-K. Feng, X.-J. Liu, Y.-G. Ma, M. Zhang, X.-D. Liu, J.-C. Shen and H.-X. Zhang, *J. Phys. Chem. A*, 2004, **108**, 6797.
116. J. A. Baiano, R. J. Kessler, R. S. Lumpkin, M. J. Munley and W. R. Murphy, *J. Phys. Chem.*, 1995, **99**, 17680.
117. B. Happ, A. Winter, M. D. Hager and U. S. Schubert, *Chem. Soc. Rev.*, 2012, **41**, 2222.

118. P. G. Bomben, K. D. Thériault and C. P. Berlinguette, *Eur. J. Inorg. Chem.*, 2011, **2011**, 1806.
119. A. K. M. K. Nazeeruddin, I. Rodicio, R. Humphry-Baker, E. Mueller, P. Liska, N. Vlachopoulos, M. Grätzel, *J. Am. Chem. Soc.*, 1993, **115**, 6382.
120. M. K. Nazeeruddin, R. Splivallo, P. Liska, P. Comte and M. Gratzel, *Chem. Commun.*, 2003, 1456.
121. M. K. Nazeeruddin, S. M. Zakeeruddin, R. Humphry-Baker, M. Jirousek, P. Liska, N. Vlachopoulos, V. Shklover, C.-H. Fischer and M. Gratzel, *Inorg. Chem.*, 1999, **38**, 6298.
122. P. Wang, S. M. Zakeeruddin, J. E. Moser, R. Humphry-Baker, P. Comte, V. Aranyos, A. Hagfeldt, M. K. Nazeeruddin and M. Grätzel, *Adv. Mat.*, 2004, **16**, 1806.
123. S.-R. Jang, C. Lee, H. Choi, J. J. Ko, J. Lee, R. Vittal and K.-J. Kim, *Chem. Mat.*, 2006, **18**, 5604.
124. G. C. Vougioukalakis, T. Stergiopoulos, A. G. Kontos, E. K. Pefkianakis, K. Papadopoulos and P. Falaras, *Dalton Trans.*, 2013, **42**, 6582.
125. M. K. Nazeeruddin, C. Klein, P. Liska and M. Grätzel, *Coord.Chem. Rev.*, 2005, **249**, 1460.
126. S. M. Zakeeruddin, M. K. Nazeeruddin, R. Humphry-Baker, P. Péchy, P. Quagliotto, C. Barolo, G. Viscardi and M. Grätzel, *Langmuir*, 2002, **18**, 952.
127. J.-K. H. W.-S. Han, H.-Y. Kim, M. J. Choi, Y.-S. Kang, C. Pac, S. O. Kang, *Inorg. Chem.*, 2011, **50**, 3271.
128. P. Wang, C. Klein, J.-E. Moser, R. Humphry-Baker, N.-L. Cevey-Ha, R. Charvet, P. Comte, S. M. Zakeeruddin and M. Grätzel, *J. Phys. Chem. B*, 2004, **108**, 17553.
129. S. Altobello, C. A. Bignozzi, S. Caramori, G. Larramona, S. Quici, G. Marzanni and R. Lakhmiri, *J. Photochem. Photobiol., A*, 2004, **166**, 91.
130. P. Wang, S. M. Zakeeruddin, R. Humphry-Baker, J. E. Moser and M. Grätzel, *Adv. Mat.*, 2003, **15**, 2101.
131. J. N. Clifford, E. Palomares, M. K. Nazeeruddin, M. Grätzel, J. Nelson, N. X. Li, J. Long and J. R. Durrant, *J. Am. Chem. Soc.*, 2004, **126**, 5225.
132. N. Hirata, J.-J. Lagref, E. J. Palomares, J. R. Durrant, M. K. Nazeeruddin, M. Grätzel and D. D. Censo, *Chem.-Eur. J.*, 2004, **10**, 595.
133. R. Argazzi, C. A. Bignozzi, T. A. Heimer, F. N. Castellano and G. J. Meyer, *J. Am. Chem. Soc.*, 1995, **117**, 11815.
134. M. Abrahamsson, P. G. Johansson, S. Ardo, A. Kopecky, E. Galoppini and G. J. Meyer, *J. Phys. Chem. Lett.*, 2010, 1725.
135. S. Sinn, B. Schulze, C. Friebe, D. G. Brown, M. Jager, J. Kubel, B. Dietzek, C. P. Berlinguette and U. S. Schubert, *Inorg. Chem.*, 2014, **53**, 1637.
136. T. Funaki, H. Funakoshi, O. Kitao, N. Onozawa-Komatsuzaki, K. Kasuga, K. Sayama and H. Sugihara, *Angew. Chem.* , 2012, **51**, 7528.
137. W. B. Heuer, H. L. Xia, W. Ward, Z. Zhou, W. H. Pearson, M. A. Siegler, A. A. Narducci Sarjeant, M. Abrahamsson and G. J. Meyer, *Inorg. Chem.*, 2012, **51**, 3981.
138. Y. Pellegrin, L. Le Pleux, E. Blart, A. Renaud, B. Chavillon, N. Szuwarski, M. Boujtita, L. Cario, S. Jobic, D. Jacquemin and F. Odobel, *J. Photochem. Photobiol., A*, 2011, **219**, 235.
139. K. P. S. Zanoni, R. L. Coppo, R. C. Amaral and N. Y. Murakami Iha, *Dalton Trans.*, 2015, **44**, 14559.
140. E. Baranoff, J.-H. Yum, I. Jung, R. Vulcano, M. Grätzel and M. K. Nazeeruddin, *Chem.-Asian J.*, 2010, **5**, 496.
141. H. Takeda, K. Koike, H. Inoue and O. Ishitani, *J. Am. Chem. Soc.*, 2008, **130**, 2023.
142. C. She, N. A. Anderson, J. Guo, F. Liu, W.-H. Goh, D.-T. Chen, D. L. Mohler, Z.-Q. Tian, J. T. Hupp and T. Lian, *J. Phys. Chem. B*, 2005, **109**, 19345.

143. P. Kar, T. Banerjee, S. Verma, A. Sen, A. Das, B. Ganguly and H. N. Ghosh, *Phys. Chem. Chem. Phys.*, 2012, **14**, 8192.
144. S. Hwang, J. H. Lee, C. Park, H. Lee, C. Kim, C. Park, M.-H. Lee, W. Lee, J. Park, K. Kim, N.-G. Park and C. Kim, *Chem. Commun.*, 2007, 4887.
145. M. Shrestha, L. Si, C.-W. Chang, H. He, A. Sykes, C.-Y. Lin and E. W.-G. Diau, *J. Phys. Chem. C*, 2012, **116**, 10451.
146. U. Mehmood, S.-u. Rahman, K. Harrabi, I. A. Hussein and B. V. S. Reddy, *Adv. Mat. Sci. Eng.*, 2014, **2014**, 1.
147. C. Qin, Y. Numata, S. Zhang, A. Islam, X. Yang, K. Sodeyama, Y. Tateyama and L. Han, *Adv. Funct. Mat.*, 2013, **23**, 3782.
148. M. K. Nazeeruddin, *J. Am. Chem. Soc.*, 2001, **123**, 1613.
149. B. S. Chen, K. Chen, Y. H. Hong, W. H. Liu, T. H. Li, C. H. Lai, P. T. Chou, Y. Chi and G. H. Lee, *Chem. Commun.*, 2009, 5844.
150. J.-H. Yum, E. Baranoff, S. Wenger, M. K. Nazeeruddin and M. Grätzel, *Energ. Environ. Sci.*, 2011, **4**, 842.
151. A. Damas, M. P. Gullo, M. N. Rager, A. Jutand, A. Barbieri and H. Amouri, *Chem. Commun.*, 2013, **49**, 3796.
152. S.-y. Takizawa, C. Pérez-Bolívar, P. Anzenbacher and S. Murata, *Eur. J. Inorg. Chem.*, 2012, **2012**, 3975.
153. A. Morandeira, G. Boschloo, A. Hagfeldt and L. Hammarström, *J. Phys. Chem. C*, 2008, **112**, 9530.
154. E. Galoppini, *Coord Chem Rev*, 2004, **248**, 1283.
155. H. Tian, J. Oscarsson, E. Gabrielsson, S. K. Eriksson, R. Lindblad, B. Xu, Y. Hao, G. Boschloo, E. M. Johansson, J. M. Gardner, A. Hagfeldt, H. Rensmo and L. Sun, *Sci. Rep.*, 2014, **4**, 4282.
156. T. Yu, P. Zhang, Y. Zhao, H. Zhang, J. Meng and D. Fan, *Org. Electron.*, 2009, **10**, 653.
157. T. Yu, P. Zhang, Y. Zhao, H. Zhang, J. Meng, D. Fan, L. Chen and Y. Qiu, *Org. Electron.*, 2010, **11**, 41.
158. M. K. Nazeeruddin and M. Graetzel, *Molecular and Supramolecular Photochemistry*, V. Ramamurthy, K.S. Schanze New York, 2003.
159. J. Pietruszka and A. Witt, *Synthesis*, 2006, **2006**, 4266.
160. T. P. Lodge, *Macromol.*, 2009, **42**, 3827.
161. V. V. Rostovtsev, L. G. Green, V. V. Fokin and K. B. Sharpless, *Angew. Chem. Int. Ed.*, 2002, **41**, 2596.
162. V. D. Bock, H. Hiemstra and J. H. v. Maarseveen, *Eur. J. Org. Chem.*, 2005, 51.
163. O. R. P. D. D. J. V. C. van Steenis, G. P. F. van Strijdonck, J. H. van Maarseveen and J. N. H. Reek, *Chem. Commun.*, 2005, 4333.
164. D. Fournier, R. Hoogenboom and U. S. Schubert, *Chem. Soc. Rev.*, 2007, **36**, 1369.
165. K. P. Chitre, E. Guillén, A. S. Yoon and E. Galoppini, *Eur. J. Inorg. Chem.*, 2012, **2012**, 5461.
166. B. S. Uppal, A. Zahid and P. I. P. Elliott, *Eur. J. Inorg. Chem.*, 2013, **2013**, 2571.
167. R. J. Detz, S. A. Heras, R. de Gelder, P. W. N. M. van Leeuwen, H. Hiemstra, J. N. H. Reek and J. H. van Maarseveen, *Org. Lett.*, 2006, **8**, 3227.
168. X. Y. Wang, A. Kimyonok and M. Weck, *Chem. Commun.*, 2006, 3933.
169. S. Badeche, J.-C. Daran, J. Ruiz and D. Astruc, *Inorg. Chem.*, 2008, **47**, 4903.
170. B. L. S. Müller, G. J. Roth, H. J. Bestmann, *Synlett.*, 1996, 521.
171. B. Beyer, C. Ulbricht, D. Escudero, C. Friebe, A. Winter, L. González and U. S. Schubert, *Organometal.*, 2009, **28**, 5478.
172. J. M. Fernandez-Hernandez, C. H. Yang, J. I. Beltran, V. Lemaur, F. Polo, R. Frohlich, J. Cornil and L. D. Cola, *J. Am. Chem. Soc.*, 2011, **133**, 10543.
173. M. Felici, P. Contreras-Carballada, J. M. M. Smits, R. J. M. Nolte, R. M. Williams, L. D. Cola and M. C. Feiters, *Molecules*, 2010, **15**, 2039.

174. D. Luvino, *Synlett*, 2007, **19**, 3037.
175. S. Lamansky, P. Djurovich, D. Murphy, F. Abdel-Razzaq, H-E Lee, C. Adachi, P. E. Burrows, S. R. Forrest and M. E. Thompson, *J. Am. Chem. Soc.*, 2001, **123**, 4304.
176. S. Bettington, M. Tavasli, M. R. Bryce, A. Beeby, H. Al-Attar and A. P. Monkman, *Chemistry*, 2007, **13**, 1423.
177. T. N. Murakami, N. Koumura, M. Kimura and S. Mori, *Langmuir*, 2014, **30**, 2274.
178. C. E. Welby, L. Gilmartin, R. R. Marriott, A. Zahid, C. R. Rice, E. A. Gibson and P. I. P. Elliott, *Dalton Trans.*, 2013, **42**, 13527.
179. A. Morandeira, G. Boschloo, A. Hagfeldt and L. Hammarström, *J. Phys. Chem. B*, 2005, **109**, 19403.
180. E. A. Gibson, A. L. Smeigh, L. L. Pleux, J. Fortage, G. Boschloo, E. Blart, Y. Pellegrin, F. Odobel, A. Hagfeldt and L. Hammarström, *Angew. Chem. Int. Ed.*, 2009, **48**, 4402.
181. A. Nattestad, A. J. Mozer, M. K. R. Fischer, Y.-B. Cheng, A. Mishra, P. Bäuerle and U. Bach, *Nature Mat.*, 2010, **9**, 31.
182. P. Qin, J. Wiberg, E. A. Gibson, M. Linder, L. Li, T. Brinck, A. Hagfeldt, B. Albinsson and L. Sun, *J. Phys. Chem. C*, 2010, **114**, 4738.
183. J. He, H. Lindström, A. Hagfeldt and S.-E. Lindquist, *J. Phys. Chem. B*, 1999, **103**, 8940.
184. H. Zhu, A. Hagfeldt and G. Boschloo, *J. Phys. Chem. C*, 2007, **111**, 17455.
185. Y. Sun, S. N. Collins, L. E. Joyce and C. Turro, *Inorg. Chem.*, 2010, **49**, 4257.
186. K. Hasan and E. Zysman-Colman, *Eur. J. Inorg. Chem.*, 2013, **2013**, 4421.
187. K. Hasan and E. Zysman-Colman, *Inorg. Chem.*, 2012, **51**, 12560.
188. C. Li, H. Wang, J. Shen and B. Tang, *Anal. Chem.*, 2015, **87**, 4283.
189. E. Amouyal, A. Homsi, J.-C. Chambron and J.-P. Sauvage, *Dalton Trans.*, 1990, 1841.
190. S. Palmas, M. Mascia, A. Vacca, J. Llanos and E. Mena, *RSC Adv.*, 2014, **4**, 23957.
191. E. A. Gibson, L. Le Pleux, J. Fortage, Y. Pellegrin, E. Blart, F. Odobel, A. Hagfeldt and G. Boschloo, *Langmuir*, 2012, **28**, 6485.
192. J. B. Goodenough, *J. Phys. Chem.*, 1982, **86**, 3492.
193. F. De Angelis, S. Fantacci, E. Mosconi, M. K. Nazeeruddin and M. Grätzel, *J. Phys. Chem. C*, 2011, **115**, 8825.
194. J. Schnadt, J. Schiessling, J. N. O'Shea, S. M. Gray, L. Patthey, M. K. J. Johansson, M. Shi, J. Krempaský, J. Åhlund, P. G. Karlsson, P. Persson, N. Mårtensson and P. A. Brühwiler, *Surf. Sci.*, 2003, **540**, 39.
195. F. Ambrosio, N. Martsinovich and A. Troisi, *J. Phys. Chem. Lett.*, 2012, **3**, 1531.
196. A. Mishra, N. Pootrakulchote, M. K. R. Fischer, C. Klein, M. K. Nazeeruddin, S. M. Zakeeruddin, P. Bauerle and M. Gratzel, *Chem. Commun.*, 2009, 7146.
197. E. Lim, *Int. J. Photoenergy*, 2013, **2013**, 7.
198. D. Schweinfurth, K. I. Hardcastle and U. H. F. Bunz, *Chem. Commun.*, 2008, 2203.
199. M. Goral, T. McCormac, E. Dempsey, D.-L. Long, L. Cronin and A. M. Bond, *Dalton Trans.*, 2009, 6727.
200. T. A. Heimer, C. A. Bignozzi and G. J. Meyer, *J. Phys. Chem. B*, 1999, **103**, 7671.
201. S. Ferrere, A. Zaban and B. A. Gregg, *J. Phys. Chem.*, 1997, **101**, 4490.
202. J. Moser and M. J. Gratzel, *J. Am. Chem. Soc.*, 1984, **106**, 6557.
203. K. Hara, T. Sato, R. Katoh, A. Furube, Y. Ohga, A. Shinpo, S. Suga, K. Sayama, H. Sugihara and H. Arakawa, *J. Phys. Chem. B*, 2003, **107**, 597.
204. J. S.-Y. Lau, P.-K. Lee, K. H.-K. Tsang, C. H.-C. Ng, Y.-W. Lam, S.-H. Cheng and K. K.-W. Lo, *Inorg. Chem.*, 2008, **48**, 708.

205. Q. Zhao, F. Li, S. Liu, M. Yu, Z. Liu, T. Yi and C. Huang, *Inorg. Chem.*, 2008, **47**, 9256.
206. S. Ladouceur, D. Fortin and E. Zysman-Colman, *Inorg. Chem.*, 2010, **49**, 5625.
207. W. Wu, S. Ji, J. Shao, H. Guo, T. D. James and J. Zhao, *Chemistry*, 2012, **18**, 4953.
208. J. Sun, W. Wu, H. Guo and J. Zhao, *Eur. J. Inorg. Chem.*, 2011, **2011**, 3165.
209. S.-y. Takizawa, C. Pérez-Bolívar, P. Anzenbacher and S. Murata, *Eur. J. Inorg. Chem.*, 2013, **2013**, 3439.
210. H.-C. Su, H.-F. Chen, F.-C. Fang, C.-C. Liu, C.-C. Wu, K.-T. Wong, Y.-H. Liu and S.-M. Peng, *J. Am. Chem. Soc.*, 2008, **130**, 3413.
211. K. J. Young, L. A. Martini, R. L. Milot, R. C. Snoeberger, V. S. Batista, C. A. Schmuttenmaer, R. H. Crabtree and G. W. Brudvig, *Coord.Chem. Rev.*, 2012, **256**, 2503.
212. Z.-T. Yu, Y.-J. Yuan, J.-G. Cai and Z.-G. Zou, *Chem.-Eur. J.*, 2013, **19**, 1303.
213. K. S. Joya, N. K. Subbaiyan, F. D'Souza and H. J. M. de Groot, *Angew. Chem. Int. Ed.*, 2012, **51**, 9601.
214. Y.-J. Yuan, J.-Y. Zhang, Z.-T. Yu, J.-Y. Feng, W.-J. Luo, J.-H. Ye and Z.-G. Zou, *Inorg. Chem.*, 2012, **51**, 4123.
215. K. J. Young, L. A. Martini, R. L. Milot, R. C. Iii, V. S. Batista, C. A. Schmuttenmaer, R. H. Crabtree and G. W. Brudvig, *Coord.Chem. Rev.*, 2012, **256**, 2503.
216. A. Tsuboyama, H. Iwawaki, M. Furugori, T. Mukaide, J. Kamatani, S. Igawa, T. Moriyama, S. Miura, T. Takiguchi, S. Okada, M. Hoshino and K. Ueno, *J. Am. Chem. Soc.*, 2003, **125**, 12971.
217. W. Wang, L. Xu, F. Liu, X. Li and L. Xing, *J. Phys. Chem. A*, 2013, **1**, 776.
218. B. F. Minaev, R. R. Valiev, E. N. Nikonova, R. M. Gadirov, T. A. Solodova, T. N. Kopylova and E. N. Telminov, *J. Phys. Chem. A*, 2015, **119**, 1948.
219. B. P. Sullivan, D. J. Salmon and T. J. Meyer, *Inorg. Chem.*, 1978, **17**, 3334.
220. M. Valiev, E. J. Bylaska, N. Govind, K. Kowalski, T. P. Straatsma, H. J. J. V. Dam, D. Wang, J. Nieplocha, E. Apra, T. L. Windus and W. d. Jong, *Comp. Phys. Commun.*, 2010, **181**, 1477.
221. P. J. Stephens, F. J. Devlin, C. F. Chabalowski and M. J. Frisch, *J. Phys. Chem.*, 1994, **98**, 11623.
222. D. Andrae, U. Haussermann, M. Dolg, H. Stoll and H. Preuss, *Theor. Chim. Acta*, 1990, **77**, 123.
223. G. Boschloo and A. Hagfeldt, *J. Phys. Chem. B*, 2001, **105**, 3039.
224. C. J. Wood, M. Cheng, C. A. Clark, R. Horvath, I. P. Clark, M. L. Hamilton, M. Towrie, M. W. George, L. Sun, X. Yang and E. A. Gibson, *J. Phys. Chem. C*, 2014, **118**, 16536.
225. A. R.Oki and R. J. Morgan, *Synt. Commun.*, 1995, **25**, 4093.
226. W. Paw and R. Eisenberg, *Inorg. Chem.*, 1997, **36**, 2287.
227. D. Wenkert and R. B. Woodward, *J. Org. Chem.*, 1983, **48**, 283.
228. G. Maerker, *J. Am. Chem. Soc.*, 1958, **80**, 2745.
229. R. A. Fallahpour, *Helv. Chim. Acta*, 2000, **83**, 384.
230. D. Ray and P. K. Bharadwaj, *Inorg. Chem.*, 2008, **47**, 2252.

9 Appendix

9.1 Atomic Coordinates of the optimised geometries of the S_0 ground states of complexes

To view molecular structures, copy text between # marks and paste into notepad, save as ".xyz" file and open it with molecular viewing program such as MSViewer or Mercury.

9.1.1 Atomic coordinates for calculated S_0 state of AS1

#
71
geometry

C	-3.01830026	-2.94842443	1.24144849
C	-3.43986613	-3.58042785	0.08032616
C	-2.89266397	-3.26840185	-1.16000300
C	-1.89479572	-2.29955123	-1.23971796
C	-1.42654832	-1.62924996	-0.10199974
C	-2.02011303	-1.98219181	1.14382404
H	-3.47437856	-3.22232850	2.18470159
H	-1.47934675	-2.07109851	-2.21469285
C	-1.68042970	-1.16793583	3.64451249
H	-2.32241235	-1.70450882	4.32328132
N	-0.53999819	-0.30694793	1.98482766
N	-0.12674463	0.31996691	3.05599043
C	-0.60712428	0.28378474	5.42731501
H	0.20905737	1.00064860	5.39577109
H	-0.34200861	-0.54748225	6.08008987
C	3.02896221	-2.93115890	-1.24697364
C	3.45427112	-3.56393362	-0.08764441
C	2.90600500	-3.25789427	1.15370061
C	1.90320490	-2.29435900	1.23627502
C	1.43125410	-1.62333528	0.10050063
C	2.02609975	-1.97010850	-1.14646371
H	3.48594323	-3.20037052	-2.19113366
H	1.48692701	-2.07058806	2.21197860
C	1.68189449	-1.15084258	-3.64495429
H	2.32583770	-1.68288918	-4.32542591
N	0.53858776	-0.29904967	-1.98255014
N	0.12212662	0.32889997	-3.05187790
C	0.60193912	0.30119948	-5.42343758
H	-0.21933248	1.01216355	-5.39033763
H	0.34319375	-0.52984044	-6.07905465
C	-0.72675368	2.79532230	-0.16617221
C	-1.45740197	3.96317951	-0.37320219
C	-2.80964130	3.88410362	-0.69154134
C	-3.40602336	2.62996151	-0.79832375
C	-2.62078091	1.50543430	-0.58199967
N	-1.31855599	1.57949954	-0.27354789
H	-1.00562961	4.94316773	-0.29809293
H	-4.45410065	2.52673110	-1.04546755
H	-3.03268001	0.50718568	-0.65789817
C	0.71539499	2.79757748	0.17131148

C	1.44261900	3.96771358	0.37760467
C	2.79483722	3.89274322	0.69701040
H	0.98819557	4.94636730	0.30108395
C	2.61278006	1.51345297	0.58974921
C	3.39461595	2.64039563	0.80583983
H	3.02743865	0.51643490	0.66678518
H	4.44270311	2.54038759	1.05423950
N	1.31065700	1.58356333	0.27991186
Ir	-0.00080388	-0.15566684	0.00140564
C	1.50261215	-1.22524396	-2.27966842
C	-1.50023475	-1.23802034	2.27912892
N	-0.81929661	-0.20477406	4.06641524
N	0.81644142	-0.19029218	-4.06396308
C	-3.55448161	5.16889080	-0.90725956
O	-3.04477030	6.25471823	-0.82309420
O	-4.84731754	4.95783403	-1.20307875
H	-5.27567165	5.81894353	-1.33090913
C	3.53611532	5.17980047	0.91157970
O	3.02369579	6.26419294	0.82482694
O	4.82907853	4.97261062	1.20943531
H	5.25506494	5.83505910	1.33635008
H	-3.25021969	-3.78724339	-2.04010070
H	3.26664411	-3.77706418	2.03233667
N	4.51953734	-4.58267528	-0.18069101
O	4.87635241	-5.12152844	0.85674018
O	4.97697104	-4.81854401	-1.29156147
N	-4.49968837	-4.60512274	0.17032359
O	-4.95727983	-4.84528693	1.28019244
O	-4.85206563	-5.14424453	-0.86848706
H	1.50300090	0.79481325	-5.78789941
H	-1.51133893	0.76988992	5.79405811

#

9.1.2 Atomic coordinates for calculated S_0 state of AS2

#
71
geometry

C	-1.93365005	-3.06561589	2.59700609
C	-2.91609321	-3.69865664	1.84717525
C	-3.06595478	-3.32168142	0.51689646
C	-2.27139392	-2.35040630	-0.08603937
C	-1.27483024	-1.70468207	0.64674220
C	-1.12789933	-2.08488426	2.00910116
H	-1.79999330	-3.34076889	3.63844861
H	-3.55497032	-4.46246919	2.26842520
H	-2.45489341	-2.11995208	-1.12611330
C	0.50152202	-1.32120816	3.95698442
H	0.33221534	-1.88906335	4.85664275
N	0.56581050	-0.39791619	1.97152669
N	1.49158422	0.20561643	2.66927118
C	2.39634642	0.07113412	4.90991921
H	2.95807243	0.91266667	4.51332790
H	3.07762934	-0.74533637	5.14960329
C	1.95159342	-3.07444316	-2.57710308

C	2.93867523	-3.69390598	-1.82203707
C	3.08626329	-3.30412413	-0.49519496
C	2.28483854	-2.33337380	0.09949093
C	1.28359676	-1.70123364	-0.63867818
C	1.13913017	-2.09429969	-1.99758840
H	1.81959110	-3.35950162	-3.61608122
H	3.58283247	-4.45686883	-2.23676201
H	2.46669932	-2.09236873	1.13743051
C	-0.49648524	-1.35972947	-3.95133838
H	-0.32425391	-1.93509897	-4.84566124
N	-0.56571516	-0.41827583	-1.97452864
N	-1.49610592	0.17228874	-2.67723122
C	-2.39914567	0.01269322	-4.91707684
H	-2.98157824	0.83961615	-4.51970150
H	-3.06096792	-0.81681771	-5.16605891
C	-0.71621433	2.71875614	0.20959266
C	-1.45444965	3.88595521	0.39210428
C	-2.78293345	3.80597162	0.79819750
C	-3.34877432	2.55151646	1.01340764
C	-2.55883870	1.42787600	0.81078662
N	-1.27868513	1.50263045	0.42145948
H	-1.02863395	4.86592049	0.22333401
H	-4.37856492	2.44725929	1.32781919
H	-2.95050760	0.42935898	0.95654491
C	0.69914468	2.72153502	-0.22585578
C	1.43270843	3.89167261	-0.40826868
C	2.76207968	3.81694229	-0.81243366
H	1.00277308	4.86992548	-0.24001687
C	2.54747577	1.43802072	-0.82520068
C	3.33311343	2.56476646	-1.02715910
H	2.94352821	0.44109810	-0.97000276
H	4.36373631	2.46459293	-1.34012975
N	1.26693389	1.50758588	-0.43618075
Ir	-0.00058670	-0.23023172	-0.00217667
C	0.09035070	-1.37651133	-2.70346978
C	-0.08418521	-1.35379221	2.70887858
N	1.45315339	-0.35549011	3.87795037
N	-1.45476886	-0.40001153	-3.88057147
C	-3.53898165	5.08938611	0.97807910
O	-3.05914117	6.17600624	0.79049528
O	-4.80593355	4.87717811	1.37031688
H	-5.24261312	5.73795158	1.46862025
C	3.51379821	5.10325248	-0.98954315
O	3.02996910	6.18791188	-0.80087455
O	4.78220053	4.89601594	-1.37983721
H	5.21601392	5.75851710	-1.47587228
N	-4.11518513	-3.98071012	-0.29879979
O	-4.79927851	-4.83470644	0.24324231
O	-4.23094590	-3.62431817	-1.46558842
N	4.14064128	-3.94790237	0.32601812
O	4.82942204	-4.80326724	-0.20811360
O	4.25591730	-3.57861362	1.48876455
H	-1.85558024	0.33645260	-5.80439638
H	1.85217279	0.37806045	5.80274372

#

9.1.3 Atomic coordinates for calculated S_0 state of AS3

#
67
geometry

C	-2.80994269	-3.51830248	1.70431931
C	-3.41895609	-4.17719341	0.64341861
C	-3.04266875	-3.86431701	-0.66268597
C	-2.06254428	-2.90088243	-0.91321175
C	-1.42694539	-2.21867144	0.12982903
C	-1.82840581	-2.55531124	1.45098679
H	-3.09754540	-3.75446952	2.72500673
H	-4.17789384	-4.92856459	0.83145730
H	-1.79363633	-2.68910171	-1.94291840
C	-1.11153614	-1.72003118	3.86264603
H	-1.64838872	-2.24275494	4.63651296
N	-0.22574762	-0.88406531	2.04319549
N	0.34694083	-0.24977047	3.03410272
C	0.22735146	-0.26455390	5.44984266
H	1.00797477	0.47430022	5.28867630
H	0.61778851	-1.08646959	6.04985427
C	2.83055408	-3.51071654	-1.68471991
C	3.44860552	-4.15387801	-0.61936767
C	3.07320556	-3.83206031	0.68483404
C	2.08447275	-2.87583756	0.92905774
C	1.43986896	-2.20940866	-0.11858456
C	1.84104832	-2.55431173	-1.43764241
H	3.11757649	-3.75352610	-2.70399266
H	4.21432924	-4.89956971	-0.80249541
H	1.81643980	-2.65643409	1.95742024
C	1.11033800	-1.74746701	-3.85492794
H	1.64686876	-2.27526696	-4.62555661
N	0.22677296	-0.89808876	-2.04067993
N	-0.35371395	-0.27738106	-3.03566942
C	-0.24567703	-0.31848422	-5.45180783
H	-1.02005783	0.42767063	-5.29461649
H	-0.64730187	-1.14727485	-6.03498051
C	-0.74347458	2.21054459	-0.07615956
C	-1.49599498	3.37698318	-0.19766936
C	-2.87951545	3.29539699	-0.32198893
C	-3.48414224	2.04021606	-0.32206248
C	-2.67597969	0.91771566	-0.20150176
N	-1.34351044	0.99470042	-0.08246136
H	-1.03725694	4.35647704	-0.20389369
H	-4.55649873	1.93450853	-0.41631701
H	-3.09154602	-0.08215289	-0.20269139
C	0.73251562	2.21441070	0.05765887
C	1.47953954	3.38500290	0.17289992
C	2.86270822	3.31008673	0.30506416
H	1.01660255	4.36255033	0.16959623
C	2.66996288	0.93084434	0.20070666
C	3.47269130	2.05749410	0.31780420
H	3.08956008	-0.06729163	0.21131234
H	4.54486050	1.95700447	0.41956881

N	1.33773962	1.00130899	0.07472955
Ir	0.00147040	-0.74388760	0.00091746
C	1.14324223	-1.81918245	-2.47753538
C	-1.13860706	-1.80597171	2.48590458
N	-0.19049614	-0.75915326	4.14212746
N	0.18263847	-0.79482462	-4.14061087
C	-3.64888687	4.57561272	-0.45369399
O	-3.13844253	5.66493107	-0.45858486
O	-4.97165310	4.36163095	-0.56509132
H	-5.41113404	5.22288432	-0.64457007
C	3.62604140	4.59434650	0.43258844
O	3.11135178	5.68169489	0.42426058
O	4.94850924	4.38659278	0.55778150
H	5.38381046	5.25021292	0.63440665
H	3.55086542	-4.33437742	1.52074100
H	-3.51269341	-4.37948735	-1.49512892
H	0.59648882	0.13019060	-5.97912171
H	-0.61714824	0.19774547	5.96145422

#

9.1.4 Atomic coordinates for calculated S_0 state of AS4

#
61
geometry

C	-2.93671296	-3.81505058	-0.87288061
C	-1.94479520	-2.95081384	-1.25258737
C	-1.42057610	-2.17683259	-0.17270926
C	-2.06015119	-2.50317240	1.01394788
H	-3.49107555	-4.51062926	-1.48657231
C	-1.88505545	-1.74787274	3.54972815
H	-2.56949959	-2.28109336	4.18770950
N	-0.64086783	-0.88163855	1.96167712
N	-0.28026759	-0.27373502	3.06272753
C	-0.87962800	-0.33544486	5.40239030
H	-0.11541930	0.43739355	5.40719008
H	-0.56966367	-1.16280411	6.04106987
C	2.93861820	-3.82182688	0.84884886
C	1.94730234	-2.95981096	1.23511202
C	1.42346645	-2.17730256	0.16113903
C	2.06287956	-2.49513784	-1.02791932
H	3.49245762	-4.52246766	1.45724439
C	1.89107421	-1.71881853	-3.55744563
H	2.57623432	-2.24703073	-4.19882770
N	0.64423816	-0.86621118	-1.96405470
N	0.28586245	-0.24844833	-3.06034391
C	0.89546823	-0.28308538	-5.39763775
H	0.10794545	0.46600225	-5.40241677
H	0.62127944	-1.10853830	-6.05471875
C	-0.71629601	2.23242638	-0.19210363
C	-1.44249082	3.39980628	-0.41591001
C	-2.78301696	3.31847869	-0.78080467
C	-3.37186282	2.06291445	-0.91480435
C	-2.59129586	0.93873068	-0.68034951
N	-1.30012247	1.01588056	-0.32972561

H	-0.99585874	4.38012193	-0.31697914
H	-4.41123250	1.95851523	-1.19583523
H	-2.99444160	-0.06208171	-0.77072784
C	0.71205569	2.23361457	0.19942372
C	1.43551314	3.40231364	0.42509468
C	2.77461254	3.32346533	0.79565977
H	0.98745719	4.38177980	0.32419648
C	2.58785716	0.94331846	0.69356127
C	3.36503035	2.06896464	0.93246825
H	2.99284952	-0.05667615	0.78479995
H	4.40319276	1.96650193	1.21864775
N	1.29791104	1.01809176	0.33791810
Ir	0.00085301	-0.71179161	-0.00069646
C	1.63742636	-1.79110524	-2.20348685
C	-1.63367524	-1.80854164	2.19478269
N	-1.03233250	-0.79718688	4.02640522
N	1.03924605	-0.76388117	-4.02727875
C	-3.52450303	4.60067097	-1.01327099
O	-3.02568250	5.68965584	-0.90347710
O	-4.80622052	4.38856261	-1.35778794
H	-5.22926025	5.25083662	-1.49355204
C	3.51280776	4.60704326	1.03102017
O	3.01426257	5.69521207	0.91210180
O	4.79090047	4.39703045	1.38997041
H	5.21180651	5.26016835	1.52732362
H	1.60232699	-2.89630237	2.25996009
H	-1.59969404	-2.87948155	-2.27688175
S	-3.28014026	-3.73215353	0.82510219
S	3.28200702	-3.72638228	-0.84846100
H	1.83091676	0.16355463	-5.73547459
H	-1.82237784	0.07674068	5.76269281

#

9.1.5 Atomic coordinates for calculated S_0 state of AS5

#
79
geometry

C	-2.47939912	-3.26943351	-1.80039401
C	-1.51775541	-2.30597329	-1.62177567
C	-1.37948854	-1.61816793	-0.39086083
C	-2.25922346	-1.94986775	0.65552157
H	-0.84703455	-2.07487468	-2.44172146
C	-2.51647219	-1.02967252	3.15494848
H	-3.31303928	-1.50328582	3.69889842
N	-0.98961130	-0.26998615	1.78940677
N	-0.82903741	0.40149539	2.89868931
C	-1.86276823	0.48426887	5.08068485
H	-1.07497760	1.22396026	5.19833201
H	-1.73180485	-0.31057934	5.81514447
C	2.48091479	-3.25689242	1.80652853
C	1.51622663	-2.29715881	1.62378795
C	1.37286281	-1.61769624	0.38882472
C	2.25121737	-1.95363249	-0.65729262
H	0.84896166	-2.06059108	2.44488992

C	2.51895113	-1.02875070	-3.15367463
H	3.32069100	-1.49799139	-3.69385976
N	0.98449467	-0.27354156	-1.79372089
N	0.82888711	0.40025173	-2.90223661
C	1.87444962	0.49183201	-5.07811337
H	1.08478251	1.22871251	-5.19828447
H	1.75432190	-0.30181366	-5.81545878
C	-0.66481304	2.81362197	-0.32615961
C	-1.32400400	3.98313548	-0.69871051
C	-2.57366100	3.90698271	-1.30681174
C	-3.14141053	2.65397384	-1.52916506
C	-2.43009265	1.52780275	-1.13511488
N	-1.22548267	1.59994732	-0.55221680
H	-0.89304477	4.96170211	-0.53441086
H	-4.11067796	2.55292798	-1.99918535
H	-2.82128532	0.52924473	-1.28430437
C	0.66773155	2.81155062	0.32112552
C	1.33057570	3.97829776	0.69551599
C	2.57912097	3.89709011	1.30525720
H	0.90336251	4.95847288	0.53114096
C	2.42737905	1.51857701	1.13136470
C	3.14167557	2.64177615	1.52786094
H	2.81427177	0.51826031	1.28056369
H	4.11007857	2.53624439	1.99888922
N	1.22426440	1.59586891	0.54617990
Ir	-0.00280600	-0.14418836	-0.00234644
C	2.01700093	-1.18063802	-1.87227391
C	-2.02158975	-1.17733037	1.87043339
N	-1.75637914	-0.06075312	3.73202459
N	1.76082523	-0.05883138	-3.73208623
C	-3.24186595	5.19233442	-1.69225010
O	-2.75817329	6.27804059	-1.50600668
O	-4.43967418	4.98857928	-2.26714654
H	-4.81864599	5.85329372	-2.48954798
C	3.25130513	5.17920878	1.69406953
O	2.77375746	6.26710909	1.50512571
O	4.44471802	4.97014091	2.27646495
H	4.82525421	5.83353909	2.50162656
H	2.56855710	-3.76515595	2.76296905
H	-2.56104732	-3.78646517	-2.75246905
C	-3.37395890	-3.62232992	-0.75966506
C	-4.35896702	-4.62435966	-0.94812941
C	-3.27270726	-2.95330340	0.50315067
C	-5.22339540	-4.96825835	0.06153080
H	-4.41531719	-5.12175299	-1.91158894
C	-4.18526039	-3.33663203	1.51989425
C	-5.13092426	-4.31337725	1.30701863
H	-5.97148915	-5.73862871	-0.09089741
H	-4.14861599	-2.86620701	2.49232387
H	-5.81154197	-4.58433078	2.10770615
C	3.37085019	-3.61705392	0.76442983
C	4.35723720	-4.61685406	0.95611667
C	3.26287112	-2.95838853	-0.50296612
C	5.21602636	-4.96860288	-0.05541692
H	4.41772122	-5.10645316	1.92335710

C	4.16652220	-3.35319717	-1.52335646
C	5.11381140	-4.32717370	-1.30711224
H	5.96607726	-5.73652927	0.09930675
H	4.11742719	-2.89699101	-2.50200756
H	5.78732555	-4.60742888	-2.11044086
H	2.84585160	0.97075508	-5.20580477
H	-2.83584803	0.95703465	5.21776980

#

9.1.6 Atomic coordinates for calculated S_0 state of AS6

#
79
geometry

C	-3.13039555	-3.18580548	-0.42063015
C	-2.15484044	-2.19664119	-0.73197632
C	-1.42014754	-1.54935834	0.23709757
C	-1.68603961	-1.91210834	1.60873934
H	-1.99887203	-1.96612601	-1.78200756
C	-0.72993273	-1.09558457	3.94171408
H	-1.17819124	-1.63458885	4.75950144
N	-0.04422731	-0.22956819	2.05119545
N	0.61972467	0.40058265	2.98596356
C	0.74212298	0.36701282	5.40059869
H	1.53072614	1.07749410	5.16685035
H	1.15356215	-0.46144844	5.97706262
C	3.13522248	-3.17894122	0.42626552
C	2.15801574	-2.19070395	0.73528763
C	1.42149213	-1.54778500	-0.23529006
C	1.68716818	-1.91413621	-1.60597805
H	2.00262127	-1.95699117	1.78469163
C	0.73001811	-1.10462474	-3.94085953
H	1.17889824	-1.64516377	-4.75728977
N	0.04368271	-0.23426680	-2.05254879
N	-0.62109971	0.39267567	-2.98893241
C	-0.74009959	0.35579485	-5.40368784
H	-1.55006795	1.04293045	-5.17319360
H	-1.12217994	-0.47736292	-5.99331127
C	-0.74260082	2.87680340	0.00692700
C	-1.50015632	4.04594321	-0.01571889
C	-2.88950212	3.96766050	-0.00282064
C	-3.49511061	2.71333686	0.02856754
C	-2.68195725	1.58793038	0.04696991
N	-1.34416988	1.66195083	0.03983991
H	-1.04199579	5.02538105	-0.04609053
H	-4.57199541	2.61114883	0.03679638
H	-3.09657893	0.58753486	0.06339607
C	0.73938510	2.87748952	-0.00969825
C	1.49594418	4.04727080	0.01394674
C	2.88535273	3.97025636	0.00030323
H	1.03692410	5.02626520	0.04569876
C	2.67984748	1.59038989	-0.05196085
C	3.49203074	2.71648301	-0.03294408
H	3.09538612	0.59039059	-0.06941384
H	4.56898789	2.61516661	-0.04199699

N	1.34198345	1.66319730	-0.04387985
Ir	-0.00031755	-0.07877740	-0.00080713
C	0.89762386	-1.17211473	-2.57280110
C	-0.89732074	-1.16688814	2.57380963
N	0.20421899	-0.12756642	4.13719364
N	-0.20542011	-0.13837363	-4.13876424
C	-3.66347333	5.25100255	-0.02732435
O	-3.15241338	6.33955914	-0.06118173
O	-4.99150303	5.04204422	-0.00678863
H	-5.43251494	5.90588209	-0.02374705
C	3.65827232	5.25419209	0.02628617
O	3.14620216	6.34226023	0.06227229
O	4.98643775	5.04647750	0.00441988
H	5.42667662	5.91065378	0.02244061
C	-3.36889953	-3.53092893	0.94781274
C	-2.62298683	-2.86470853	1.94765185
C	3.37282358	-3.52839188	-0.94122875
C	2.62500792	-2.86664500	-1.94259762
H	2.80582511	-3.12348781	-2.98361322
C	4.34478966	-4.51703722	-1.24605076
C	5.05248006	-5.13710532	-0.24579234
C	4.81873542	-4.79435397	1.10677112
H	5.79171779	-5.89308344	-0.48797385
C	3.88497116	-3.84000218	1.43301011
H	5.38170156	-5.29279413	1.88913586
H	3.70726954	-3.58282664	2.47334418
C	-4.33944337	-4.52028563	1.25497208
C	-5.04438900	-5.14559227	0.25603316
C	-4.80944804	-4.80742351	-1.09747085
H	-5.78235166	-5.90225627	0.49996987
C	-3.87745174	-3.85210214	-1.42594365
H	-5.37007283	-5.31017646	-1.87876276
H	-3.69900128	-3.59829794	-2.46697733
H	4.52022343	-4.77941396	-2.28534803
H	-4.51596338	-4.77909037	2.29498443
H	-2.80454872	-3.11828612	2.98934121
H	0.03766189	0.87790195	-5.96201505
H	-0.04188664	0.86296174	5.97370649

#

9.1.7 Atomic coordinates for calculated S_0 state of AS7

#
73
geometry

C	2.64389680	-3.33501794	-1.92509535
C	3.33763413	-3.98599249	-0.91549763
C	3.09013268	-3.67871545	0.42908130
C	2.13392508	-2.70093950	0.73441996
C	1.41152106	-2.02301742	-0.25218007
C	1.69018294	-2.36472358	-1.60177946
H	2.84571113	-3.58447260	-2.96333248
H	4.07544011	-4.74106128	-1.16888591
H	1.95174875	-2.47570016	1.78104304
C	0.77187601	-1.52758305	-3.94484268

H	1.24177797	-2.04760230	-4.76276741
N	0.04317861	-0.69550154	-2.05507129
N	-0.61046954	-0.05822922	-2.99267983
C	-0.69597509	-0.06377561	-5.40843268
H	-1.45479518	0.67911386	-5.17695493
H	-1.14268316	-0.88080105	-5.97531279
C	-2.63856064	-3.32406327	1.94729092
C	-3.33337243	-3.98312973	0.94303445
C	-3.08869397	-3.68491028	-0.40358589
C	-2.13405541	-2.70752357	-0.71734899
C	-1.41048026	-2.02267246	0.26294034
C	-1.68680913	-2.35516448	1.61579647
H	-2.83929500	-3.56598281	2.98751790
H	-4.07017919	-4.73679530	1.20313433
H	-1.95471386	-2.48853529	-1.76587070
C	-0.77127966	-1.49480831	3.95164764
H	-1.24012549	-2.00866936	4.77403447
N	-0.04396806	-0.67791466	2.05487563
N	0.60695689	-0.02967793	2.98688411
C	0.68549087	-0.00797615	5.40280338
H	1.46657364	0.70989214	5.16630719
H	1.10258377	-0.82175879	5.99612583
C	0.74016753	2.40811803	-0.02569245
C	1.49751150	3.57765406	-0.01746239
C	2.88612087	3.50020237	-0.05375096
C	3.49160100	2.24603623	-0.09407462
C	2.67883044	1.12022701	-0.09709287
N	1.34114816	1.19349670	-0.06608595
H	1.04022412	4.55719510	0.01894214
H	4.56814236	2.14406212	-0.12097848
H	3.09421328	0.12052729	-0.12221938
C	-0.74110515	2.40811103	0.01313587
C	-1.49844705	3.57760477	0.00332215
C	-2.88709612	3.50037839	0.03673163
H	-1.04105441	4.55714747	-0.03227654
C	-2.68004962	1.12030693	0.08216701
C	-3.49271051	2.24622023	0.07622899
H	-3.09553171	0.12070402	0.10777727
H	-4.56933979	2.14419126	0.10068286
N	-1.34229937	1.19359133	0.05385964
Ir	-0.00028580	-0.54731546	-0.00067148
C	-0.91398917	-1.59765490	2.58257800
C	0.91564789	-1.61739892	-2.57498352
N	-0.16906943	-0.56480385	-4.14321334
N	0.16660267	-0.52743682	4.14166924
C	3.65820063	4.78526585	-0.04475021
O	3.14560719	5.87277726	-0.00433784
O	4.98623877	4.57878717	-0.08724346
H	5.42553295	5.44397382	-0.07846803
C	-3.65894684	4.78549816	0.02565669
O	-3.14585828	5.87298950	-0.01084503
O	-4.98716595	4.57929697	0.06130375
H	-5.42685186	5.44377204	0.05116519
C	3.82119006	-4.41506327	1.52504722
H	3.42739996	-5.43000950	1.64480704

H	4.88788881	-4.51081643	1.30582671
H	3.72033144	-3.91037448	2.48810255
C	-3.81533516	-4.43142924	-1.49563665
H	-3.33834536	-5.39778704	-1.69240165
H	-4.85365372	-4.63675856	-1.22402579
H	-3.81741712	-3.87336853	-2.43452843
H	0.10305943	0.39640556	-5.99068040
H	-0.11073756	0.48571465	5.96107341

#

9.1.8 Atomic coordinates for calculated S_0 state of AS9

#
67
geometry

C	-1.63975970	2.29767937	-2.85978231
C	-2.69566202	2.94149229	-2.23892193
C	-3.00142622	2.63937115	-0.90645715
C	-2.24531231	1.69495179	-0.20393036
C	-1.17649136	1.02580942	-0.80910590
C	-0.88102275	1.34705806	-2.15819931
H	-1.41093134	2.54194294	-3.89152090
H	-3.29127897	3.67905445	-2.76244430
H	-2.50428338	1.49701266	0.82799533
C	1.62472716	2.29465608	2.87092072
C	2.67607500	2.94888892	2.25319272
C	2.98357066	2.65590455	0.91911152
C	2.23384562	1.70988703	0.21187061
C	1.16973066	1.03035586	0.81375165
C	0.87227230	1.34260448	2.16454369
H	1.39460336	2.53194119	3.90399772
H	3.26681603	3.68772291	2.78042593
H	2.49412337	1.51884690	-0.82103855
C	-0.61463468	-3.40308409	-0.40241150
C	-1.23312569	-4.57511565	-0.84527381
C	-2.40622392	-4.49866964	-1.58570707
C	-2.94136623	-3.24782608	-1.87371792
C	-2.27727524	-2.11996365	-1.41011830
N	-1.14546048	-2.18886061	-0.69199465
H	-0.80522674	-5.54345239	-0.62324465
H	-3.85295649	-3.13876164	-2.44852783
H	-2.64743686	-1.12153078	-1.60841919
C	0.63781857	-3.39990352	0.39337376
C	1.26273891	-4.56879481	0.83543044
C	2.43601997	-4.48643663	1.57492735
H	0.83966576	-5.53929185	0.61360791
C	2.29449076	-2.10837528	1.40017004
C	2.96506361	-3.23291642	1.86252915
H	2.65945608	-1.10806005	1.59866444
H	3.87677971	-3.11933350	2.43625443
N	1.16220868	-2.18299258	0.68336489
Ir	0.00182069	-0.42047184	-0.00114579
C	-0.25238318	0.61243771	2.74872849
C	-1.89445846	-1.01115075	2.33953405
C	-0.74956137	0.78138142	4.04652953

C	-2.42273628	-0.87832631	3.61146996
H	-2.32073701	-1.70073620	1.62324055
H	-0.28633814	1.50322076	4.70621461
H	-3.27687121	-1.47565439	3.90531598
C	-1.83440809	0.03835321	4.48212173
H	-2.22179486	0.17388137	5.48577385
N	-0.83898582	-0.29436562	1.91179545
C	1.90120417	-0.98735667	-2.34535707
C	0.24851288	0.62751338	-2.74597756
C	2.42841230	-0.84441319	-3.61664478
H	2.33179154	-1.67808854	-1.63275200
C	0.74428794	0.80644857	-4.04294350
H	3.28633776	-1.43463259	-3.91375126
H	0.27594413	1.52846862	-4.69882131
N	0.84128287	-0.27956160	-1.91368285
C	1.83404460	0.07298816	-4.48244882
H	2.22047443	0.21644247	-5.48536808
C	-4.14585447	3.36162790	-0.28010158
O	-4.82253403	4.18924625	-0.83685032
C	4.12274649	3.38945379	0.29630159
O	4.79425403	4.21828105	0.85753862
H	-2.89124477	-5.40376004	-1.93327259
H	2.92587588	-5.38908139	1.92205832
O	-4.36568142	2.99113918	1.00541684
H	-5.11544494	3.51736662	1.32256922
O	4.34415487	3.02812595	-0.99154887
H	5.09005023	3.56140973	-1.30604062

#

9.1.9 Atomic coordinates for calculated S_0 state of AS10

#
69
geometry

C	1.78692733	2.48464285	2.78471526
C	2.83876200	3.09553640	2.12492964
C	3.09517763	2.77335901	0.78675045
C	2.29398691	1.84207843	0.11745467
C	1.22808948	1.20644908	0.76237722
C	0.98299453	1.54726902	2.11660039
H	1.59675682	2.74397649	3.82058258
H	3.46881992	3.82265278	2.62206342
H	2.51525645	1.62734020	-0.91988691
C	-1.68948767	2.47249927	-2.85646603
C	-2.70817879	3.15347972	-2.21354832
C	-2.97203564	2.88832639	-0.86438188
C	-2.21282698	1.94196603	-0.16801835
C	-1.18160339	1.23532037	-0.79538179
C	-0.92688922	1.52085131	-2.16057207
H	-1.49194026	2.68937059	-3.90070075
H	-3.30579241	3.89298860	-2.73199747
H	-2.43840264	1.77293556	0.87673991
C	0.56370644	-3.18806248	0.39675242
C	1.14755582	-4.42364031	0.76264358
C	2.37095855	-4.38473352	1.46430844

C	2.94388160	-3.16731540	1.76119025
C	2.30109492	-1.98821538	1.35371268
N	1.14916859	-1.99179443	0.68825669
H	3.88103231	-3.10227428	2.30070074
H	2.72615499	-1.01392503	1.56484439
C	-0.68817632	-3.17411709	-0.31174874
C	-1.31356629	-4.39665015	-0.65189555
C	-2.53497923	-4.33103077	-1.35502363
C	-2.38379820	-1.93641351	-1.29492086
C	-3.06649170	-3.10139805	-1.67743373
H	-2.77531954	-0.95301371	-1.52771051
H	-4.00093527	-3.01596590	-2.21876528
N	-1.23228677	-1.96495845	-0.62940929
Ir	-0.00719775	-0.21715085	0.00477104
C	0.16854524	0.76703068	-2.76942109
C	1.80656914	-0.86669091	-2.38639419
C	0.62259368	0.90705804	-4.08628846
C	2.29253872	-0.76257593	-3.67785075
H	2.24969390	-1.54796609	-1.67239350
H	0.14428468	1.62174456	-4.74302540
H	3.12978229	-1.37465300	-3.98954235
C	1.68431776	0.14454664	-4.54477989
H	2.03867262	0.25774331	-5.56333073
N	0.77387636	-0.13090702	-1.93621935
C	-1.84954181	-0.71397322	2.40996293
C	-0.14596915	0.86221288	2.74531293
C	-2.33582913	-0.54473716	3.69440637
H	-2.31792402	-1.40056413	1.71744272
C	-0.59886259	1.06679873	4.05409319
H	-3.19936036	-1.10986692	4.02252908
H	-0.09357264	1.78336928	4.68821957
N	-0.78543327	-0.03761646	1.94016862
C	-1.69384030	0.36609945	4.53265216
H	-2.04797971	0.52995103	5.54438300
C	4.23755361	3.45981474	0.11834520
O	4.95204366	4.27509723	0.64538058
C	-4.07506897	3.65229833	-0.21386792
O	-4.75342784	4.48221643	-0.76529339
O	4.40845547	3.07134570	-1.16926649
H	5.16119046	3.57515988	-1.51441592
O	-4.25417148	3.31886497	1.08796561
H	-4.97835500	3.87141454	1.41939482
H	-3.04383035	-5.24726648	-1.63572173
C	0.48463427	-5.64474420	0.40833242
C	-0.69200953	-5.63187853	-0.27226229
H	2.84892515	-5.31162289	1.76368703
H	0.94416628	-6.58509534	0.69336511
H	-1.18288149	-6.56189834	-0.53826002

#

9.1.10 Atomic coordinates for calculated S_0 state of AS11

#
79
geometry

C	1.63257053	-3.67940407	-2.71537099
C	2.61121994	-4.36469181	-2.01745005
C	2.83985475	-4.05978066	-0.67016510
C	2.08584114	-3.06979559	-0.03135239
C	1.09401395	-2.35847069	-0.71482120
C	0.87546983	-2.68378870	-2.07709451
H	1.46065891	-3.92863692	-3.75687066
H	3.20326151	-5.13776751	-2.49107283
H	2.28429375	-2.87047414	1.01352808
C	-1.98958846	-3.43346980	2.81242463
C	-3.03824199	-4.04089901	2.14416131
C	-3.25532022	-3.75425915	0.79115732
C	-2.41594675	-2.86272552	0.11461227
C	-1.35287494	-2.23084822	0.76747963
C	-1.14958947	-2.53347369	2.13771096
H	-1.83132128	-3.66593966	3.85990082
H	-3.69637795	-4.73879217	2.64664027
H	-2.60533264	-2.67351432	-0.93407263
Ir	-0.07180414	-0.85444441	-0.00035729
C	-0.02249073	-1.85080791	2.77354062
C	1.72233557	-0.32169410	2.42940977
C	0.39859524	-2.02594991	4.09708293
C	2.18023348	-0.46625356	3.72706306
H	2.22032426	0.33393801	1.72781489
H	-0.13632684	-2.71118525	4.74137420
H	3.05156453	0.08646076	4.05546000
C	1.50061389	-1.33722323	4.57760683
H	1.83250587	-1.48023384	5.59995709
N	0.65256397	-0.98736382	1.95755676
C	-1.79065284	-0.24179046	-2.47124769
C	-0.17833774	-1.92208243	-2.74642476
C	-2.23006304	-0.37251071	-3.77697548
H	-2.24383337	0.46985891	-1.79408875
C	-0.58433695	-2.08795210	-4.07564723
H	-3.04146111	0.24793999	-4.13727489
H	-0.09534840	-2.82883714	-4.69435432
N	-0.79261488	-0.98703300	-1.96204084
C	-1.60996106	-1.31589583	-4.59532904
H	-1.92622068	-1.44920541	-5.62378256
C	3.89831409	-4.83197220	0.04169160
O	4.56959153	-5.69913440	-0.45857174
C	-4.39903385	-4.43297858	0.11677915
O	-5.14426477	-5.21568968	0.65074851
O	4.04366948	-4.46068784	1.33787112
H	4.74081695	-5.02168389	1.71087776
O	-4.53359310	-4.07781348	-1.18466353
H	-5.29099574	-4.57350149	-1.53077745
C	2.37261337	0.76540466	-1.27244371
N	1.19953010	0.85190167	-0.64062923
C	0.69191165	2.08159391	-0.36351260
C	1.37363332	3.26292798	-0.70311830
C	2.60848095	3.14962510	-1.36027654
C	3.10618470	1.89291554	-1.64984230
C	-0.59873746	2.14090929	0.30856971
C	-1.17461200	3.38008506	0.63848614

C	-0.47331875	4.61950843	0.30417713
C	0.79092940	4.56119132	-0.36411296
N	-1.21205418	0.96229415	0.59311984
C	-2.39360513	0.98412694	1.21476627
C	-3.02958369	2.17453463	1.57618804
C	-2.41965372	3.38049291	1.28609995
N	-1.03087043	5.77443369	0.63196470
C	-0.36628355	6.90340770	0.31715331
C	0.90530179	6.84474239	-0.35504035
N	1.45645070	5.65989476	-0.68296166
C	-0.91847965	8.16864526	0.65115907
C	-0.23751543	9.31406369	0.33137683
C	1.01886084	9.25583775	-0.33418028
C	1.58145758	8.05271123	-0.67138662
H	2.72967805	-0.23745288	-1.47434345
H	3.14316676	4.05296617	-1.62598853
H	4.05324491	1.76671497	-2.16051015
H	-2.83797420	0.01832756	1.42327360
H	-3.98956230	2.13607259	2.07673867
H	-2.87390232	4.32896218	1.54440645
H	-1.87609047	8.19228450	1.15817038
H	-0.65599815	10.28128336	0.58740126
H	1.53318714	10.17977632	-0.57500517
H	2.53767648	7.98630242	-1.17695523

#

9.1.11 Atomic coordinates for calculated S_0 state of AS12

#
69
geometry

C	-2.54970119	1.30743739	-2.87818520
C	-3.74845356	1.55191870	-2.23109208
C	-3.84328063	1.34207981	-0.85032395
C	-2.73004798	0.90640156	-0.12340607
C	-1.50473178	0.66198719	-0.75119417
C	-1.43337184	0.86073195	-2.15319421
H	-2.48851682	1.47470003	-3.94812993
H	-4.61872320	1.90149091	-2.77257605
H	-2.83750240	0.77338601	0.94523955
C	0.52295218	3.70476522	2.25001043
C	1.14437146	4.60867684	1.40651070
C	1.53482167	4.20098764	0.12550172
C	1.29120475	2.89243736	-0.30554865
C	0.65951407	1.96202471	0.52560379
C	0.27923399	2.39047404	1.82225573
H	0.22607360	4.03227607	3.24069466
H	1.33416618	5.62847965	1.71649236
H	1.59838718	2.61920877	-1.30642250
C	0.95632743	-2.95389882	0.26725770
C	0.89422213	-4.33932554	0.10380967
C	-0.23102216	-4.87999416	-0.49004874
C	-1.27626656	-4.08030932	-0.92281530
C	-1.14116925	-2.71209102	-0.72861231
N	-0.06281145	-2.16012729	-0.14942054

H	1.68722396	-5.00235108	0.41621823
H	-2.15460544	-4.50656739	-1.38785758
H	-1.91418281	-2.02013153	-1.03994502
C	2.11783801	-2.27092799	0.88781640
C	3.20683462	-2.95924777	1.42693847
C	4.26194814	-2.24683631	1.98484802
H	3.23748757	-4.04085602	1.42067226
C	3.09225366	-0.23234876	1.44798844
C	4.20682862	-0.85744083	1.99303784
H	2.99570939	0.84646367	1.43455743
H	5.00521091	-0.26070748	2.41705728
N	2.07178511	-0.91555633	0.90769726
Ir	0.22288247	0.01913233	0.10872657
C	-0.36774908	1.38122257	2.65922919
C	-1.07961294	-0.85025810	2.75883229
C	-0.83906294	1.58444561	3.96193675
C	-1.55692273	-0.69966311	4.04878043
H	-1.16414927	-1.79493520	2.23843800
H	-0.74010505	2.56008215	4.41919623
H	-2.02081265	-1.53784021	4.55397013
C	-1.43501111	0.54775298	4.66042640
H	-1.80421551	0.70810981	5.66719510
N	-0.49983917	0.15376845	2.07425405
C	2.04692805	-0.17774278	-2.35856430
C	-0.14089545	0.56215591	-2.76924783
C	2.39176230	-0.07683103	-3.69486846
H	2.76363986	-0.50463254	-1.61679064
C	0.16010581	0.68064302	-4.13162546
H	3.39374830	-0.33406765	-4.01546843
H	-0.60114265	1.02505673	-4.81906104
N	0.81914503	0.12878873	-1.89871773
C	1.42494988	0.36343628	-4.59842119
H	1.65818495	0.45862541	-5.65310104
C	-5.16019486	1.60356668	-0.19911313
O	-6.14050437	2.00594040	-0.77181193
C	2.20212848	5.21203225	-0.74578046
O	2.41178014	6.35537741	-0.43163470
O	-5.15492078	1.33138156	1.12900791
H	-6.04273759	1.53118255	1.46079784
O	2.56343140	4.71214073	-1.95309023
H	2.97497884	5.44033195	-2.44406645
N	-0.31109602	-6.35823193	-0.66555784
O	0.63369491	-7.01311548	-0.25771264
O	-1.31481306	-6.79304218	-1.20045182
H	5.11057084	-2.77191932	2.40797693

#

9.1.12 Atomic coordinates for calculated S_0 state of AS13

#
71
geometry

C	-1.33773260	-2.62240014	-3.29718364
C	-0.22008391	-3.26902790	-3.79577247
C	1.02438766	-3.06570204	-3.18878274

C	1.14154861	-2.21675354	-2.08264468
C	0.02925993	-1.54803455	-1.56348045
C	-1.22340910	-1.76702270	-2.18982493
H	-2.29646803	-2.78992022	-3.77565076
H	-0.28830684	-3.93372709	-4.64798368
H	2.11789668	-2.09522066	-1.63237725
C	1.08903692	-3.24669232	2.79170889
C	-0.08240343	-3.87179490	3.18267041
C	-1.30153281	-3.46334778	2.63016475
C	-1.33968653	-2.43213201	1.68506271
C	-0.17153624	-1.78190988	1.27705476
C	1.05424884	-2.20887410	1.84686694
H	2.02718134	-3.57359410	3.22667112
H	-0.07611582	-4.67508765	3.90893359
H	-2.29949583	-2.15335804	1.27053908
C	0.20179169	2.79918306	-0.50069486
C	0.30980477	4.03119732	-1.14792344
C	0.46123399	4.03668440	-2.52269848
C	0.50298249	2.85787394	-3.24811089
C	0.38775181	1.67209382	-2.53364052
N	0.24367193	1.63695759	-1.19948140
H	0.27761261	4.97484543	-0.62243893
H	0.61952724	2.86607124	-4.32332521
H	0.41224335	0.71096025	-3.03174557
C	0.03478395	2.68061868	0.96722427
C	0.03040937	3.78930770	1.81526981
C	-0.13360258	3.57460889	3.17172114
H	0.15178423	4.80184426	1.45792480
C	-0.26958051	1.24552639	2.77985590
C	-0.28726610	2.29815222	3.68617590
H	-0.38362416	0.21975200	3.10739890
H	-0.41412974	2.13361050	4.74756193
N	-0.11574176	1.42489606	1.45845234
Ir	-0.01054289	-0.22452608	-0.02033494
C	2.24751597	-1.49999062	1.38598320
C	3.03209571	0.21186432	-0.01242285
C	3.56290759	-1.77459791	1.77887426
C	4.34805604	-0.02274505	0.34359421
H	2.77421548	0.98092678	-0.72821122
H	3.75430966	-2.57176331	2.48496183
H	5.13943587	0.57352972	-0.09319845
C	4.61593225	-1.03896833	1.26044287
H	5.63458849	-1.25623588	1.56159493
N	2.00435822	-0.49747976	0.49013704
C	-3.00645905	0.45781563	0.06849522
C	-2.35674785	-1.04971151	-1.60687668
C	-4.33490638	0.39657578	-0.31233426
H	-2.69077879	1.06978275	0.90287546
C	-3.68761188	-1.14361852	-2.03111100
H	-5.07727465	0.97264860	0.22583338
H	-3.93941384	-1.79030361	-2.86122158
N	-2.03752242	-0.23799873	-0.55523688
C	-4.67970742	-0.42283888	-1.38693713
H	-5.71082650	-0.50101016	-1.71286417
C	2.19863420	-3.78651469	-3.76198115

O	2.14818578	-4.53519707	-4.70432572
C	-2.53590352	-4.16851692	3.08388845
O	-2.55385738	-5.06976439	3.88298836
O	3.35539052	-3.51103555	-3.11203329
H	4.05135824	-4.02606497	-3.54831060
O	-3.66204807	-3.68679970	2.50414754
H	-4.40174658	-4.20719436	2.85342177
N	0.57902142	5.34484225	-3.23086572
O	0.53981325	6.34799610	-2.53961020
O	0.70534583	5.30007272	-4.44067465
N	-0.14210880	4.74881419	4.09259455
O	0.00188770	5.84648251	3.58246259
O	-0.29308621	4.51168435	5.27683187

#

9.1.13 Atomic coordinates for calculated S_0 state of AS14

#
97
geometry

C	-3.23455468	-2.99554797	-1.22258150
C	-3.90666905	-3.40451286	-0.08476152
C	-3.59875976	-2.81559838	1.14775060
C	-2.61786840	-1.82237654	1.23126412
C	-1.91603851	-1.40062978	0.09862072
C	-2.24769396	-2.00049948	-1.14067366
H	-3.48499569	-3.45495001	-2.17276700
H	-4.67230728	-4.16918442	-0.12698765
H	-2.41469828	-1.38276865	2.19908315
C	-3.23157109	2.98567674	1.23966068
C	-3.90653609	3.39442667	0.10344699
C	-3.60163209	2.80535548	-1.12973923
C	-2.62082356	1.81225377	-1.21554231
C	-1.91611437	1.39077069	-0.08458459
C	-2.24480375	1.99072202	1.15545465
H	-3.47970702	3.44518415	2.19039894
H	-4.67214964	4.15902169	0.14745921
H	-2.42011600	1.37244291	-2.18378407
Ir	-0.44149488	-0.00499905	0.00528947
C	-1.49190882	1.50447338	2.30935129
C	0.19457305	0.02967433	3.00420802
C	-1.65653413	1.93139908	3.63286100
C	0.06921818	0.41932926	4.32608021
H	0.91412215	-0.72007350	2.70349238
H	-2.39882682	2.68469281	3.86172128
H	0.69785756	-0.03296806	5.08312481
C	-0.88077597	1.38986730	4.64419634
H	-1.01365876	1.71710814	5.66949872
N	-0.56232223	0.54661801	2.01884294
C	0.18685563	-0.03893595	-2.99522234
C	-1.49765358	-1.51411468	-2.29636963
C	0.05829125	-0.42844102	-4.31682798
H	0.90692979	0.71098546	-2.69621551
C	-1.66544847	-1.94093702	-3.61951270
H	0.68491685	0.02412481	-5.07538033

H	-2.40818289	-2.69431948	-3.84663950
N	-0.56741405	-0.55624473	-2.00804081
C	-0.89224493	-1.39918007	-4.63268755
H	-1.02753033	-1.72638135	-5.65768368
C	-4.35313722	-3.28443388	2.34410142
O	-5.21423145	-4.12839123	2.32828358
C	-4.35907936	3.27382741	-2.32429354
O	-5.22022907	4.11768179	-2.30651922
O	-3.97222200	-2.66374618	3.48896850
H	-4.52313695	-3.02885803	4.19792369
O	-3.98096790	2.65289303	-3.46996623
H	-4.53370025	3.01776500	-4.17762709
C	4.54409118	2.38507245	-0.27785772
C	3.89216778	1.17723319	-0.10886315
C	4.66904855	-0.00741886	-0.00547444
C	6.07683945	-0.00807670	-0.00912909
C	6.71247867	1.24999971	-0.17540955
C	5.95900324	2.39914651	-0.31812095
C	2.48706887	0.74232651	-0.05293490
C	2.48659724	-0.75506909	0.05270539
C	3.89155458	-1.19134238	0.10176927
C	4.54322523	-2.39982876	0.26710119
C	5.95832123	-2.41523159	0.30005091
C	6.71214124	-1.26677019	0.15371000
N	1.34561206	1.35273965	-0.11988502
N	1.34483700	-1.36420423	0.12537366
C	1.26176682	2.77457625	-0.06240602
C	1.25888926	-2.78595943	0.06949654
C	0.57112738	-3.48694725	1.07071717
C	0.45966004	-4.86334476	1.01102505
C	0.99212329	-5.57667883	-0.07495497
C	1.64167436	-4.87714366	-1.09991891
C	1.77447762	-3.49301098	-1.01804948
C	0.57030881	3.47746055	-1.05974673
C	0.46135563	4.85400340	-0.99841881
C	1.00028499	5.56563842	0.08548798
C	1.65344421	4.86421084	1.10687381
C	1.78358631	3.47993668	1.02328708
H	4.00183471	3.31621309	-0.37057185
H	7.79614822	1.30642372	-0.19204063
H	6.46289943	3.34988653	-0.45279935
H	4.00061208	-3.33050783	0.36232328
H	6.46201339	-3.36648525	0.43183585
H	7.79582899	-1.32421137	0.16471888
H	0.12830192	-2.94908814	1.89932808
H	-0.05535858	-5.41654816	1.78750890
H	2.03726538	-5.39250141	-1.96555386
H	2.27111625	-2.95885617	-1.82069298
H	0.12264454	2.94096771	-1.88664361
H	-0.05644683	5.40865424	-1.77201478
H	2.05388982	5.37823482	1.97107399
H	2.28314579	2.94433093	1.82314715
O	0.81496305	-6.91517894	-0.04212855
O	0.82545269	6.90448416	0.05442418
C	1.33224465	7.69497022	1.12673128

H	1.07489940	8.72229849	0.88013729
H	2.41959121	7.60214075	1.20875495
H	0.86385414	7.42116916	2.07705451
C	1.31403637	-7.70720895	-1.11690751
H	1.05531744	-8.73381023	-0.86872244
H	2.40117075	-7.61723558	-1.20471813
H	0.84132166	-7.43237827	-2.06479259

#

9.1.14 Atomic coordinates for calculated S_0 state of AS15

#
89
geometry

C	2.58034526	-3.33757249	-1.72671216
C	3.15630448	-4.02770579	-0.67502037
C	2.81035268	-3.69556376	0.64049845
C	1.89043241	-2.67291709	0.89293889
C	1.30385021	-1.95401039	-0.15171214
C	1.65873293	-2.30889872	-1.47569679
H	2.85326108	-3.60571529	-2.74165020
H	3.86804311	-4.82543822	-0.84781001
H	1.63889451	-2.45265535	1.92200159
C	-2.91259560	-3.02493919	1.74319347
C	-3.55604911	-3.65957680	0.69582629
C	-3.17047043	-3.38176369	-0.62117849
C	-2.14451942	-2.46716369	-0.87989334
C	-1.48773829	-1.80452428	0.16035099
C	-1.88329625	-2.10579920	1.48614738
H	-3.21728069	-3.25022327	2.75948687
H	-4.35109422	-4.37324932	0.87274360
H	-1.86661097	-2.28661778	-1.90993941
Ir	-0.01406831	-0.41590075	0.00038041
C	-1.15538985	-1.39763467	2.53633028
C	0.52326713	0.18423802	2.96127053
C	-1.35481831	-1.54842583	3.91424135
C	0.36349204	0.06987236	4.33091998
H	1.25351968	0.85872834	2.53451855
H	-2.10381805	-2.24269808	4.27172621
H	0.98071762	0.66018664	4.99684556
C	-0.59651484	-0.81915176	4.81467079
H	-0.74853748	-0.94070166	5.88145556
N	-0.20596288	-0.52711132	2.08173213
C	-0.48150050	0.22422013	-2.96345782
C	1.01007220	-1.53313654	-2.53005717
C	-0.33753795	0.08459769	-4.33249329
H	-1.13039595	0.97915867	-2.53999675
C	1.18833143	-1.71430958	-3.90723793
H	-0.88455971	0.73734744	-5.00149889
H	1.85408288	-2.49030017	-4.26136432
N	0.16422991	-0.55941416	-2.08021830
C	0.51502883	-0.91018372	-4.81148493
H	0.65036089	-1.05486269	-5.87762974
C	3.45243636	-4.46942466	1.74041745
O	4.24642396	-5.36269719	1.58144488

C	-3.88826774	-4.09530106	-1.71501672
O	-4.77604160	-4.89405018	-1.54892347
O	3.05727952	-4.06555710	2.97396140
H	3.51805529	-4.63177514	3.61163927
O	-3.44561070	-3.75438079	-2.95127700
H	-3.96280205	-4.27562744	-3.58410109
C	-2.15271062	4.68330915	0.25065022
C	-0.97149062	3.97266012	0.14255448
C	0.24775637	4.68775248	0.00019244
C	0.31928937	6.09332420	0.00177971
C	-0.91113515	6.79110998	0.12088440
C	-2.10131342	6.09766093	0.23218883
C	-0.60878137	2.54932926	0.09285252
C	0.88281959	2.47322612	-0.09476263
C	1.38829531	3.85261682	-0.14133915
C	2.63605128	4.43996401	-0.24156896
C	2.72848575	5.85216017	-0.22046711
C	1.61443241	6.66282426	-0.11351922
N	-1.27357223	1.44128806	0.13232556
N	1.43087704	1.30300797	-0.13879739
C	-2.66953706	1.42843361	0.44370787
C	2.81616030	1.14791185	-0.45815743
C	3.67387892	0.51470087	0.44421383
C	5.01349708	0.33300609	0.11332022
C	5.49651407	0.74820585	-1.12642033
C	4.63166087	1.35177875	-2.03783708
C	3.29493564	1.55586507	-1.70765490
C	-3.58377350	0.90466678	-0.47304989
C	-4.93724793	0.86224673	-0.15173186
C	-5.38104404	1.30620548	1.09266453
C	-4.46264859	1.79883333	2.01823232
C	-3.10963439	1.86489080	1.69761125
H	-3.10775260	4.18687021	0.35754420
H	-0.91446181	7.87634717	0.12430811
H	-3.03033962	6.65004401	0.31884437
H	3.53648767	3.84941356	-0.34346269
H	3.70930738	6.30738816	-0.30070775
H	1.72807501	7.74209793	-0.11550014
H	3.29589494	0.16409542	1.39650395
H	5.67731091	-0.14939125	0.82220523
H	6.53767789	0.59079918	-1.38550240
H	4.99541288	1.66252679	-3.01139218
H	2.61913425	2.01898256	-2.41838019
H	-3.23882299	0.53093615	-1.42920290
H	-5.64448329	0.46634543	-0.87222867
H	-6.43472609	1.25680761	1.34392872
H	-4.79739076	2.13059464	2.99520565
H	-2.39275783	2.24229389	2.41867803

#

9.1.15 Atomic coordinates for calculated S_0 state of AS16

#
73
geometry

C	1.84510631	5.62075785	0.32443377
C	1.23425005	6.45206306	-0.60566133
C	0.23642413	5.92623165	-1.42054661
C	-0.11205688	4.5917148	-1.27086094
C	1.45351129	4.28446865	0.42684599
H	2.62108543	6.01625576	0.96615473
H	1.53251495	7.4904772	-0.69107355
H	-0.88252491	4.14408297	-1.88450657
C	-3.97415578	2.79784932	1.25302497
C	-3.87232709	3.16170913	2.58958735
C	-2.62319249	3.12167067	3.20137001
C	-1.52686138	2.72044699	2.45202165
C	-2.83466947	2.4001101	0.55079328
H	-4.93844472	2.82647233	0.76355835
H	-4.75244244	3.47063622	3.14134126
H	-0.53860259	2.6753652	2.88995121
C	-2.84854714	1.99407044	-0.86742008
C	-1.57070481	1.2859044	-2.6821674
C	-4.00580818	1.94367556	-1.64695823
C	-2.68491828	1.21868751	-3.50603527
H	-0.58631524	1.03441842	-3.05407089
H	-4.96600405	2.20440026	-1.22231519
H	-2.57283129	0.90777703	-4.53751777
C	-3.92799991	1.5526521	-2.97757533
H	-4.82218524	1.50938724	-3.58834821
N	-1.63578485	1.66325216	-1.39206019
C	2.01269516	1.14787393	2.19870469
C	2.04875984	3.32863369	1.37986264
C	3.03612237	1.41346842	3.09670381
H	1.55989625	0.16687644	2.14228331
C	3.08233993	3.65497843	2.26020377
H	3.39255781	0.62935041	3.75342183
H	3.49919175	4.65317845	2.27142066
N	1.51967914	2.07355782	1.35548442
C	3.58329969	2.69258569	3.12740455
H	4.38602648	2.93806669	3.8128621
H	-0.26916286	6.53426637	-2.16071926
H	-2.49284645	3.39648664	4.24090593
C	1.52270326	-0.42005345	-1.37218145
C	2.47558041	-1.08102243	-2.14997584
C	3.34643475	-0.34389462	-2.9428531
C	3.24732022	1.04415962	-2.93765122
C	2.28808269	1.6425204	-2.13290666
N	1.43883175	0.93920478	-1.36188275
H	4.08979699	-0.84623793	-3.55073909
H	2.54883073	-2.16088557	-2.12970959
H	3.90361292	1.66060577	-3.53976443
H	2.18383441	2.7188833	-2.09558776
C	0.55339488	-1.11782421	-0.50713142
C	0.43758823	-2.50560006	-0.47906878
C	-0.48360062	-3.09778562	0.37942605
H	1.03966539	-3.12891444	-1.122364
C	-1.13252492	-0.9052879	1.07355087
H	-1.74343742	-0.24040743	1.66932435
N	-0.23880782	-0.31719584	0.25470589

C	-1.2841814	-2.27542838	1.17962116
H	-2.0195035	-2.69926695	1.84896342
N	-0.68275512	-4.49495663	0.42460483
C	0.13341271	-5.58101858	0.22434195
C	-0.70022093	-6.66468132	0.41596587
N	-1.95348727	-4.93174163	0.74384166
N	-1.95124664	-6.2095575	0.7242231
C	-0.36571956	-8.10039722	0.2059757
O	0.60090695	-8.45747587	-0.41653774
O	-1.26776159	-8.90646492	0.76719412
H	-1.02127189	-9.82437295	0.56983027
C	1.58935071	-5.55516655	-0.1073378
O	2.08104437	-4.88937831	-0.98873751
O	2.26614557	-6.35757019	0.70390299
H	3.18054637	-6.44155616	0.38747464
Ru	-0.00766077	1.7526669	-0.05757478
N	0.47460361	3.77802936	-0.37391348
N	-1.61554098	2.36290874	1.15762758

#

9.1.16 Atomic coordinates for calculated S_0 state of AS17

#
73
geometry

C	-1.92651534	-5.46305998	0.19781784
C	-1.32690242	-6.28100272	-0.74823173
C	-0.27243718	-5.78314971	-1.51610995
C	0.17774183	-4.47510236	-1.34167267
C	-0.41117195	-3.62312842	-0.39929562
C	-1.47700836	-4.14531329	0.37846605
H	-2.74272163	-5.85807478	0.79378791
H	-1.67213364	-7.29972619	-0.88504901
H	1.00686906	-4.12579448	-1.94737286
C	3.95773564	-2.61940047	1.35970282
C	3.83791147	-2.95331403	2.70064579
C	2.57616621	-2.95158978	3.29818350
C	1.44144467	-2.61542207	2.56069655
C	1.53081172	-2.26832702	1.20713222
C	2.81884001	-2.28089168	0.61193600
H	4.94122207	-2.62599950	0.90139332
H	4.71760019	-3.21753512	3.27685326
H	0.47583196	-2.63557962	3.05439503
Ir	0.03184237	-1.67483637	-0.03029339
C	2.86426141	-1.92541714	-0.80435309
C	1.57425418	-1.27121280	-2.65317410
C	4.01184700	-1.90709366	-1.60849929
C	2.67776690	-1.24147636	-3.48620517
H	0.58441012	-1.03685411	-3.02188077
H	4.96936653	-2.16831971	-1.17743997
H	2.56006686	-0.97431250	-4.52902873
C	3.92343834	-1.56590835	-2.94728443
H	4.81257879	-1.55562976	-3.56790560
N	1.65466171	-1.59874959	-1.34979612
C	-1.93682406	-1.05624659	2.24150296

C	-2.05150419	-3.22815469	1.35926430
C	-2.94592189	-1.30988852	3.15244333
H	-1.44465913	-0.09355133	2.20030685
C	-3.07943236	-3.53203799	2.26232389
H	-3.26067182	-0.53461201	3.83993609
H	-3.51556998	-4.52233090	2.26009907
N	-1.49734816	-1.97900047	1.36543946
C	-3.52891009	-2.57786100	3.15883738
H	-4.32119471	-2.81725832	3.85947444
H	0.20665306	-6.42183742	-2.25189447
H	2.47553514	-3.22035846	4.34530869
C	-1.54474046	0.60533500	-1.35987243
C	-2.52332553	1.28646112	-2.08827435
C	-3.42456698	0.56547766	-2.86263852
C	-3.33324544	-0.82200684	-2.88916566
C	-2.34789161	-1.43886452	-2.12855008
N	-1.47371112	-0.74853413	-1.38059443
H	-4.18823097	1.08309282	-3.43188049
H	-2.59740724	2.36532624	-2.04238987
H	-4.01423816	-1.42384884	-3.47867256
H	-2.23950297	-2.51646477	-2.10296634
C	-0.54089682	1.29953766	-0.51746976
C	-0.40243180	2.68767525	-0.52547959
C	0.54036128	3.27834770	0.30804048
H	-1.00105307	3.30588434	-1.17554156
C	1.17469981	1.09837693	1.03522627
H	1.78482677	0.42528384	1.62495213
N	0.25308203	0.51624925	0.25018548
C	1.34889110	2.47043986	1.10913563
H	2.10270701	2.90070903	1.75354781
N	0.74336326	4.68257308	0.32272940
C	-0.10585190	5.74799503	0.20277908
C	0.71964559	6.84925971	0.32498661
N	2.02583923	5.13756126	0.52873926
N	2.00013806	6.41862775	0.51694390
C	0.32753920	8.27137738	0.16953514
O	-0.73312483	8.61311939	-0.29046643
O	1.28650985	9.10695909	0.58107593
H	0.97719327	10.01309491	0.42425348
C	-1.58343528	5.68859302	-0.00419336
O	-2.12739106	5.09091887	-0.90116771
O	-2.21785055	6.38041156	0.93895488
H	-3.15975964	6.43390044	0.70914519

#

9.1.17 Atomic coordinates for calculated S_0 state of AS18

#
40
geometry

C	1.78565719	0.55422290	0.36812885
C	3.03231340	-0.06568080	0.47461322
C	4.18122495	0.71112769	0.52304915
C	4.05932126	2.09492504	0.46451040
C	2.79205885	2.64677759	0.34759130

N	1.67595819	1.90309945	0.29954928
H	5.15483758	0.24046029	0.59959774
H	3.11281994	-1.14425920	0.50015841
H	4.92582095	2.74407685	0.49585547
H	2.65280403	3.71732837	0.28057185
C	0.51473915	-0.19545994	0.31943966
C	0.46515215	-1.58607342	0.42118607
C	-0.76312735	-2.22495937	0.33362906
H	1.36254468	-2.16613690	0.56479710
C	-1.79561188	-0.09036744	0.13271150
H	-2.66857839	0.53805957	0.02077001
N	-0.61162613	0.54315677	0.18515231
C	-1.92452591	-1.46620631	0.19432375
H	-2.89712414	-1.93457335	0.13937774
N	-0.86834180	-3.64165816	0.41783224
C	-0.09462544	-4.64508688	-0.08473389
C	-0.75696549	-5.79939296	0.28868981
N	-1.96282203	-4.17586172	1.05351573
N	-1.88140602	-5.45479881	0.97908635
C	-0.29812775	-7.18525443	0.05889438
O	0.80975024	-7.45962901	-0.33442727
O	-1.24174693	-8.09336265	0.34460628
H	-0.85437388	-8.96812075	0.18659739
C	1.17575466	-4.48293768	-0.85445834
O	2.16709774	-3.94519531	-0.42886899
O	1.06112263	-5.01085999	-2.07292394
H	1.92691223	-4.96579142	-2.50982702
Re	-0.35069616	2.72379935	-0.09454024
Cl	0.18141248	2.03431479	-2.46492173
C	-0.69497027	3.15249262	1.76098055
O	-0.89689970	3.40442508	2.87039100
C	-2.18187622	3.15138159	-0.58213020
O	-3.27453212	3.35575583	-0.87872966
C	0.16137057	4.56193325	-0.46723015
O	0.50570945	5.63580723	-0.69336911

#

9.1.18 Atomic coordinates for calculated S_0 state of AS19

#
99
geometry

Ir	-0.00463612	0.18728685	-0.00447877
C	2.23225804	3.13804368	-2.54134254
C	1.63811268	4.35303356	-2.21036770
C	0.64169992	4.37088426	-1.23975517
C	0.26262977	3.17966362	-0.61874293
C	1.80411421	1.99119004	-1.89093606
C	-0.78849508	3.12113807	0.42096668
C	-1.37239049	4.26568061	0.96634457
C	-2.35526337	4.13723294	1.94240967
C	-2.73006106	2.86126832	2.35496201
C	-2.10559550	1.76695490	1.77692640
H	3.00852225	3.09488736	-3.29482089
H	2.23308582	1.02505629	-2.11913612

H	-3.49046761	2.73228897	3.11478159
H	-2.36076975	0.75764083	2.06967232
N	-1.16003790	1.88557170	0.83132717
N	0.84605705	2.00384021	-0.95058474
H	-1.06764228	5.25316528	0.65215034
H	0.16762164	5.30833283	-0.98845109
C	-3.02737714	5.32073517	2.57347634
O	-3.88729643	5.23058087	3.40730600
O	-2.55513239	6.48686405	2.09510832
H	-3.02559337	7.20826121	2.54164249
C	2.09767760	5.59235860	-2.91996332
O	2.96578205	5.59996832	-3.75014491
O	1.42592030	6.68659603	-2.51611347
H	1.76630535	7.44862912	-3.01066936
C	2.93895772	1.92886840	1.61445504
C	3.92584357	2.62781806	2.29672325
C	2.04053892	1.13898019	2.34156426
C	4.03836645	2.55159782	3.69127258
C	3.16915040	1.75368479	4.42450239
C	2.17945281	1.04895132	3.74191838
N	0.99758120	0.35569226	1.85020641
C	0.38262422	-0.33656627	2.80962007
C	-0.95179384	-1.29729710	1.05630489
C	-1.88917498	-2.30447040	0.66659599
C	-0.64614253	-1.24223454	2.42645720
C	-2.27854888	-2.60555334	-0.66261674
C	-2.48333958	-3.12698753	1.66543412
C	-1.26338755	-2.07013788	3.44200440
C	-3.16791729	-3.60178962	-0.97462192
H	-1.84533828	-2.03292211	-1.46534716
C	-3.38906140	-4.12934720	1.37911492
C	-3.76483454	-4.40036995	0.04557580
H	-3.40631542	-3.77744203	-2.01433289
H	-3.78068158	-4.69388767	2.21301398
O	-1.03753347	-2.01691313	4.62780946
O	-2.19709006	-2.97668915	2.99330849
N	-4.65428647	-5.38649101	-0.25347949
C	-5.01440250	-5.66594367	-1.63983364
H	-5.73872963	-6.47644243	-1.66358408
H	-5.47041792	-4.79501265	-2.12068864
H	-4.14549003	-5.97399541	-2.23023043
C	-5.23526879	-6.19795621	0.81082889
H	-5.92379345	-6.91930174	0.37761306
H	-4.46708860	-6.75128262	1.36086023
H	-5.79493540	-5.58331139	1.52284130
S	0.99701869	-0.06776294	4.41621665
H	3.26255165	1.67508267	5.50206986
H	4.81650358	3.10771152	4.20185215
H	4.62844899	3.23569303	1.73702082
H	2.88228900	1.97212138	0.53689007
C	-3.19484697	1.29492254	-1.71256281
C	-4.28279039	1.77159482	-2.43168775
C	-2.16960864	0.62874132	-2.39438021
C	-4.37182840	1.59332496	-3.81859795
C	-3.37403784	0.91370001	-4.50588152

C	-2.28236009	0.43179460	-3.78610685
N	-1.01077041	0.06721803	-1.86097091
C	-0.28036349	-0.56609820	-2.77928591
C	1.18868474	-1.17540218	-0.97691584
C	2.28197759	-1.98206421	-0.53085162
C	0.88614982	-1.25694871	-2.34644612
C	2.70879222	-2.13130055	0.81251293
C	3.01378678	-2.75021165	-1.48041368
C	1.64209410	-2.02697079	-3.31255069
C	3.75280317	-2.94080754	1.18067962
H	2.17948876	-1.59330303	1.58084205
C	4.07520176	-3.56440537	-1.13760115
C	4.48328110	-3.68633348	0.20834927
H	4.01117976	-3.01000192	2.22812147
H	4.56225856	-4.10359089	-1.93729734
O	1.41774854	-2.08497340	-4.49842260
O	2.71428415	-2.73161488	-2.81373161
N	5.52564686	-4.48675463	0.56301935
C	5.91750346	-4.61863138	1.96259159
H	6.76849239	-5.29170664	2.03264515
H	6.21573868	-3.65611392	2.38954032
H	5.10891875	-5.03411408	2.57254637
C	6.24286212	-5.25043303	-0.45244293
H	7.04270860	-5.81481615	0.02063560
H	5.58402876	-5.96013391	-0.96344929
H	6.69255878	-4.59374763	-1.20373566
S	-0.92186152	-0.50430273	-4.39656018
H	-3.44585104	0.75534951	-5.57631171
H	-5.23066039	1.97578786	-4.35857433
H	-5.08285039	2.28229170	-1.90678498
H	-3.15338410	1.41190249	-0.63980052

#

9.1.19 Atomic coordinates for calculated S_0 state of AS20

#
95
geometry

C	2.25497117	5.17904913	2.63954437
C	3.21495435	5.80060910	1.85662420
C	3.28643320	5.49886165	0.49093932
C	2.39387866	4.58461020	-0.07758174
C	1.41686748	3.94410765	0.68796902
C	1.36159002	4.25895808	2.07003928
H	2.20813310	5.41847632	3.69649349
H	2.48629916	4.39578961	-1.14026935
N	-0.41829022	2.67655234	2.10616962
C	-1.95048312	5.38521603	-2.40473826
C	-2.86471000	6.04544384	-1.59928209
C	-2.94870100	5.71189106	-0.24173828
C	-2.11521628	4.72637073	0.29614086
C	-1.18615014	4.04488835	-0.49312310
C	-1.11588743	4.39400163	-1.86601423
H	-1.89324399	5.64983024	-3.45513009
H	-2.21583844	4.51463172	1.35361689

N	0.56023190	2.70471473	-1.95427637
Ir	0.06911655	2.55215627	0.07441281
H	-3.50885719	6.81185441	-2.00994460
H	3.90403956	6.51291532	2.29111216
C	-0.13101328	3.65289786	-2.65421362
C	0.14103184	3.84843812	-4.01302575
C	1.10873690	3.08824537	-4.64899487
H	-0.40300076	4.60492743	-4.56313687
C	1.49866652	1.96933604	-2.57732548
C	1.80402646	2.12635959	-3.91784110
H	1.32403109	3.24571565	-5.69994005
H	2.01627742	1.24420422	-1.96384541
H	2.57348985	1.51342352	-4.37046818
C	0.32639471	3.56114852	2.83399334
C	0.05733622	3.73905650	4.19561464
C	-0.96113749	3.02537112	4.80631047
H	0.64279526	4.44662151	4.76791428
C	-1.40578107	1.98591501	2.70441942
C	-1.70992464	2.12774223	4.04710442
H	-1.17462692	3.17035105	5.85942744
H	-1.96467936	1.31160093	2.06971768
H	-2.52007694	1.55342776	4.47886905
C	4.29765213	6.12610645	-0.40653145
O	4.42624782	5.87597505	-1.58118859
O	5.08198950	7.02266166	0.23314994
H	5.70083637	7.37998940	-0.42149504
C	-3.91177906	6.37943733	0.67965647
O	-4.04328107	6.11246868	1.85016797
O	-4.64651237	7.33482861	0.06715834
H	-5.23794589	7.71350443	0.73502732
C	-3.27606296	-0.21400518	-1.16651673
C	-2.73995574	-1.46714238	-0.95953794
C	-1.42545679	-1.57120719	-0.46950486
C	-0.70449871	-0.38318861	-0.20544279
C	-2.50338579	0.92099716	-0.87972810
C	-0.77346790	-2.81661065	-0.20643924
C	0.65140234	-0.43551271	0.30214527
C	1.29155862	-1.68237942	0.56002186
C	0.52715117	-2.85257989	0.29233140
C	2.61239375	-1.65100348	1.05120539
H	3.14248074	-2.57476212	1.25823922
C	3.23072429	-0.43790933	1.26475551
C	2.53488116	0.74596407	0.98664408
H	-4.28426142	-0.08800844	-1.54248118
H	-3.29927872	-2.37406921	-1.15793918
H	-2.89623768	1.92034285	-1.02443312
H	4.24466066	-0.38340183	1.64226651
H	2.98887650	1.71758336	1.13905441
N	0.80709703	-4.19421278	0.42071959
N	-1.27890355	-4.07148675	-0.37269154
C	-0.32139089	-4.89304375	0.01528344
N	1.28851368	0.74798313	0.51770444
N	-1.25971960	0.84558578	-0.41018495
C	0.73887325	-7.10521136	-0.29624336
C	0.70321788	-8.52011210	-0.30615198

C	-0.36153505	-6.35056561	0.01690085
C	1.79200805	-9.35616976	-0.63493028
C	-0.52099565	-9.14846964	0.00677415
C	-1.62868372	-7.00593005	0.37460080
C	1.67202539	-10.72371113	-0.64306629
H	2.74621111	-8.90367096	-0.88802013
C	-0.66831683	-10.52216525	0.00285802
C	0.42905478	-11.35245846	-0.32175199
H	2.53377420	-11.32308050	-0.90057773
H	-1.63992222	-10.92338026	0.25194368
H	1.66656792	-6.61529694	-0.58462297
O	-2.64565215	-6.47771875	0.71643134
O	-1.61588940	-8.40564317	0.32501850
N	0.30586917	-12.71051219	-0.32934195
C	1.44242952	-13.55819306	-0.67125172
H	1.13944687	-14.60088732	-0.61439640
H	1.79898833	-13.36795055	-1.68887817
H	2.27741368	-13.41435125	0.02203075
C	-0.97353953	-13.33152549	-0.00618289
H	-0.87266179	-14.41265560	-0.06289785
H	-1.29982541	-13.07595865	1.00716645
H	-1.75735519	-13.02814847	-0.70799693
H	1.60730795	-4.60664644	0.87302315

#

9.1.20 Atomic coordinates for calculated S_0 state of AS4.1

#
67
geometry

C	3.16933984	-3.56657702	-0.69589279
C	3.36807446	-4.24867110	0.49774310
C	2.58700138	-3.91291928	1.59921937
C	1.63732223	-2.91090241	1.46202577
N	1.43803480	-2.24371799	0.31051052
C	2.19937210	-2.56519896	-0.77230856
H	3.76797778	-3.81846281	-1.56103767
H	4.11861015	-5.02762034	0.56454862
H	2.70452514	-4.41578820	2.55130639
H	1.01000388	-2.61997141	2.29410299
C	-3.17668071	-3.55898360	0.70401368
C	-3.37677670	-4.24314259	-0.48821323
C	-2.59504260	-3.91122026	-1.59038263
C	-1.64341419	-2.91077257	-1.45527722
N	-1.44280343	-2.24160843	-0.30514248
C	-2.20471542	-2.55938637	0.77836290
H	-3.77583286	-3.80787437	1.56966979
H	-4.12885785	-5.02073622	-0.55341339
H	-2.71354321	-4.41583990	-2.54142114
H	-1.01554893	-2.62277040	-2.28796100
C	0.70072060	2.12955411	0.23097910
C	1.43429856	3.29093587	0.45989861
C	2.75014120	3.20481854	0.90270596
C	3.30653770	1.94341037	1.10848490
C	2.52459544	0.82443217	0.86100402

N	1.25054859	0.89843332	0.43354377
H	1.01111263	4.27444762	0.30147685
H	4.32653173	1.83232915	1.45219346
H	2.91948761	-0.17171842	1.00906849
C	-0.69686506	2.13037947	-0.23595183
C	-1.42799683	3.29266599	-0.46808578
C	-2.74395902	3.20809817	-0.91083796
H	-1.00276309	4.27571636	-0.31230385
C	-2.52340280	0.82736577	-0.86262356
C	-3.30297052	1.94730050	-1.11324812
H	-2.92035642	-0.16835275	-1.00805253
H	-4.32314444	1.83742256	-1.45681185
N	-1.24923676	0.89986251	-0.43525542
Ru	-0.00095238	-0.73458966	0.00106069
C	3.49819240	4.48906530	1.13299932
O	3.00957335	5.57100322	0.95190248
O	4.74945931	4.26619924	1.55619832
H	5.19306769	5.11936684	1.69081227
C	-3.48927242	4.49327292	-1.14480494
O	-2.99840388	5.57468110	-0.96664921
O	-4.74094301	4.27186412	-1.56757630
H	-5.18274025	5.12558332	-1.70462546
C	-1.92597438	-1.77936066	1.99924826
C	-0.60941654	-0.11908662	2.96802829
C	-2.62539749	-1.94029339	3.19688431
C	-1.26706821	-0.23515399	4.18403958
H	0.19634706	0.59073663	2.83614537
H	-3.42547279	-2.66448273	3.27253058
H	-0.97448758	0.39388993	5.01582360
C	-2.29668710	-1.16376566	4.30076112
H	-2.83605011	-1.28204798	5.23329903
N	-0.91975335	-0.86732514	1.89339661
C	0.60888803	-0.12635730	-2.96709758
C	1.92227348	-1.78707956	-1.99478440
C	1.26665174	-0.24590547	-4.18270804
H	-0.19566073	0.58513076	-2.83678552
C	2.62172667	-1.95153290	-3.19192423
H	0.97540179	0.38206379	-5.01577064
H	3.42057147	-2.67724486	-3.26595662
N	0.91766202	-0.87304667	-1.89094017
C	2.29469099	-1.17652151	-4.29736413
H	2.83413186	-1.29748023	-5.22951295

#

9.1.21 Atomic coordinates for calculated S_0 state of AS4.2

#
67
geometry

C	3.21416565	-3.46888691	-0.73180128
C	3.47239825	-4.11615960	0.46737983
C	2.69670310	-3.81780605	1.58910836
C	1.67046827	-2.87673164	1.51314764
C	1.38881431	-2.20357498	0.31814749
C	2.18187088	-2.52110691	-0.81439502

H	3.81965296	-3.70787563	-1.59992174
H	4.26762116	-4.85061263	0.52954469
H	2.88915764	-4.32737876	2.52832954
H	1.08097824	-2.67808293	2.40170876
C	-3.23929983	-3.43572560	0.76072460
C	-3.50258083	-4.09318114	-0.43180746
C	-2.72425531	-3.81274470	-1.55631535
C	-1.69033883	-2.87934354	-1.48968542
C	-1.40340022	-2.19626284	-0.30157274
C	-2.19926217	-2.49568685	0.83396331
H	-3.84701570	-3.66058648	1.63104025
H	-4.30378723	-4.82170509	-0.48666356
H	-2.92084680	-4.33028816	-2.49032650
H	-1.09914931	-2.69453113	-2.38010972
C	0.72104873	2.22147229	0.19026978
C	1.45816609	3.39058098	0.37087219
C	2.79620875	3.31250822	0.74543026
C	3.37386920	2.05760554	0.92845749
C	2.58461459	0.93227002	0.73080750
N	1.29266563	1.00434320	0.37573280
H	1.02368236	4.37085382	0.22755464
H	4.41151047	1.95503520	1.21687873
H	2.98118115	-0.06746304	0.85864565
C	-0.70682243	2.22446311	-0.20848556
C	-1.43779165	3.39668024	-0.39374256
C	-2.77568973	3.32420287	-0.76994137
H	-0.99865591	4.37520689	-0.25269951
C	-2.57631360	0.94298647	-0.74683891
C	-3.35935706	2.07167773	-0.95019019
H	-2.97804225	-0.05516237	-0.87100282
H	-4.39694512	1.97338868	-1.24032697
N	-1.28467007	1.00964487	-0.38962700
Ir	-0.00178514	-0.75434205	0.00096554
C	3.54745959	4.59771517	0.93082760
O	3.05626163	5.68401743	0.77288827
O	4.82387306	4.38798923	1.29279234
H	5.25623864	5.25024862	1.39682926
C	-3.52023094	4.61269061	-0.95967658
O	-3.02443474	5.69685970	-0.80164833
O	-4.79656759	4.40840504	-1.32518878
H	-5.22460488	5.27253070	-1.43175288
C	-1.85920528	-1.76795093	2.05393301
C	-0.42828405	-0.15585747	2.98274166
C	-2.47882889	-1.92473462	3.30130642
C	-1.00780078	-0.27648176	4.23246072
H	0.39439687	0.52499892	2.80899960
H	-3.28656354	-2.63652756	3.41002448
H	-0.64166339	0.32189119	5.05745254
C	-2.05745527	-1.18235341	4.39104436
H	-2.53648388	-1.30819580	5.35570649
N	-0.83539069	-0.87313804	1.91847354
C	0.43050294	-0.18789152	-2.98627153
C	1.84740829	-1.80298810	-2.04150621
C	1.00855274	-0.32639229	-4.23483684
H	-0.38582303	0.50223549	-2.81922264

C	2.46520844	-1.97797178	-3.28728869
H	0.64766275	0.26697062	-5.06571289
H	3.26670403	-2.69785319	-3.38853249
N	0.83121981	-0.89821447	-1.91492135
C	2.04981661	-1.24341997	-4.38456265
H	2.52695999	-1.38401201	-5.34812523

#

9.1.22 Atomic coordinates for calculated S_0 state of AS4.3

#
34
geometry

Re	-0.00249836	1.71017522	-0.05247418
C	-0.00858698	1.97868420	-1.97127669
O	-0.01235433	2.13413063	-3.11588192
C	-1.37486807	3.06907360	0.18644078
O	-2.21600218	3.83785654	0.33965324
C	1.36846429	3.07198309	0.17755361
O	2.20902263	3.84258582	0.32476991
Cl	0.00499387	1.22246414	2.42099736
C	2.88587647	-2.35913610	-0.06160693
C	3.48654921	-1.10159423	-0.10323331
C	2.67200577	0.01883602	-0.14006215
C	0.73815311	-1.27118075	-0.09216975
C	1.49812587	-2.43819438	-0.05647223
H	4.56254883	-0.99293318	-0.10251848
H	3.09661113	1.01305650	-0.16596583
H	1.03852561	-3.41632727	-0.01905998
C	-0.73711354	-1.27274998	-0.08957679
C	-1.49449360	-2.44143128	-0.05304602
C	-2.88241683	-2.36531389	-0.05336099
H	-1.03269839	-3.41865088	-0.01893411
C	-2.67386286	0.01321820	-0.12910749
C	-3.48589761	-1.10898403	-0.09098911
H	-3.10064390	1.00657660	-0.15230531
H	-4.56211785	-1.00261470	-0.08648412
N	-1.33243675	-0.05410735	-0.13296038
N	1.33072464	-0.05132457	-0.13908327
C	-3.65744149	-3.64250566	-0.01048703
O	-3.15718228	-4.73773717	0.01329184
O	-4.98851026	-3.43219742	-0.00283474
H	-5.42211071	-4.29860761	0.02925032
C	3.66374844	-3.63460587	-0.01905479
O	3.16588081	-4.73081424	0.00954153
O	4.99439371	-3.42152549	-0.01770998
H	5.42992396	-4.28695883	0.01461316

#